

Mechanical Properties of Strand PET Foams at Different Length Scales

Von der Fakultät für Ingenieurwissenschaften
der Universität Bayreuth
zur Erlangung der Würde eines
Doktor-Ingenieurs (Dr.-Ing.)
genehmigte Dissertation

von

M.Sc (hons) Amir Fathi

aus

Teheran

Erstgutachter: *Professor Dr.-Ing. Volker Altstädt*

Zweitgutachter: *Professor Dr.-Ing. Alois K. Schlarb*

Tag der mündlichen Prüfung: *6. November 2018*

Lehrstuhl für Polymere Werkstoffe

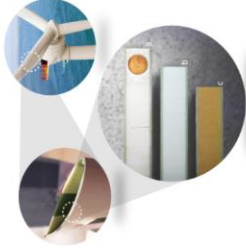
Universität Bayreuth

2018

PET STRAND FOAMS structure-properties

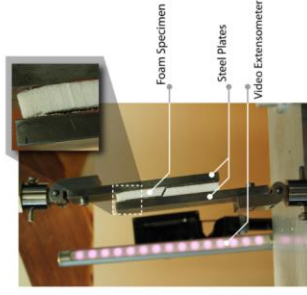
Local Shear

- Sandwich bending method
- Uniformity of deformation localization
- Comparison to PVC foam & Balsa



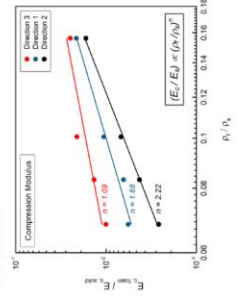
Global Shear

- Effect of foam density
- Shift in mechanism
- Stress concentrations



Effect of Foam Density

- Density scaling laws
- Correlations with microscopic mechanisms
- Shift in deformation mechanism
- Analogies to wood



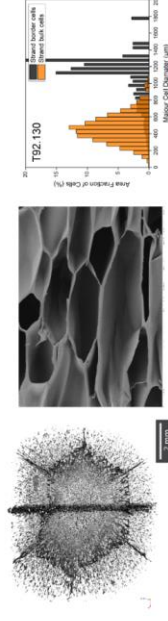
Microscopic Compression

- Cell deformation mechanisms (in-situ SEM)
- Microscopic root cause of anisotropy



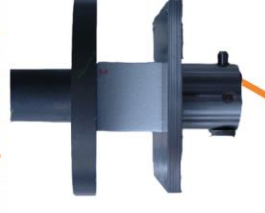
Morphology Definition

- Honeycomb-like structure
- Dual cell type
- Quantitative morphology analysis



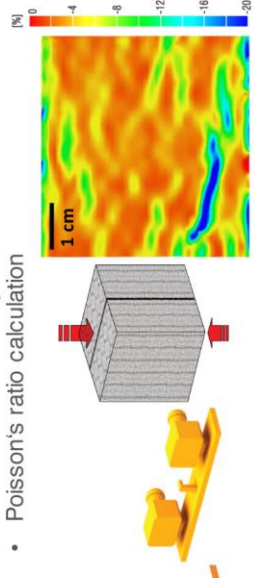
Macroscopic Compression

- Global response
- Stress-strain behavior
- Mechanical anisotropy



Mesoscopic Compression

- Local response (optical analysis)
- Deformation uniformity & localization
- Poisson's ratio calculation



Kurze Zusammenfassung

Kunststoff-Hartschäume weisen einen breiten Einsatz in strukturellen Anwendungen auf. Das mechanische Verhalten von Schäumen wird durch das Eigenschaftsprofil des jeweiligen Basismaterials sowie die Dichte und Morphologie der Zellstruktur des Schaumes bestimmt [1]. Hiervon haben das Basismaterial und die Schaumdichte den größten Einfluss auf die mechanischen Eigenschaften. Daneben kann auch die Zellmorphologie einen erheblichen Einfluss auf die makroskopischen Eigenschaften des Schaumes haben. Das Verständnis des komplexen Zusammenspiels von Zellmorphologie, Zelldeformation und resultierenden mechanischen Eigenschaften des Schaumes ermöglichen zukünftig Schäume mit gezielt verbessertem Eigenschafts-Gewichts-Verhältnis. In der vorliegenden Arbeit werden Struktur-Eigenschafts-Beziehungen von PET-Schäumen (Strand PET Foams) in einem Dichtebereich von 80 bis 200 kg/m³ aufgestellt. Extrudierte PET-Schäume können als eine geschäumte Honigwabenstruktur, gefüllt mit Schaum beschrieben werden. Es wird gezeigt, dass diese Schäume eine zu Holz sehr ähnliche Morphologie aufweisen, da einige Zellen sehr ausgeprägte Dehnungen und Orientierungen in Richtung der Plattendicke aufweisen. Die Kombination der holzähnlichen Mikrostruktur mit der einer Honigwabe führt zu einem deutlich anisotropem mechanischen Verhalten. Für eine quantifizierte Analyse des Morphologieeinflusses wird das Verhalten der Hartschäume unter Druckbelastung auf verschiedenen Längenskalen analysiert und diskutiert. Darauf aufbauend werden durch optische Messungen Vollfeld-Verformungsmuster mit den lokalen Zelldeformationsmechanismen korreliert. Es konnten hierbei zwei fundamental-unterschiedliche Deformationsmechanismen identifiziert werden. Bei einer Belastung orthogonal zur Schaumplatte erfolgt eine starke axiale Deformationsantwort der ineinander verhakten und gedehnten Zellen, gefolgt von einem lokalen, plastischen Knicken der Zellwände. Im Gegensatz hierzu zeigt sich bei einer Belastung in Plattenebene eine plastische Deformation der Zellwände und -stege. Die Deformation unter Belastung in Richtung der Plattenebene erwies sich als geordnet und regelmäßig mit geometrischen Ähnlichkeiten zu einer hexagonalen Form. Auch unterschiedliche Deformationsmechanismen auf Zellebene (Knicken oder Biegen) zeigen unterschiedliche, charakteristische Verläufe in den Druckspannungs-Stauchungs-Kurven. In einem weiteren Schritt wurden die zuvor ermittelten Korrelationen für unterschiedliche Schaumdichten überprüft. Hierdurch wird im Rahmen eines völlig anderen experimentellen Versuchsaufbaus bestätigt, dass die Zelldeformation bei Belastung senkrecht zur Bauteilebene dehnungsdominiert (stretch-dominated) erfolgt und bei einer Belastung in Plattenebene eher eine biegungsdominierte Deformation der Zellen vorliegt (bending-dominated). Die Versuchsergebnisse der Dichtevariationsstudie sowie der in-situ Deformationsmessungen stehen demnach in Einklang und bestätigen die zugrundeliegende Hypothese. Ebenso wurde aufgezeigt, dass bei PET-Schäumen mit hoher Dichte (200 kg/m³) die gemessenen mechanischen Eigenschaften unterhalb derer liegen, die bei Anwendung der Dichteskalierung zu erwarten wären. Die Reduzierung des Zellenaspektverhältnisses bei hohen Dichten bewirkt einen veränderten Deformationsmechanismus, wodurch es zu einer Abweichung der Versuchsergebnisse von den theoretisch zu erwartenden mechanischen Eigenschaften kommt.

Short Summary

Rigid polymer foams are used in a broad range of structural applications. The mechanical behavior of foams is governed by the properties of the base material, the relative foam density (ρ), and the morphological features of the cellular structure [1]. Clearly, the first two, namely material type and relative density, have the highest impact on the mechanical properties. Nevertheless, the cellular morphology, too, can have a strong influence on the resulting macroscopic properties. Foams with complex cell morphologies usually have anisotropic mechanical responses. Understanding the relations between cell morphology, cell deformation mechanisms, and the mechanical properties in such foams will enable future foam generations with even better performance to weight ratios. In the present thesis, structure-properties correlations at different length scales are established for strand PET foam in a density range of 80 to 200 kg/m³. Strand PET foam can be described as a foamed honeycomb, filled with foam. It is shown that the cell morphology of strand PET foam has huge analogies to that of wood, since a fraction of cells are highly elongated and oriented through the panel thickness. The combination of both honeycomb- and wood-like morphology results in strong anisotropy in mechanical properties. Following quantitative morphology analysis, the multi-scale compression response of strand PET foam (T92.100) is identified and discussed. The full-field crush patterns of the foam specimens were correlated to the local cell deformation mechanisms. Two fundamentally different cell deformation mechanisms were observed. When loaded in the out-of-plane direction, the interlocked elongated cells activate a strong axial deformation response, followed by local plastic buckling of the cell walls. This behavior was manifested as several irregular shear bands throughout the specimen thickness. On the contrary, the cell deformation mechanism in the in-plane loading direction is governed by a weaker plastic bending of the cell walls and struts. The full-field deformation maps in the in-plane loading were orderly and regular, with geometrical similarities to hexagonal shapes. A two-stage plastic yielding of the foam cells located in different strand regions caused this regularity in strain fields. Different cell level deformation mechanisms (buckling or bending) also left distinct signatures on the global stress-strain curves. For example, the axial deformation and buckling of the elongated foam cells cause a post-yield softening response in the out-of-plane stress-strain curve. In the next step, the findings are extended to other foam densities. The fitted curves to the property-density data had different slopes for the out-of-plane and in-plane loading directions. This also confirmed, from a completely different experimental approach, that the cell deformation mechanisms in the out-of-plane and in-plane loadings are stretch-dominated and bending-dominated, respectively. The findings from both density-scaling approach and the in-situ deformation measurements agreed well and verified the hypotheses. Last but not least, it is demonstrated that in the high density PET foam (200 kg/m³), the measured mechanical properties are lower than the predicted values using the density scaling laws. The reduction of cell aspect ratio at this density creates a shift in the deformation mechanism. This makes the macroscopic measurements deviate from the theoretical predictions.

Acknowledgements

Firstly, I would like to express my sincere gratitude to my advisor and mentor Professor Volker Altstädt for his continuous support and guidance on my PhD work and throughout my time at the Department of Polymer Engineering. Also, I would like to thank the rest of the thesis committee: Prof. Alois Schlarb for his insightful comments and suggestions, as well as Prof. Dr.-Ing. Uwe Glatzel and Prof. Dr. Nuri Aksel.

My sincere thanks go to the fellow members of the Department of Polymer Engineering and New Materials Bayreuth (NMB) for their kind encouragement and support. I would especially like to thank Andreas Mainz and Alexander Brückner for their help with mechanical tests, Jacqueline Uhm and Anne Lang for their support with microscopy and micro CT measurements. I am grateful to Daniel Raps and Jan-Hendrik Keller for the fruitful discussions and ideas during my thesis. I would like to acknowledge the help and insights from Dr. Julia Gensel and Jürgen Kaiser during in-situ SEM measurements and optical deformation analysis at NMB. Also, I need to sincerely thank Dr. Peter Gutmann for his kind peer review of the thesis and great comments. Furthermore, I would like to thank “Oberfrankenstiftung” for the financial support and funding the project “Sandwich-SIM” (P-Nr. 03796). I would also like to thank the support of the colleagues at the Department of Construction and CAD at the University of Bayreuth.

I would like to thank my family for always being there for me: my mother, Prof. Azizeh Javadi, not only for her scientific support and guidance, but for all the sacrifices she made for my education throughout my academic journey; also my father, Prof. Hamid Fathi, who has always been a role model for me.

And above all, I would like to thank my wife, Ronak, who has been my best partner, friend, inspirer and supporter over the past 10 years. Without her, this would not have been possible.

Amir Fathi

30. May 2018, Erlangen

Material Disclaimer

In the current study, commercial grades of PET foams were used (see Chapter 4.1 for detailed material specifications). To this date, there are only few suppliers for PET strand foams. The material used in this thesis was kindly provided by AIREX AG (Switzerland), which is one of the pioneers in the field of commercial polyester foams. Foam grades, densities, and dimensions were chosen carefully to cover a range of applications for PET foams.

Table of Contents

1	Introduction	1
1.1	Background and Motivation.....	1
1.2	Scope of Thesis	3
2	State of the Art.....	9
2.1	Sandwich Structures	9
2.2	Foam Core Materials.....	11
2.2.1	General Classification	11
2.2.2	Strand PET Foams	15
2.2.3	Polyvinyl Chloride (PVC) Foams.....	20
2.2.4	Polymethacrylimide (PMI) Foams	21
2.3	Constitutive Models of Foam Properties.....	21
2.3.1	Overview of Micromechanical Models.....	23
2.3.2	Bending-Dominated Structures	26
2.3.3	Stretch-Dominated Structures.....	30
2.3.4	Standard Model of Gibson and Ashby.....	34
2.4	Mechanical Properties of Foam Core Materials.....	35
2.4.1	Closed-Cell PVC Foams	35
2.4.2	PMI Foams	41
2.4.3	Extruded Foams	46
2.5	Determination of Foam Core Shear Properties.....	47
2.5.1	Direct Shear Test.....	48
2.5.2	Sandwich Bending Test	50
2.6	Brief Review of Wood's Properties	53
2.7	Optical Deformation Analysis	57
3	Goals of the Thesis	59
4	Experimental.....	61
4.1	Commercial PET Foam.....	61
4.2	Sandwich Specimens (Bending Tests).....	63
4.3	Morphology Analysis	65
4.4	Compression Tests	66
4.5	Shear Tests.....	70
4.5.1	Direct Shear Test.....	70

4.5.2	Sandwich Bending Test	70
5	Results and Discussion	72
5.1	Morphology Analysis	72
5.1.1	Definition of Honeycomb-Like Structure	72
5.1.2	Definition of Dual Cell Morphology	74
5.1.3	Quantitative Morphology Analysis	74
5.2	Compressive Response of PET Foam	86
5.2.1	Global (Macro) Compressive Response	86
5.2.2	Local Compressive Response	89
5.2.3	In-Situ (Micro) Compressive Response	99
5.2.4	Effect of Foam Density on Compression Properties	111
5.2.5	Scaling of Compressive Properties with Foam Density	116
5.2.6	Change of Failure Mechanism with Density	118
5.3	Shear Response of PET Foam	124
5.3.1	Global Shear Response	124
5.3.2	Scaling of Shear Properties with Foam Density	126
5.3.3	Local Shear Response	128
6	Summary	143
7	Outlook and Future Work	145
8	References	146

Recurring Abbreviations

ASTM	American Standard Test Method
DSC	Differential Scanning Calorimetry
EPLA	Expanded poly(lactic acid)
EPP	Expanded polypropylene
EPS	Expanded polystyrene
ETPU	Expanded thermoplastic polyurethane
EVA	Ethylene-vinyl acetate
LDPE	Low-density polyethylene
LM	Light Microscopy
MIP	Maximum Intensity Projection
OCC	Open cell content
PA	Polyamide
PEI	Polyetherimide
PET	Polyethylene Terephthalate
PLA	Poly(lactic acid)
PMDA	Pyromellitic dianhydride
PMI	Polymethacrylimide
PMMA	Poly(methyl methacrylate)
PS	Polystyrene
PU	Polyurethane
PVC	Polyvinyl chloride
SAN	Styrene-acrylonitrile copolymer
SEM	Scanning Electron Microscopy
TPO	Thermoplastic Olefin
TPU	Thermoplastic polyurethane
UTM	Universal Test Machine
VOI	Volume of Interest
XPS	Extruded polystyrene
μ-CT	Micro-Computer Tomography

List of Symbols

b	Sandwich beam width (m)
d	Distance between sandwich facesheets centroids (m)
D	Sandwich bending stiffness (Nm ²)
\bar{E}	Relative foam Young's Modulus
E_f	Young's modulus of the foam (MPa)
E_s	Young's modulus of cell wall material (MPa)
F	Force acting on a cell strut (N)
G	Core shear modulus (MPa)
I	second moment of area of a cell strut
l	Cell wall or strut length (m)
L_1	Loading span length in sandwich bending (m)
L_2	Support span length in sandwich bending (m)
M_f	Fully plastic moment of a cell strut
p_0	Initial gas pressure in a foam cell (MPa)
P	Midpoint force in sandwich bending tests (N)
t	Cell wall or strut thickness (m)
t_f	Sandwich facesheet thickness (m)
t_c	Sandwich core thickness (m)
T_g	Glass Transition Temperature (° C)
U	Sandwich shear stiffness (N)
w_t	Midpoint deflection in sandwich bending tests (m)
$\bar{\rho}$	Relative foam density
ρ_f	Foam density (kg/m ³)
ρ_s	Density of cell wall material (kg/m ³)
σ_f	Maximum normal stress (tension/compression) in facesheets (MPa)
$\bar{\sigma}_{el}$	Elastic buckling collapse stress of elastomeric foam (MPa)
$\bar{\sigma}_{pl}$	Plastic collapse stress of plastic foam (MPa)
$\bar{\sigma}_{cr}$	Crushing strength of brittle foam (MPa)
$\sigma_{y,s}$	Yield stress of cell wall material (MPa)
$\sigma_{y,f}$	Yield stress of foam material (MPa)
$\sigma_{MOR, s}$	Modulus of rupture of cell strut material (MPa)
τ_c	Maximum shear stress in the core (MPa)
ν_{ij}	Poisson's ratio when compressed in direction i and extended in direction j
ϕ	Fraction of solid material contained in the cell struts
$\phi - 1$	Fraction of solid material contained in the cell walls
ΔK	Stress Intensity Factor

1 Introduction

1.1 Background and Motivation

Today, man made foams have found numerous applications in insulation, packaging, filtering, cushioning, sports, bioengineering and structural applications as sandwich core materials. However, most synthetic foams are still inferior to natural cellular materials in terms of performance to weight ratio. Natural foams such as wood, bone, coral, and cork [2] are morphologically optimized to provide the most efficient balance between mechanical properties and weight. Based on their load-bearing requirements, they have evolved over millions of years and perfected their microstructural features. The high strength and stiffness to weight ratios of natural cellular materials are usually the result of how the solid material is distributed within their cellular structures. This highlights an important fact: The cell morphology of a cellular structure (or foam) can have significant influence on its mechanical properties. Anisotropic cellular materials usually have complex morphologies and directionality in their cell structures and consequently properties. For example, the stiffness of wood can be up to 10 times higher when loaded along the grain direction.

In materials engineering, it is well-established that besides the inherent material properties, the processing method can highly influence the final properties of a component. In the world of polymer foams, in particular, the link between processing and properties is made through the cellular morphology and microstructure (beside the change in material properties caused by processing). Most polymer foams have rather simple cell structures and are either isotropic or only slightly anisotropic. Tuning the cellular structure of foams with the aim of exploiting the benefits of structural anisotropy has been less considered in the past, possibly due to the limited processing capabilities. However, with recent developments in foam processing methods and die technologies, it is anticipated and desirable to tailor the cell structure according to the target applications' requirements. This approach can help to elevate the lightweight performance of engineering foams and achieve most optimum properties. Inducing the desired cell morphology through process variations can include adjusting the cell size for insulation applications; modifying cell shape and orientation for better mechanical properties in specific directions; and controlling the effect of cell gas through open cell content (OCC). These and other morphological features can be varied during the foaming process and have large impacts on the final properties of the foam. Nevertheless, the cell morphology-property correlations must be first understood before they can be efficiently applied to the processing methods.

With this said, as a technically relevant polymer foam with complex process-induced cell morphology, strand PET foam is considered. Strand PET foam is produced through an extrusion process with a special die technology. At the end of the extruder, the polymer melt is transferred through a multi-hole breaker plate, which helps to achieve larger expansion. The individual expanding strands leaving the breaker plate are then pressed together through a calibration unit to create the foam sheets (see chapter 2.2.3 for a full description of strand foam extrusion process). Therefore, this thesis will provide a platform for understanding the structure-property relations in strand foams. The findings can be then applied to optimizing the existing processes or developing new ones. Being based on semi-crystalline polyesters, PET foams have recently become more attractive as structural sandwich core materials. Commercial strand PET foam panels are processed through state-of-the-art foam extrusion method, yielding a multi-scale foam structure with multiple types of cell shapes, sizes, and aspect ratios. The foam properties are anisotropic, and the out-of-plane stiffness and strength can be up to 3 times higher than the in-plane values. However, the underlying links between cell morphology, cell deformation modes, and the anisotropic macroscopic properties have not been systematically discussed in the literature.

In the past few decades, several empirical approaches have been suggested for creating models to predict the mechanical properties of open-cell and closed-cell foams. One mutual objective of these works has been relating the foam properties to density and cell morphology. In this case, some approaches treat the foam material as a continuum similar to compact materials [3–10]. Other classes of more complex models include micromechanical considerations, where information is needed about the actual cellular structure of the foams [10]. For simple foam geometries, with idealized equiaxed unit cells, the analytical models can provide meaningful predictions, which are verified with experimental data [2, 11, 12]. Nevertheless, moving from idealized cell morphologies to complex cell structures, the conventional models fail to correctly capture and predict the properties. One root cause for this inability is that the underlying modeling logics usually assume a single deformation mechanism dominating other deformation modes at all densities. Consequently, the mathematical relations extracted are based on the assumed deformation mechanism(s). However, in many cases, the deformation mechanism changes with foam density as a result of the spontaneous change in cell morphology [13, 14]. Obviously, in such cases, the model predictions will no longer be accurate unless the actual changes in the deformation modes are taken into account. Here too, the unique cell morphology of strand foams and the interesting links between different scale deformation phenomena are both technically and scientifically relevant. The obtained knowledge will enable

more reliable and realistic models, which are capable of correctly predicting the macroscopic behavior of the foams. Correct material models are crucial to design optimization of parts, and give potential for further sustainability improvements.

1.2 Scope of Thesis

In order to highlight the positioning of strand PET foams and the scope of this thesis, it is helpful to provide a global classification of structural foams based on their processing methods. Each specific processing method can be utilized to yield foam products, which usually share similarities in their cellular morphologies and the resulting properties. The specific morphological features induced by the foaming process method will then control the mechanical properties, of course together with the base solid materials properties. From a processing perspective, structural polymer foams can be mainly divided into three categories: block molded foams, bead foams, and extruded foams. Foam injection molding is not considered in this classification, as it usually yields structures including a combination of foamed and compact regions. **Figure 1** shows exemplary Scanning Electron Microscopy (SEM) images of foams made through each of these processing roots. Chemically molded foams usually have homogeneous cell sizes and, in some cases, a slight orientation of the cells in the foam rise (expansion) direction. Therefore, most molded foams are either isotropic or slightly anisotropic in properties (see Chapter 2.5.1). Examples of structural foams belonging to this category are polymethacrylimide (PMI), polyvinyl chloride (PVC), polyurethane (PU), and epoxy foams. Bead foam (or particle foam) components are made by thermally fusing expanded (or pre-expanded) foamed beads. Examples of commercially available bead foams are expanded polystyrene (EPS), expanded polypropylene (EPP), and expanded thermoplastic polyurethane (ETPU).

The foamed beads themselves are produced through either a pressurized vessel expansion method (batch process) or continuous foam extrusion coupled with a breaker plate and a pelletizing unit. In addition, expandable polystyrene (EPS) pellets carrying blowing agent(s) in their bulk are usually produced through suspension polymerization and expanded to desirable densities in a pre-foaming step. The cell morphology of individual beads could be either homogeneous or extremely heterogeneous depending on the type and configuration of the manufacturing process (see **Figure 1**).

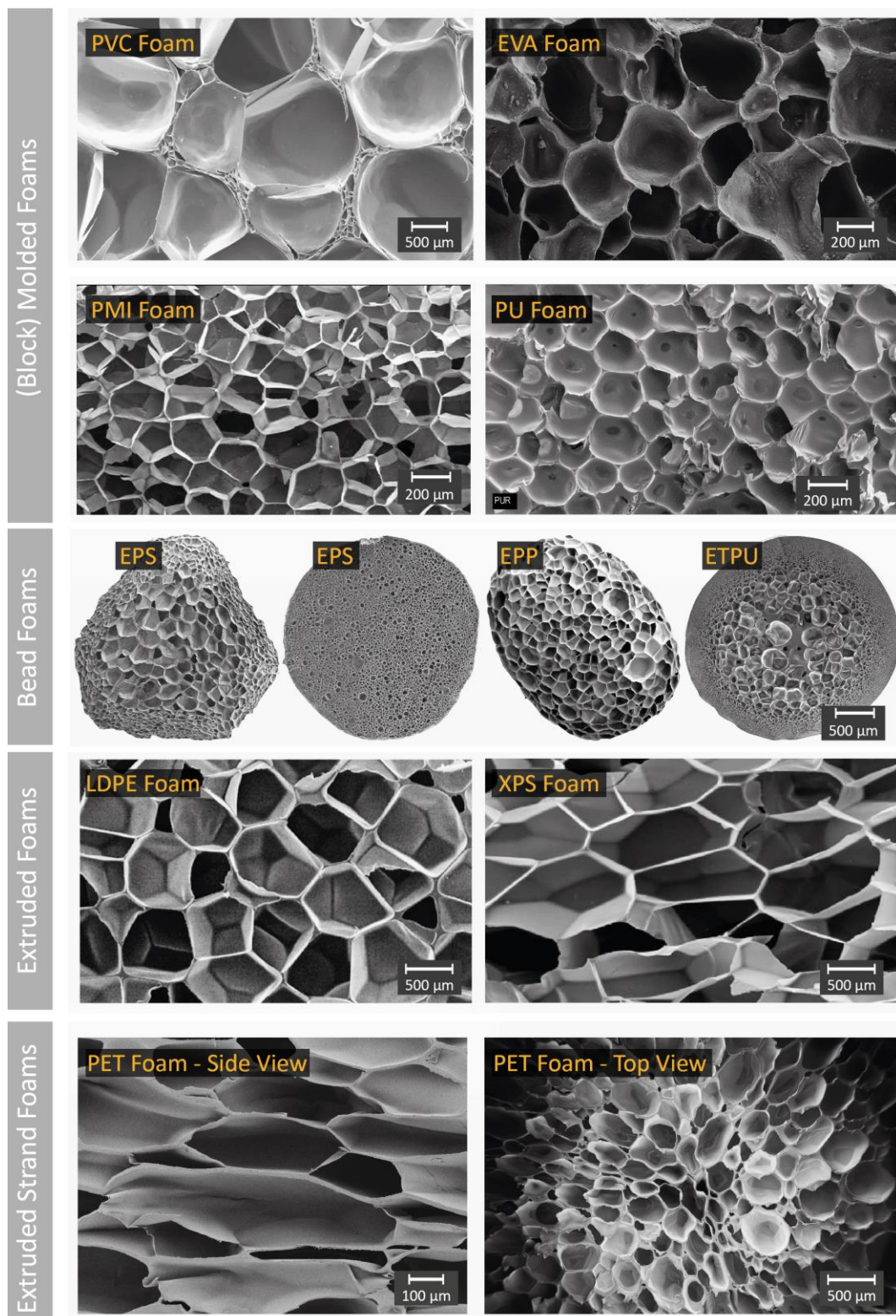


Figure 1 Classification of polymer foams based on their processing methods (Some images are reproduced from [15–18] and courtesy of the authors).

Morphological variations such as solid skin thickness and radial cell size distribution can be created by applying relevant process parameters. The bead morphology has immense effects on the mechanical properties of the molded components. For example, beads expanded through a batch process usually have fewer and larger cells near the bead center (thicker cell walls) and a higher cell density region near the bead skin. This radially-varying cell morphology creates an integral reinforcing effect in vessel expanded bead foams. In contrast, the cell morphology is very different in most extruded bead foams. Extruded bead foams usually have regular cell sizes across the whole bead cross-section. At a macroscopic level, the global properties of bead foam components are usually isotropic, especially for thicker parts with small variation of density through thickness.

Unlike most block molded foams and bead foams, extruded polymer foams usually show anisotropic mechanical properties. In many cases, this is due to the cell orientation, imposed by the extensional melt stresses during foam expansion. Mechanical properties of extruded foams are less studied in the literature. Hence, understanding the structure-properties relations in extruded foams can provide a basis for further developments and engineering opportunities. **Figure 2** shows compressive stress-strain curves of foam samples corresponding to the three processing categories mentioned above. The EPP sample (30 kg/m^3) shows fully isotropic properties, while the PVC foam (60 kg/m^3) behaves transversely isotropic with somewhat higher yield strength in the out-of-plane direction. In contrast, the stress-strain curves of the extruded strand PET foam in different loading directions suggest a highly anisotropic mechanical response. For a sample with nominal density of 110 kg/m^3 , the compression modulus and strength in the out-of-plane direction are almost 3 times higher than the in-plane (transverse) directions. The yielding signature and the stress variation in the plateau region of the curves also suggest completely different failure mechanisms for different loading directions. The root cause for the mechanical anisotropy of PET foam is its unique cell morphology.

Mechanical properties of typical chemically molded foams (e.g. PVC and PMI foams) and the more classical bead foams (e.g. EPS and EPP) are well studied in the literature. This includes some fundamental conclusions about their structure-property relations (see Chapters 2.4). In contrast, literature works on extruded structural foams is scarce. Except for the limited works on extruded polystyrene (XPS) and low-density polyethylene (LDPE) foams [19–21], the structure-property correlations in extruded foams are less known. In extruded foams, the cellular morphology is more complex, and the mechanical responses are usually anisotropic. This is especially true for extruded strand foams.

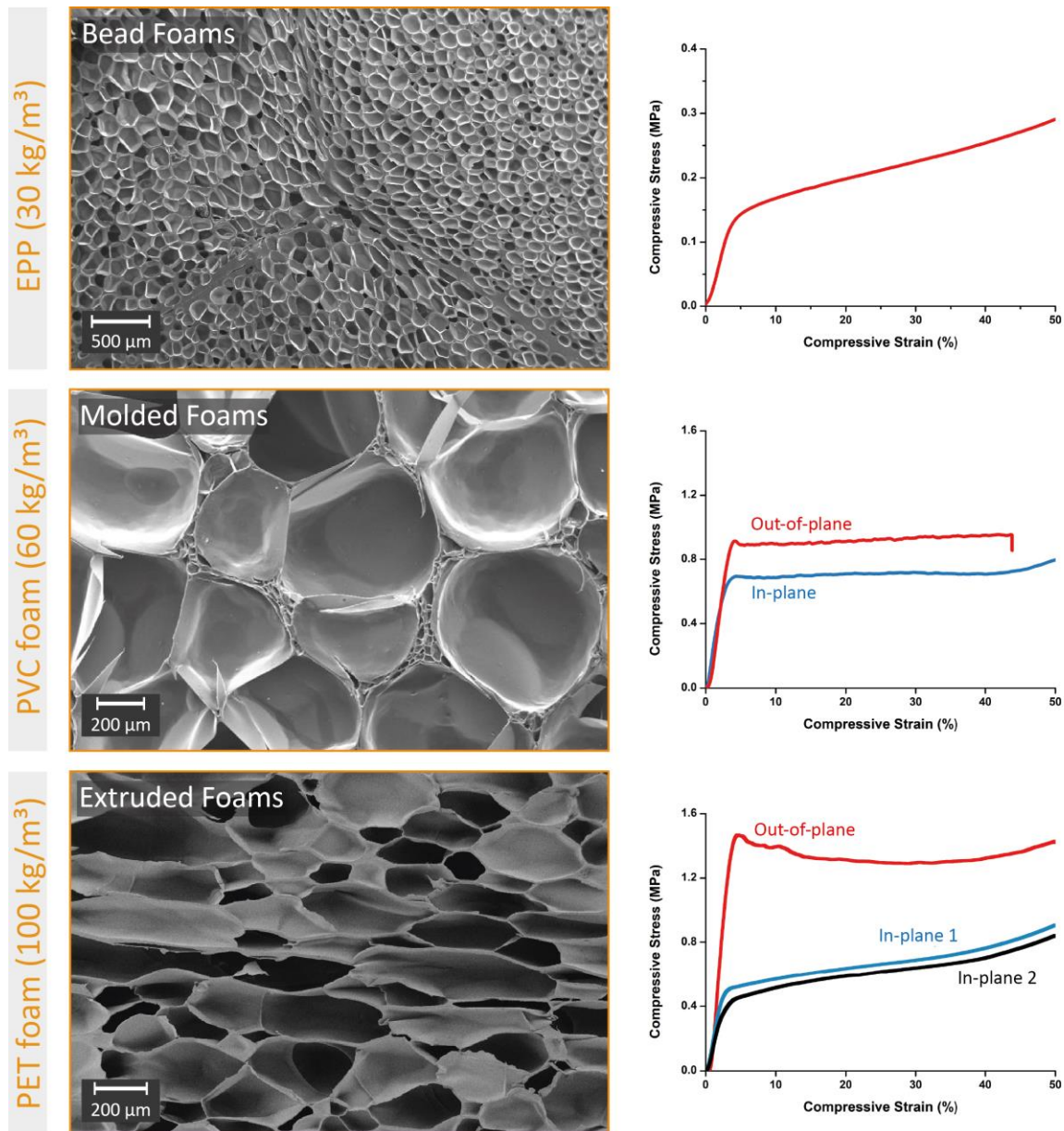


Figure 2 Compressive stress-strain curves of EPP (top), cross-linked PVC foam (middle), and strand PET foam (bottom).

The strand foam technology has the potential to be applied in foaming polymers with low melt strengths and elasticities. Therefore, understanding the fundamental relations between their unique structures (determined by the process) and the resulting mechanical properties is essential. Strand PET foam can be structurally described as a foamed honeycomb, which is filled with foam. **Figure 3** shows a schematic break down of the morphology of strand PET foams. The hexagonal strands are formed and expanded during the foam extrusion process using an orifice die, which is sometimes referred to as breaker plate (see **Figure 7** in chapter 2.2.2).

After the die, the individual expanding strands are pressed together by a calibration unit and are packed together to form the final foamed extrudate with minimum inter-strand defects and/or voids. The density mismatch between the strand surface and strand bulk results in the higher density hexagonal border regions. The higher density zones can be recognised in the μ -CT image of a single hexagon shown in **Figure 3**. The foam panels also have two different types of cell shapes and sizes in the strand border and strand bulk zones. Hence, the mechanical properties of strand PET foams are governed by a combination of honeycomb-like and wood-like material responses, which will be fully presented and discussed in the results chapter. This is a unique behavior for polymer foams, and the learnings can be further extended to fit the needs of newer applications.

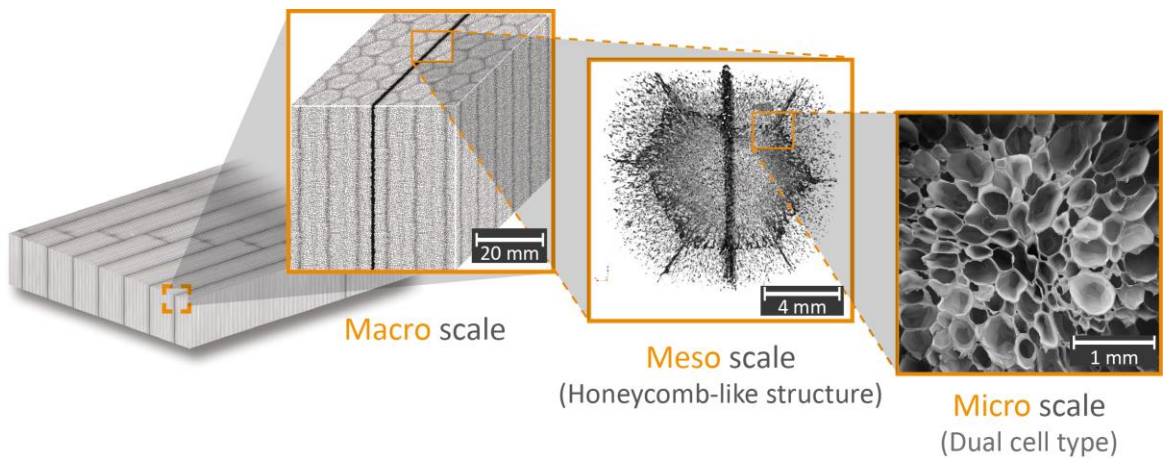


Figure 3 Multi-scale morphology of commercially available strand PET foams.

It is both scientifically and industrially relevant to understand the role of the unique multi-scale morphology of PET strand foams on their anisotropic macroscopic mechanical properties at different foam densities. Once the relations between the cell deformation (micro), the local crush patterns (meso), and the global specimen deformation (macro) are understood, the learnings could be applied to optimize the properties according to different applications. This includes extending and applying the knowledge to other types of strand foams. Beside the in-service application requirements, thermoplastic PET foams are often used in manufacturing methods, which involve mechanical loads applied on the foam components. Examples of these processing methods are thermal compression molding or prepreg technologies. In most sandwich processing methods, the core material is exposed to different levels of compressive stresses. Therefore, it is also important to understand the behavior of the foam panels at different densities and in different loading directions.

In the results chapter, at first a comprehensive definition of the foam structure is provided (chapter 5.1). These quantitatively determined morphological features can be also used to build more realistic constitutive material models (e.g. for FEM purposes) to predict the properties of strand foams. Detailed information about the strands (hexagon dimension, skin thickness, etc.) and cell morphologies (cell shape, size, aspect ratio, wall thickness, etc.) are obtained through multiple state-of-the-art microscopy techniques and reported for the range of foam densities studied in this work. After morphology definition, the mechanical properties of strand PET foams are studied in compression and shear in chapters 5.2 and 5.3. The investigations are made on a range of foam densities (80 to 200 kg/m³), covering the boundaries of current commercial grades available and most practical applications. The links between different level deformation mechanisms are made in a way that one could understand how the cell deformation behavior can dictate the local deformation and consequently the macroscopic mechanical properties. The microscopic deformation mechanisms of the foam cells are discussed in chapter 5.2.3. The in-situ SEM visualizations of cell deformations are later linked to the local sample deformation maps. This whole chain of deformation mechanisms at different length scales can be also used for verification of multi-scale FEM simulations. In Chapters 5.2.4 to 5.2.6, the effect of foam density on compression properties and the shifts in deformation mechanisms due to density change are presented. Furthermore, the information about properties-density scaling and the fitted data were correlated to the morphological features and the activated microscopic deformation types. Moving to chapter 5.3, the shear response of PET foams are also studied using two different methods, which are both commonly applied in the literature and industry. The effect of foam density on shear properties is identified and discussed using direct foam shear test. In parallel, sandwich bending tests are utilized to represent “close-to-practice” loading conditions and obtain information about the local shear deformation maps and failure patterns. The sandwich testing experiments also involved specimens with two other core materials namely Balsa wood and PVC foam as benchmark.

2 State of the Art

2.1 Sandwich Structures

For almost a century now [22], sandwich structures have been used in diverse industrial applications to provide lightweight flexural stiffness and strength. The sandwich concept can be expressed as increasing the bending stiffness of a panel without adding significant weight. This can be realized by separating two stiff face sheets using a lightweight core material (see **Figure 4**).

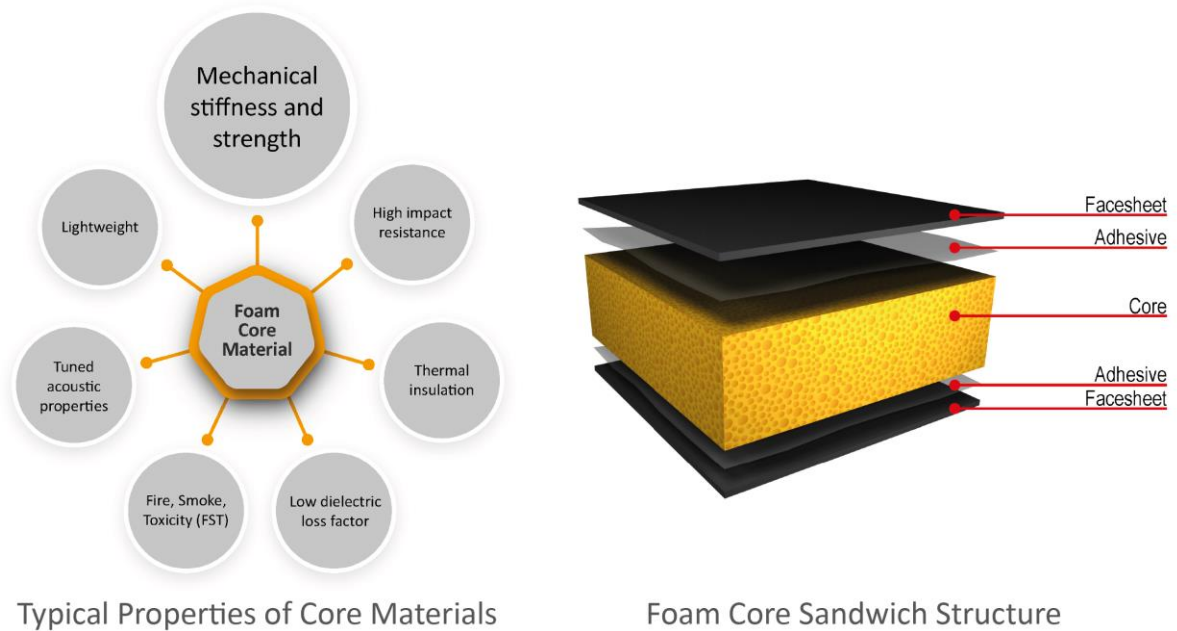


Figure 4 Components of a sandwich structure (right) and different functionalities reported for advanced foam core materials (left).

When a sandwich beam is loaded in flexure, bending loads are carried by the *facesheets* in form of in-plane compression and tension stresses. Thus, sandwich face sheets are usually made of strong and stiff materials such as steel, aluminum, or polymer composites. Fiber reinforced composite face sheets, for example glass fiber or carbon fiber reinforced epoxies, can be used to fulfill a range of requirements such as anisotropic mechanical properties, freedom of design, and good surface finish. On the other hand, the main function of the *core material* is to support the face sheets, prevent their buckling and keep them in relative position to one another. Earlier designs of sandwich panels were often based on metal honeycombs or wood as core materials. However, the introduction of polymeric foams revolutionized the range of sandwich applications

due to a wide variety of possible materials, densities, functionalities, and available processing methods [23, 24]. In addition to their desirable lightweight nature and mechanical role, polymer foam cores can offer additional advantages due to their inherent cellular structure. This includes special thermal, acoustic, and dielectric properties, which give them functionalities like heat and sound insulation. Foam cores have relatively high impact strengths and very low resin uptake.

Today, advanced foam cores play a major role in aviation, marine, automotive, wind energy, sports and several other industries. However, being usually the weakest component, the mechanical properties of the core material are critical for the global stability and mechanical response of the sandwich assembly. It is true that the whole sandwich structure gives the desired effect, but the core material must fulfill the most complex mechanical requirements. In particular, the core material must have sufficient shear and compression strength and stiffness to provide global stability. To highlight the importance of shear and compression properties, **Figure 5** shows examples of core shear failure (PVC foam) and core compressive failure (PU foam) in sandwich four-point bending tests.

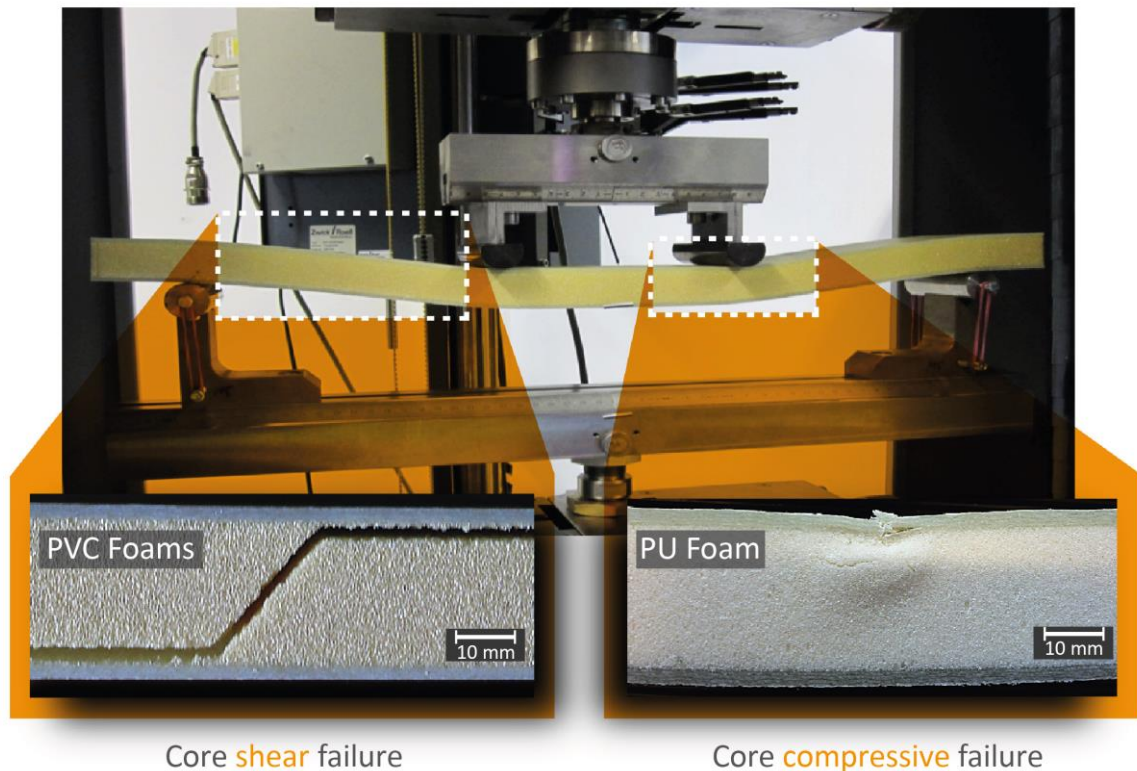


Figure 5 Frequently observed failure modes of sandwich core materials. Left: core shear failure; Right: core compressive failure.

Although shear is usually the dominant stress mode in the core material, normal stresses (compression and tension) could be also significant and sometimes comparable to shear stresses in magnitude. Most applications of foams involve compressive loading [25]. The out-of-plane (through thickness) compression response is important for stabilizing the foam during most typical applications as well as the manufacturing processes. In sandwich structures in particular, out-of-plane compression properties of the foam core are critical near the loading and/or support points (see the right image in **Figure 5**). In-plane compression properties, on the other hand, are crucial in bending applications with large span lengths, where normal stresses become increasingly larger and can compete with shear stresses [26]. The scope of this thesis, and the findings and discussions thereof, are about structure-property relationships in strand PET foams. This is a new generation of thermoplastic foam cores with unique static and fatigue mechanical properties.

In order to comprehend the correlations shown for strand PET foams, it is first helpful to understand their positioning among other foam types. Therefore, in the following a brief introduction is given to the most popular foam core materials (chapter 2.2), followed by a review of the theoretical models available for predicting foam properties based on information about density and cell morphology (Chapter 2.3). In Chapter 2.4, a summary of the literature works on the mechanical properties of PVC, PMI, and some other foams is reviewed. Finally, the available methods for measuring core shear properties are discussed in Chapter 2.5, and a review of the literature conclusions thereof is given.

2.2 Foam Core Materials

2.2.1 General Classification

With advances in material recipes, new processing techniques, and die/mold technologies, several thermoplastic and thermoset foams are today commercially available in a broad density range. These foams can offer different physical, chemical, and mechanical properties. According to Ashby [11], by foaming a solid material, a range of elastic moduli can be achieved spanning up to four orders of magnitude. Low-density foams ($\rho/\rho_s \sim 0.01$) collapse under small stresses, whereas denser foams ($\rho/\rho_s \sim 0.05$) are used in load-bearing applications [2]. The foam properties are highly controlled by the inherent properties of the base polymer material. Foams made of elastomers show elastic properties, while foams made of ductile thermoplastics can absorb energy by yielding and large plastic deformations. Similarly, brittle materials can be used

to make foams with high strength and stiffness, yet brittle crush behavior. Moreover, other properties of the base polymer material such as strain rate sensitivity, temperature dependency, and creep behavior usually govern the same properties in the foams.

Foams based on commodity polymers such as polyolefins, poly(methyl methacrylate) (PMMA) and polystyrene (PS), and poly(lactic acid) (PLA) are mainly used in packaging, protection, and construction (e.g. insulation) applications due to their low density, high impact resistance, and low thermal conductivity [21]. Soft and flexible foams (with elastomeric behavior) are more suitable for sports, leisure and furniture sectors, since they can offer suitable mechanical properties such as cushioning response, controlled resilience (and hysteresis), and little plastic deformation [21]. Examples of flexible foams include ethylene–vinyl acetate (EVA), polyurethane (PU), and thermoplastic polyurethane (TPU) foams. On the other hand, rigid foams based on PVC, PU, PET and styrene–acrylonitrile copolymer (SAN) are largely utilized as structural sandwich core materials in marine, wind energy, and construction [27]. Foams based on technical and high temperature polymers, such as polymethacrylimide (PMI), polyamide (PA), polyetherimide (PEI), and polyarylsulfones can be used in more advanced applications such as aerospace and automotive. Technical polymers usually offer higher performance in terms of thermo-mechanical properties and chemical resistance. **Table 1** summarizes the classification of polymer foams based on target application(s).

The focus of the present thesis is on rigid thermoplastic strand PET foam, which is finding newly emerging structural applications in wind industry, automotive, marine, and other industries. In most applications, especially as structural sandwich core materials, the typical counterparts to PET foams are PVC, SAN, and PMI foams. Also, the range of available densities and the mechanical properties are rather comparable in these rigid foams. **Figure 6** compares the compressive and shear modulus of rigid PVC, SAN, PMI, and PET foams in the commercially available density range (data reported in **Figure 6** is extracted from the manufacturers' datasheets). One can see that for the same density, PMI foam has higher compressive and shear modulus than other foam core materials. The properties of SAN, PVC and PET foams are rather comparable in the density range of 50 to 150 kg/m³, which is relevant for most structural applications.

Table 1 Classification of commercially available polymer foams based on target applications.

Category	Base Chemistries	Typical Applications	Main Properties
Commodity	PMMA, PS, Polyolefins (PE, PP, TPO), PLA	Packaging, Protection, Construction, Insulation	Low density, Impact resistance, Low thermal conductivity, Price friendly
Elastomeric	EVA, PU, TPU	Cushioning, Sports, Leisure, Household, Furniture	Soft and flexible, controlled resilience, Low plastic deformation
Rigid	SAN, PVC, PET, PMI	Structural Applications, Sandwich Structures , Construction, Marine, Wind Energy	High stiffness and strength , Fatigue resistance, Moderate thermal resistance, Low water uptake
Technical / Performance	PMI, PA6, PA12, PEI, Polyesters (PBT, PET)	Aviation, Aerospace, Automotive, Printed Circuit Borads (PCBs)	High stiffness & strength, High thermal resistance, Chemical resistance

Therefore, in order to provide a benchmark for direct application-oriented comparison, PVC and PMI foams are frequently mentioned and referred to in this thesis. Both PVC and PMI foams are among most frequently used sandwich core materials and are perceived as competitors to PET foams. SAN foams are not considered in this thesis, as their applications are still limited compared to PVC and PMI foams. From an economical standpoint, PVC foams are still cheaper than PMI and PET foams. Nevertheless, there are major environmental concerns associated with the use of PVC products. On the other hand, PET foams are recyclable and produced, at least partially, from recycled materials. Today PET foams are also much cheaper than their first introduction in the early 2000s. According to an unofficial report by a supplier, the price of strand PET foam in 2014 was almost 50 % lower than its price back in 2006. This is probably due to the more established processing techniques and improvements in recipes and equipment. In the following, some background information is given for PET, PVC, and PMI foams as well as

their processing methods. In chapter 2.4, a more thorough literature review is given on the mechanical properties of these rigid foam core materials.

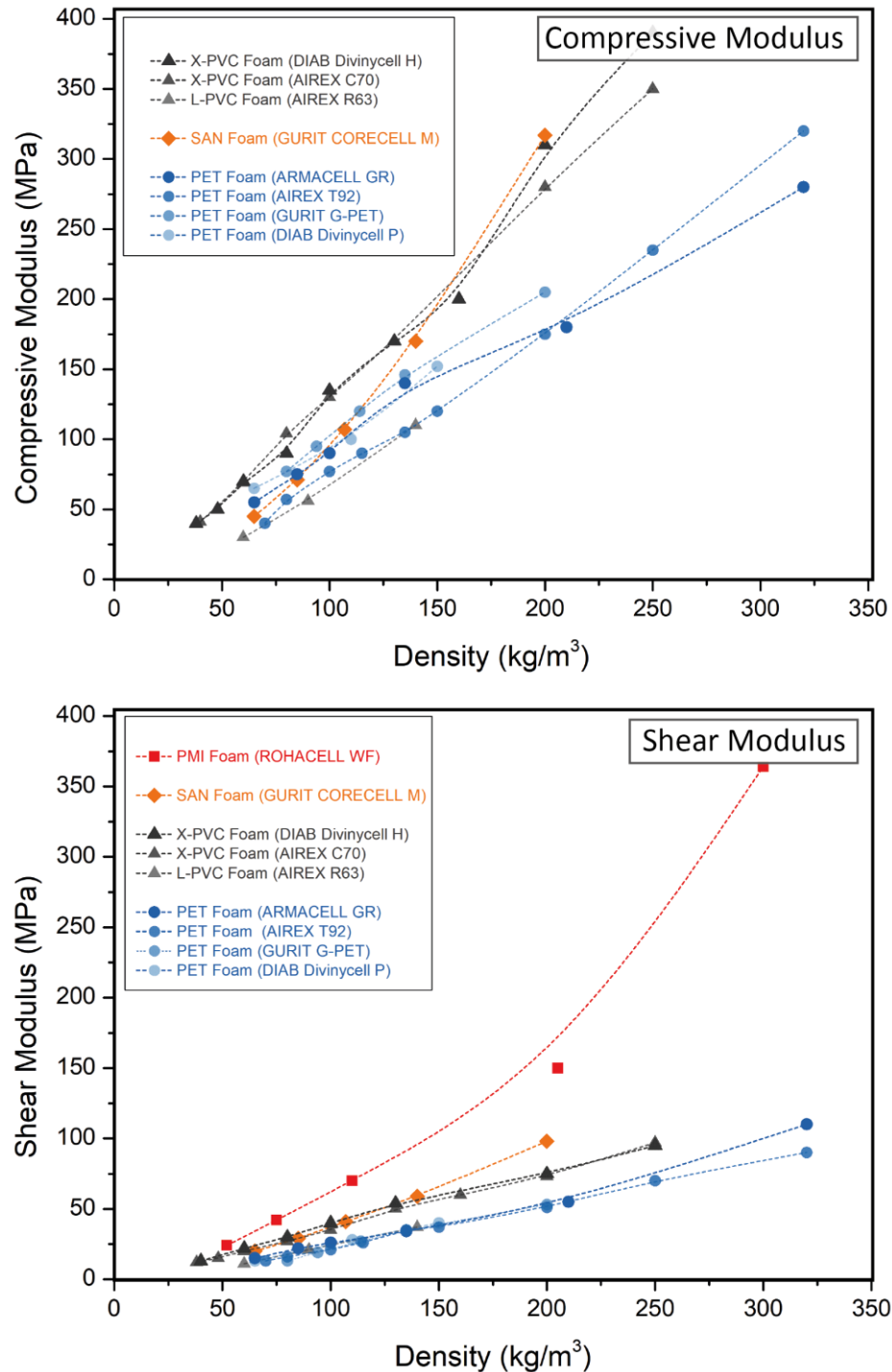


Figure 6 Comparison between the mechanical properties of commercially available PMI, SAN, PVC, and PET foams (from 2018 manufacturers' datasheets).

2.2.2 Strand PET Foams

Extruded PET foams are receiving growing attention as relatively new structural core materials. Due to key advantages, PET foams could be suitable alternatives to traditional sandwich core materials. These polyester-based foams are thermoformable and have good thermal stability (up to 150 °C processing temperatures and above 100 °C long-term thermal stability). This makes them suitable for prepreg methods and resin systems with relatively higher curing temperatures. PET foams are reported to have low density, relatively good fatigue performance, and high chemical and thermal resistance [28–30], but their static strength and stiffness are usually lower than PVC and PMI foams of comparable densities (see **Figure 6**). PET foams are compatible with a variety of processes including lamination, thermoforming, vacuum forming, compression molding, and resin infusion [30]. Also, PET foams can be heated and pressed into complex geometries, in combination with thermoplastic face sheets. This makes it possible to create high impact resistant full thermoplastic sandwich structures with complex profile shapes, enabling them to be used in emerging applications including automotive industry. Being made from semi-crystalline polyesters, PET foams are chemically resistant to many solvents and have low dielectric properties. Last but not least, from a sustainability perspective, PET foams are recyclable, and are partially produced from recycled materials [31]. One general drawback of most polyester foams is hydrolysis instability though.

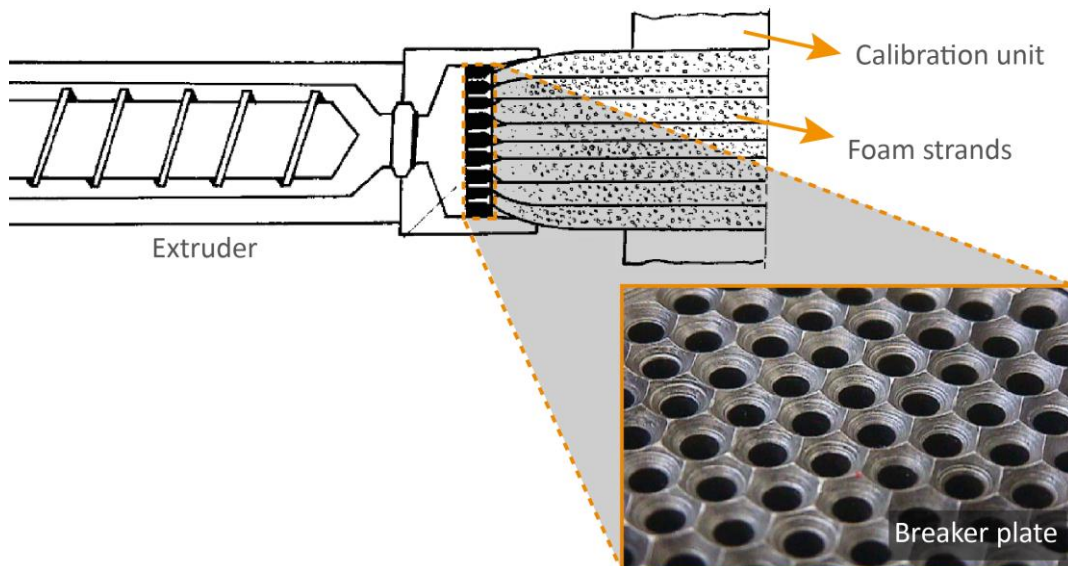


Figure 7 Schematic illustration of the extrusion die technology usually applied to create strand foams [36, 37].

Most commercial PET foams are processed through the (coalesced) strand foam extrusion technology. This method was first developed and introduced in the early 1990s by The Dow Chemical Company for producing low density polyethylene (PE) and polypropylene (PP) foams [32–35]. The main difference compared to classical foam extrusion is the die technology, which enables expanding and stabilizing low melt strength polymers (see next paragraph). In strand extrusion method, instead of a slit die, the gas loaded melt is transferred through a breaker plate, after which several individual foam strands expand and are pressed together to yield low density foam sheets (see **Figure 7**).

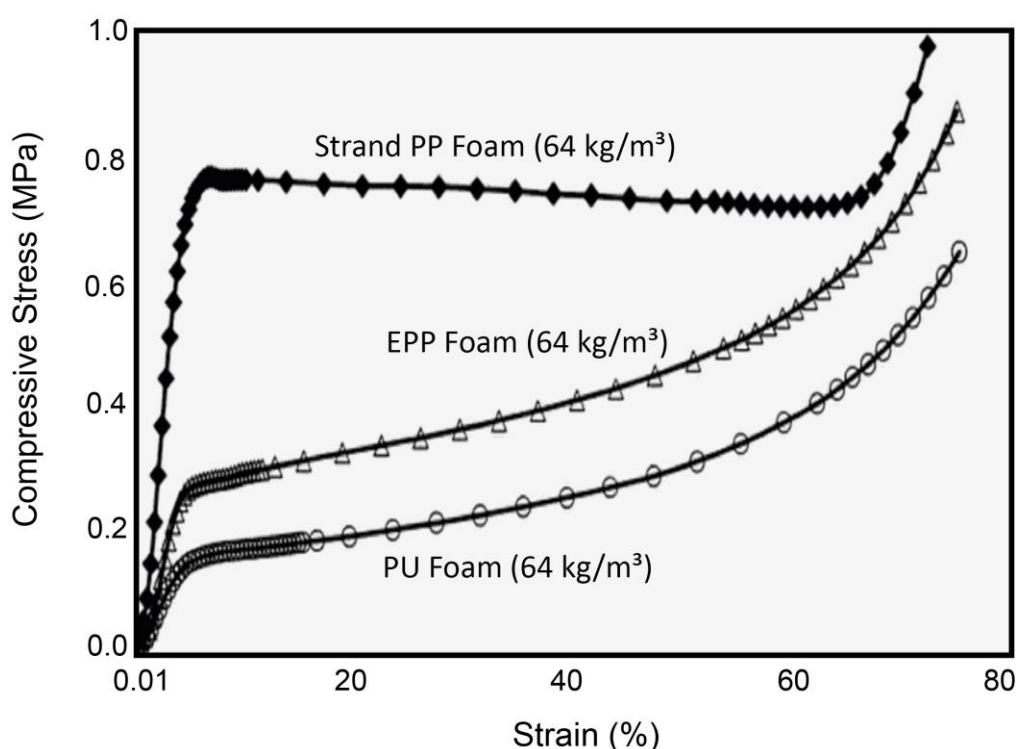


Figure 8 Comparison of the compressive stress-strain response of different foams at the same density of 64 kg/m^3 (reproduced from work of Koenig [32]).

Generally, linear polyolefins have weak melt properties and show little strain hardening effects. Therefore, achieving a large degree of expansion and proper cell stabilization during foam extrusion is very challenging for such polymers (only low thickness foam sheets are usually possible). Therefore, the original driver for developing strand foam technology was the need for higher thickness extruded foam planks based on low melt strength polymers, as mentioned by Park and Garcia [33]. Strand foam extrusion technology enabled processing of low melt strength polymers into low density foams with higher extrudate thickness (up to several centimeters). Already by the late 1990s, Dow introduced several new coalesced strand foams for different

applications [32]. Beside the possibility to create low density foams, the strand technology allows for a controllable amount of cell orientation, which improves the mechanical properties in the strand direction. Koenig [32] shows this improvement by comparing the compression behavior of strand PP foam and EPP both at a density of 64 kg/m³ (**Figure 8**).

Today, beside the polyolefin foams available by Dow, the strand extrusion technology is also applied by other suppliers to produce foams from other low melt strength polymers. A well-known example is the strand PET foam studied in this thesis. Similar to linear polyolefins, foaming thermoplastic polyesters is technically challenging, due to their low melt strength and elasticity [38–43]. Furthermore, polyesters have narrow processing windows, slow crystallization kinetics, and fast thermal degradation, which all make their processing and foam stabilization difficult [21]. Nevertheless, by using the strand foam technology and chemically modifying the polymer chains [38, 42, 44–46], foaming of PET is nowadays widely practiced and commercial grades are available in a relatively wide density range of 80 to 300 kg/m³. Most PET foams reported in literature are based on branched polyesters [31, 42, 47, 48]. In commercial foam grades, the raw materials are usually a mixture of virgin and recycled (or scrap) PET [49–54]. Before foam extrusion, polyesters of different intrinsic viscosities and recycled materials are chemically modified to yield suitable rheological properties for foaming. The chemical modification is performed using chain extenders, which have active branching sites and can condense two or more polyester chains. Examples of chain extenders are pyromellitic dianhydride (PMDA) and epoxides [21].

In foam extrusion of PET, it is usually challenging to maintain the necessary back-pressure in order to prevent foaming within the extruder [30]. Furthermore, the pressure-drop rate at the die opening is usually small, which limits the degree of foam expansion. Therefore, in conventional foam extrusion processes, the thickness of die opening is usually not too large. In addition, extruding high thickness foam plates will usually yield irregular cell morphology and consequently different density profiles through the panel thickness. Hence, most commercially available PET foams are processed through the strand foam extrusion method. These foam sheets can be realized at higher thicknesses (at least up to 50 mm in case of PET foam grade studied here) with more uniform macro and micro structures [30, 33, 55]. The foam extrusion process is usually performed on a single-screw extruder, which is used for melting the material recipe, reaction of the chain extenders, injection and solution of physical blowing agent(s) into the melt, cooling, foam expansion, and stabilization. The gas-loaded polymer melt is then

expanded through the breaker plate (or orifice die), as schematically depicted in **Figure 7** [36, 56, 57].

The design parameters of the breaker plate (such as shape, size and relative distance of the holes) can have significant effects on the quality and properties of the foam. Nevertheless, no specific information is disclosed by the supplier about the exact design features and dimensions of the breaker plate. For the strand PET foam studied here, the orifices are designed and arranged in a way that expanding strands, in shape of hexagonal prisms, come to contact with each other and are joined and adhered to form a coalesced strand structure. The expanded strands are usually pulled through a shaping die (calibration unit), in which they are compressed together, and the intra-strand voids are removed from the extrudates. No further detailed information about the foam extrusion process is disclosed by the manufacturer. At the end of the extrusion step, sheets of PET foams with thicknesses in the range of about 40-60 mm and widths of about 400-900 mm are obtained (see chapter 4.1).

After the extrusion process, the foam sheets undergo a set of post-processing steps including multiple rearrangements and welding. The post-processing steps result in foam panels with the hexagonal strands (and consequently the foam cells) oriented through the panel thickness, tremendously improving the out-of-plane properties. Another advantage of this post-processing step is that foam sheets can be made with no limitations on the sheet thickness. **Figure 9** shows the individual post-processing steps performed on extruded sheets. The final foam panels are highly anisotropic in properties with excellent out of plane compressive strength and modulus [24].

The anisotropy associated with the mechanical properties of extruded PET foam is the result of the special strand extrusion method described above, and consequently the induced multi-scale foam morphology. While the mechanical properties of conventional core materials such as PVC and PMI foams have been rather well studied and established in the literature, mechanical properties of PET foams have been so far only briefly discussed [24, 28, 44, 58–60]. This is mainly due to the fact that low density commercial PET foams are relatively recent technological developments [61].

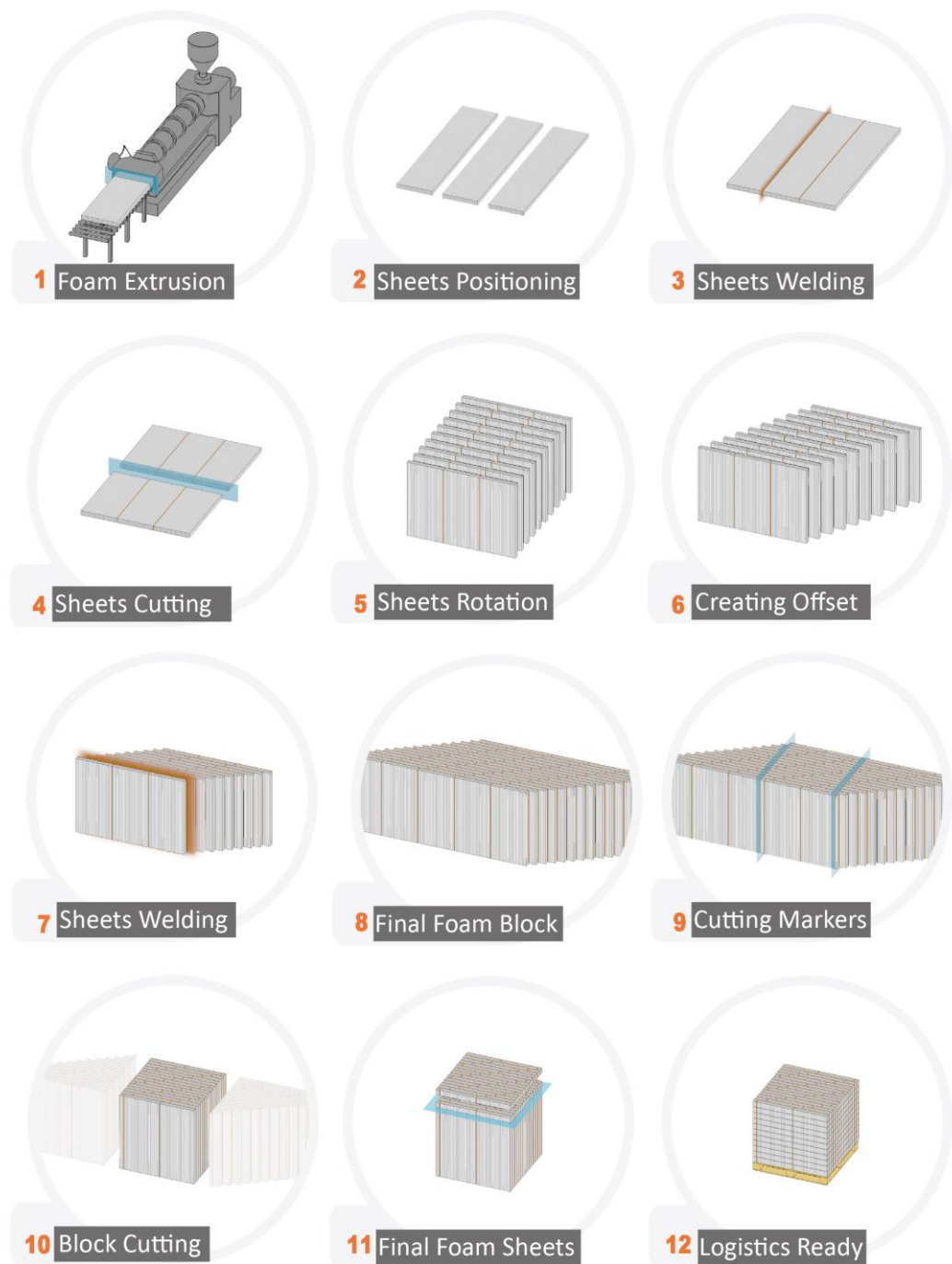


Figure 9 Schematic illustration of the post-processing steps performed on strand PET foam sheets. Steps 3 and 7 involve welding; Steps 4, 9, and 11 involve cutting.

2.2.3 Polyvinyl Chloride (PVC) Foams

PVC foams are known to have high strength and stiffness to weight ratios, as well as good resistance against chemicals, moisture, and fire. Closed-cell PVC foams are lightweight core materials, which are used extensively in high performance sandwich structures for marine, aerospace and automotive applications. In general, PVC foams have relatively high toughness and good impact and fatigue resistance. However, the ranges of strength and stiffness possible with PVC foams are relatively low compared to some other foam cores. Furthermore, applications can be limited in high temperature conditions [62–64]. Linear PVC foams usually show good toughness and impact resistance, while having little permanent deformations. However, the compressive strength and modulus of linear PVC foams are lower than cross-linked PVC foams at similar densities. Cross-linked PVC foams are more temperature resistant than linear PVC foams [65]. Therefore, they can be used in pre-preg sandwich processing technologies. Nevertheless, cross-linking the molecules means lower ductility and elongation at break. This can limit the impact resistance of the foam cores. PVC foams are usually closed-cell and have low resin absorption during processing. However, one draw back associated with PVC foams is the environmental concerns and sometimes the issues of outgasing [22]. When outgassing occurs, the entrapped blowing agent in the foam is forced out by elevated temperatures to form bubbles or blisters between the core and sandwich skin, which can lead to premature delamination.

Depending on the base polymers and additives used (e.g. plasticizers, cross-linking agents, processing aids, etc.), PVC foams are available in a range of hardnesses (flexible, semi-rigid, and rigid) [21]. Rigid cross-linked PVC foams, which are mainly used as sandwich core materials, are produced in blocks and then cut into foam sheets with desired thicknesses. The foam blocks are manufactured in closed molds by chemical foaming processes, where the materials mixture is heated and expanded (for details of processing methods for PVC foams see Chapter 4.1.3. in reference [21]). However, a precise process control is required to ensure different reaction steps take place correctly and according to the defined kinetics. Extended know how is needed on the reaction kinetics (blowing agent activation, foam expansion, foam stabilization, and cross-linking), in order to ensure PVC foam blocks posses the target density, morphology and properties profiles. Examples of commercial grade PVC foams include Airex® C70 from 3A Composites and Divinycell® H from DIAB group.

2.2.4 Polymethacrylimide (PMI) Foams

PMI foams are classified as advanced high-performance core materials. These foams are known to have excellent mechanical properties, high thermal/dimensional stability, very low resin uptake, high impact strength, as well as resistance against most solvents. Due to their higher manufacturing costs, PMI foams are usually more expensive than other foam core materials and are typically used in aviation and aerospace industries. Commercially available PMI foams have been extensively studied in the recent past [13, 14, 66–69].

The production methods of PMI foams are reviewed and available in patents and literature [21, 70]. The process usually involves radical copolymerization of base monomers containing several additives including cross-linking agents, initiators for polymerization reaction, and blowing and nucleating agents, and other processing aids. Foam sheets are usually produced in two steps. In the first step, compact polymer sheets are created through thermal treatments, and in the second step, the sheets are expanded to form foam panels with desired densities (usually ranging between 30 and 300 kg/m³). PMI foams can have heat resistance up to 220 °C. Recently, a new generation of PMI foam was introduced which could be classified as bead foam. The expandable PMI beads are commercially named ROHACELL® Triple F [71]. This grade of PMI foam can be molded using bead foaming processes allowing for the production of complex geometries with high compression strength and excellent temperature and fire resistance.

2.3 Constitutive Models of Foam Properties

Although the purpose of this thesis is not developing micromechanical models, it is useful to provide a basic description of the modeling approaches in the literature and their practical implications. This will help better appreciate the findings and correlations demonstrated for PET foams in the results section.

Similar to compact polymers, the mechanical properties of polymer foams are also viscoelastic. Therefore, the properties are generally time-dependant. However, the magnitude of the time-dependant viscous response strongly depends on the measurement temperature in relation to the T_g of the base polymer (see **Figure 10**). Elastomers usually have T_g values much lower than the application temperatures and therefore their properties are highly viscoelastic. A famous example is the low resilience PU foam, also referred to as memory foam. These memory foams exhibit slow recovery and relaxation and therefore high hysteresis during compression loading [72]. However, most structural foams have T_g values much higher than application temperatures

and therefore their properties are more dominated by a rigid and glassy response (the strand PET foam studied here has a T_g of ~ 80 °C). Therefore, the deformation behavior and failure response of rigid foams can be well described by elastic-plastic models. Nevertheless, depending on the base polymer and its T_g , some rigid foams show stronger strain rate dependencies in their properties (see chapters 2.4.1 and 2.4.2 for closed-cell PVC and PMI foams).

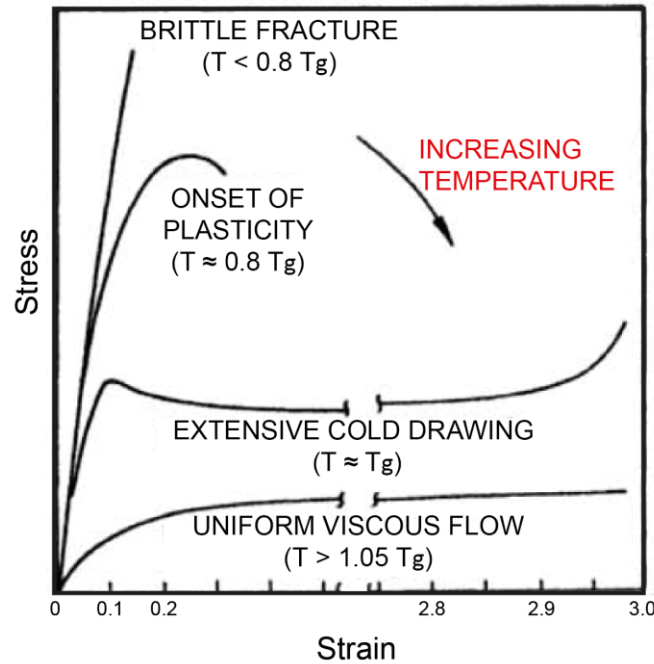


Figure 10 Schematic illustration of how the tensile stress-strain behavior of a polymer changes with temperature in relation to the T_g (reproduced from [25]).

Different model foams have been proposed to predict the deformation and failure behavior of cellular materials. Most existing models are idealized and only suitable for rather simple geometry foam cells and limited density ranges. However, most advanced foams (especially extruded foams) have complex cell morphologies, which are far from idealized and regular. Idealized constitutive models may not accurately capture and predict the mechanical behavior of such foams [16].

In the following, a summary of the most relevant existing models is provided. In alignment with the scope of this thesis, the review is limited to those models, which relate the elastic response (e.g. E modulus) and plastic response (e.g. yield strength) to the relative foam density and the cell morphology. Viscoelasticity and the effect of time and temperature on foam properties are not included in this review, due to the above-mentioned reason. Nevertheless, the viscoelastic properties of foams are highly controlled by the properties of the base polymer material. There

is very limited literature available about the effect of cell morphology on the viscoelastic response of polymer foams. However, the cell size of soft PU foams is reported to have a strong effect on the viscoelastic response (e.g. recovery time) due to adhesive effects and the role of cell surface [72].

2.3.1 Overview of Micromechanical Models

As a first step to modelling the constitutive behavior of foams, the cell morphology and the resulting mode(s) of cell deformation should be taken into account. In general, it is agreed that the cell deformation mechanisms in the elastic regime are elastic bending of the cell struts and axial stretching of the cell walls [11, 73–79]. Furthermore, it is known that in the post-yielding zone, different (but known) collapse modes can occur. This includes plastic bending (yielding of the joints and formation of plastic hinges), elastic buckling as in case of elastomeric foams, plastic buckling, and finally brittle fracture [11, 12, 25, 80–83]. The exact mode of deformation or combinations of different modes are determined by the base polymer material (e.g. elastomeric, ductile, or brittle material behavior) and the geometrical characteristics of the foam cells such as cell shape, orientation, and wall/strut length and thickness. The cell deformation mechanism is also influenced by foam density, as density has an effect on the cell morphology too. It will be shown in the next chapters that the cell deformation mechanism has a significant impact on the macroscopic foam properties.

Nevertheless, there are sometimes confusing literature data on the micromechanics of foams. One reason could be due to the morphological complexities, which can vary from case to case. As outlined by Gibson [25], part of the confusion could be related to the understanding about the cell deformation mechanisms, which are then used to derive analytical equations for moduli and strength. Unless the correct deformation mechanisms are identified and applied in the models, the predicted values will deviate from the experimental values. In most literature works, a particular and fixed cell morphology is assumed for the entire foam volume and effort is made to analyze its response to the applied loads [25]. However, there are usually multiple types of cell shapes with varying geometrical features of walls and struts, which result in combinations of different deformation mechanisms. Unless these effects are carefully accounted for, accurate prediction of foam properties at different densities would be almost impossible. The literature review below is first focused on the idealized models capturing the effect of density on properties. Later, models considering higher levels of morphological complexities are briefly mentioned.

Earlier approaches to experimental modeling of foam behavior assumed that the properties depended linearly on the relative foam density. However, later works in the literature shed more light on the relations between properties and foam density. Extensive literature works on different foam types conclude that most of the experimental data can be described by the general power law relation in Eq. 1, which links the relative foam properties to its relative density. The terms Φ_f and Φ_s could be any mechanical properties of the foam and the solid material it is made of, respectively. The proportionality constant, C , and the power law exponent, n , are usually obtained from experimental tests.

$$\frac{\Phi_f}{\Phi_s} = C \left(\frac{\rho_f}{\rho_s} \right)^n \quad (1)$$

However, in the analytical approaches most available models first assume a simplified and idealized definition of the unit cell geometry, such as cubic cells, equiaxed polyhedrals, or tetrakaidecahedron cells. The foam properties are then analytically related to foam density using mathematical relations derived from deformation theories. The idealized cubic models proposed by Gibson and Ashby [11, 12, 84] for open- and closed-cell foams, as well as their extensions to consider anisotropy [84–86], are among the most well-known models. In the cubic model, foam cells are assumed as cubic elements with struts having square cross-sections with constant thickness and length. The cubic model itself and the obtained property-density relations are discussed in chapter 2.3.2.

With the expansion of the computational power, more accurate models based on realistic morphological descriptions are developed. As a first attempt to increasing complexity, some literature models already consider further morphological features such as the ratio of the solid material located in the cell walls and cell struts, respectively (see parameter \emptyset in the standard Gibson and Ashby model discussed in chapter 2.3.4). As an example, using FEM models with Kelvin unit cells, Mills [16] suggested that at the same foam density, samples with higher concentration of solid material in the cell walls show stronger mechanical response. In another work, Mills [87] tried to capture the effect of solid material distribution on the mechanical properties of low-density EPS and LDPE foams. The model assumed that 100% of the solid material was concentrated in the cell walls (meaning no strut-thickening effect) and yielded predictions close to experimental data. This agreement was attributed to the fact that in the chosen EPS and LDPE samples, the volume fractions of solid material in the cell faces were measured around 98% and 93%, respectively.

As a next step to increasing complexity, models based on tetrakaidecahedron cell shapes were proposed [88–92]. These models are more capable of representing a realistic definition of the cellular structure and therefore yielding better results compared to cubic models [15]. For example, Subramaniam [93] looked at the effect of varying strut (edge) thickness on the yielding and plastic behavior of foams (**Figure 11**). The results showed that assuming constant values for struts cross-sectional areas will result in overestimation of the yield strength, as in reality failure of the weakest (thinnest) strut sections happen at lower stress levels. One main conclusion was that an accurate description of the strut thickness variation along the strut length is essential for precise predictions of the foam's stiffness and strength.

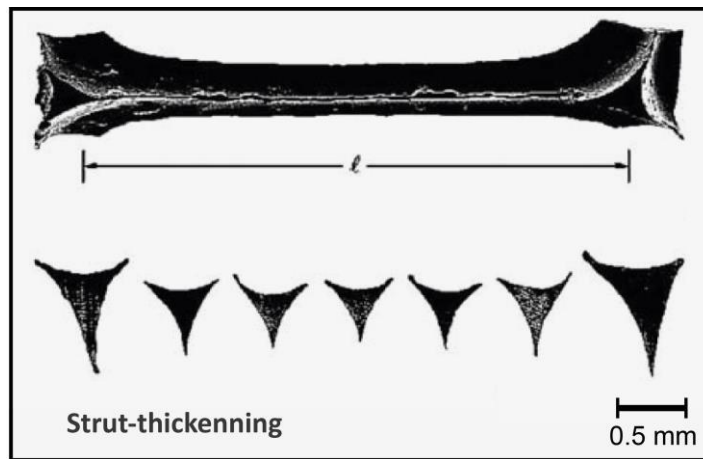


Figure 11 Demonstration of strut-thickening effect in foams (reproduced from [93]).

Pierron [94, 95] has also worked on similar local cell deformation and collapse caused by the local variation of the cell morphology. In that work, effort is made to improve the predictions of the compression response of elastic PU foams using optical deformation measurements. By measuring and mapping the local deformation patterns, correlations were made between local cell morphology and the resulting local collapse modes. As advised by Li [96], experimental measurements at different scales (e.g. global and local) should be coupled with the analytical approaches to yield realistic models capable of correctly describing the foam behavior.

According to a more recent work by Ashby [12], cellular structures and lattices can be generally divided to two main categories, based on their principle cell deformation responses: *Bending-dominated* and *stretch-dominated* structures. The distinction made between the two types of structures and the understanding about their mechanical responses will be extremely important for processing the data obtained in this thesis. In the results section, it is illustrated that strand PET foams can have a combination of both bending- and stretch-dominated responses, when

loaded in different directions. Therefore, in the following chapters both deformation responses are reviewed in more details.

2.3.2 Bending-Dominated Structures

Most isotropic foam materials can be classified as bending-dominated structures. These are generally cellular materials with the specific characteristic of low nodal connectivity [97]. The term “nodal connectivity” describes how many cell struts (or edges) meet at a cell vertice. Most bending-dominated foams have nodal connectivity values in the range of 3-4 [1]. Due to the low nodal connectivity, the cell struts have more freedom to bend under external loads. Assuming bending as the main micromechanical deformation mode for cell struts, the standard open-cell and closed-cell cubic models developed by Gibson and Ashby [25] can describe the mechanical properties of these structures rather well. **Figure 12** shows an ideal unit cell of an open-cell foam.

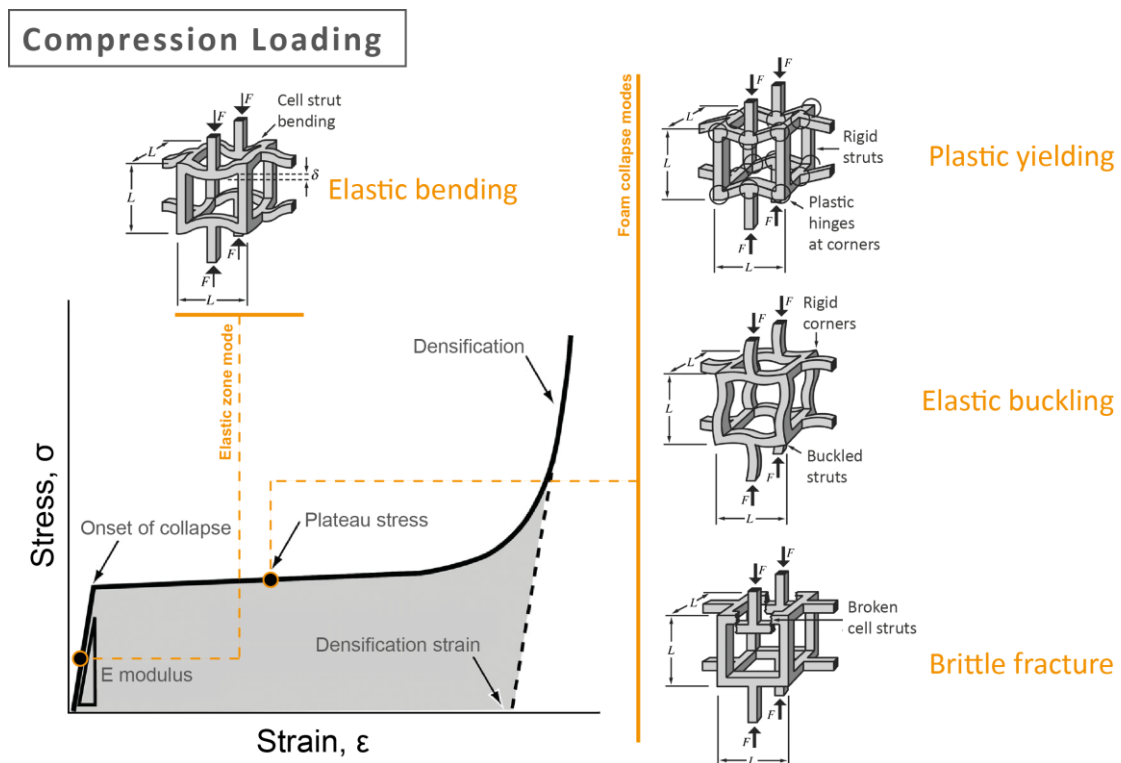


Figure 12 Typical compressive stress-strain curve of an open-cell foam with bending-dominated mechanical behavior. Different cell deformation mechanisms in the elastic and plateau regions are illustrated using idealized unit cells, reproduced from [12].

For this unit cell, the relative density $\bar{\rho}$ can be geometrically related to the cell strut thickness, t , and length, l , using Eq. 2. Here, ρ_s is the density of the solid material, and ρ_f is the foam density. Obviously, this relation assumes a simple, idealized, and equiaxed cell morphology for the foam material. In addition, this relation is usually valid for lower density foams (where $t \ll l$) [25].

$$\bar{\rho} = \frac{\rho_f}{\rho_s} = \left(\frac{t}{l}\right)^2 \quad (2)$$

For the idealized unit cell, the elastic deformation mode is assumed as bending of the struts, which is true especially at lower foam densities [25]. The Young's modulus of the foam can be then calculated from linear elastic deflection of a beam of length l , loaded at its midpoint by a force F . An external compressive stress, σ , imposes a force ($F \propto \sigma \cdot l^2$) on the cell struts, which will make them bend and create a midpoint deflection ($\delta \propto F \cdot l^3 / E_s \cdot I$). The deflection δ is dependant on the force (F), the strut length (l), elastic modulus of the solid material (E_s), and the second moment of area (I) of a strut with thickness of t . According to Ashby [12], the compressive strain taken by the whole cell can be then given by ($\epsilon \propto 2\delta/l$). After some mathematical rearrangements of the linear elastic theory ($E_f = \sigma/\epsilon$), the relative elastic modulus of the foam (\bar{E}) can then be related to the foam density, as expressed by Eq. 3. Note the power law exponent, $n=2$, which fits well with the experimental measurements reported for open-cell foams.

$$\bar{E} = \frac{E_f}{E_s} \propto \left(\frac{\rho_f}{\rho_s}\right)^2 \quad (3)$$

At higher loads, the cell struts in open-cell foams begin to fail by *plastic bending*, *elastic buckling* or *brittle fracture*. All three collapse mechanisms can happen and compete with each other. The mode which requires the lowest stress will dominate in each cell [11, 12]. Derivations of similar relations as Eq. 3 have been made for other collapse modes of the unit cells, which could relate the yield or failure stresses to relative density. For example, the cell struts can yield and plastically bend when their fully plastic moment ($M_f = \sigma_{y,s} \cdot t^3/4$) is exceeded by the applied compressive load. This is schematically shown in top right unit cell in **Figure 12**. The relative plastic failure strength ($\bar{\sigma}_{pl}$) of the foam can be then given by Eq. 4, in which the constant of proportionality is reported to be around 0.3. In a similar way, one can calculate the failure stresses for the elastic buckling of elastomeric foams ($\bar{\sigma}_{el}$) and the brittle fracture of less ductile foams ($\bar{\sigma}_{cr}$). These are shown in Eq. 5 and 6, respectively. The crushing stress of a brittle foam is normalized by the modulus of rupture of a strut ($\sigma_{MOR,s}$).

$$\bar{\sigma}_{pl} = \frac{\sigma_{pl,f}}{\sigma_{y,s}} \propto \left(\frac{\rho_f}{\rho_s}\right)^{3/2} \quad (4)$$

$$\bar{\sigma}_{el} = \frac{\sigma_{el,f}}{E_s} \propto \left(\frac{\rho_f}{\rho_s}\right)^2 \quad (5)$$

$$\bar{\sigma}_{cr} = \frac{\sigma_{cr,f}}{\sigma_{MOR,s}} \propto \left(\frac{\rho_f}{\rho_s}\right)^{3/2} \quad (6)$$

For idealized closed-cell foams, similar empirical relations can be obtained by mathematical modeling based on different unit cell types and geometrical characteristics/boundary conditions. The most well-known relations are those by Gibson and Ashby [25], which are extensions of the theories mentioned above for open-cell foams. Details of the mathematical procedures can be found in references [11, 12, 25]. Eq. 7 to 10 show the relations suggested for linking relative foam density to relative elastic modulus (\bar{E}), plastic bending collapse stress (σ_{pl}), elastic collapse stress (σ_{el}), and brittle crush stress (σ_{cr}) in closed-cell foams [11].

$$\bar{E} = \frac{E_f}{E_s} \propto \left(\frac{\rho_f}{\rho_s}\right)^3 \quad (7)$$

$$\bar{\sigma}_{pl} = \frac{\sigma_{pl,f}}{\sigma_{y,s}} \propto \left(\frac{\rho_f}{\rho_s}\right)^2 \quad (8)$$

$$\bar{\sigma}_{el} = \frac{\sigma_{el,f}}{E_s} \propto \left(\frac{\rho_f}{\rho_s}\right)^3 \quad (9)$$

$$\bar{\sigma}_{cr} = \frac{\sigma_{cr,f}}{\sigma_{MOR,s}} \propto \left(\frac{\rho_f}{\rho_s}\right)^2 \quad (10)$$

In Eq. 7 to 8, true closed-cell foam cells with no strut-thickening are assumed. The relations are derived using the same method explained above for open-cell foams, except that relative density is slightly differently related to the cell wall thickness and length ($\bar{\rho}=t/l$). In these relations, only a bending mechanism is assumed for the cell walls/struts when deriving the equations. This assumption is not always true, as in higher relative densities, cell walls also respond by stretching and axial straining. The idealized cubic models proposed by Gibson and Ashby assume bending of the cell struts as a basis for deriving mathematical relations. These models predict power law exponents of $n=2$ and $n=3$ for the relative elastic modulus (\bar{E}) of open-cell and closed-cell foams, respectively. Similarly, the values of $n=1.5$ and $n=2$ are suggested for the

plastic bending failure stress (σ_{pl}) of open- and closed-cell foams. Hence, cellular materials showing this type of response are referred to as bending-dominated structures.

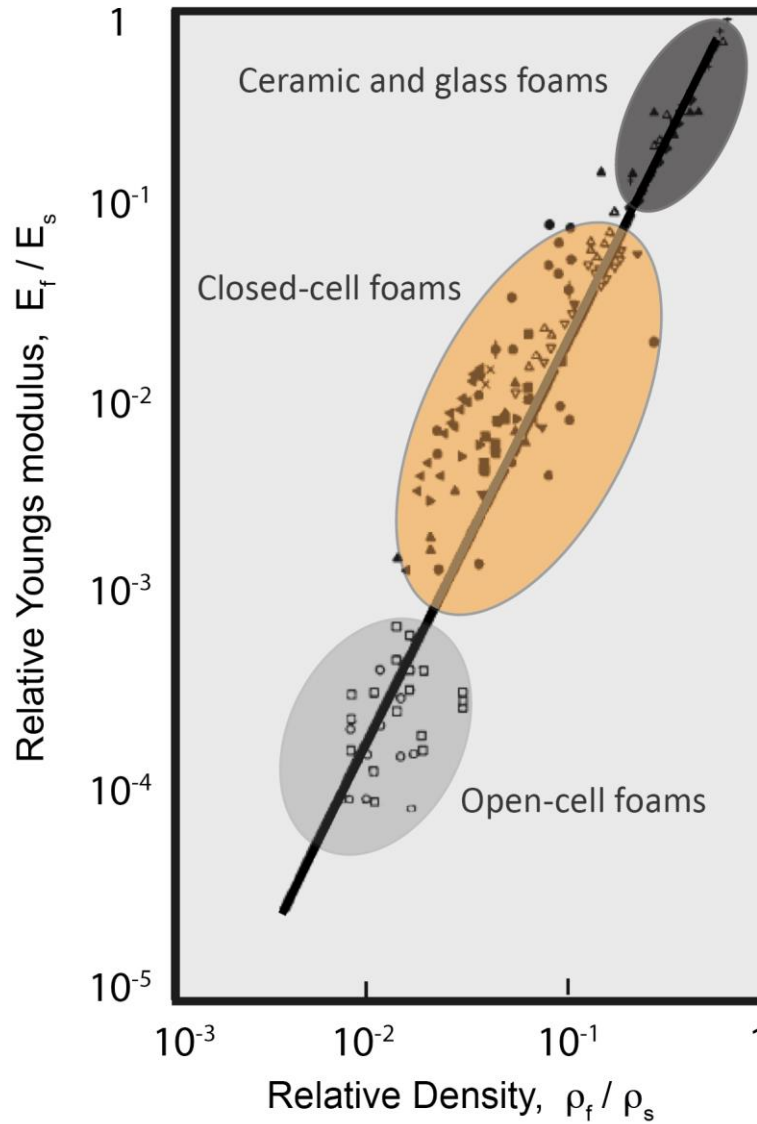


Figure 13 The relative Young's modulus (E_f / E_s), plotted against relative foam density (ρ_f / ρ_s) for different classes of foams, reproduced from [25].

Most polymer foams show bending-dominated mechanical responses. Therefore, in many cases their properties can be predicted up to acceptable levels using the relations above. **Figure 13** shows a master curve reproduced from [25], including the modulus-density trends for open-cell, closed-cell and brittle foams. Assuming bending as the main deformation mechanism is fair for open-cell foams. However, it has been experimentally demonstrated, that the cell walls are usually stretched (instead of bending), increasing the contribution of the axial wall stiffness to

the foam properties [25]. Therefore, the applicability of the standard models may be limited to closed-cell foams with lower fraction of the solid material in the cell walls. The mechanical properties of such thin-walled foams will be still mostly governed by the bending of struts, similar to open-cell foams.

Nevertheless, in some practical cases the concentration of solid material in the cell walls can be almost as high as in the cell struts. Therefore, many closed-cell foams can deviate from the analytical relations mentioned above for bending-dominated structures. The behavior of foams with higher degrees of nodal connectivity or cell orientation can result in a stretch-dominated response, which requires additional model considerations. This is explained below in more detail.

2.3.3 Stretch-Dominated Structures

Unlike bending-dominated structures, the stretch-dominated lattices and foams have morphological constraints, which prevent their struts from bending. Due to their higher nodal connectivity (usually exceeding 5), these structures cannot bend when loaded [12]. As a result, stretch-dominated structures usually undergo deformations along the strut length, including stretching (in tension) and axial compression. When loaded in compression, stretch-dominated structures first respond by an axial compression of the struts. The failure then begins by few sets of struts first yielding plastically in a nonuniform manner, and then buckling, or fracturing. Stretch-dominated cellular structures, such as Balsa wood, usually have elongated cells. Therefore, compressive stresses along the direction of cell orientation usually result in local yielding and plastic buckling of the cell walls and struts. In contrast, transverse loading of such foams will result in a similar response as in case of bending-dominated foams, involving plastic bending of the cell struts [97]. Similar to bending-dominated structures, here also the failure mechanism with the lowest collapse stress determines the strength of the structure as a whole. Reproduced from [12], Eq. 11 to 14 show the analytical relations derived for scaling different failure modes to foam density for stretch-dominated structures.

$$\bar{E} = \frac{E_f}{E_s} \approx \frac{1}{3} \left(\frac{\rho_f}{\rho_s} \right) \quad (11)$$

$$\bar{\sigma}_{pl} = \frac{\sigma_{pl,f}}{\sigma_{y,s}} \approx \frac{1}{3} \left(\frac{\rho_f}{\rho_s} \right) \quad (12)$$

$$\bar{\sigma}_{el} = \frac{\sigma_{el,f}}{E_s} \propto \left(\frac{\rho_f}{\rho_s}\right)^2 \quad (13)$$

$$\bar{\sigma}_{cr} = \frac{\sigma_{cr,f}}{\sigma_{cr,s}} \propto \left(\frac{\rho_f}{\rho_s}\right) \quad (14)$$

Nevertheless, here as well, for each failure mode a fixed and unique deformation is assumed for all foam cells. In reality, depending on the foam type, morphology, and loading directions, there seems to be a combination of stretching, bending, and buckling phenomena responsible for cell level deformation. The mechanical properties of stretch-dominated structures are stronger than the bending-dominated structures of the same relative density. This is because the mechanisms of deformation in stretch-dominated structures involve “*hard modes*” such as stretching and axial compression rather than the “*soft modes*” like bending. Due to the mentioned deformation mechanisms, the initial yielding in stretch-dominated structures is usually followed by local plastic buckling or brittle collapse of the cell struts. This is manifested in the post-yield softening phenomena seen in their stress-strain behavior (see **Figure 14**).

Figure 15 shows the data for relative modulus and strength versus relative density for different foams, honeycomb, and lattices. The data can be compared to the two lines drawn for ideal bending-dominated and ideal stretch-dominated mechanical behavior. Stretch-dominated structures have elastic moduli which scale linearly with relative foam density ($n=1$). In contrast, the elastic modulus-density scaling in ideal bending-dominated foams are governed by power law constant ($n=2$). As shown in **Figure 15**, honeycombs loaded in the out-of-plane direction have ideal stretch-dominated behavior, while most foams are reported to be in the region of bending-dominated structures.

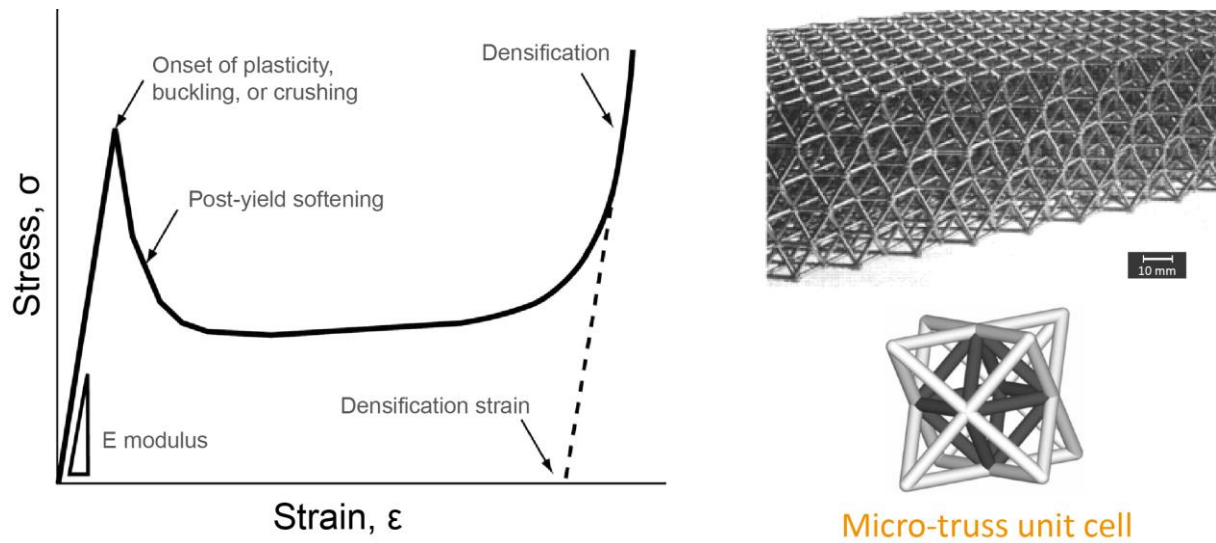


Figure 14 Typical compressive stress-strain curve of a lattice with stretch-dominated mechanical behavior, reproduced from [12].

For closed-cell foams with thicker cell walls, stretching of the walls together with other effects, such as cell orientation and axial deformation, can cause the cell behavior to deviate from ideal bending-dominated. For these foams with a combination of cell deformation mechanisms, the values of power-law exponent, n , are usually between 1 and 2. One implication of these discussions is the fact that using correct design criteria for nodal connectivity, lattice structures with superior performance to those of ordinary foams can be realized. Fleck has discussed morphological phenomena which promote more stretch-dominated responses in cellular lattices [1].

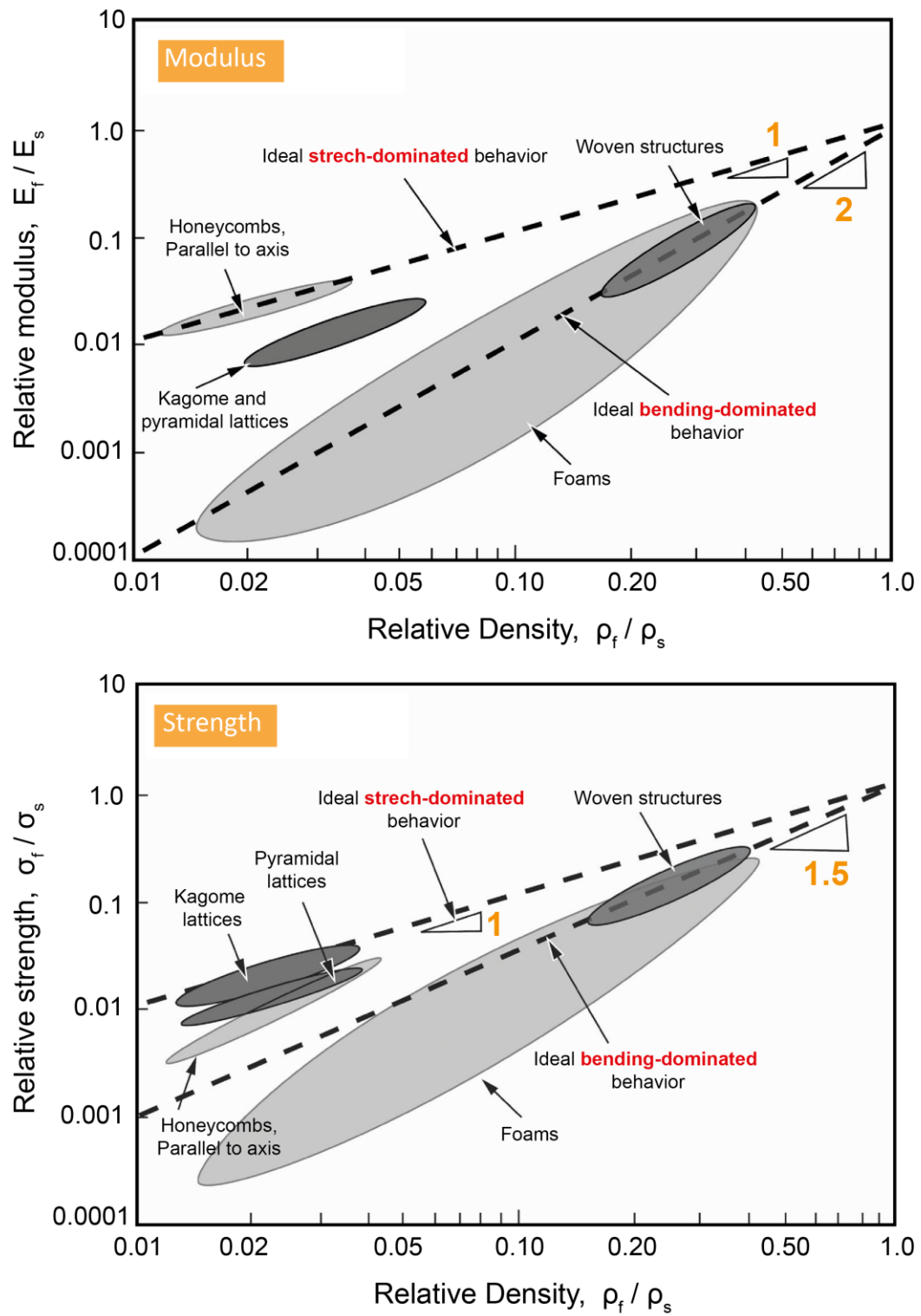


Figure 15 Scaling of relative modulus (E_f/E_s) and relative strength (σ_f/σ_s) with relative density (ρ_f/ρ_s) for different cellular materials. The dashed lines show the scaling for ideal bending- and stretch-dominated behaviors (Graphs reproduced from [12]).

2.3.4 Standard Model of Gibson and Ashby

The discussions made in the previous chapters, and the mathematical relations derived thereafter, are based on a series of assumptions. For example, the closed-cell cubic model reviewed in chapter 2.3.2 may underestimate the axial stretching of the cell walls. This is in particular true for foams with thicker cell walls. In these cases, the microscopic deformation mechanism of the foam cells can involve a combination of both bending and stretching. Therefore, further efforts have been made to improve the accuracy of the analytical models by decoupling the effect of cell struts (bending) and cell walls (stretching). One example is the famous model of Gibson and Ashby [25], which already takes into account different deformation modes of cell struts and cell walls, as well as the effect of cell gas. In this model, the linear deformation zone can be described by Eq. 15. The linear elastic modulus is determined by cell strut bending ($n=2$), cell wall stretching ($n=1$), and the contribution of the cell gas.

$$\bar{E} = \frac{E_f}{E_s} = \phi^2 \left(\frac{\rho_f}{\rho_s} \right)^2 + (1 - \phi) \left(\frac{\rho_f}{\rho_s} \right) + \frac{p_0 (1 - 2\nu_f)}{E_s (1 - \frac{\rho_f}{\rho_s})} \quad (15)$$

Hence, the model relates the macroscopic properties (in this case E modulus) to the foam density and cell morphology [98]. The parameter ϕ refers to the fraction of solid material building the cell struts, and $(1-\phi)$ is the fraction of solid material contained in the cell walls. This model has been used in some literature works to fit the property-density data, and experimentally determine the distribution of solid in the cell struts and walls. Most foams are somewhere between a perfectly open-cell and a perfectly closed-cell structure, meaning that the solid material is partially concentrated in the cell struts and partially in the cell walls. Therefore, the response and scaling of properties with density should be somewhere between perfect open- or closed-cell foams [68]. Superimposed on the deformation behavior of the cell struts and walls is the effect of cell gas entrapped inside the cells (third term in Eq. 15) [25].

Still in many practical cases, linking the foam properties with density is made using the general power-law relation in Eq. 1, and the experimentally determined data. In many cases, the power-law exponent n is reported to be between 1 and 2, indicating a combination of both bending- and stretch-dominated responses. In this thesis, too, the in-plane and out-of-plane properties of PET foam are related to the relative foam density using this generic power law relation. It will be shown that in-plane loading is always controlled by bending phenomena, regardless of foam density. However, the out-of-plane loading is controlled by a stretch-dominated mechanism,

which is due to the high orientation of foam cells. At higher foam densities, out-of-plane loading is also governed by bending, since no significant cell orientation exists any more.

2.4 Mechanical Properties of Foam Core Materials

In alignment with the previously discussed foam classification, the reviewed literature data is grouped and presented for the most popular structural foams belonging to each processing category. This is because foams produced through the same processing route usually share similarities in their morphological features as well as structure-property relations. As main performance competitors to PET foam (in particular as sandwich core materials), the mechanical properties of PVC and PMI foams are particularly discussed in more detail. Despite their good properties to price ratio, PU foams are deliberately excluded from this review, though some aspects of their mechanical properties are discussed in [99–103]. The basic mechanical properties of some bead foams, extruded foams, and wood are also briefly reviewed. Wood is a more traditional core material, which is still in extensive use today. The microstructure and properties of wood are very relevant to the PET foam studied in this thesis, as there are several analogies between their mechanical properties at different deformation length scales. Mechanical properties of PVC and PMI foams have been extensively investigated in the literature. Nevertheless, most studies are focused on the macroscopic mechanical response. There is rather limited information about the role of foam morphology and its impact on the macroscopic properties. However, the few available studies [13, 14] already provide an excellent foundation and benchmark for the findings presented in this thesis.

2.4.1 Closed-Cell PVC Foams

Mechanical properties and failure behavior of cross-linked PVC foams are usually indicative of brittle material behavior [98]. Depending on the base polymer mixture and the target density (expansion degree), PVC foams can show slight anisotropy in their morphologies and therefore properties. However, in most practical applications, properties of PVC foams are assumed isotropic. Anisotropy, if any, is usually more significant at lower foam densities, as demonstrated for some foams and woods [2, 25]. This is because in low-density foams (e.g. below 200 kg/m³), the cells are highly expanded, and the directionality of foam cells is typically more pronounced. Additionally, assuming comparable cell densities, the cell walls are usually thinner and slenderer in lower density foams. Hence, when loaded in compression along their length, the foam cells can undergo buckling. However, there have also been contradictory reports, such as the one by Gdoutos [26], in which a higher density PVC foam (250 kg/m³) is shown to be more anisotropic

than a lower density foam grade (100 kg/m^3). In the 250 kg/m^3 PVC foam sample, the compressive strength and modulus were 40 % and 65 % higher in the out-of-plane direction than the in-plane direction, respectively. This could be due to special cell structure features of the two foam grades making their properties deviate from theoretical assumptions.

Viana [98] has done a comprehensive study on the tensile properties of PVC foams in a wide range of densities. An almost isotropic tensile response is reported for PVC foams, which could indicate that the loading direction has insignificant impact on the cell deformation mechanism in tension mode. Nevertheless, in other loading modes such as compression and shear, the cell deformation mechanisms could be more complex and dependant on the loading direction. Deshpande [104] has also studied the tensile properties of PVC foams at 100 and 200 kg/m^3 densities and made efforts to create constitutive material models for their mechanical properties. They reported anisotropy in both tension and compression, with the strength values almost 20 % higher in the out-of-plane direction. Their work suggested applying transversely isotropic material behavior for describing the mechanical properties of PVC foams.

In reference [105], it is shown that strength and stiffness of cross-linked PVC foams are higher in tensile loading compared to compressive loading (Tensile strength is defined as the stress level where specimen ruptures and compressive strength is defined as the highest compressive stress value before post-yield softening). This effect is more pronounced at lower densities, as for example the tensile strength of a 60 kg/m^3 sample is shown to be up to 70 % higher than its compressive strength. In [104], a similar trend is reported with lower yield strength values in uniaxial compression tests compared to uniaxial tensile tests. This behavior was attributed to the fact that in tension, bending and stretching of the cell struts and walls control the deformation, whereas in compression there are other effects such as elastic and plastic buckling as well. Gdoutos [26] too, showed different stress-strain behavior for PVC foams in tension and compression. On the other hand, the energy absorption values (e.g. in impact tests) are higher in compression than tension, which is due to much larger strains the samples undergo in compression. Impact resistance of PVC foams drastically increase with foam density, as shown in [105].

In particular, compression properties of (chemically molded) cross-linked PVC foams have been thoroughly discussed in references [106–108]. It is generally agreed, that the compression properties of PVC foams are transversely isotropic, meaning that strength and stiffness are higher in the out-of-plane direction (foam rise direction) compared to the in-plane (transverse)

directions [106, 107, 109, 110]. An example of compression response of cross-linked PVC foam with a density of 60 kg/m^3 was already shown in **Figure 2**. This directionality of the compression properties, too, stems from different cell deformation mechanisms when loaded in each direction. Tagarielli [111] argued that in out-of-plane loading, axial yielding followed by local plastic buckling control the cell deformation, whereas in-plane loading triggers plastic bending of the cell walls and struts. The reported difference in cell deformation mechanisms of PVC foams is probably due to slight orientation of the foam cells through sample thickness. In [106], it is shown using optical deformation analysis that in-plane deformation of PVC foam is homogeneous, while the out-of-plane response involves more heterogeneous local deformations. This is because buckling of the cell walls, and the formation of shear bands, are local phenomena and take place at random locations depending on the local loading conditions and cell geometrical features.

The influence of strain rate on the compression properties of PVC foams has been discussed in [62, 63, 111–117]. The sensitivity of foam properties to strain rate is usually governed by the dependency of the parent solid material's properties on strain rate [111]. In case of PVC foams, properties do depend on strain rate, as shown by Viana [98] using hysteresis loops confirming a viscoelastic response. However, the effect of strain rate is more pronounced in higher density foams. For example, the compression properties of high density PVC foams (e.g. $250\text{--}300 \text{ kg/m}^3$) have been demonstrated to be more affected by the strain rate than lower density PVC foams [64, 111]. Tagarielli [111] showed that when the strain rate is increased from quasi-static range to values around 3000 s^{-1} , the compressive yield strength of high density PVC foam is almost doubled, while the same property was only 30 % higher in a lower density foam grade. In the same work, it is shown that the dependency of properties on strain rate for Balsa wood is high and comparable with higher density PVC foams. Other authors [97] also showed higher dependency of properties on strain rate in Epoxy foams when the density is increased. This may be rooted in the change of deformation mechanism from low-density to high-density foams, and different impact of strain rate on each deformation mechanism.

Foam density usually has the strongest impact on the mechanical properties of foams. Some relations between mechanical properties and density of PVC foams are discussed in [25, 68, 105, 118, 119]. In [105], the elastic modulus, tensile strength and impact properties of PVC foams are scaled with foam density. Obviously, the properties (e.g. strength and elastic modulus) increase with foam density. Zenkert [68] reported a power law constant, n , between 1.1 and 1.2 for all static tensile properties of PVC and PMI foams. In particular, they reported $n=1$ for the tensile

modulus and strength of PVC foams. This may indicate that tensile properties of PVC foams are governed by axial deformation modes such as stretching. The result of that work is reproduced in **Figure 16**, where the tensile stress-strain curves of different density PVC foams are shown in the left graph in red color. The same stress-strain curves are shown in the right graph of **Figure 16**, where the tensile stress is normalized with the relative density, ($\bar{\rho}^n$), in which $n=1.1$. For both PVC and PMI foams the normalized tensile stress-strain curves can collide into a single curve, suggesting that the micromechanical deformation mechanism in tensile mode remains unchanged at different foam densities [13, 68].

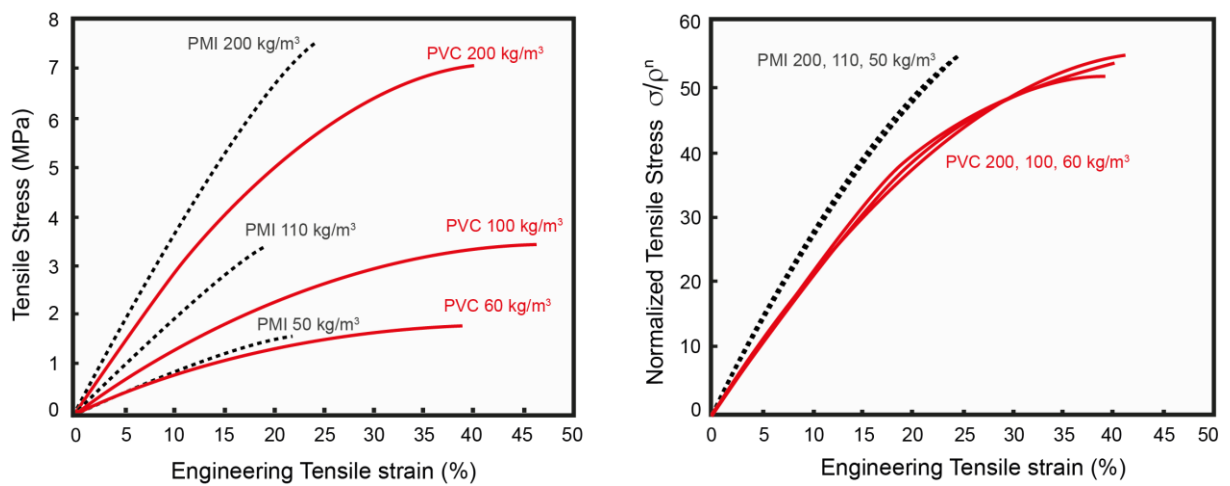


Figure 16 Engineering tensile stress-strain curves of PVC and PMI foams at different densities (left), and density normalized tensile stress-strain curves of the same samples (right), reproduced from [68].

Nevertheless, in most practical applications involving compression and shear loading modes, scaling of properties with density is not straightforward and sometimes scaling is only possible for a limited range of densities. For example, in compression loading of closed-cell foams it is usually not possible to perfectly fit the experimental values of strength/modulus to one single mathematical relation for all densities (see **Figure 19** for PMI foams for example). This highlights an important fact: The cell deformation mechanisms in compression and shear may change with foam density, which is mainly due to the variations in the cell morphological features. Therefore, the macroscopic mechanical response at a certain relative density could be different to the predicted values from analytical models. Ashby already argued in his earlier work [11], that some empirical relations obtained for density-properties may be only valid in lower range densities, as the mode of deformation can change at higher densities due to the change of cell wall/strut length and thickness.

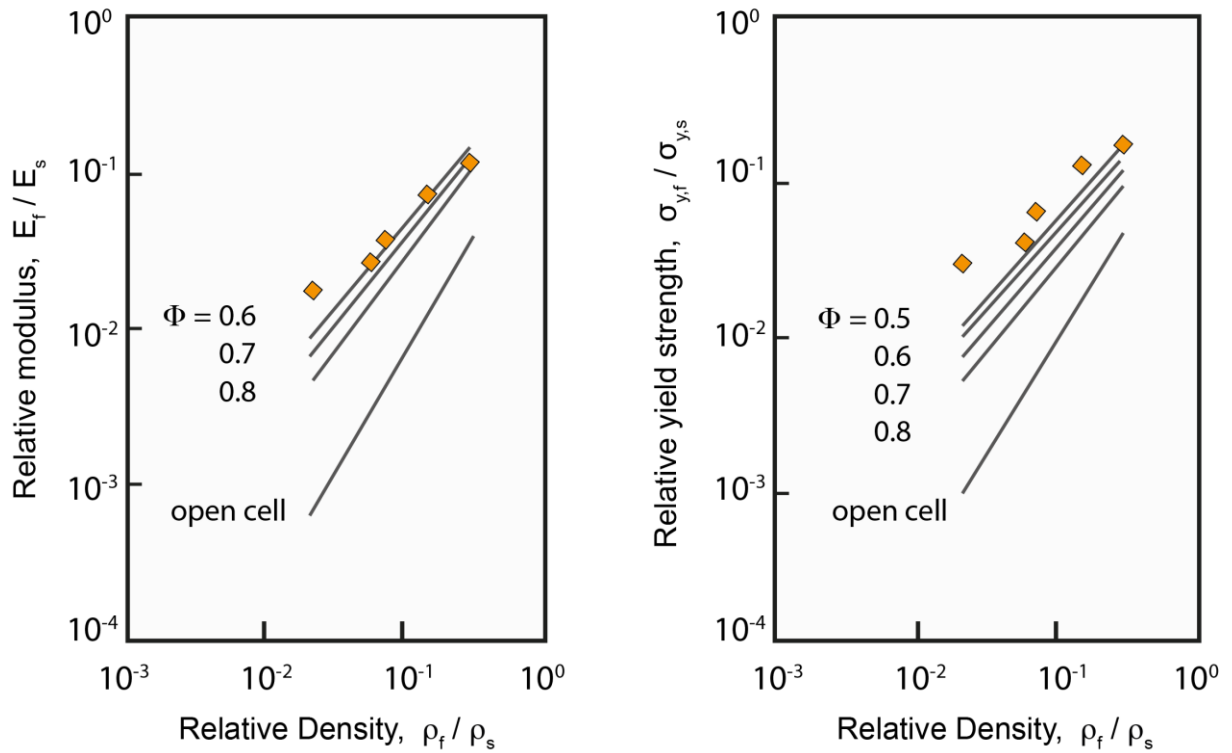


Figure 17 Relative Young's modulus (E_f/E_s) and relative yield strength ($\sigma_{y,f}/\sigma_{y,s}$) versus relative density (ρ_f/ρ_s) for PVC foam, reproduced from the work of Viana [117].

Other studies on density-properties relations in PVC foams have taken into consideration the effect of cell morphology, namely the fraction of solid material in the cell struts (Φ) and cell walls ($1-\Phi$) using the standard model of Gibson and Ashby described in Eq. 15. As previously discussed, this model assumes power law constants of 2 and 1 for the components describing the deformations of cell struts and cell walls, respectively. In other words, a bending-dominated micromechanism is assumed for the cell struts, and cell walls represent more stretch-dominated behavior. In reference [98], it is shown that fitting the experimental data was best done using Φ values between 0.5-0.6 (**Figure 17**). Colloca [105] also studied PVC foams in a range of densities (60-250 kg/m³) and reported a similar Φ value of 0.52. The standard Gibson and Ashby model assumes a bending response for the cell struts, which works well for predicting the tensile behavior of PVC foams. However, when studying the compression properties, any deviations from the assumption of bending-dominated response will result in discrepancies between the predicted and measured values. For example, the mechanisms of cell deformation can change from bending only and involve other modes (e.g. axial deformations) when the foam morphology is different at varying densities.

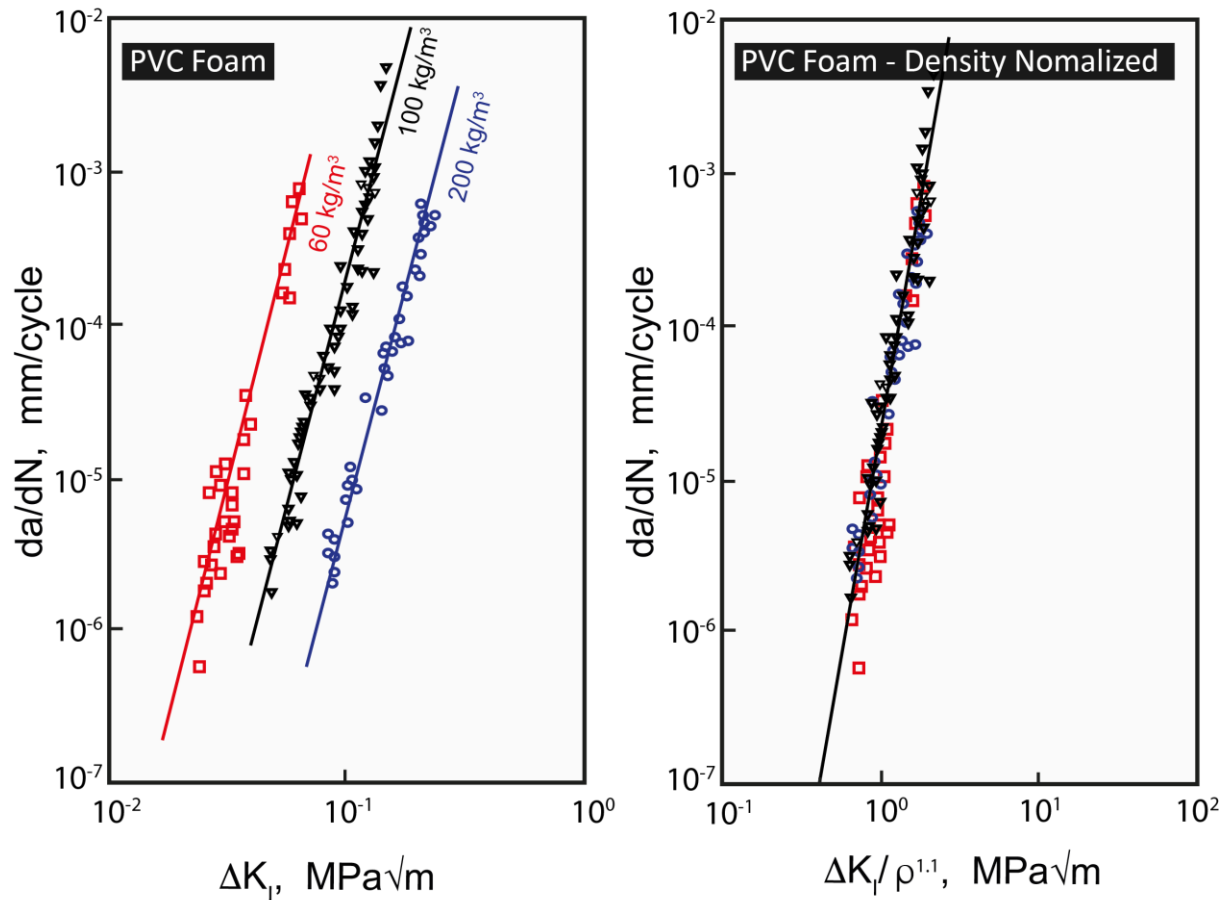


Figure 18 Fatigue crack growth data (da/dN versus ΔK_I) for different densities of PVC foams (left graph) and the same data in normalized representation (right graph). Data and curves are reproduced from the work of Zenkert [68].

The literature work on fatigue of foams is rather limited. McCullough [120] studied the fatigue of Aluminum foam and showed that the slope of Wöhler S-N diagrams are considerably lower in the compression-compression fatigue than the tension-tension fatigue. He also showed that the shape and slope of the S-N curves are not much influenced by the foam density. Harte [121] also demonstrated that at the same loading ratio (ratio of maximum stress to the yield strength of the foams), the fatigue limit of Al foams remain almost unchanged at different foam densities. Some earlier works on fatigue of polymeric foams are described in [68, 69, 122–124]. Kanny [124] studied the fatigue properties of cross-linked PVC foam cores in shear (sandwich bending) and showed that the fatigue endurance increased with foam density. In other studies [68, 69], density-dependent fatigue performance of PVC foams have been investigated in different loading modes. One main conclusion from these works is that in fatigue loading too, the deformation mechanism and failure mode changes with increasing foam density. The tension-tension fatigue of PVC foams in a density range of 60–200 kg/m³ is discussed in [68]. It is shown that the S-N

curves presented for different densities of PVC foam had very similar slopes, suggesting no effect of foam density in fatigue degradation rate of PVC foams [13, 66, 68]. This indicated insensitivity of tensile-tensile fatigue strength degradation on foam density. In the same work [68], Zenkert applied the scaling rules discussed above to relate the fatigue crack growth rate in PVC and PMI foams to their relative densities. As seen in **Figure 18**, by normalizing the stress intensity factor (ΔK) to $(\bar{\rho}^n)$, the da/dN curves of different density foams will all collide into a single curve. This also suggests that the deformation mechanisms in the fatigue crack growth experiments (controlled by tensile phenomena) remains the same for different foam densities. In that work, Zenkert showed that fatigue crack growth rates (represented by slope m in Paris-law fitted curves) were almost independent of the PVC foam density.

Fracture toughness of PVC foam cores has been reviewed in [17, 98, 105, 112, 125–130]. It has been demonstrated, that the fracture toughness and impact resistance of PVC foams have linear dependence on foam density ($n=1$) [98, 105]. On the contrary, idealized standard models [25] predict power law exponent, $n=2$, for the dependency of fracture toughness on density in closed-cell foams. This discrepancy might be caused by the more complex cellular morphology of these foams. One more conclusion reported in the literature is that crack propagation in the PVC foam core always starts in the region near face/core interface, which is referred to as “sub-interface” (see chapter 5.3.3 for a similar observation in this thesis and the discussions thereafter). This phenomenon could be attributed to the density variation of PVC foam through the panel thickness and the stress concentration effects near the interface region.

Finally, yet importantly, from a theoretical approach some properties such as fracture toughness should have strong dependencies on the cell size. This is because the crack growth in foam is stepwise and one cell at a time [68]. However, so far the literature information about the effect of cell size on macroscopic properties of polymer foams is very limited. Zenkert showed that the mode I fracture toughness of PVC foams decreases with larger foam cells at the same density [128].

2.4.2 PMI Foams

PMI foams are characterized as stiff and crushable, with no strain hardening in the plateau region. Instead, PMI foams usually show a strain softening effect after yielding, which is indicative of localized cell crushing effects. Several bands of failed cells are formed transverse to loading direction, with gradual extension of multiple damage fronts through the specimen thickness [10]. In the literature, this behavior has been referred to as localized progressive

collapse [96]. In general, PMI foams are known to be more brittle than PVC foams [68], and their tensile behavior scales well with foam density. This can be seen in the **Figure 16**, where the normalized tensile stress-strain curves of PMI foams at three densities are nicely fallen into a single curve.

Compression properties of PMI foams are thoroughly discussed in [10, 13, 14, 96, 131]. The majority of works report isotropic properties for PMI foams [14]. Nevertheless, in some cases a slight transversely isotropic response has been demonstrated, with the highest mismatch between out-of-plane and in-plane behavior reported for large deformation levels close to the densification zone [10, 96]. In reference [10], models are suggested to relate the global engineering strains of the foam with the local cell deformations (here represented and quantified by the size of local crushed bands and the average distance between the collapsed bands). In other words, an analytical model is proposed, which can relate the size of the crushed zones to the global strain level. For example, at a global engineering strain of 30%, there are regions with almost 70% local straining and other regions with less than 5% strain. This highlights the localization of cell crush in PMI foams.

The geometrical features of the foam cells can substantially affect the macroscopic response of the foams. It should be reminded from previous sections, that the cell deformation mechanisms (particularly in compression and shear loading) can change with foam density due to the change in cell morphology. In low-density PMI foams, thinner and longer cell struts have lower buckling collapse strengths. Therefore, besides bending as the main deformation mode, some cells can undergo buckling of struts and walls [13, 14, 104]. In contrast, the cell deformation of high-density PMI foams, with less slender cell walls, is more governed by plastic bending of the struts or brittle fracture. What makes predictions more challenging is that the effect of density on cell morphology is not always regular and straightforward. For example, increasing the density will not necessarily lower the cell wall or struts slenderness in PMI foams. This is depending on the processing parameters and boundary conditions, other properties such as cell density could also change with varying foam density. In the study by Arezoo [14], a relatively high-density PMI foam performed weaker than regular model predictions, because this particular sample had more slender cell walls. This suggested that buckling (as a secondary cell deformation mechanism) weakened the expected bending-only mechanical response at this density. For this grade with high relative density and the highest slenderness ratio, the values of strength and stiffness measured were lower than the theoretical predictions in reference [132]. Here, the high slenderness promoted easier buckling of the struts and walls. Hence, newer models are to be

developed and verified, which are capable of taking into account the role of morphological cell features and capturing the combinations of different cell deformation mechanisms. This will allow for correctly scaling the stiffness and strength of the foams with their relative densities.

In other works by Zenkert [13, 68], the relations between density and the mechanical properties of PMI foams in tension, compression, and shear loadings in both static and fatigue regimes have been discussed. It is shown, that the static tensile stress-strain curves of PMI foams can be density normalized and collapse into one single curve (see **Figure 16** from reference [68] and top row in **Figure 19** from reference [13]). This is because in tensile loading, cell walls and struts undergo axial stretching followed by plastic deformation and rupture, which is independent of cell size and cell wall thickness. This claim is verified in other works on tensile properties of PMI foams too [14], where it is shown using in-situ SEM measurements that the cell deformation mechanism did not change with foam density.

In compression loading, however, the microscopic deformation mechanism can completely change at different foam densities. High-density PMI foam cells show collapse by means of plastic bending, whereas low density PMI foam cells can additionally undergo buckling due to their thinner and longer cell struts [13, 14, 104]. For this reason, the density normalized compression curves in the middle row of **Figure 19** did not yield a single relation. The deformation mechanism in shear loadings is also not scaled well with density (bottom row in **Figure 19**) and the authors encourage further investigations to understand the micromechanics of shear deformations in such foams. Arezoo showed in [14, 67] that the compressive modulus of PMI foam scales with relative density with power law exponent of $n=1.47$. This value suggests that the cell deformation mechanism is a combination of bending-dominated ($n=2$) and stretch-dominated ($n=1$) responses. The contribution of each deformation mode depends on the exact cell morphology and varies at different densities.

As a learning from the works of Zenkert and Arezoo [13, 14], one cannot necessarily conclude that cell slenderness is higher in low-density foams and therefore more buckling takes place. In fact, the slenderness of the cell walls can be varied at the same density. Therefore, the deformation mechanism can change at any density, so it may not be correct to assign distinct deformation mechanisms to a low-density and a high-density range. The work of Arezoo shows that one high-density PMI foam sample was affected by buckling of the walls, because despite its high density this sample had the highest length to width ratio of cell wall and struts.

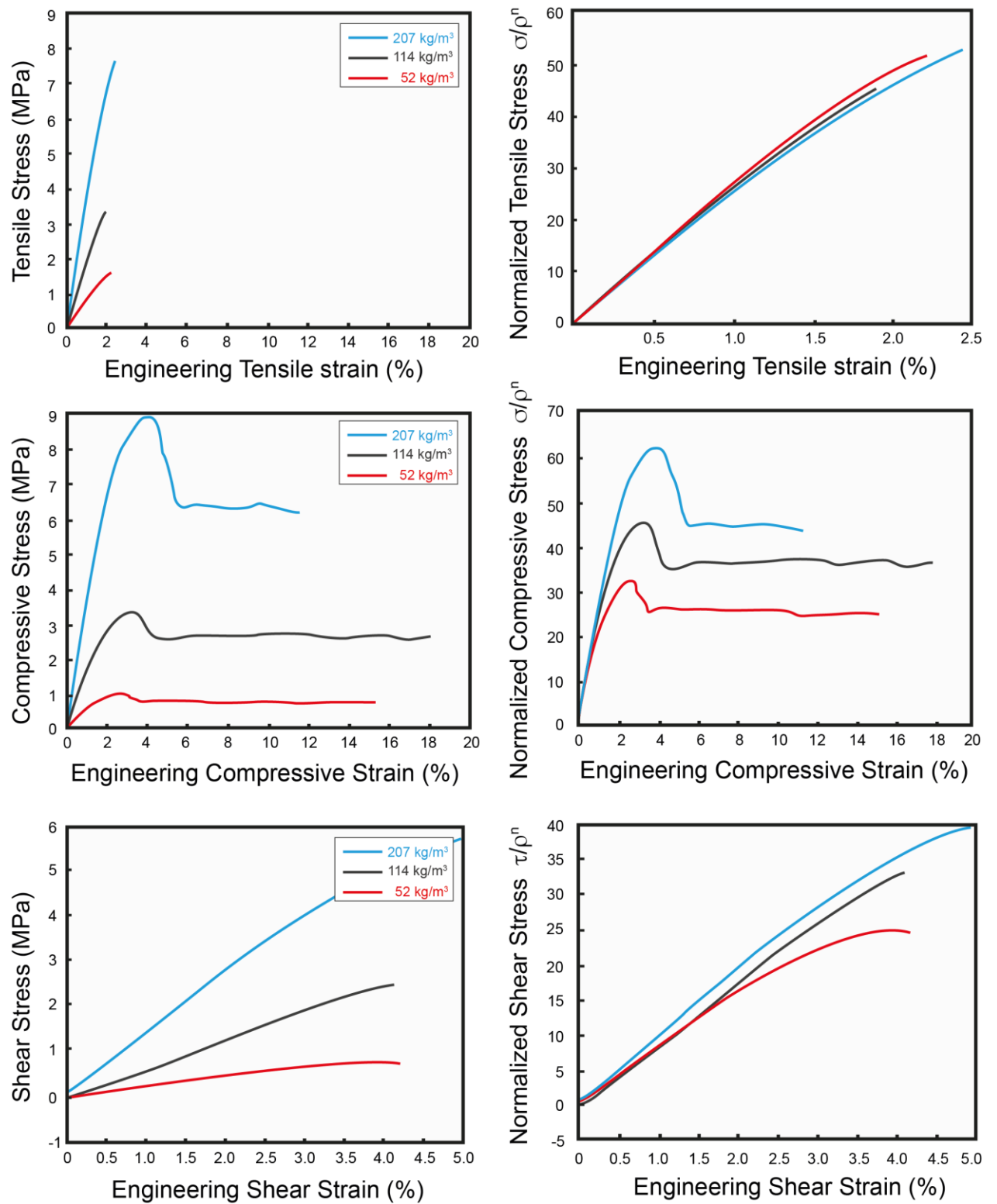


Figure 19 Density normalized tensile, compressive, and shear stress-strain curves of PMI foam with different densities, reproduced from [13].

Furthermore, it is known that for low-density foams the mechanical behavior in tensile loading could largely deviate from the compression properties [96]. One reason for this could be that when loaded in compression, the cell deformation of low-density foams involves local buckling of the weaker walls and struts. This causes a reduction in the analytically predicted mechanical properties.

Arezoo et al. [67] have also discussed the effect of strain rate and temperature on PMI foams. They reported an insensitivity of the test results to specimen dimensions (samples with thicknesses of 4 to 15 mm were tested). In the same work, the material response was indicated as isotropic. It is shown that at all foam densities, the compression properties are only mildly influenced by the low range strain rates (below 1000 s^{-1}). However, at higher strain rates the material behavior is changed to more brittle response. This was especially the case for the highest density PMI foam, which had a lower collapse stress at higher strain rates. In contrast, Li [96] reported that shear strength of PMI foam is insensitive to strain rate. Arezoo [67] showed that the effect of temperature on the PMI foam properties is large. The material behavior was indicated as elastic-brittle, elasto-plastic, and rubbery for temperatures of $-70 \text{ }^{\circ}\text{C}$, -40 to $70 \text{ }^{\circ}\text{C}$, and $200 \text{ }^{\circ}\text{C}$, respectively. Higher density foams had higher tendency to embrittlement at lower temperatures. One other important conclusion from this work is that similar to PVC foams, the sensitivity of PMI foam properties to temperature and strain rate is more rooted in the sensitivity of the parent solid material on the same properties, than the cell morphology. In another work, Siivola [133] showed that beside the role of temperature, the stiffness and strength of PMI foams decrease with humidity too. They reported a more severe degradation of properties when both temperature and humidity effects are combined.

Shear fatigue performance of PMI foams are comprehensively discussed by Zenkert, Burman, and Shipsha in [66, 68, 69, 134, 135]. Taking into account parameters such as stress ratio and maximum load, they identified and proposed maximum allowed strain rates (or frequencies) to prevent undesired local heating in the foam core. They reported shear fatigue S-N curves of the PMI foam cores with different densities and modelled the fatigue degradation. Using a modified test setup, it is identified that reversed loadings ($R < 0$) could significantly decrease the fatigue life of the foams. They also showed that sandwich stiffness (force divided by deflection) is not a good indication for fatigue health, as the stiffness only started decreasing at the last stages of the fatigue life. Initiation, size, and the location of shear failure during fatigue tests have also been discussed in the mentioned work. In addition, it is shown that the S-N curves of different density PMI foams have almost similar slopes. The same phenomenon was shown for PVC foams in the

previous chapter. Impact performance of PMI foam core sandwich structures for aviation applications are studied in [136], where it is shown that the foam core density can have considerable influence on the amount of damage detected by ultrasonic scans.

2.4.3 Extruded Foams

With the advancements made in foam processing methods, different equipment and die technologies can be exploited to improve the mechanical properties by inducing directionality. For example, extruded polystyrene (XPS) foam is deliberately made anisotropic in order to provide high compressive properties, as required by the final application such as insulation [16]. High compressive strength is required especially if the insulation foam is used in ceilings or cellars as it should carry higher loads. XPS foams are available in different thicknesses ranging from 20 to 200 mm [19].

Systematic literature on the properties of XPS foam is yet scarce. Heinz [19] has studied the mechanical properties of XPS foam (Styrodur 3035 CS) provided in sheet thickness of 80 mm and a nominal foam density of 33 kg/m^3 . He showed that the density variation within different locations in the foam plates were within 2 %, indicating stable foaming process. In addition, SEM analysis of the cell morphology showed that cell size distribution is quite homogeneous, and no appreciable difference could be seen between the bulk and surface of the 80 mm thick foam sheets. Nevertheless, compression tests revealed highly anisotropic mechanical properties for XPS foam. The out-of-plane modulus and strength (foam expansion direction) was 3 times higher than the in-plane direction. This is quite interesting, as the orientation of the foam cells through the expansion direction was not so significant. It was shown that the anisotropy in XPS foam is more related to the special configuration of the foam cells rather than their elongation/directionality. The cells are formed in a way that arrays of cell walls are aligned through the sample thickness, probably causing a more axial response against compressive loads (see **Figure 20**). In other words, adjacent neighboring cells through the thickness direction could be imagined as larger cells strongly oriented through the thickness. This arrangement can resist against bending of the walls and will activate a more stretch-dominated behavior. In contrast, the in-plane loading of the samples could still result in a more compliant bending-dominated response.

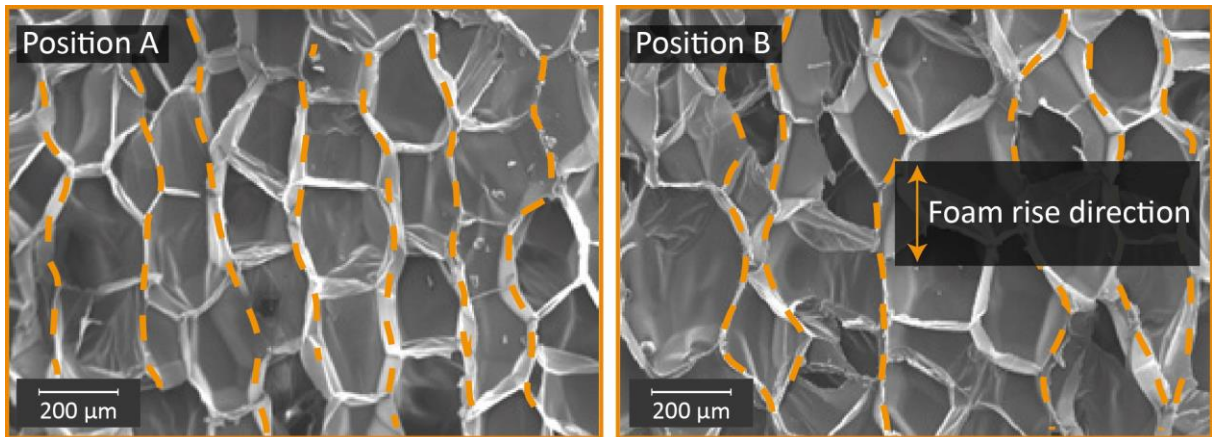


Figure 20 Alignment of XPS foam cell walls in the out-of-plane loading direction, driving a more axial deformation response [19].

Moreover, Heinz [19] studied the effect of specimen shape (cubes or cylinders) and specimen size on the compression properties of XPS foam. His results confirmed that for the same sample volume, the specimen shape has no influence on the measured properties neither in out-of-plane, nor in the in-plane directions. However, the effect of specimen size was definitely noticeable. In this case, the comparisons were made between cubic samples with dimensions of 50 and 8 mm, respectively. Results showed that the seating effects, associated with damaged surface cells, were stronger in the smaller samples, probably due to the smaller contact surface with the loading plates. Furthermore, the value of compressive modulus was more affected by the specimen size. In the out-of-plane direction, the smaller samples had about 15 % higher modulus. However, in the in-plane loading direction, the trend was almost reversed, and the in-plane modulus of the larger cubes was almost 60 % higher than the smaller samples. Jebur [20] has also investigated the anisotropy of extruded foams. In that work it is shown that extruded low-density polyethylene (LDPE) foam ($\rho = 40 \text{ kg/m}^3$) has transversely isotropic mechanical behavior and stronger response in the cell orientation direction. Correct process optimization tools can be exploited to improve the performance of LDPE foams, as they are finding new applications in impact protection and packaging.

2.5 Determination of Foam Core Shear Properties

It is well-known that the mechanical performance of sandwich structures highly depends on the properties of the core material. If the face sheets are designed so that they are elastically stable, the most critical stress mode applied on the core material is shear [27]. An important function of a foam core material is to provide high shear stiffness and strength, as most of the shear stresses

are taken by the bulky core material. As a result, correct understanding of the shear properties of the foam core is also a primary requirement for design of sandwich structures. **Table 2** compares the shear modulus and strength of typical core materials.

Table 2 Shear properties of commercially available sandwich core materials [24].

Sandwich Core Material	Shear Modulus [MPa]	Shear Strength [MPa]
Balsa wood	100-190	1.8-4.9
Al honeycomb (W direction)	151-450	0.9-2.2
Aramid honeycomb (W direction)	10-120	0.4-1.1
PP honeycomb (W direction)	9-15	0.3-0.6
Fibre reinforced PU foam	63-193	2.1-5.5
PMI foam	20-150	0.4-5.0
PVC foam (Cross-linked)	13-95	0.4-4.7
PET foam	20-55	0.6-2.0
PS foam	8-20	0.2-0.6
PU foam	3-5	0.9-2.2

The test methods for measuring core shear properties are among most frequently discussed topics in the literature on structural foam cores. Several experimental methods are available in the literature for determination of core shear response [27, 137–140]. In particular, two methods have been more popular. The first one yields core shear properties through the use of a three-point or four-point bending test on a sandwich beam specimen [137]. The second method obtains core shear properties by applying direct shear loads on the foam [139]. Different advantages and disadvantages have been associated with the two approaches [66, 140–143]. In the following, the two methods are introduced and briefly reviewed.

2.5.1 Direct Shear Test

In direct shear test (or block shear test), rectangular foam specimens are glued between two stiff plates and are directly loaded in shear. The shear strain is calculated from the relative

displacement of the two test plates. Direct shear tests have been used in many works [141, 143–147] to directly obtain the shear properties of different core materials, including newly developed foams. The main advantages of this method are that core shear strains and shear modulus can be directly measured (this is not directly possible in sandwich flexural tests). Furthermore, a state of pure shear stress can be realized by using correct specimen geometry. Since direct shear testing provides material specific information about the core, it is commonly used in the industry to measure shear properties of core materials. The values, therefore, could be used for design of sandwich structures in different applications.

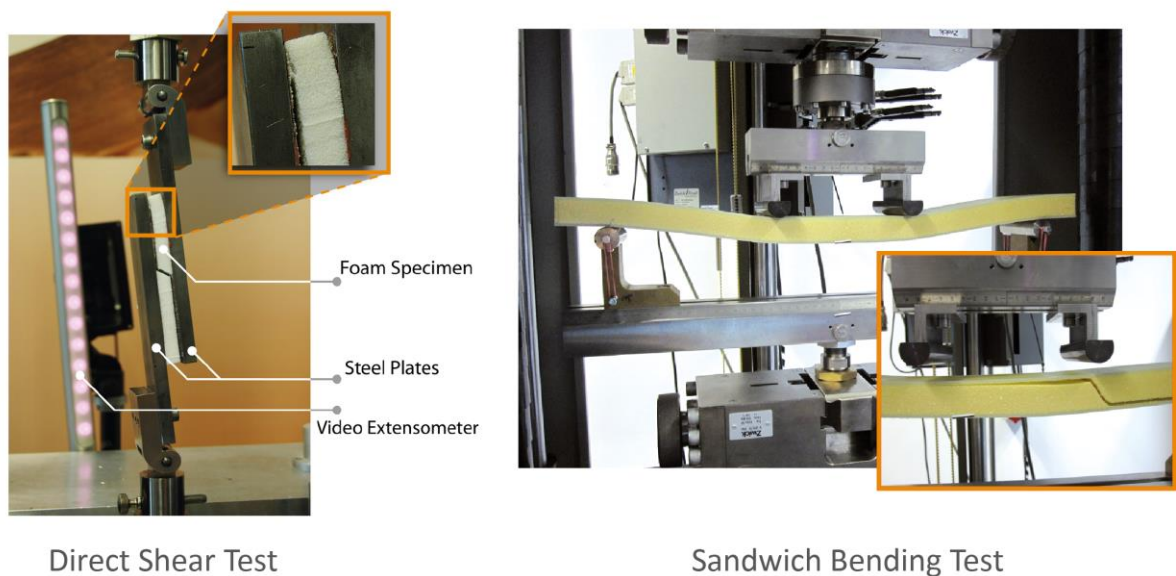


Figure 21 Available methods for obtaining core shear properties. Left: Direct shear (block shear) test; Right: Sandwich bending test.

Nevertheless, in block shear tests, specimen preparation is relatively complicated and time-consuming. Another challenge is related to stress concentrations and mixed stress modes usually occurring at the free corners, which can lead to inaccuracy in measurements (see the magnified section in the left image of **Figure 21**). In the works done by Grediac [141] and Benderly [148], parasitic effects in direct-shear testing are identified, quantified, and correlated to the sample geometry. It is shown that shear strain gradients near the sample edges leads to errors in the displacement between the two steel plates. However, using higher aspect ratio specimens it is possible to minimize this error. By FEM calculations, it is demonstrated in [149] that the error could be minimized to less than 3 % if the specimen aspect ratio is more than 12. Kiepert [145] attempted to reduce the effects of stress concentrations by geometrical optimization of the

specimen ends/edges. He illustrated that shaping the end of the rectangular specimens had no significant influence on the shear fatigue performance of the foam cores.

2.5.2 Sandwich Bending Test

Another popular method to determine the shear properties of core materials is the sandwich-bending test. This method provides means of testing the sandwich system in authentic in-service conditions, meaning that the effect of the whole sandwich assembly on core shear properties is taken into consideration. In addition, sample preparation and the testing procedure are rather straightforward. Sandwich bending tests have been extensively used in the literature to determine the core shear response [66, 69, 132, 134, 135, 143, 146, 150–159].

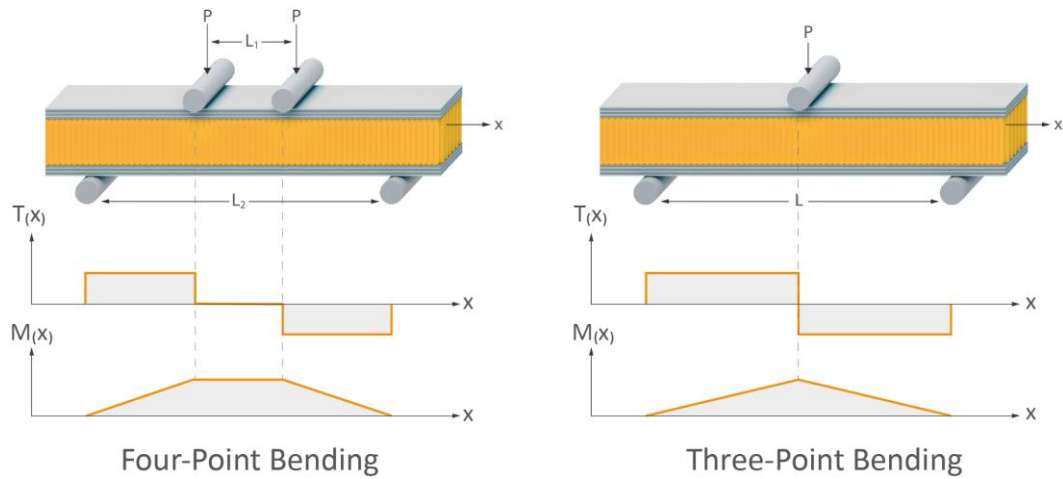


Figure 22 Bending moment (M_x) and transverse force (T_x) profiles in beams loaded in three-point and four-point bending.

In both three- and four-point bending experiments, it is possible to create a constant and uniform state of shear stress in large sections of the core [66]. The magnitude of core shear stress is comparable to transverse forces, T_x , shown in **Figure 22**. For a sandwich beam loaded in four-point bending, the maximum normal stress (tension/compression) in the face sheets and the maximum shear stress in the core can be calculated using Eq. 16 and Eq. 17, respectively. Here, P is the applied mid-point force; L_1 and L_2 are the loading and support span lengths; t_f is the thickness of the face sheets; b is the sandwich beam width; and d is the distance between the centroids of the face sheets [28].

$$\sigma_f = \frac{P(L_2 - L_1)}{2t_f db} \quad (16)$$

$$\tau_c = \frac{P}{db} \quad (17)$$

Hence, it is possible to design the testing span length in a way that shear stresses in the core reach the shear strength, before the tensile/compression strength of the face sheets is reached. One can then accurately measure the core shear strength, τ_c , using the midpoint force at the instance of core shear failure. There are several advantages associated with sandwich bending tests for determining core shear properties, as reviewed in [146].

However, one drawback of bending tests is that obtaining core shear strains, and therefore shear modulus, is experimentally difficult. Sandwich bending tests usually provide only information about core shear strength and sandwich stiffness values. Measuring core shear strain during sandwich bending directly requires additional measurement equipment. Nevertheless, an analytical method has been proposed and applied in the literature [143, 153, 155], which can provide core shear modulus by means of simple sandwich bending tests. In this method, sandwich beams are tested in a series of bending experiments with different span lengths. The effects of bending stiffness and shear stiffness are then distinguished, which allows for calculating core shear modulus (see reference [125] for more details on this analytical method). Usually, the sandwich stiffness (force divided by deflection) obtained from bending tests includes combined effects of both bending and shear deformations. Thus, only obtaining sandwich stiffness will not help with understanding the individual shear and in-plane contributions. Using the experimental method described below, it is possible to decouple shear stiffness and bending stiffness. This is important because shear stiffness is more controlled by the core material, while bending stiffness is more governed by the face material.

For a given sandwich beam loaded in three-point bending, the midpoint deflection is expressed by Eq. 18, in which w_t is the total midpoint deflection, consisting of bending deflection and shear deflection. Parameters D and U are bending stiffness and shear stiffness of the sandwich beam, respectively. The first term on the right side of Eq. 18 is the beam deflection due to bending and the second term corresponds to deflection caused by shear deformations. One should note that larger span lengths drive higher deflections by influencing both bending and shear components,

though the effect is stronger on bending component due to a cubic dependence on span length. A rearrangement of Eq. 18 leads to Eq. 19, where C is the sandwich compliance (w_t/P).

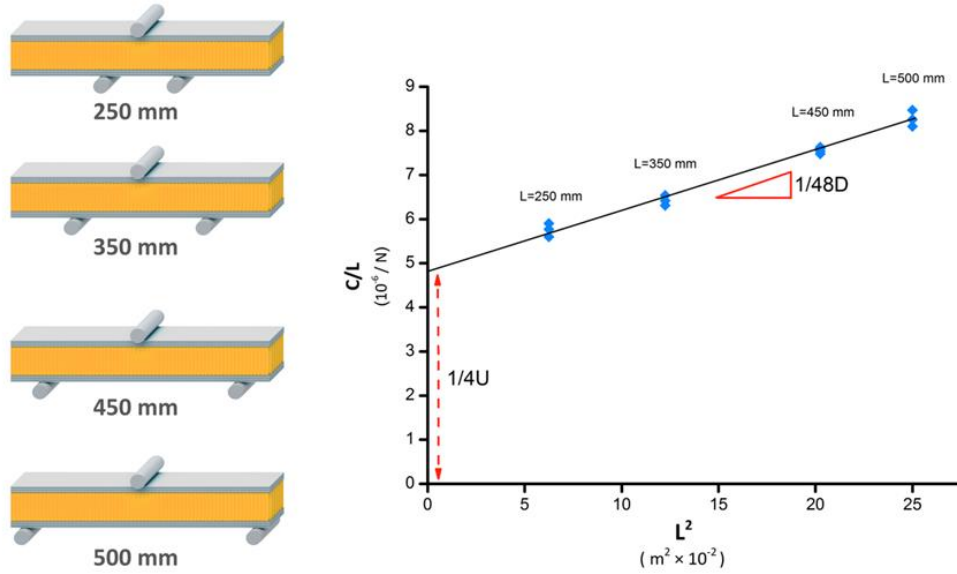


Figure 23 Graphical illustration of the analytical method to determine the sandwich bending stiffness and sandwich shear stiffness [24].

$$w_t = \frac{PL^3}{48D} + \frac{PL}{4U} \quad (18)$$

$$\frac{C}{L} = \frac{L^2}{48D} + \frac{1}{4U} \quad (19)$$

$$U = b t_c G \quad (20)$$

Eq. 19 shows a linear relationship between C/L and L^2 , in which $1/48D$ is the slope and the y-intercept is equal to $1/4U$. Thus, the beam's bending stiffness, D , and shear stiffness, U , can be determined by testing the sandwich beam over a series of different span lengths and plotting the values of C/L against L^2 , and consequently a data fitting step. This approach is reproduced from [21] and graphically shown for a PVC foam core sandwich structure in **Figure 23**. Another advantage of this analytical method is that the effective shear modulus of the core can be estimated using Eq. 20, which is a derivation of sandwich theory [27]. Here, U is sandwich shear stiffness, b is the sandwich beam width, t_c is the core thickness and G is the core shear modulus.

2.6 Brief Review of Wood's Properties

It will be shown in the results section, that the morphology-property relations observed for PET foams show strong analogies to those of wood. Hence, it is useful to briefly review how the mechanical properties of wood depend on its cell structure.

Wood is one of the oldest structural cellular materials known. Humans have used wood in load-bearing structures for more than five millennia [2]. The structure of wood can be analyzed at different length scales. At the macroscale, wood's structure is defined by the radial growth of rings, which have different densities and cell sizes due to different growth rates during cold and warm seasons. At the microscopic scale, wood is made of thin and elongated cells (with the shape of hexagonal prisms), which are squeezed together like straws, parallel to the axis of the tree [2]. At the molecular level, the cell walls are made of a fiber-reinforced composite material. Cellulose microfibrils (up to 45 wt.%) are dispersed in a blend matrix of lignin and semi-crystalline hemicellulose. The strong and stiff crystalline cellulose fibers are also oriented in the axial direction (parallel to the elongated cells), giving the cell wall material stiffness values three times higher in the axis of the cell. Hence, as suggested by Ashby [2], wood can be described as a foamed fiber composite. Both foam cells and the cellulose fibres in the cell walls are aligned mainly along the grain direction, resulting in a highly anisotropic mechanical response [2, 25]. In a time span of 100 million years, wood has optimized its morphology to yield most efficient properties. There is a wide range of woods with different densities and properties. Balsa is the lightest wood with densities in the range of 100-300 kg/m³. On the other hand, oak is about 5 times stiffer, stronger, and tougher than Balsa, with densities around 750 kg/m³ [2]. However, being a natural structure, the density, cell morphology, and properties of wood are not uniform and show high local variations. Therefore, there is usually large scatter reported for the measured properties of wood. In reference [2], it is shown that properties of Balsa can vary up to 20% and are strongly affected by moisture and temperature. Whisler [160] showed a wide scatter in the shear failure strain of Balsa, which was attributed to its natural structure and wide variation of local density. In this thesis, a similar effect was visually captured [59] for the variation of shear strain during sandwich bending tests (see Chapter 5.3.3). The mechanical response of Balsa wood in different loading modes is already studied and well-established. The mechanical behavior of wood is comparable to those of honeycombs and similar models as honeycombs could be applied to study their properties [161]. Different aspects such as the influence of density, and structural anisotropy on the macroscopic properties have been already identified.

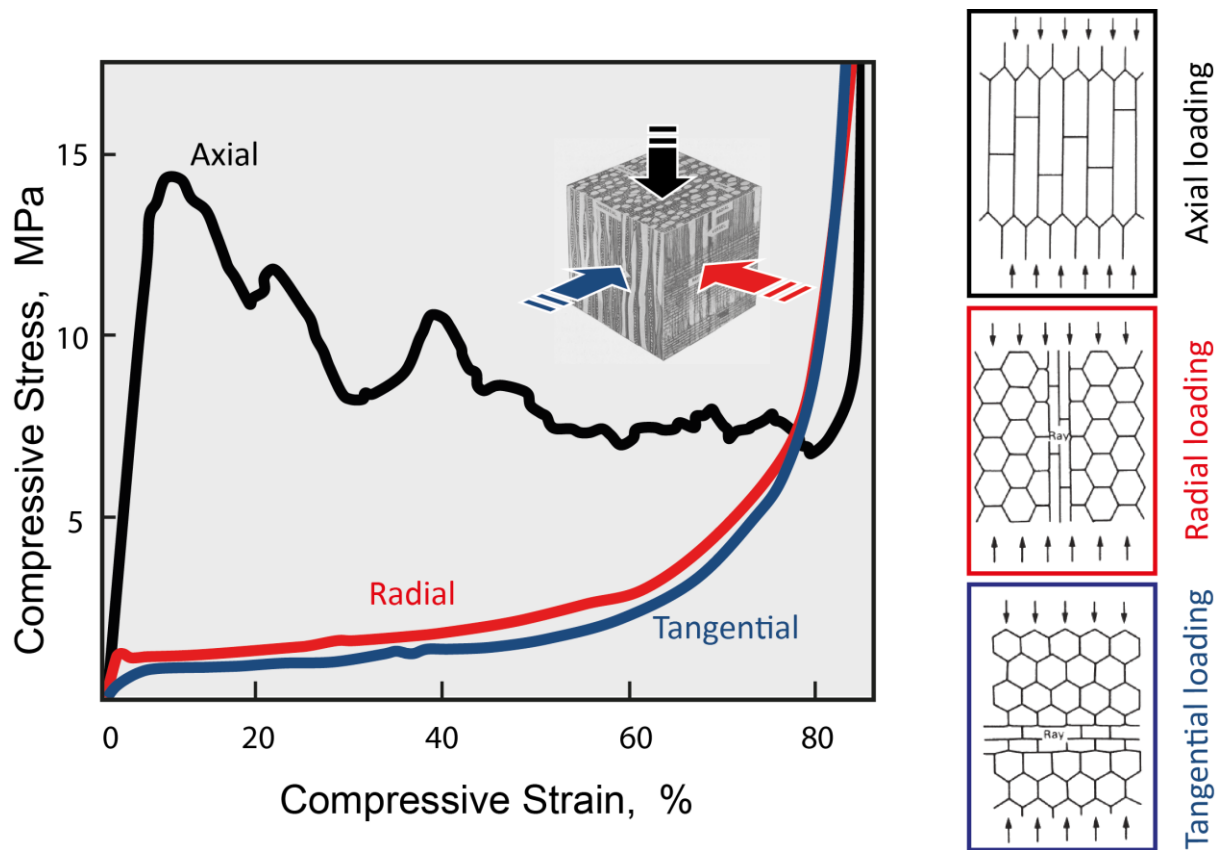


Figure 24 Compressive stress-strain curves of Balsa wood, when loaded in axial, radial and tangential directions (reproduced from [25]).

Figure 24 shows the stress-strain curves of Balsa wood when compressed in different loading directions. The Young's modulus and yield stress in the axial direction are much higher than the radial and the tangential directions. In both transverse loading directions (radial and tangential), the stress-strain curves and the yield stress values are very similar, with the exception that a small yield drop is seen in the radial direction. Nevertheless, after yielding, the stress-strain curves in both directions rise smoothly and the sample is gently densified. In contrast, the axial stress-strain curve in **Figure 24** is categorically different. The Young's modulus and yield stress are much higher, and a strong post-yielding stress drop is manifested through a serrated plateau zone [25]. The high mechanical anisotropy of wood is mostly related to the cell shape, and the fact that elongated cells are stiffer and stronger when loaded along the cell axis, than when loaded across it [25]. Gibson has showed that the different stress-strain behaviors in the axial and transverse directions are related to the different cell deformation mechanisms (see **Figure 25**). In axial loading, the elastic regime is controlled by axial compression of the elongated cells, with little evidence of cell wall bending. The cell collapse then happens through yielding and plastic buckling (or fracture) of cell arrays adjacent to each other, one array after another. This

behavior causes the step-wise stress drop and rise seen in **Figure 24**. In contrast, in both radial and tangential direction, the deformation starts with uniform bending of the cell walls followed by their collapse in form of plastic yielding, similar to most foams.

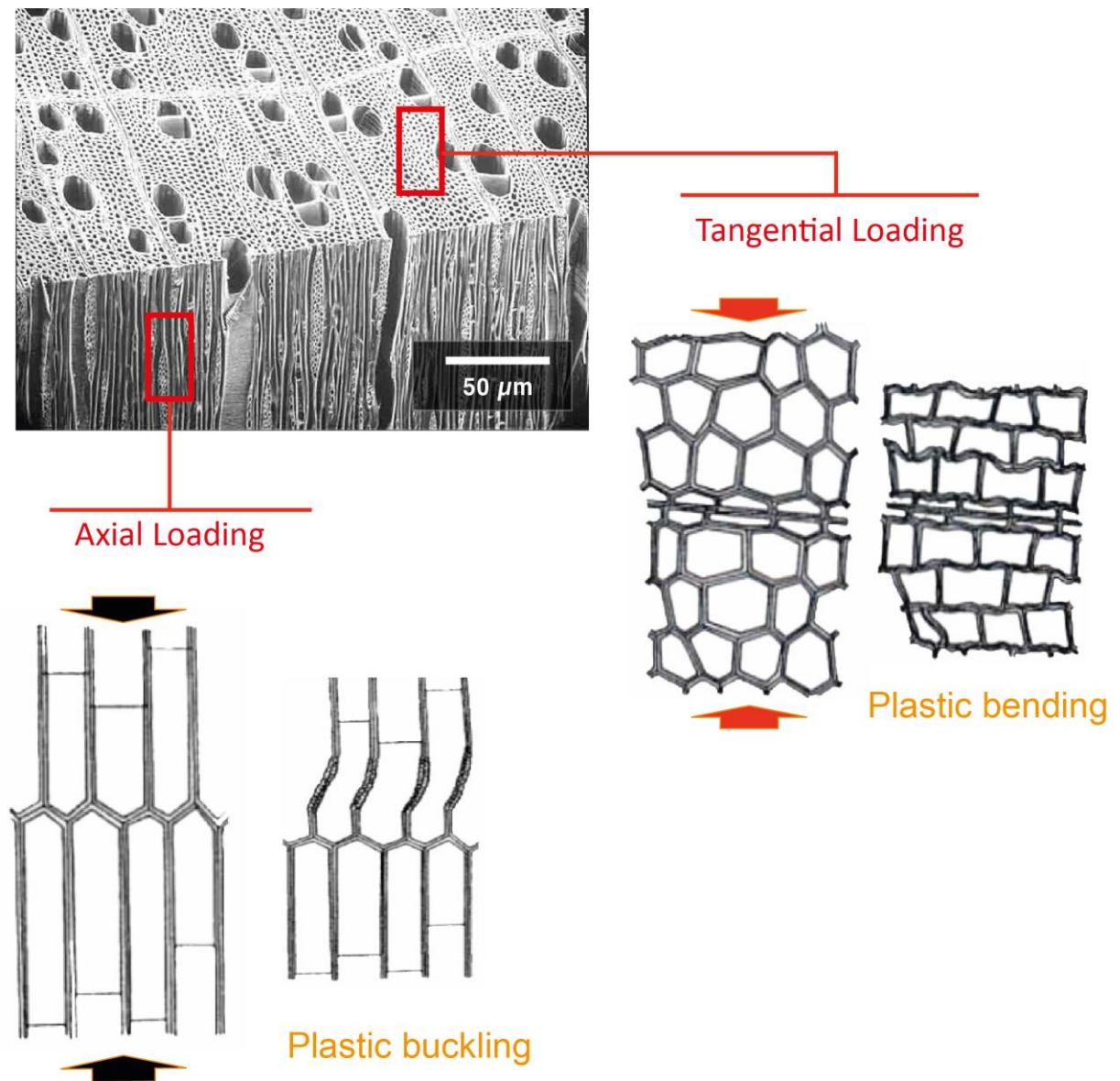


Figure 25 Different cell deformation mechanisms in wood when loaded in the axial and the tangential direction (reproduced from [25]).

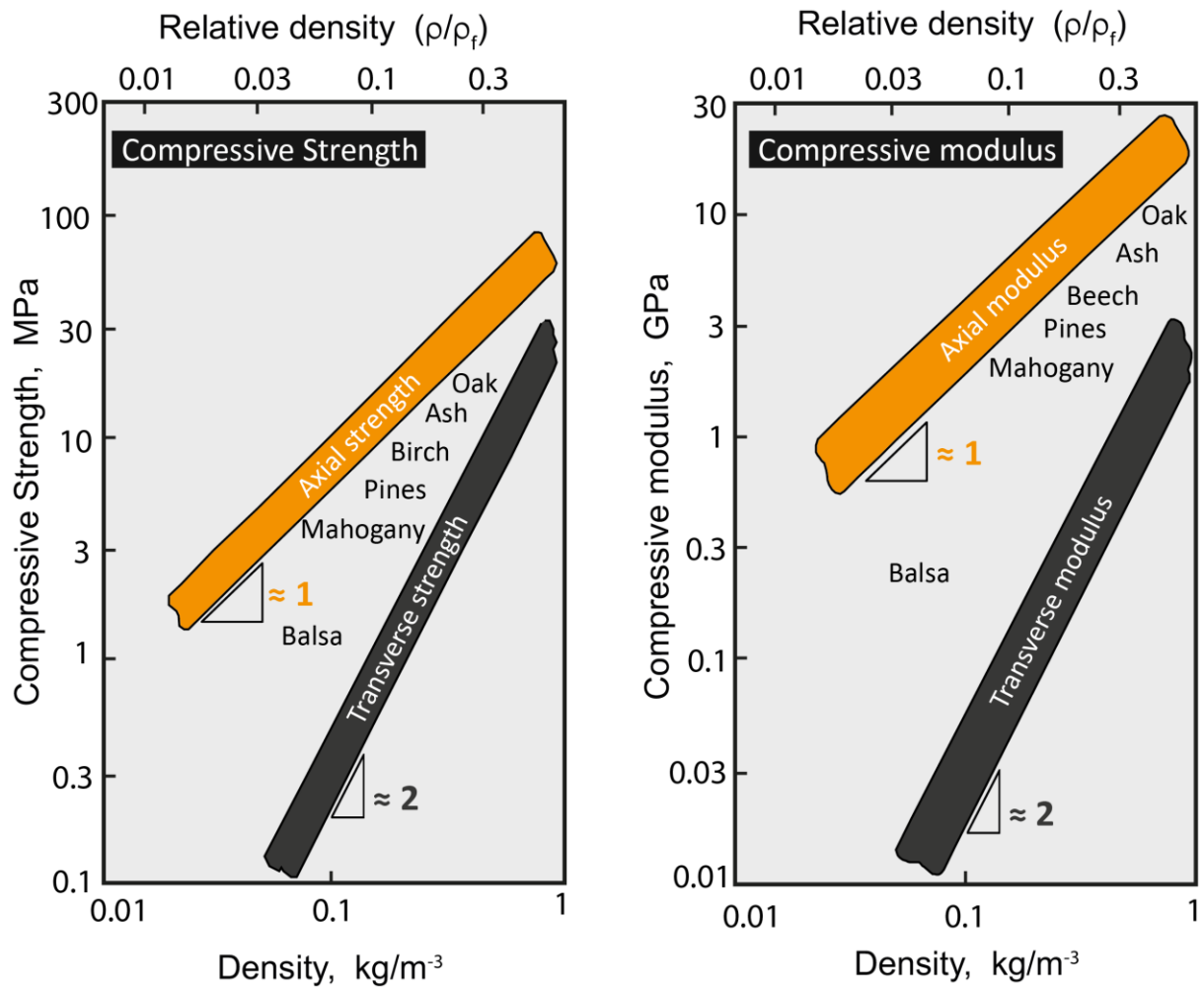


Figure 26 Scaling of relative compression properties with relative density in wood, reproduced from [2].

The scaling of wood's properties with its density has been thoroughly discussed in the literature [2, 25, 111]. **Figure 26** shows how the Young's modulus and compressive strength in the axial and transverse directions change with density. The axial modulus has a linear dependence on density and follows Eq. 11 with power law constant, $n \sim 1$. This is because in axial compression or extension, the modulus of the foam is that of the cell wall material (E_s), linearly reduced by the fraction of the regions occupied by cell walls. On the contrary, the transverse modulus varies with the square of density ($n \sim 2$). This behavior is described by Eq. 3, which considers a bending deformation mode for the cell struts. The different slopes of the axial and the transverse loading directions indicate that anisotropy is higher at lower densities.

2.7 Optical Deformation Analysis

Optical strain measurements are becoming more attractive for studying the deformation behavior and mechanical properties of foam materials. Therefore, plenty of recent literature is already available on optical deformation measurement methods for studying foams' behaviors [100, 106, 107, 162–174]. These methods perform contactless and are particularly suitable for soft polymeric materials [163].

Using optical deformation analyses, it is possible to measure full-field surface strain patterns instead of average strains between two marks on the sample (e.g. video extensometers) or point strain values (e.g. local strain gauges). Optical methods are independent of sample geometry and can be used when testing complicated specimen shapes. Since yielding is a local phenomenon, deformation patterns in the post-yielding regime become irregular and rather difficult to measure with conventional extensometers. In this case, optical strain analysis can provide means of studying local deformations in foams and can link this information to the cell structure. Information on local deformation of foams can also help to understand the failure phenomena and possibly verify numerical simulations.

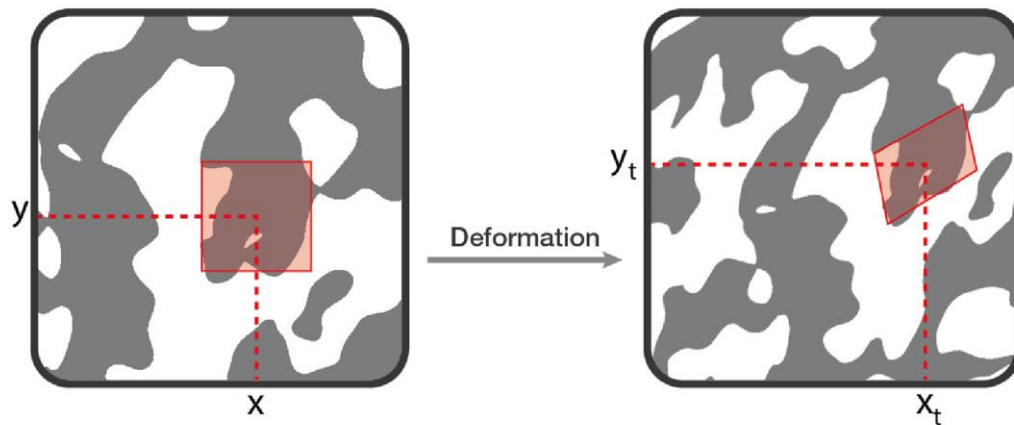


Figure 27 Schematic illustration of the grayscale distribution of a facet in the nondeformed (left) and the deformed (right) states, reproduced from [162].

One relatively recent method is Digital Image Correlation (DIC). In the DIC method, one compares a series of images, captured at various deformation levels, with a reference image initially taken before loading. The fundamental principle is based on the fact that the gradient of grayscale values of a specific area (here called a facet) in the undeformed state corresponds to

the gradient of grayscale values of the same area in the deformed states, as schematically shown in **Figure 27** [162]. This provides a physical mean to track and locate the displacement of several facets during the whole deformation process. Each facet, therefore, can function as a local virtual strain gauge. The quality and precision of the measurement are strongly influenced by the surface visual details and contrast. In order to produce fine features, usually a random paint pattern is applied on the surface of the specimen. Manually defined sizes of the facets and the level of facet overlap play an important role in determining the precision and the resolution of the measurement. Definition of an adequate facet size is based on the operator's experience, specimen conditions and proper lighting. Smaller facets will capture more local deformation features, while larger facets can have more distinguishable grayscale values and eventually result in measurements that are more precise. In this thesis, optical analysis is performed using the DIC method to study the local deformation of foam samples during both compression and sandwich shear tests.

3 Goals of the Thesis

The main goal of this thesis is to provide a fundamental understanding of the anisotropic mechanical behavior of strand PET foams, in relation to the multi-scale foam morphology. This understanding is essential for component design, as well as new foam process developments. With this said, the following subgoals are defined for this thesis.

- One aim of the present thesis is to capture and understand the effect of the multi-scale morphology on the anisotropic mechanical properties of strand PET foam, particularly in compression loading. It is expected that different cell types follow distinct deformation mechanisms, which control the local crush patterns and the global macroscopic stress-strain behavior. As shown in **Figure 28**, the aim is to demonstrate how the local cell morphology determines the cell deformation mechanisms, the local crush patterns and ultimately the global mechanical response.

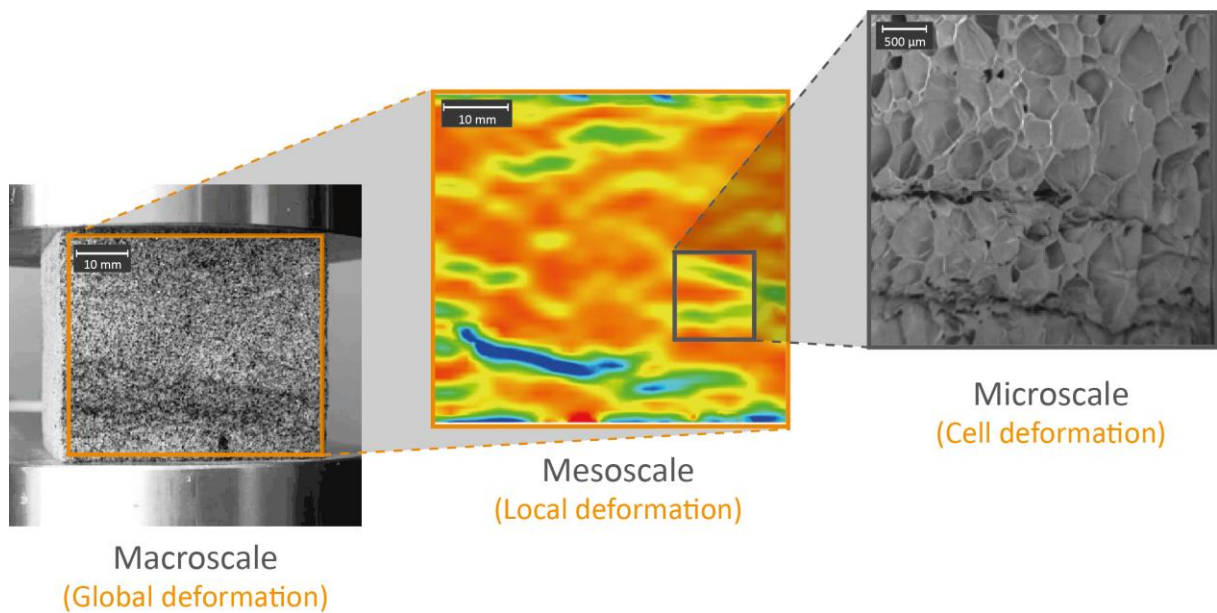


Figure 28 Illustration of how cell level deformation mechanism in strand PET foam controls the global macroscopic response via local crush patterns.

- Another goal of this thesis is to investigate the effect of foam density on the mechanical properties. Later, the objective is to establish correlations between the density scaling behavior and the morphology-controlled deformation mechanisms in different loading directions. A side objective is to show how the deformation mechanism shifts with foam

density and discuss the impact of this mechanism shift on the accuracy of density scaling relations.

- The last objective of this thesis is to establish systematic experimental data on the morphology (strand level, cell level) and properties (global, local, and cell level deformations) of strand PET foam on a multi-scale level. These are crucial for enabling multi-scale FEM simulations of mechanical properties of such foams. The mechanical response measured and visually illustrated here can be utilized to verify multi-scale FEM simulations, capable of correctly linking the cell level deformation to the macroscopic response of strand foams.

4 Experimental

4.1 Commercial PET Foam

The PET foam studied in this thesis (Airex T92 series) is a commercially available core material produced and supplied by Airex AG, Switzerland. T92 is a high performance closed-cell thermoplastic foam, manufactured by state-of-the-art strand foam extrusion process (see chapter 2.2.3). The range of foam densities available by the manufacturer, at the time this study was conducted, was between 80 and 220 kg/m³. Four different foam grades were used, namely T92.80, T92.100, T92.130 and T92.200. These grades had nominal densities of 92, 112, 136 and 211 kg/m³, respectively. **Table 3** compares the measured densities of all four grades in comparison with the data from manufacturer's material datasheet.

Table 3 Nominal density values of different PET foams (AIREX T92) studied in this thesis.

Foam Density [kg/m ³]		
	<i>Material Datasheet</i>	<i>Measured Values</i>
T92.80	85 (80-90)	91.99 ± 1.81
T92.100	105 (102-112)	112.23 ± 4.47
T92.130	135 (127-143)	135.85 ± 2.76
T92.200	210 (200-220)	210.83 ± 2.05

The T92.100 grade ($\rho \sim 100 - 110$ kg/m³) is the most industrially popular grade due to its suitable properties to weight ratios. Therefore, some measurements and tests were only performed on this foam grade. There were some minor variations in density and properties of the T92.100 samples used during the early and late phases of this thesis (time span of almost four years). Therefore, the values reported for compression modulus and strength of this grade in chapters 5.2.1 and 5.2.4 are slightly different. Nevertheless, this small variation has no major impact on the main correlations and interpretations made.

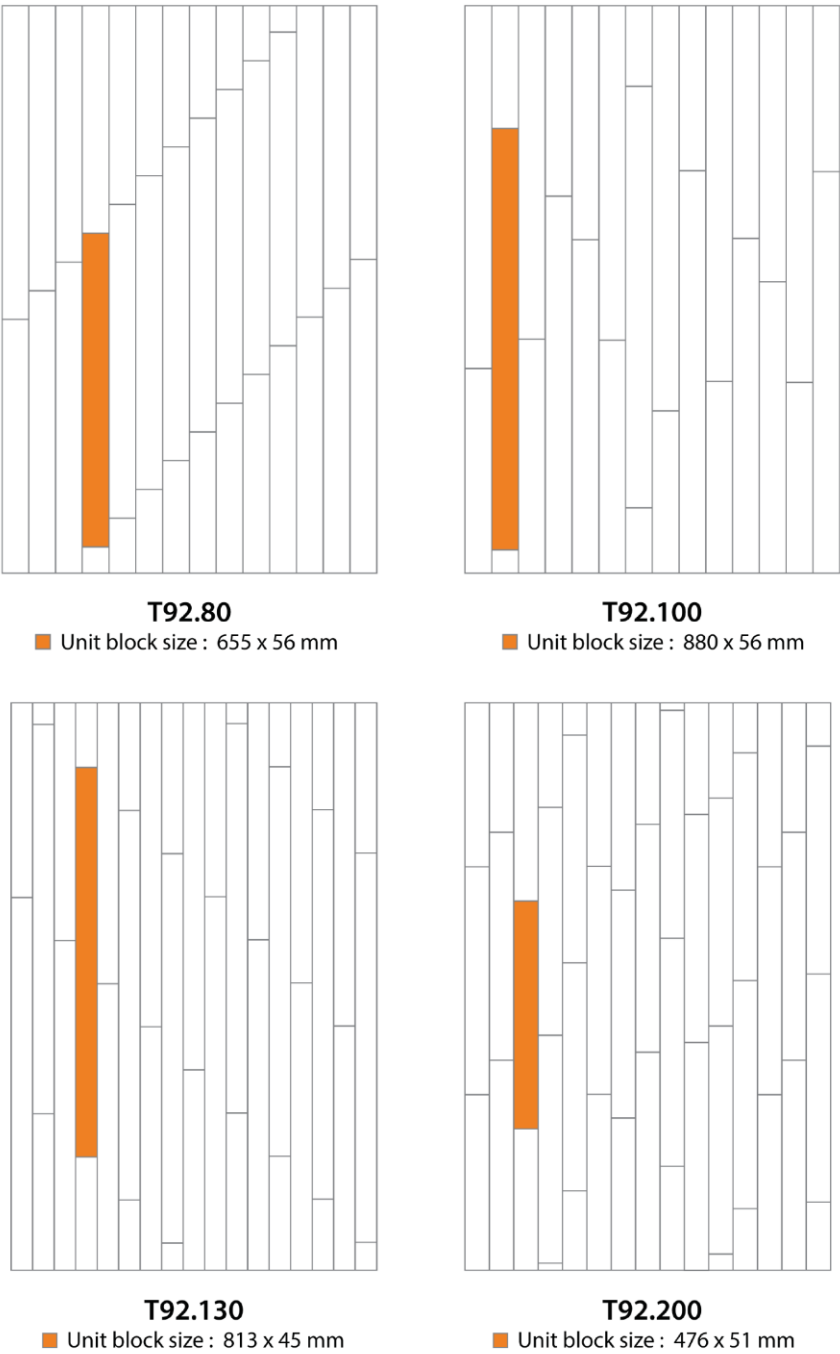


Figure 29 Schematic illustration of the foam sheets from each density class and the corresponding size of the extruded foam blocks.

As mentioned earlier, strand PET foams are produced by welding individual extruded foam blocks in a way that the extrusion direction is aligned with the panel thickness. Macroscopic inspection of the foam sheets showed that the dimensions of individual extruded blocks were different for each foam grade. No information could be found or disclosed by the supplier on the

root cause to the different extrudate dimensions. **Figure 29** schematically shows the configuration of the foam sheets and the corresponding dimensions of the extruded blocks for each foam density.

The materials were sourced in form of flat sheets, which were then cut into corresponding specimen sizes for different tests. Foam sheets with two thicknesses were used. The 1220×610×50 mm foam sheets were used for compression tests; and the 1220×610×12 mm sheets were utilized for direct shear tests (**Figure 30**).

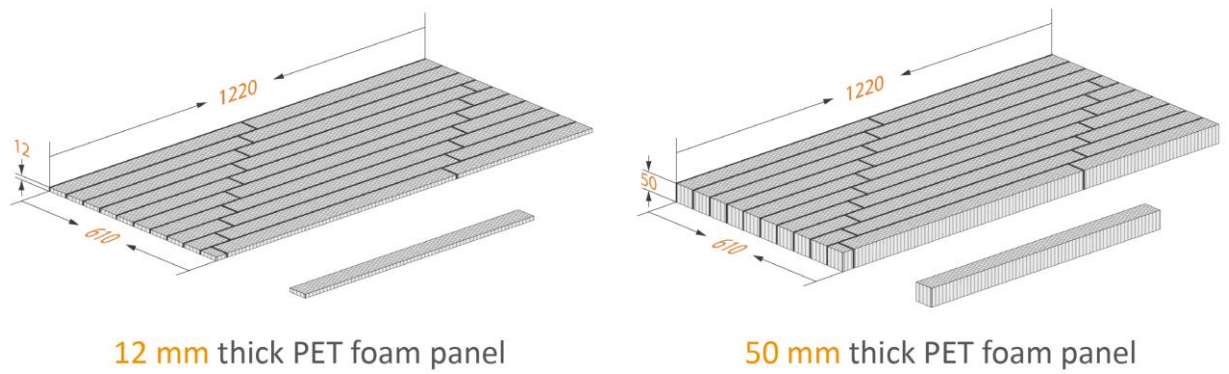


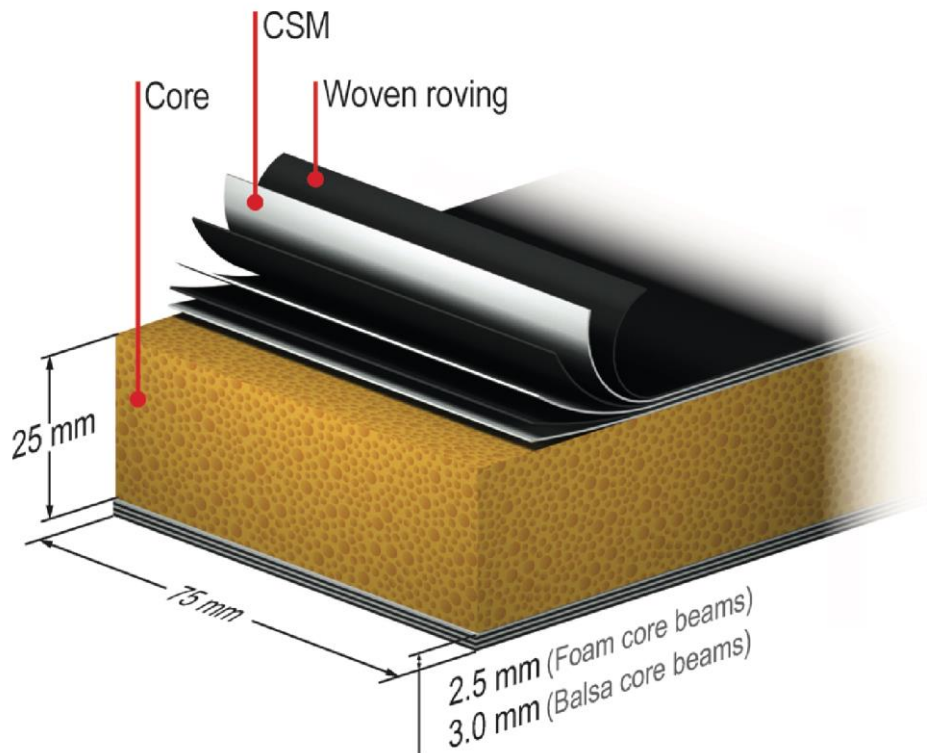
Figure 30 Schematic illustration of strand PET foam sheets with different thicknesses.

4.2 Sandwich Specimens (Bending Tests)

For obtaining shear properties of PET foam using sandwich bending experiments, sandwich panels were provided by AIREX AG, Switzerland. The sandwich panels were created using Vacuum Assisted Resin Infusion (VARI). Curing took place at room temperature and post curing of the infused panels was not considered. In addition to the PET foam core (Airex T92.100), two other core materials were utilized: end-grain Balsa (Baltek SB.50), and cross-linked PVC foam (Airex C70.55). Based on the manufacturer's datasheets, the nominal densities of PET foam, PVC foam, and Balsa were 105, 60 and 94 kg/m³, respectively. **Table 4** provides information about the three core materials according to their material datasheets.

Table 4 Density and shear properties of sandwich core materials reported from their material data sheets [28].

	PET foam (T92.100)	Cross-linked PVC foam (C70.55)	Balsa (Baltek SB.50)
Density [kg/m ³]	105 (102-112)	60 (54-69)	94 (-)
Shear Modulus [MPa]	21 (min. 18)	22 (min. 18)	106
Shear Strength [MPa]	0.9 (min. 0.75)	0.85 (min. 0.70)	1.8

**Figure 31** Sandwich dimensions and stacking sequence of the face sheets in sandwich specimens.

Sandwich specimens had identical glass-fiber/epoxy laminate sheets on both sides of the core. A combination of epoxy resin (PRO-SET 117LV) and a hardener (PRO-SET 226) provided by Pro-Set Inc. (Bay City, MI, USA) were used to impregnate the glass fabrics and bond them to the core. In foam core systems, face sheets had three combined layers of glass mats. Each combined layer comprised of a 300 g/m² chopped strand mat (CSM) and a 600 g/m² 0/90 woven roving fabric.

Stacking sequence of the face sheets of foam core sandwich beams is schematically shown in **Figure 31**. Face laminates of the Balsa core beams had four combined layers of glass-fiber mats (CSM + woven roving), in order to avoid face failure. Average face sheet thickness of the foam core and Balsa core specimens were about 2.5 and 3.0 mm, respectively. The fiber content in the laminates was theoretically estimated to be about 45 vol. %.

Following the curing of the sandwich panels, specimens were cut to correct sizes using a diamond-coated circular saw. The direction of cutting was parallel to the 0/90 fibers in order to provide maximum mechanical properties of the face laminates. All specimens were 600 mm in length, 75 mm in width, and had a core thickness of 25 mm.

4.3 Morphology Analysis

Different types of imaging equipment with a range of capabilities (e.g. different magnifications and different sizes of view field) were employed to understand and precisely define the morphology and structural features of PET foam (**Figure 32**). This included Light Microscopy (LM), Scanning Electron Microscopy (SEM), as well as Micro-Computer Tomography (μ -CT).

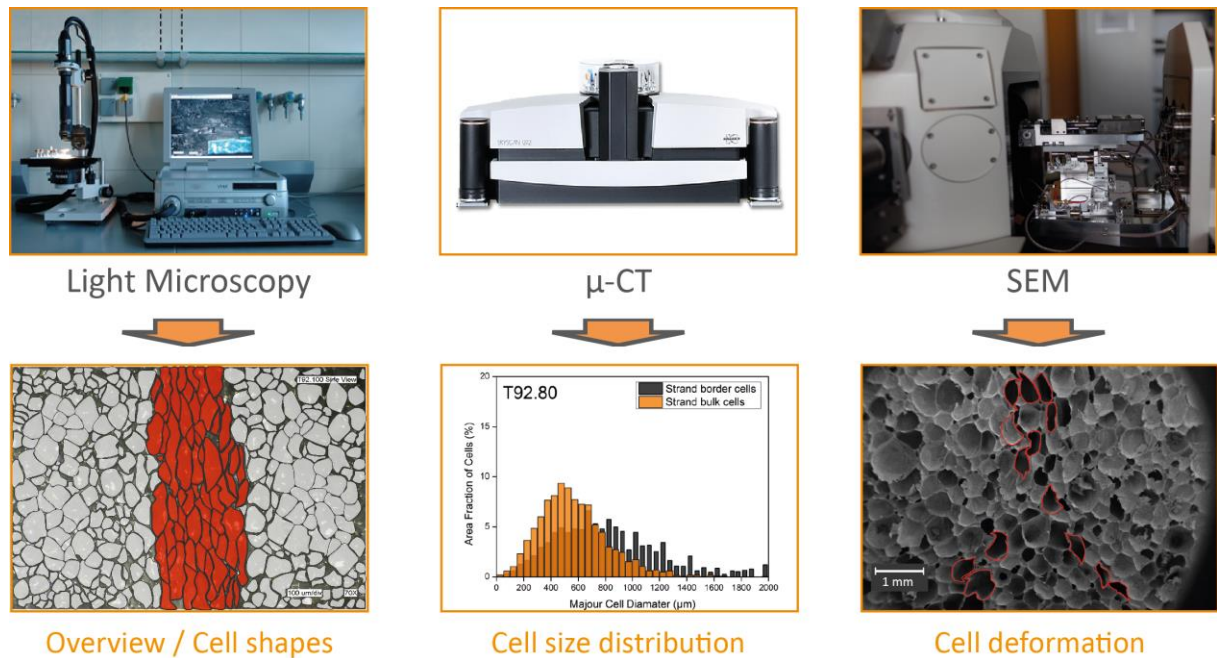


Figure 32 Overview of different optical techniques used to define the morphology of PET foams.

At first, a basic overview of the cell structure was made using a **Keyence VHX 1100** light microscope, at a magnification of 70 X. The large view field (several millimeters across) allowed

for observing different types of foam cells in the strand border and strand bulk regions. On the other hand, real time deformation modes of the cell walls during compression tests were captured using SEM equipment **Zeiss EVO MA 15**, operating at an acceleration voltage of 2 kV. Prior to characterization, samples were sputtered with a ~ 10 nm thin gold layer. Finally, yet importantly, a high-resolution μ -CT device (**Skyscan 1272**, Bruker Corporation) with a resolution of $2.5 \mu\text{m}/\text{pixel}$ was used to measure and accurately quantify the geometrical features of the foam cells such as cell size and aspect ratio distributions. The captured data included information from relatively large number of cells (several thousands of cells per specimen). The equipment performed at an acceleration voltage of 40 kV and a current of $248 \mu\text{A}$ during imaging. All images were taken to a maximum rotation of 180° with an increment of 0.23° . The subsequent projections were transformed to slices perpendicular to the direction of imaging, which could be then analyzed and viewed as a three-dimensional model using the software CTVol (Bruker MicroCT). For quantitative cell analysis, the data was exported from several 2D images, which were selected from different cross-sections. This ensured that a large number of individual foam cells were counted in for morphological analysis.

For each density, one μ -CT measurement was conducted on small cylindrical samples (diameter of ca. 8 mm) at a voxel resolution of $2.25 \mu\text{m}/\text{pixel}$. The images were used to determine the average cell wall and strut thicknesses. The measured average cell wall thickness values for different density PET foams are in the range of 15-35 micron (see Chapter 5.1.3). Therefore, a resolution of 2.25 micron per pixel was assumed acceptable for the purpose of this thesis. Additionally, a second μ -CT measurement was done on larger cubic samples (~ 20 mm) at a resolution of $6.25 \mu\text{m}/\text{pixel}$ in order to measure cell size and aspect ratio distributions.

4.4 Compression Tests

Uniaxial compression tests were carried out using different equipment and different specimen dimensions (**Figure 33**). In all compression tests, the same nomenclature was used for different loading directions, as depicted in **Figure 34**. Out-of-plane (through thickness) loading is denoted as Direction 3, whereas the two in-plane directions will be referred to as Direction 1 and Direction 2, respectively. The in-plane directions are sometimes referred to as transverse directions.

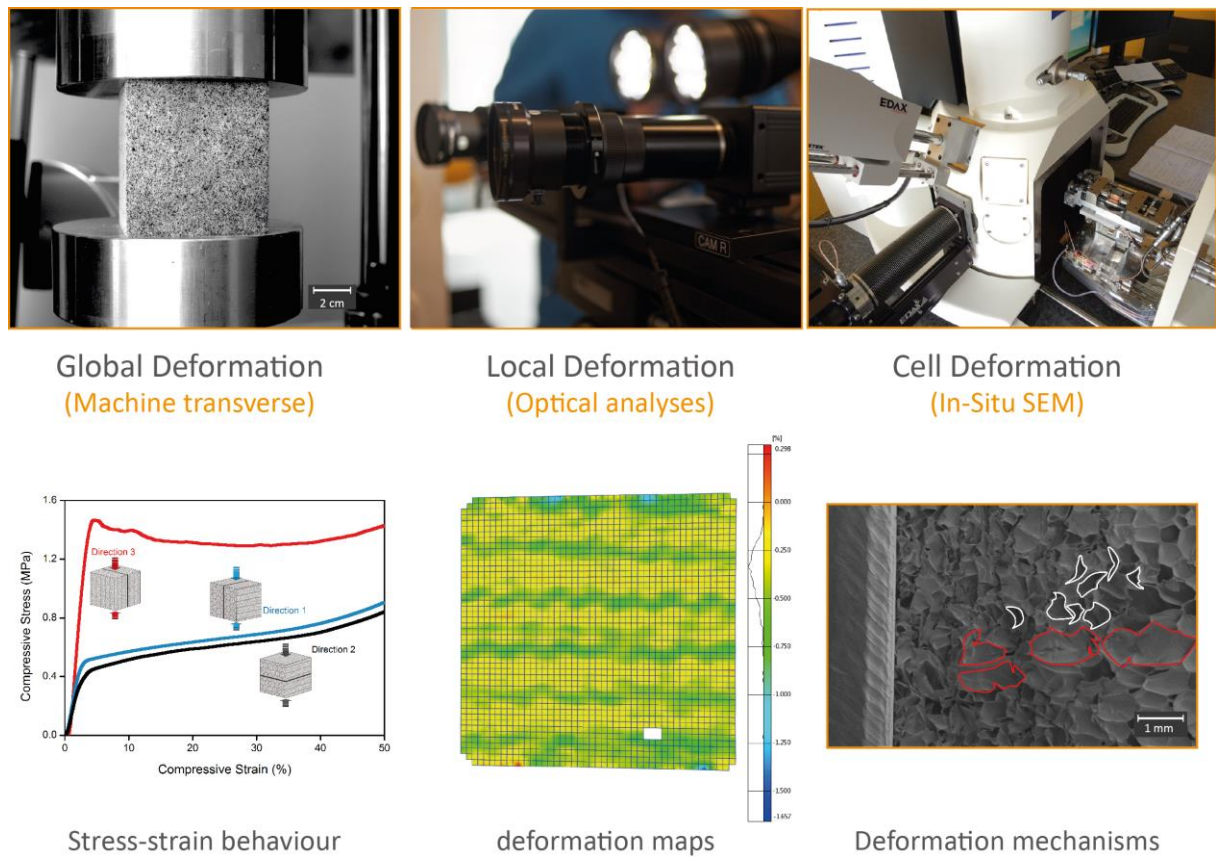


Figure 33 Compression tests of strand PET foams using different length scale measurement methods.

As depicted in **Figure 33**, the mechanical deformation of PET foam samples was analyzed at different length scales. This included the global specimen deformation (macro), the local deformation distributions (meso), and the cell wall deformation mechanisms (micro). For all data representations, the same global stress values (measure by machine load cell) were used. For obtaining the global stress-strain response, compression tests followed the standard method DIN 53 421. Cubic specimens with dimensions of 50×50×50 mm were cut out of foam sheets using a circular saw and conditioned prior to testing. No surface treatments were considered for the specimens. In order to account for the influence of the weld lines, all test specimens included a weld line in their centers. Compressive loading took place at a constant strain rate of 10 %/min, using a **Zwick 1485** Universal Testing Machine (UTM) with a 10 kN load cell. A pre-force of 5 N was applied prior to loading. The global engineering strains were measured using the crosshead movement of the machine transverse. No correction factors were included for the calculation of elastic modulus. However, sample sizes were chosen large enough to minimize the measurement error, associated with early crushing of the surface cells. Values of compression modulus are reported as the slope of the global stress-strain curves in initial linear zone.

However, a more accurate calculation of the Young's modulus is performed using optical analysis (see local deformation in **Figure 33**). All tests were performed in a controlled environment at a temperature of 23 °C and 55 % relative humidity.

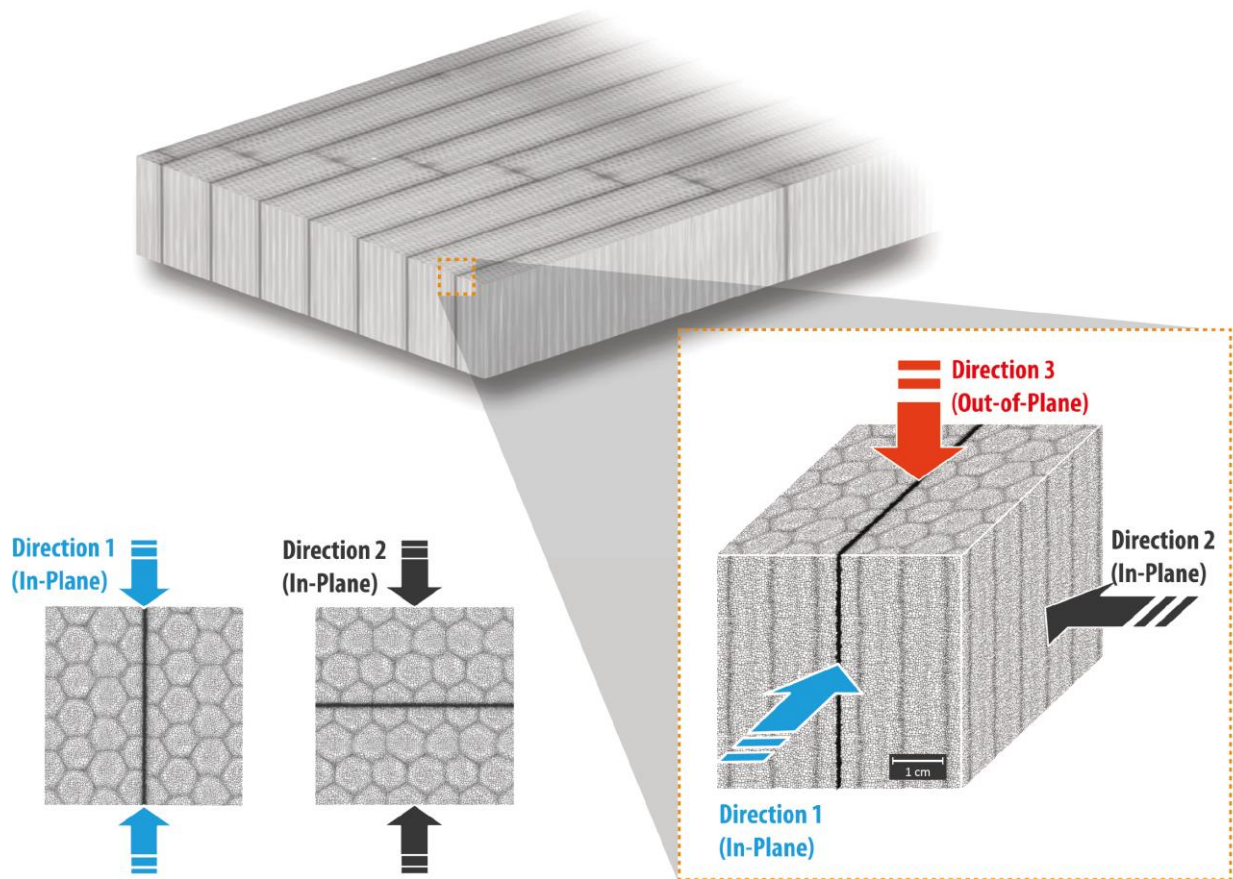


Figure 34 Nomenclature used for different loading directions of strand PET foams.

The local compressive deformations of foam samples were studied with the aid of Digital Image Correlation (DIC). Measurements were done using optical strain analysis equipment **Aramis 2M**, from GOM GmbH, Germany. The same sample size of 50×50×50 mm was used in order to enable direct comparison between the global and local straining behavior. However, for the optical analysis, specimen surfaces were sprayed using a marker aerosol to create a random pattern for ensuring good grayscale distribution (see **Figure 35**). The optical equipment consisted of two high-speed cameras (resolution of 1624 x 1236 pixels) for capturing images; a controller (trigger box) to operate the cameras; and a computer for data acquisition and results evaluation.

Image recording was performed at a frame rate of 5 images per second, and an analog signal was simultaneously received from the test machine in order to obtain different parameters for each

recorded image (e.g. force values and time steps). Depending on the measuring volume size, the relative position and the angle of the two cameras were adjusted, followed by a calibration procedure. In this investigation, overlapping quadratic subsets (facets) with a size of 14 pixels and a step size of 10 pixels between two subsets were used.

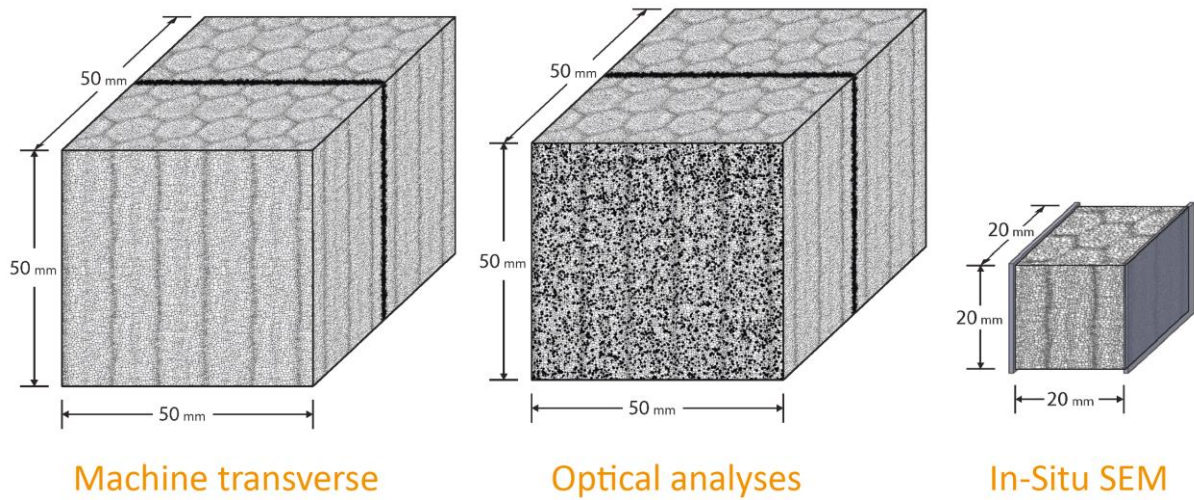


Figure 35 Schematic illustration of foam specimens used for global (left), local/optical (middle), and in-situ compression tests.

As the smallest length scale measurement within this thesis, microscopic deformation behavior of the foam cells were studied using SEM equipment **Zeiss EVO MA 15** (see details in section 4.3), coupled with a mechanical testing module **Kammrath & Weiss** with a 5 kN load cell (see right image in **Figure 33**). The in-situ compression tests were strain controlled and the deformation rate for all tests was 20 $\mu\text{m/s}$. The applied strain rate was much lower than the global compression tests. Nevertheless, this would not pose any problems, as the purpose of in-situ SEM tests was mainly the verification of cell deformation mechanisms. Cubic foam specimens with dimensions of ca. 20×20×20 mm were initially cut using a circular saw. Based on the loading direction, the corresponding view surface of each sample was smoothly cut using a skipel razor. This was done to ensure a smooth specimen surface and least damage caused to the surface foam cells. Before testing, the specimens were sputtered with a ~10 nm thin gold layer and finally glued between two stiff steel plates (thickness of ca. 2 mm) to ensure a uniform transfert of compressive loads to the specimens. The steel plates had dimensions of ca. 22×22×22 mm and were cut out of a larger sheet. The steel plates had a polished and smooth surface. In order to make a pure focus on the cell deformation mechanisms and avoid any external effects, no weld lines were included in the cubic microscopic compression test samples.

4.5 Shear Tests

4.5.1 Direct Shear Test

Quasi-static direct shear tests were performed on PET foam samples using a block shear test setup. The test procedure followed the standard method ASTM C 273 [139]. This method provides information about shear behavior of core materials with shear loading direction parallel to the steel plates (shear loading representative of sandwich bending applications). The samples were tested in tension loading using a **Zwick & Roell Z020** UTM with a 15 kN load cell (see left image in **Figure 19**). After applying a 20 N pre-force, the specimens were loaded in shear with a constant extension (0.5 mm/min) of the two universal joints. The two joints were attached to the ends of the steel plates using steel bolts following the standard specifications. This ensured a uniform transmission of the loads across the width of the specimen. A video extensometer (**VideoXtens, Zwick Roell**) was used to measure the relative displacement of the steel plates, from which shear strain values were calculated. All tests were performed at 23 °C and a relative humidity of 55 %.

For the direct shear tests, rectangular foam specimens with dimensions of 145×50×12.5 mm were cut from the foam sheets using a circular saw. A two-component adhesive system (a mixture of Araldite Haerter HY 991 and Araldite AW 134, with a ratio of 3/10) was used to glue the samples between the Steel loading plates. It was important to use the correct amount of adhesive to make sure foam specimens were sufficiently glued to the steel plates and are rigidly supported. Before testing, specimens were dried in a vacuum oven with a temperature of 50 °C for 2 hours, in order to decrease the influence of moisture, and ensure a full reaction of the adhesive system. The specimens were rested in ambient conditions for at least 6 hours before testing.

4.5.2 Sandwich Bending Test

Quasi-static four-point bending tests were performed according to the standard test method ASTM C 393. The setup (see right image in **Figure 21**) had loading and support span lengths of 150 and 500 mm, respectively. The loading bars were designed according to the standard recommendations and were made of polished steel cylinders with a diameter of 25 mm. Sandwich specimens were tested at 23 °C in a **Zwick & Roell Z020** UTM with a 50 kN load cell, at a constant crosshead speed of 4 mm/min.

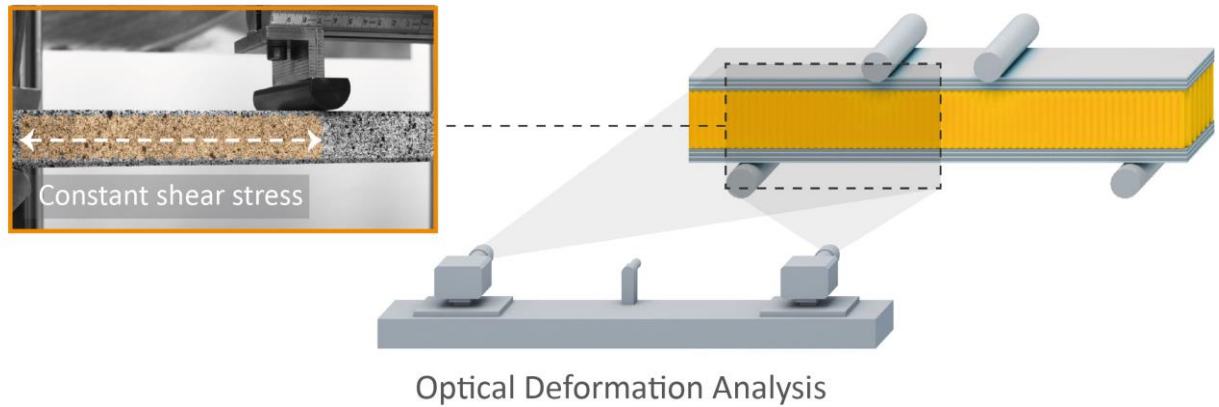


Figure 36 Schematic illustration of sandwich four-point bending coupled with optical deformation analysis to study the full-field distributions of core shear strains.

For measuring local shear deformations of foam core materials, the same optical deformation equipment as for compression tests was used. This made it possible to measure the shear strain distributions on the longitudinal cross-section of sandwich specimens. Here also, the sandwich samples were sprayed with a marker aerosol to create a random pattern for ensuring good grayscale distribution (see **Figure 36**).

5 Results and Discussion

5.1 Morphology Analysis

It was shown in previous chapters that, how the solid material is distributed within the cell walls and struts has a great impact on the cell deformation response and the macroscopic mechanical properties of cellular materials. Therefore, the first step in studying the properties of foams is to understand, characterize and quantify their structures as deep as possible [25]. As discussed in the introduction section, the morphological features of PET strand foams have similarities and analogies to both honeycombs and wood. This is the reason for the high mechanical anisotropy and the much higher properties in the out-of-plane direction. In the following, these similarities are described and discussed in more detail.

5.1.1 Definition of Honeycomb-Like Structure

Ashby called the bee honeycomb “*the queen of cellular structures*” [161]. In general, strand foams can be described as foamed honeycombs, filled with foam. However, the local foam density of the honeycomb cells (hexagonal strand border regions) is higher than the local foam density inside the honeycomb cells (strand bulk regions). This effect is shown in **Figure 37**, in which a μ -CT snapshot of one single hexagon is illustrated in the middle image.

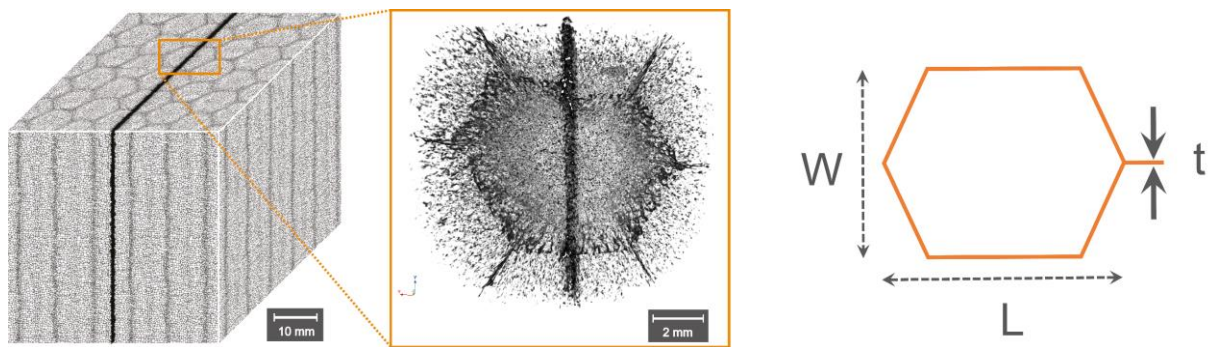


Figure 37 Illustration of the honeycomb-like features seen in PET strand foams. The μ -CT image shows higher foam density in hexagonal strand border regions.

One can observe that the interface regions of the hexagonal foam strands (honeycomb cell walls) have higher density than the strand bulk regions. The μ -CT sample shown in **Figure 37** was deliberately cut from a location including a weld line. The weld line is evident in the middle of the hexagon as a vertical dark line, which has naturally the highest density due to the melting of the foam during welding. In the results presented below, the two foam regions, namely the

higher density and lower density regions, will be distinguished and denoted as strand border and strand bulk, respectively. Beside the density difference, it will be shown in the next chapter that the strand border and strand bulk regions also differ in their foam cell shapes and morphologies.

In order to measure the dimensions of the hexagonal strands for each foam density, the μ -CT data was modified using a Maximum Intensity Projection (MIP) filter. In doing this, it was possible to render the highest intensity value through out the specimen thickness at each pixel. This data modification step allowed for obtaining a more pronounced contrast between the two regions. As an example, **Figure 38** shows the resulting image for PET foam sample T92.200, and how different characteristic lengths (L , W , and t) are measured.

	L [mm]	W [mm]	t [μ m]
T92.80	10.33 ± 0.07	8.02 ± 0.11	600 ± 64
T92.100	10.65 ± 0.32	6.91 ± 0.36	721 ± 117
T92.130	8.36 ± 0.31	6.44 ± 0.49	588 ± 58
T92.200	10.14 ± 0.16	6.46 ± 0.06	769 ± 103

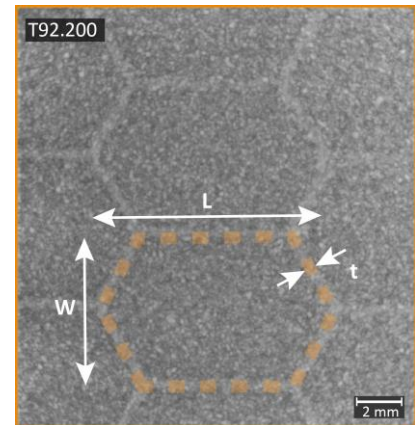


Figure 38 Characteristic lengths of the hexagonal strands in PET foam, determined by μ -CT data and post processing steps.

The table included in **Figure 38** summarizes the dimensions of hexagons, as well as the thickness of strand border regions for different PET foam grades. For each foam density, the hexagon geometrical features were manually measured at multiple points and average values are reported. The border zone thickness, t , is reported based on at least 35 measurement points for each density. The dimensions of the hexagons were similarly measured at multiple locations (10 measurements for W and 4 measurements for L). Therefore, the reported values are rather representative, considering the stochastic nature of foams and the fact that each of the three length values can slightly vary in different regions of a sample. The values suggest that all four foam densities have more or less comparable dimensions of hexagonal strands. Nevertheless, a more thorough discussion would not be possible, since these dimensional details are dependant on the process parameters and equipment used, which are not disclosed by the material supplier.

5.1.2 Definition of Dual Cell Morphology

Beside the density difference between the strand border and strand bulk zones, further studies confirmed that the cell shapes in the two regions are also profoundly different. **Figure 39** shows optical microscopy images taken from top and side views of the T92.100 foam sample. The strand border cells (shown in red) are elongated, flattened, and oriented through the panel thickness (extrusion direction). In contrast, the strand bulk cells (shown in grey) are more regular and have smaller aspect ratios. Further analysis of the strand border cells suggested that they are made of highly elongated tetrakaidecahedron cells.

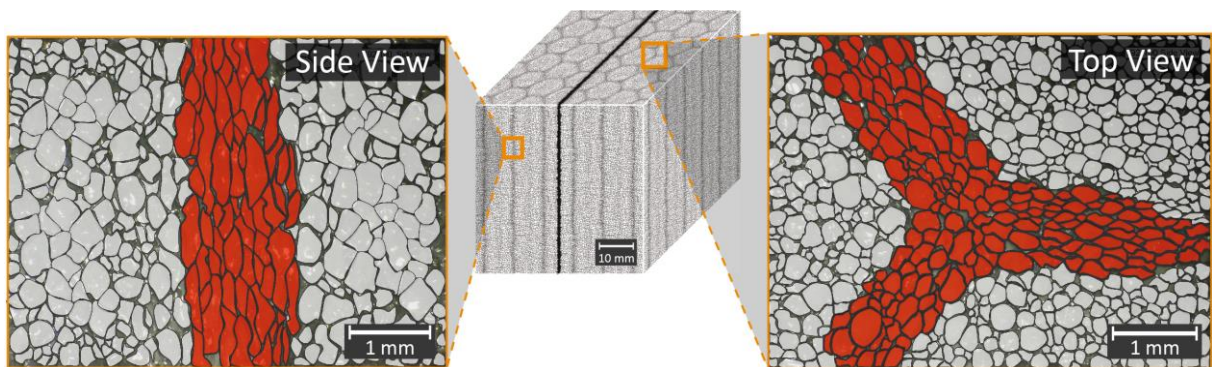


Figure 39 Optical microscopy images of PET foam sample (T92.100) taken from top and side views. The images show the two types of foam cells.

5.1.3 Quantitative Morphology Analysis

Due to the complex geometrical features of the foam panels, e.g. two distinct cell regions, standard SEM or LM images would not be much representative, unless several images are combined to generate a larger data. In addition, distinguishing the two cell type regions, namely strand border and strand bulk, would be difficult using conventional cell analysis methods. Hence, high-resolution μ -CT measurements were employed to measure detailed foam cell features. Following μ -CT captures, several data processing steps were done in order to produce meaningful values and diagrams. In the first step, MIP filter was used to exaggerate the higher density of the strand border regions. Then, the resulting image was utilized to define a Volume of Interest (VOI) encompassing the strand border region only. In the next step, the defined strand border VOI was subtracted from the full volume to yield the strand bulk VOI. **Figure 40** shows the multiple steps of data refinement and selection.

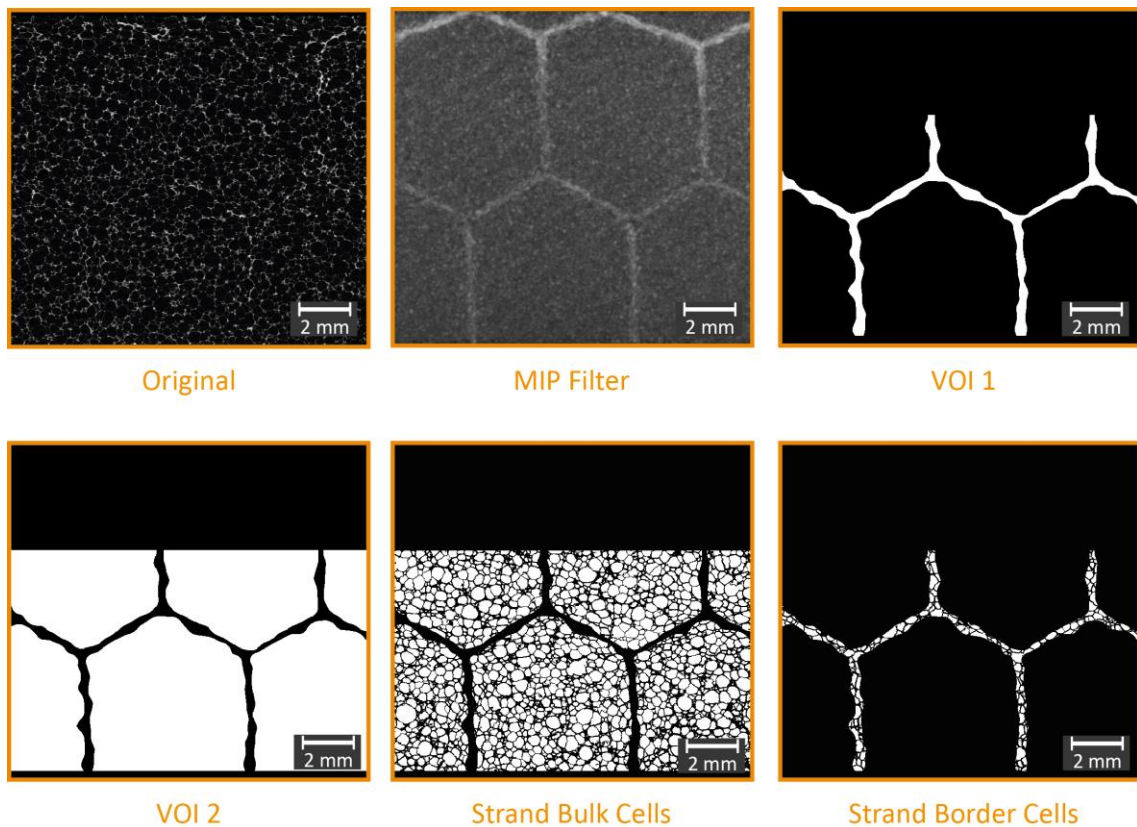


Figure 40 Exemplary 2D images taken from different post processing steps to create two distinguished data sets for strand border cells and strand bulk cells.

After the manual definitions shown in **Figure 40**, the two VOIs were separately applied to all original 2D images in order to crop out the cells located in strand bulk and strand border zones, respectively. This allowed for obtaining two separate data sets, which included only the cells in the border and bulk regions. Therefore, for each density the strand border and strand bulk cells could be distinguished and analyzed separately. **Figure 41-43** show 3D models generated from only the strand border region (blue), only the strand bulk region (red), and the combination of both zones for a representative foam sample. In the next step, a series of digital and numerical corrections and filters were applied to improve the data quality of the 2D images. This was a necessary step before using the automatic morphology analysis tool. The morphology analysis wizard was then run, which yielded different quantitative information for each cell within a 2D image. Then, several 2D images were selected from different cross-sections of the sample, which were far enough from each other to avoid multiple measurements on the same cells. For each foam density and VOI, the cell information obtained from all individual 2D images were merged to create cell morphology data based on several thousand foam cells. This approach suggested a rather high accuracy in the values reported.

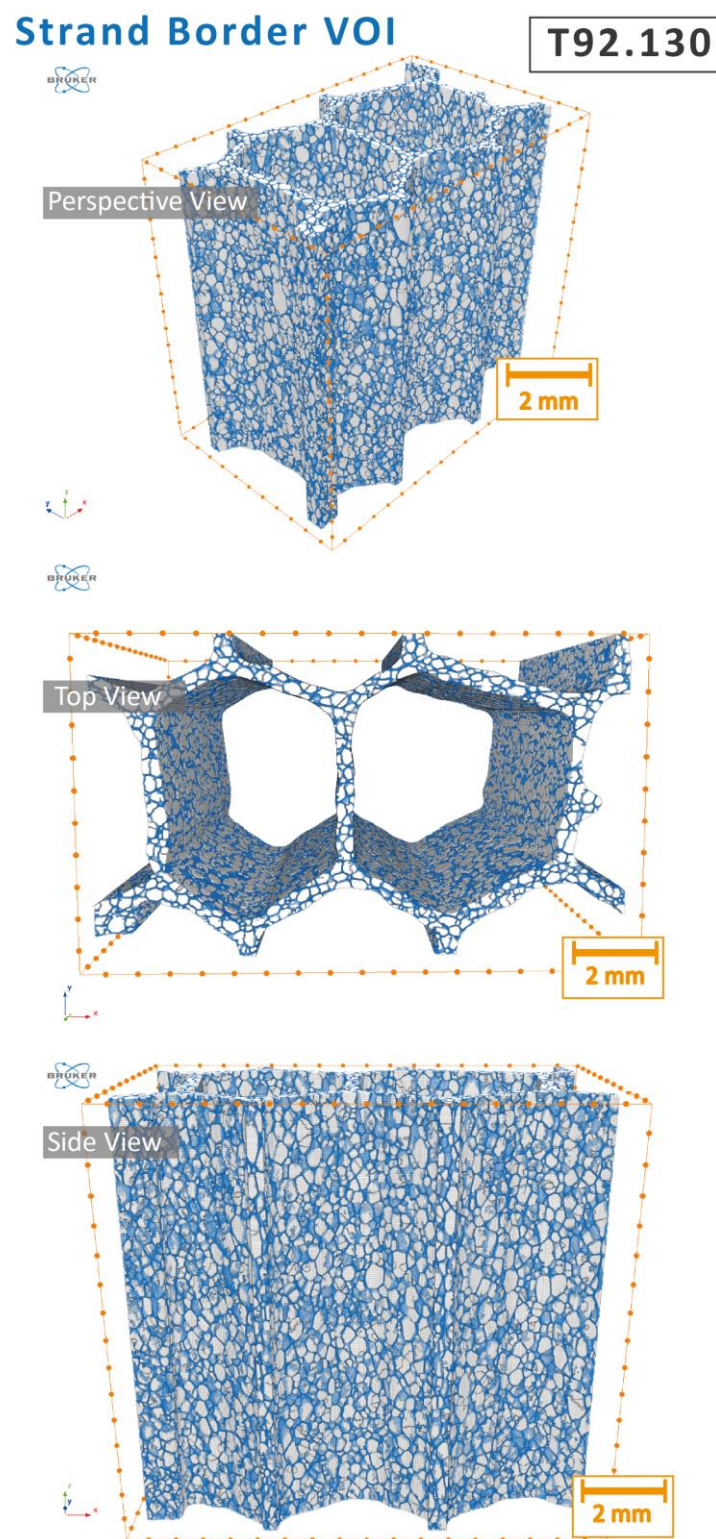


Figure 41 3D model of the foam cells in the strand border VOI, created by μ -CT data from T92.130 sample.

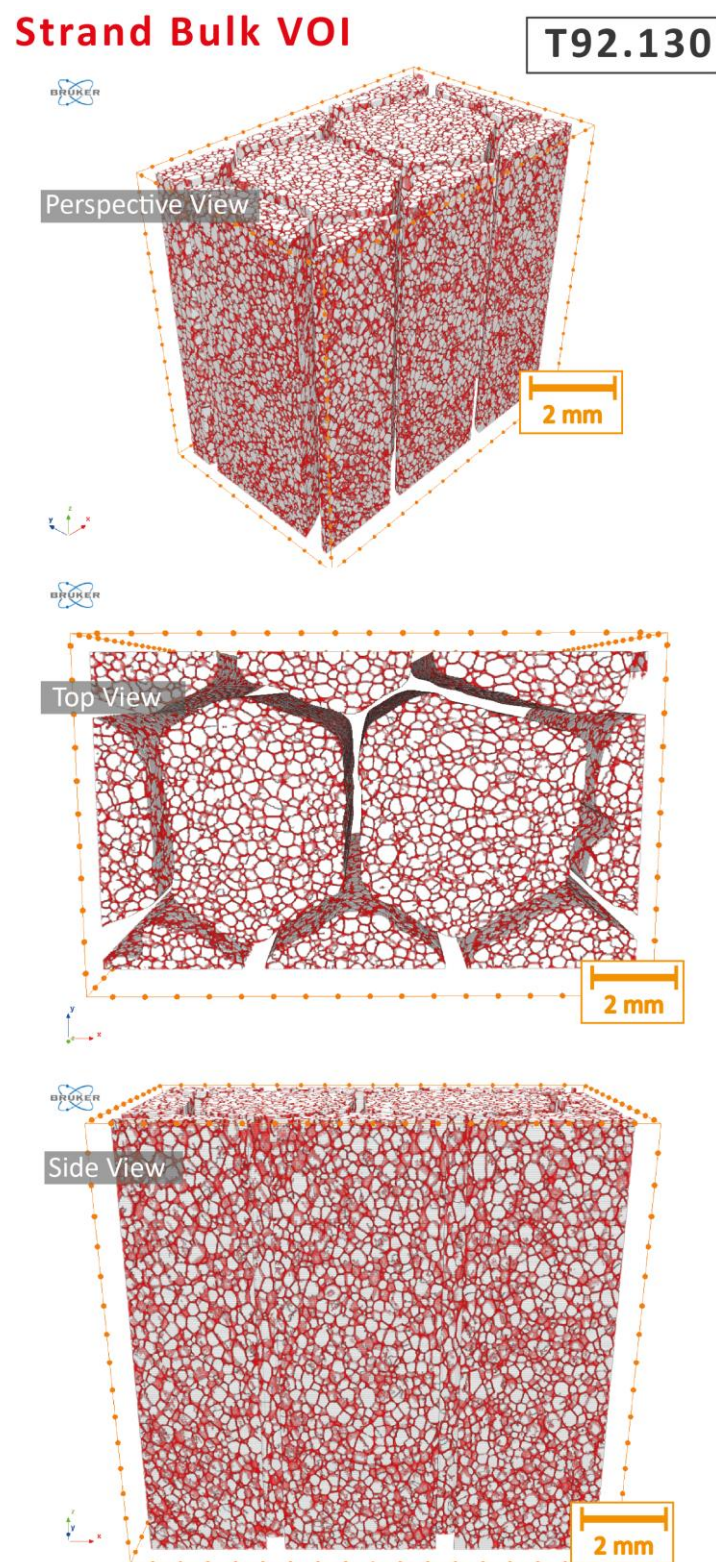


Figure 42 3D model of the foam cells in the strand bulk VOI, created by μ -CT data from T92.130 sample.

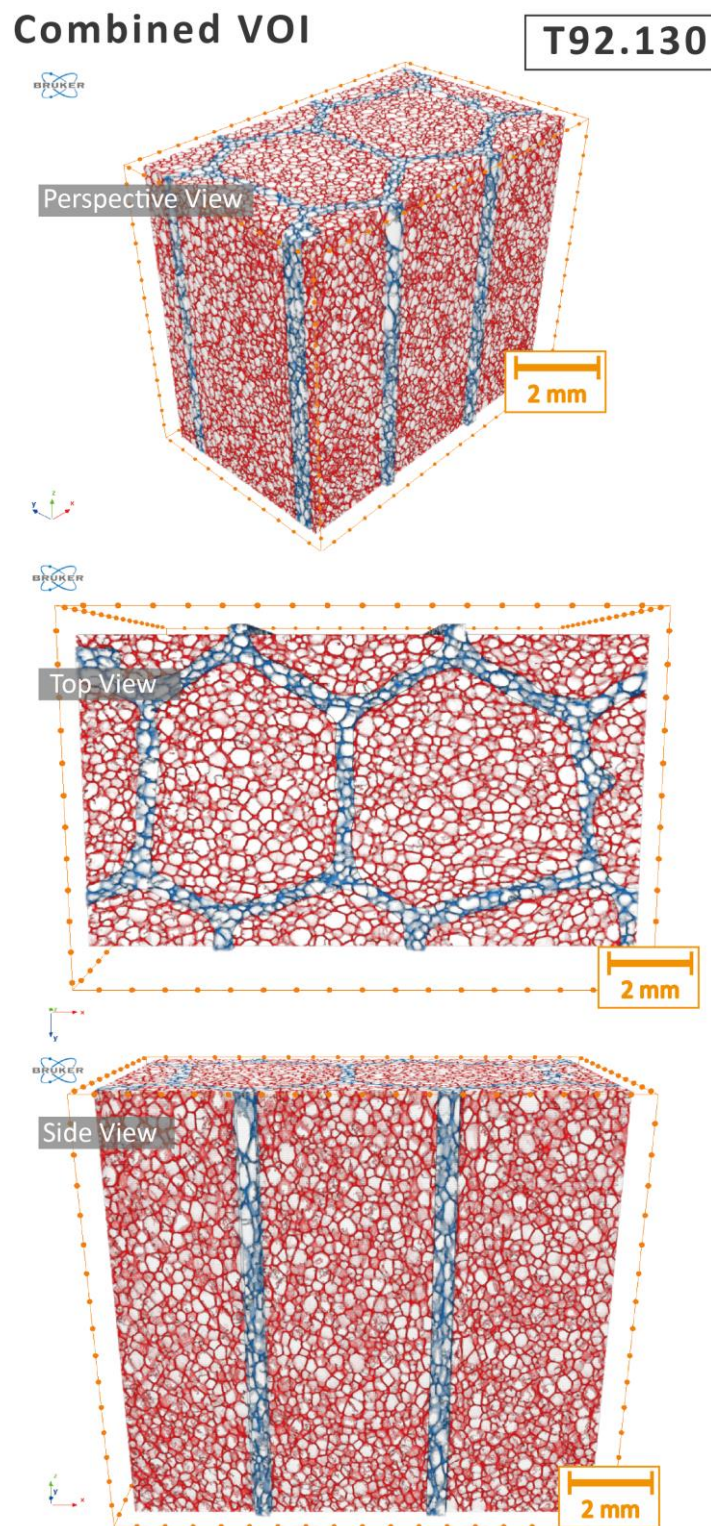


Figure 43 3D model of the combination of foam cells in the strand border and strand bulk VOIs, created by μ -CT data from T92.130 sample.

Figure 44 shows exemplary 2D images of the strand border zones, which were used for obtaining cell size and aspect ratio distributions. For each foam density, two images are shown in a row. One can notice that the 2D images in **Figure 44** consist of stripes of foam cells with different widths and locations on the images. This is due to the generally small volumetric fraction of the hexagonal strand border zones (thickness of ca. 600-750 μm), and consequently the smaller areas of the 2D images intersecting with the border region VOI. Also depending on the location of the chosen 2D plane (along the specimen width), different number of cell stripes can be seen on the images, which also corresponds to the number of intersections between the strand border VOI and the chosen 2D plane. The cell images shown in **Figure 44** suggest that the T92.80, T92.100, and T92.130 samples have elongated and higher aspect ratio cells in the strand border region, but the average cell aspect ratio of the T92.100 sample is lower than T92.80 and T92.130, due to relatively larger cell widths. Unlike the three lower density foams, the cell orientation in the T92.200 sample (highest foam density) is minor and only few cells are slightly elongated through the thickness.

Similar to strand border cells, exemplary 2D images of the strand bulk cells are shown for each foam density in **Figure 45**. The images show that the lower density foams (samples T92.80 and T92.100) have larger cells and a wider range of cell size distribution in their strand bulk region. Also, in both samples, there exists a fraction of bulk cells, which are more elongated and have higher aspect ratios. This is more evident in the T92.100 sample in which, unlike all other densities, the morphology of strand bulk cells is quite similar to the strand border cells (large and elongated foam cells in both zones). In contrast, the strand bulk cells of the higher density foams (T92.130 and T92.200) are smaller and more consistent in size. Interestingly and despite their large density difference, the T92.130 and T92.200 samples seem to have comparable cell morphologies in the strand bulk zones (though a hardly visible orientation of the cells can be seen in the T92.130 sample). This may indicate that the density difference between the T92.130 and T92.200 samples is more induced by the different cell sizes (i.e. expansion levels) in the strand borders zones.

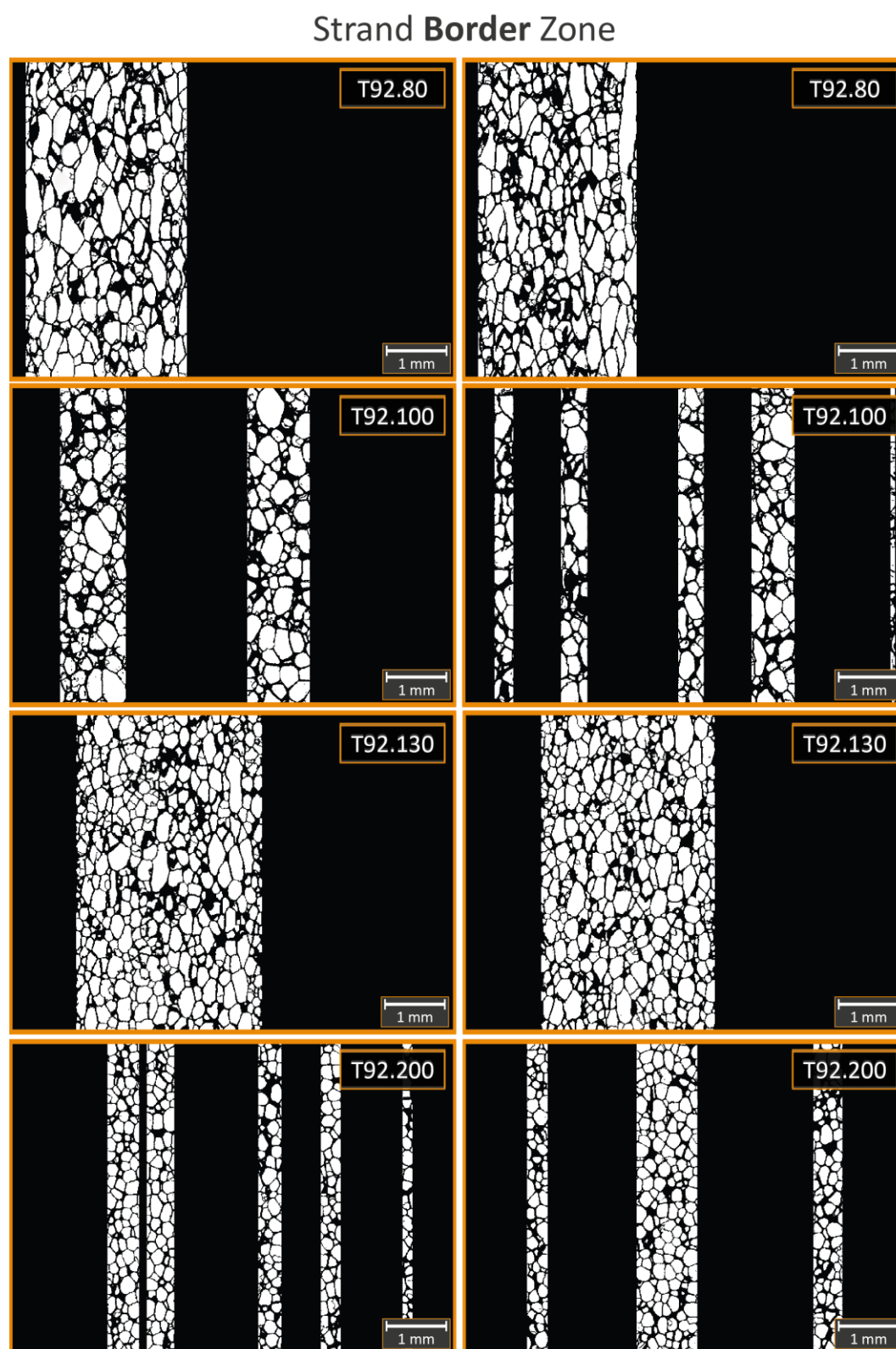


Figure 44 2D μ -CT snapshots of different density PET foams, consisting of only those foam cells located in the strand border zones.

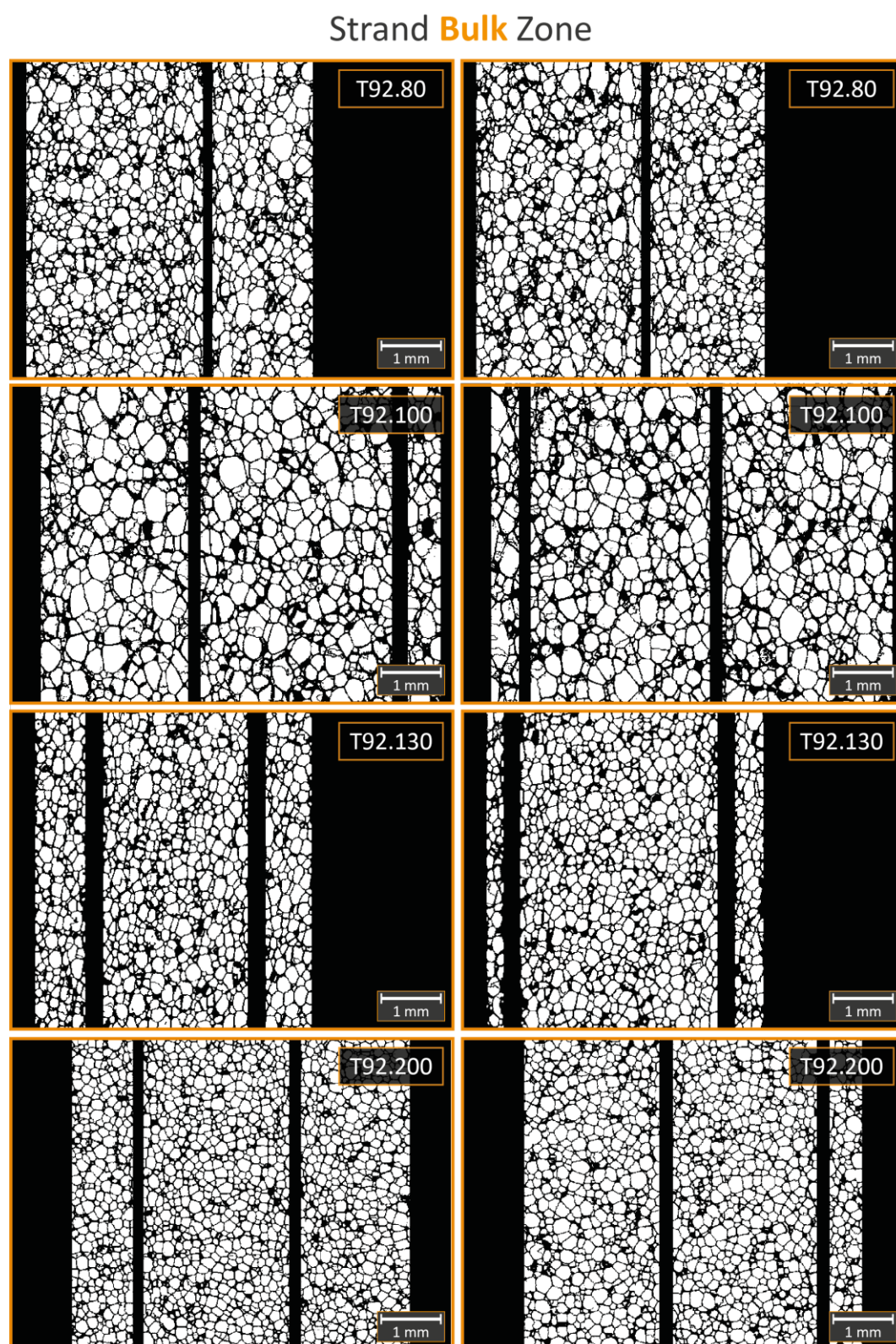


Figure 45 2D μ -CT snapshots of different density PET foams, consisting of only those foam cells located in the strand bulk zones.

For a quantitative morphology comparison between different foam densities, **Figures 46** and **47** show distribution bar charts of the major cell diameter and the cell aspect ratio, respectively. The orange bars correspond to the strand bulk cells and the grey bars represent the elongated strand border cells. It is important to emphasize that, all distribution bar charts are created based on area fraction of the cells, rather than number fraction or cell count. In other words, the fraction of cells reported for each size class is determined by the total area of the cells belonging to the same size class. This representation of the distribution charts would be more suitable, as it could better capture and highlight the weight of the larger cells, which are statistically fewer in number compared to the much smaller cells. Despite their fewer numbers, the large and elongated foam cells occupy larger volumes and constitute more solid material in their walls and struts. Therefore, their geometrically dominating effects on the mechanical response of the foam should be properly captured. Hence, area fraction values are shown on the y-axes of all distribution bar charts. The cell size distribution charts depicted in **Figure 46** confirm the general qualitative observations discussed in the previous paragraphs. The three lower density samples (T92.80, T92.100, and T92.130) have very broad size distribution of the elongated strand border cells (grey bars). In all three samples, there are large fractions of border cells ranging from 1 to 2 mm in major diameter. Interestingly, the distribution of border cell size in the T92.130 sample is even more shifted to larger cells, with a narrow peak around 1200 μm . This means in the T92.130 sample, more than 50 % area fraction of the cells in the strand border zone have major diameters between 1100-1300 microns. Unlike the lower density grades, the strand border cells in T92.200 sample have a symmetric and narrow Gaussian distribution with the peak values around 500 microns.

On the other hand, the size distribution charts of the strand bulk cells (orange bars) in **Figure 46** show a different trend. Compared to the border cells, the bulk cells are generally smaller and uniform in size. Therefore, the orange distribution bars are narrower and shifted to the left hand side. However, the offset between border and bulk cell distributions is more significant in the lower density samples, indicating larger cells in the strand border zones. Also when comparing the grey and orange bars for the T92.100 sample, one clearly sees that strand bulk cells have comparably larger sizes.

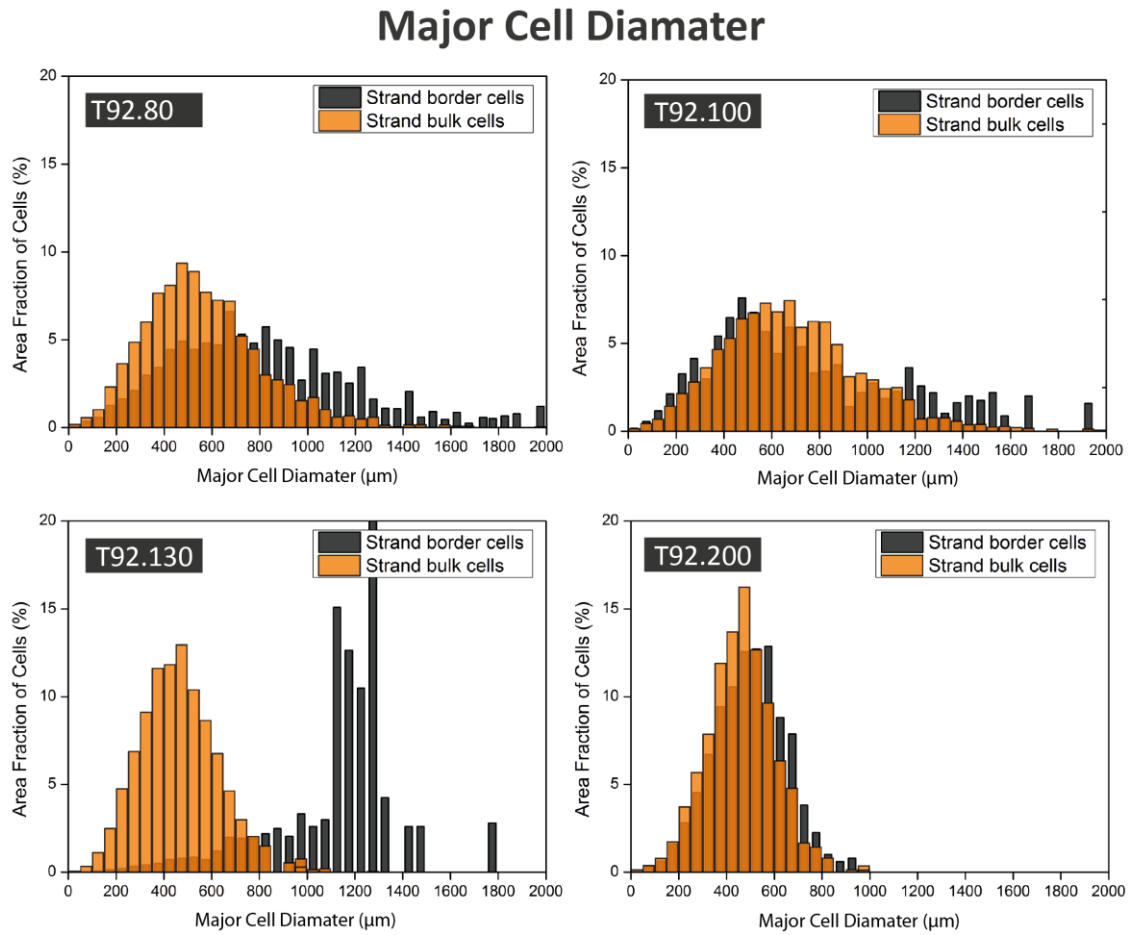


Figure 46 Distributions of major cell diameter in the strand border cells (grey) and strand bulk cells (orange) for the four PET foam densities.

In contrast, the border and bulk cells in the T92.200 sample are almost identical in their size distributions, with peak values around 500 microns. This confirms that in the highest density sample, the strand border cells are also regular in size and aspect ratio (no significant elongation in strand border cells for T92.200 sample). The results also suggest that the increase in foam density from sample T92.130 to T92.200 is more related to the expansion and morphology of the strand border regions at the interface of hexagonal strands.

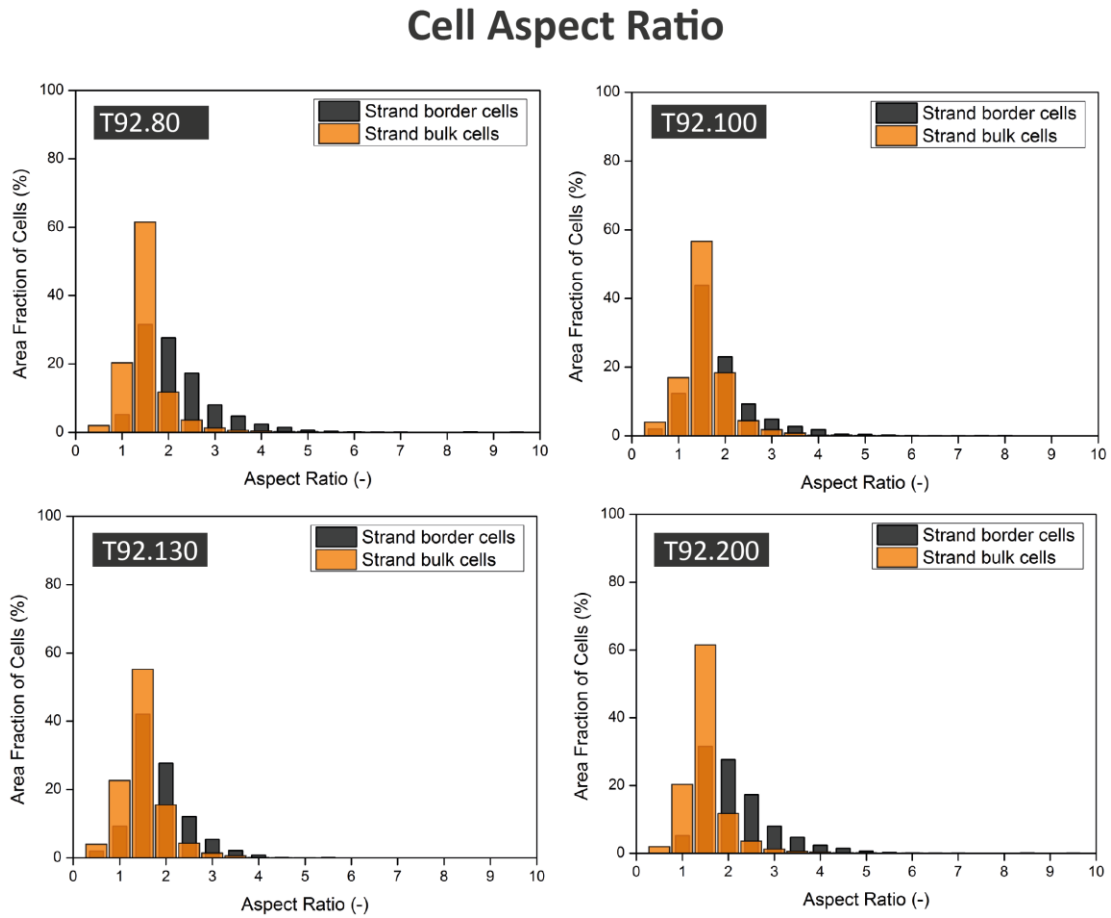
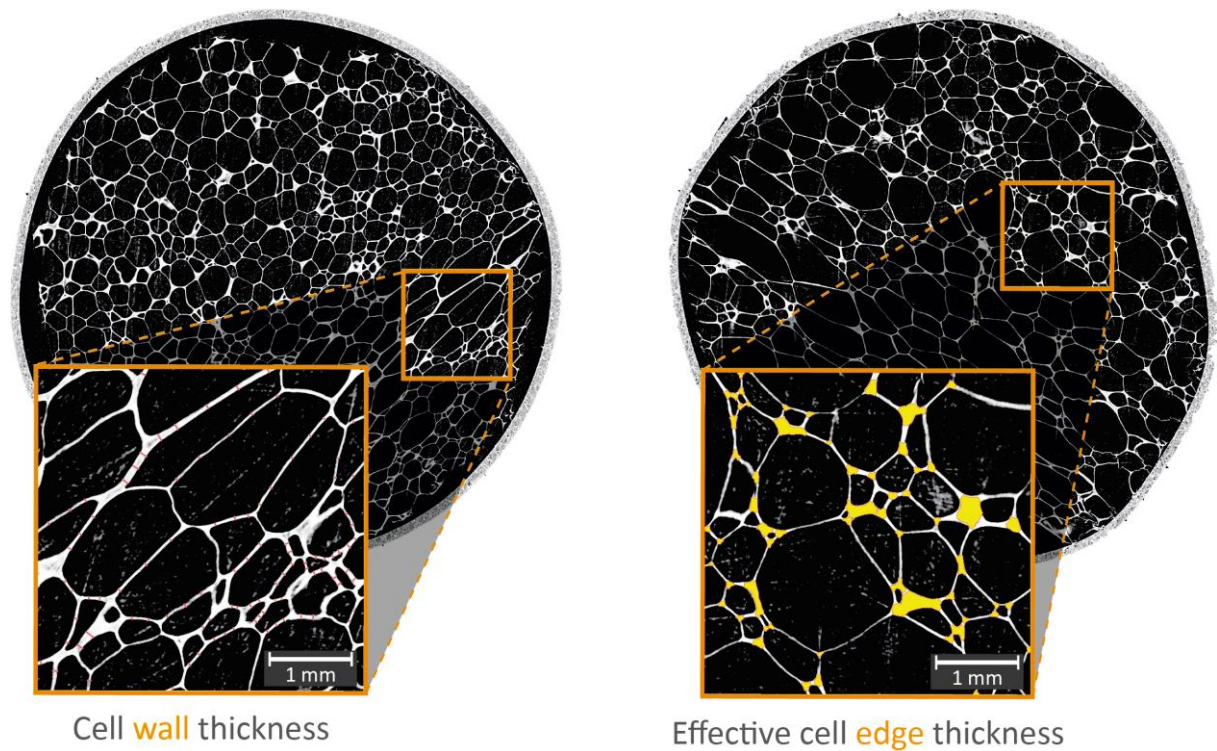


Figure 47 Distributions of cell aspect ratio in the strand border cells (grey) and strand bulk cells (orange) for the four PET foam densities.

Figure 47 shows the distributions of cell aspect ratio for different foam densities. Here too, the orange bars belong to strand bulk cells and the grey bars represent the elongated strand border cells. In the lower density foams (T92.80, T92.100 and T92.130 samples), the strand bulk cells have a sharp average aspect ratio of 1.5 (ca. 60 % area fraction in all three samples). In the strand border cells (grey bars), the aspect ratio peak also appears at 1.5 for all four densities. However, area fractions of cells with aspect ratios from 1.5 to 4 are much higher in the strand border distributions compared to the strand bulk regions. Therefore, the offset between the orange and grey bars in **Figure 47** highlights the higher aspect ratios of the elongated strand border cells.

Finally, for the determination of cell wall and strut thickness, the high resolution μ -CT images (2.5 $\mu\text{m}/\text{pixel}$) were used. The manual size analysis was performed on 2D images using the free-source software ImageJ. **Figure 48** shows exemplary images of how the values are measured with ImageJ and the table summarizes all measured values. The average cell wall and strut

thickness values are higher in the strand border than the strand bulk regions at all densities. Interestingly, the offset between the strand border and bulk values is comparable for both wall thickness and effective strut (edge) thickness. This offset is smaller in the T92.130 sample, though. It will be shown that the deformation mechanisms of the foam cells are more governed by the orientation of the cells rather than wall/strut thickness.



Foam Sample	Wall thickness [μm]		Effective strut thickness [μm]	
	<i>Strand border</i>	<i>Strand bulk</i>	<i>Strand border</i>	<i>Strand bulk</i>
T92.80	16.95 ± 6.30	13.26 ± 3.40	54.08 ± 28.81	41.22 ± 22.13
T92.100	18.12 ± 7.91	15.10 ± 3.88	60.49 ± 32.75	47.78 ± 22.19
T92.130	19.25 ± 7.28	17.13 ± 4.50	59.33 ± 26.82	52.65 ± 27.53
T92.200	36.50 ± 27.80	25.34 ± 8.61	135.92 ± 80.66	88.33 ± 40.09

Figure 48 High-resolution μ -CT images used to determine average cell wall thickness and effective cell strut thickness.

In this chapter, the unique morphology of strand PET foams was described and quantified using diverse optical techniques. It was shown that strand PET foam has a regular structure

comparable to a honeycomb configuration. Additionally, it was shown that a fraction of foam cells has a significant orientation through panel thickness analogous to the structure of wood. The distributions of cell size and cell aspect ratio were captured and presented for all foam densities. Finally, average values of wall thickness and effective strut thickness were measured and reported.

5.2 Compressive Response of PET Foam

The compression test is the most frequently used method for mechanical characterization of foams [15]. In this chapter, different length scale compressive properties of strand PET foams are discussed. The main structure-properties correlations are first established for the T92.100 sample with a nominal density of 112 kg/m³. This PET foam grade is the most industrially popular according to the material supplier. It will be seen that most observations on this foam density are directly transferable to other densities too.

5.2.1 Global (Macro) Compressive Response

Figure 49 shows the global compressive stress-strain curves of PET foam T92.100 in the three loading directions. The out-of-plane (Direction 3) stress-strain curve is distinct and different to the two in-plane directions (Directions 1 and 2). Not only are the compressive modulus and strength much higher in the out-of-plane loading, but the deformation mechanisms and therefore the stress-strain signatures are also fundamentally different.

The much higher compressive modulus and strength in Direction 3 is a result of the unique foam morphology. Firstly, the higher density hexagonal strand border regions induce a honeycomb-like response. Secondly, Direction 3 is parallel to the foam extrusion and consequently the elongated foam cells, which mimic a mechanical response similar to that of wood when loaded in the axial direction. In Direction 3, a linear behavior is seen until the yield point, which is followed by a sharp drop in the stress level. This type of post-yield softening is an indication of highly localized deformation [175]. At higher strains, the plateau region levels off and the failure is extended through the sample thickness. The variation of stress level in the plateau zone depends on how smoothly the failure extends from one array of failed foam cells to the next adjacent layers. Eventually, at higher strain levels, the densification kicks in, indicating complete failure of foam cells through the sample thickness. In the densification zone, usually the cell walls begin to touch each other, and the sample behaves similar to a solid material.

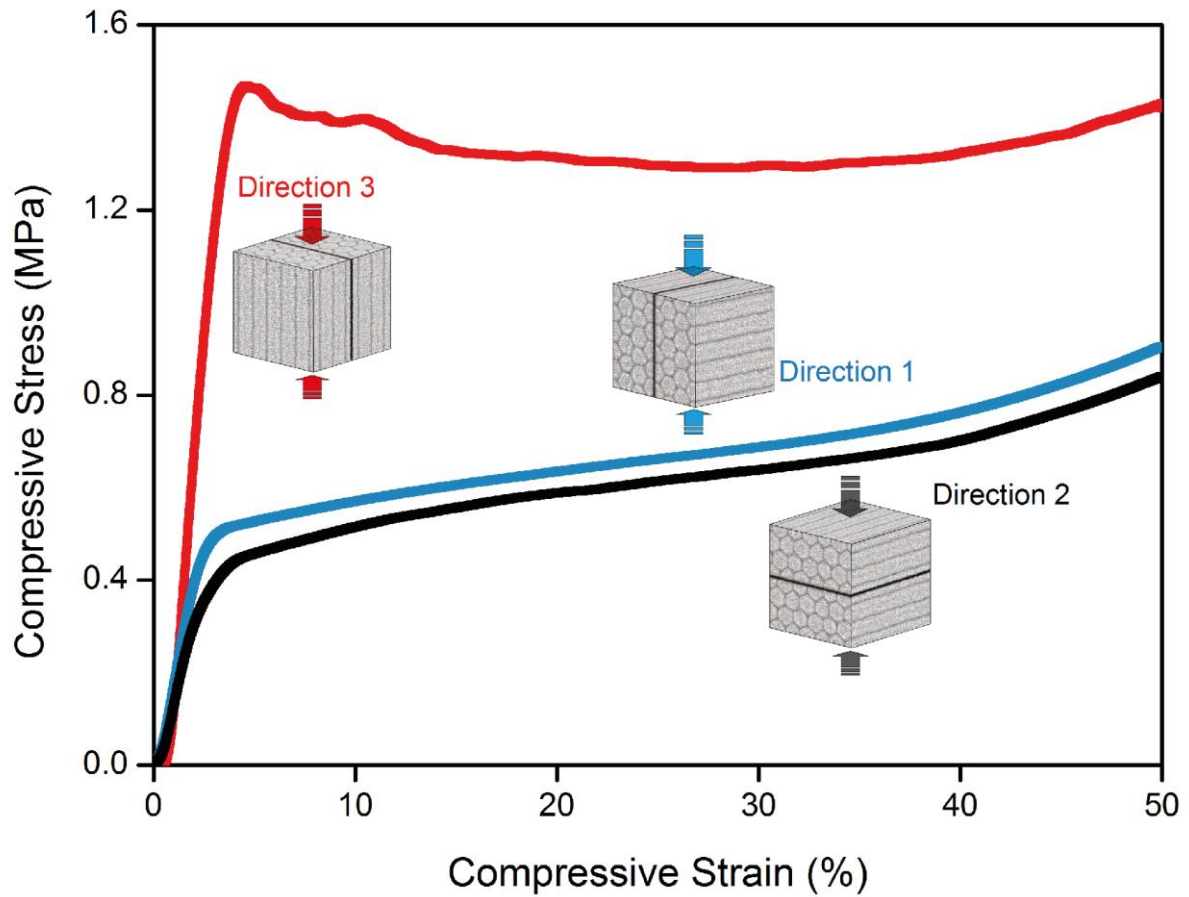


Figure 49 Compressive stress-strain curves of PET foam (T92.100) in the three loading directions.

In contrast, the compressive response in both in-plane directions (Directions 1 and 2) are rather similar and much weaker than the out-of-plane direction. The deformation mechanism in the in-plane directions seems to be fundamentally different, resulting in lower strength and stiffness. After the linear region, a smooth yielding is seen, after which the samples undergo a gentle ductile densification as they are compressed to higher strains. Unlike the out-of-plane direction, the smooth transition to the plateau region in the in-plane compression suggests more homogeneous and uniform (less localized) cell deformations. **Table 5** summarizes the global compression properties of the PET foam (T92.100) in all three loading directions. E_c (**Global**) is the compression modulus measured by the crosshead movement of the loading plates, and $\sigma_{10\%}$ is the stress level recorded at the compressive strain of 10%. In many practical cases, $\sigma_{10\%}$ can be used as a measure of the compressive strength.

The measured out-of-plane compressive modulus of PET foam T92.100 is lower than the values reported in the manufacturer's product datasheet. This could be due to different strain

measurement methods and the fact that in this work, no correction factor was applied to the compressive modulus measured by the machine's crosshead movement.

The local cell crush at the specimen's loading surfaces often causes experimental errors and leads to underestimation of the Young's modulus. This is particularly the case in stiffer foams and needs to be accounted for. Obviously, the local deformations near the specimen surfaces cause inaccuracies in the measured values of compressive modulus. This is sometimes referred to as *seating effects*. A similar case has been reported in other literature work such as the study by Li on PMI foams [96]. In that work, the lower values of measured Young's modulus are attributed to the error caused by the crosshead displacement of the equipment and possible seating effects. The values of compression modulus measured by optical deformation analysis are much higher and closer to the datasheets. It should be also reminded that for all calculations and data representations, the global compressive stress values applied to the specimen surfaces and measured by the machine load cell are used.

Table 5 Global compression properties of PET foam (T92.100) in the three loading directions.

Foam Sample	E_c (Global)	E_c (Average Local)		
	Machine	Optically	$\sigma_{10\%}$	σ_{yield}
	Transverse [MPa]	determined [MPa]	[MPa]	[MPa]
Direction 1	24.5 ± 0.7	33.1	0.56 ± 0.08	0.51 ± 0.07
Direction 2	20.3 ± 0.5	29.8	0.51 ± 0.04	0.45 ± 0.05
Direction 3	57.9 ± 0.8	103.2	1.39 ± 0.05	1.47 ± 0.09

Hence, the macroscopic mechanical response of strand PET foam is highly anisotropic. This level of anisotropy is rare in polymeric foams, and roots in the special foam morphology and consequently the deformation mechanisms at smaller length scales. Furthermore, the compression response of strand PET foam suggests large similarities to that of wood. This is obvious when comparing the stress-strain curves of PET foam in **Figure 49** with those of wood in **Figure 24**. Even details such as yielding behavior and post-yield deformation phenomena seem to have large similarities with wood. Understanding the analogies to wood tremendously

helped to better comprehend and interpret the local deformation behavior of strand PET foam in the next chapters. Some learning from wood's structure-properties relations are directly applicable here.

5.2.2 Local Compressive Response

5.2.2.1 General Observations

The global mechanical properties of foams are governed by the local deformation and failure of the foam cells. Studying the local failure patterns is necessary for better understanding the mechanisms responsible for different stress-strain behaviors discussed in the previous chapter. One of the earlier literature works on the localization of deformation in crushable foams is the one by Li and coworkers [10]. The local compressive strains in PMI foam were measured and quantified in discontinuous points on the specimen surface. It was shown that in the plateau region of the stress-strain curve, up to 70 % local strains were recorded while some regions on the specimen were less than 5 % strained. This highlights the magnitude and impact of localized deformation in foams.

In this thesis, full-field distribution of compressive strains on the surface of foam samples were calculated and visualized with the aid of optical deformation equipment. Due to the geometrical regularities and the structural symmetry in PET foam samples, the surface deformation patterns should represent, up to an acceptable degree, the conditions in the specimen bulk. **Figures 50-52** show the distribution of compressive strains in the T92.100 foam samples loaded in the three directions and at different compressive stress levels. A red to blue color spectrum represents the intensity of the compressive strain (in %). Since compression is indicated with negative strain values, the red colors correspond to smaller deformation, whereas blue regions show higher compressive strains.

The distributions of compressive strains in out-of-plane loading (Direction 3) are shown in **Figure 50**. Before yielding, the deformation is highly localized on the specimen surfaces near the loading plates, while the specimen bulk remains almost undeformed (see image 1 in **Figure 50**). At a compressive stress of 1.35 MPa (shortly before yielding), most of the sample bulk experiences strain values below 1 %, while the specimen edges are already more than 10 % strained. This is due to the high out-of-plane stiffness of the foam specimens and the fact that surface cells are more compliant since they are partially damaged during specimen preparation (see *seating effects* in chapter 5.2.1). After yielding, highly localized and irregular deformation

patterns become evident, as shown in images 2-4 in **Figure 50**. Multiple deformation bands (shear bands) are formed transverse to the loading direction, which then extend through the specimen thickness with increasing compression.

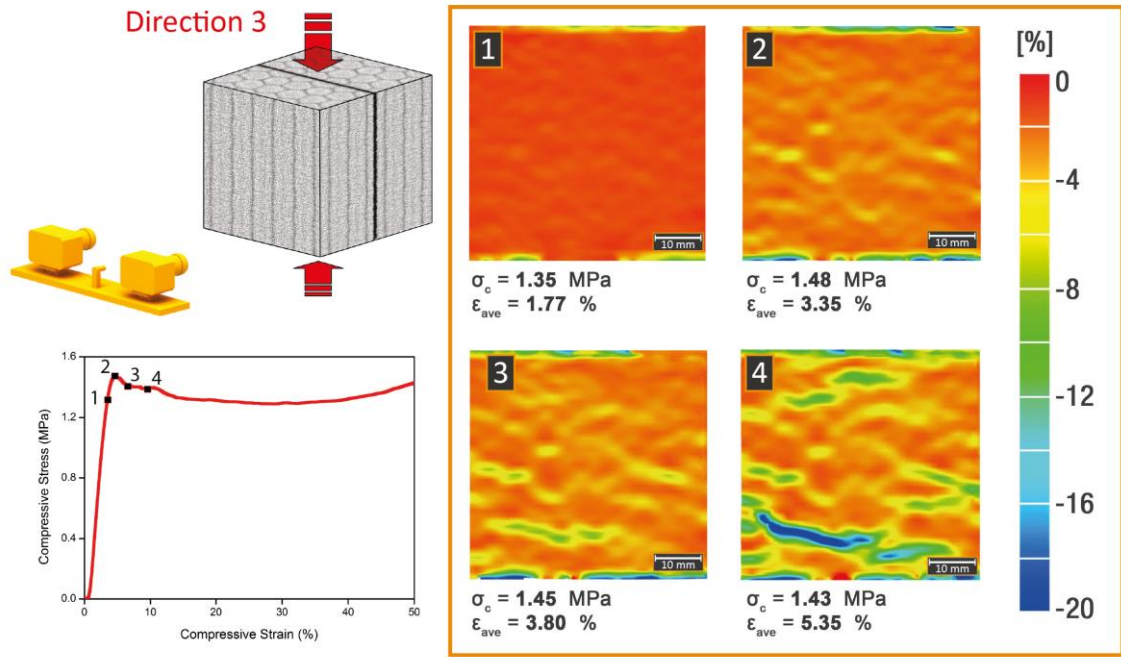


Figure 50 Contour plots of the distribution of compressive strains on the surface of PET foam (T92.100) when loaded in Direction 3 (Out-of-plane).

In the two in-plane loading directions (**Figure 51** and **Figure 52**), the deformation patterns are distinctly different to the out-of-plane direction. The strain patterns are orderly and regular, with geometrical features revealing the hexagonal shape of the foam strands. From a qualitative perspective, one can immediately notice that in both in-plane directions, higher deformations take place at the strand border regions. This observation suggests that transverse loading results in a more compliant response and eventually higher deformation of the elongated and flattened foam cells in the strand border zones. In contrast, the strand bulk regions have significantly lower deformations until relatively high global strain values (see the red regions in **Figures 51** and **52**). The visual difference between deformation maps of Direction 1 and 2 lies in the spatial positioning of the elongated border cells relative to the loading directions (see **Figure 53**). The flattened border cells are aligned with and located inside planes of strand border zones or honeycomb cell walls. Therefore, depending on the loading direction, the deformation is highest on those planes, which are located perpendicular to the loading direction. This case is represented by plane number 2 in **Figure 53**.

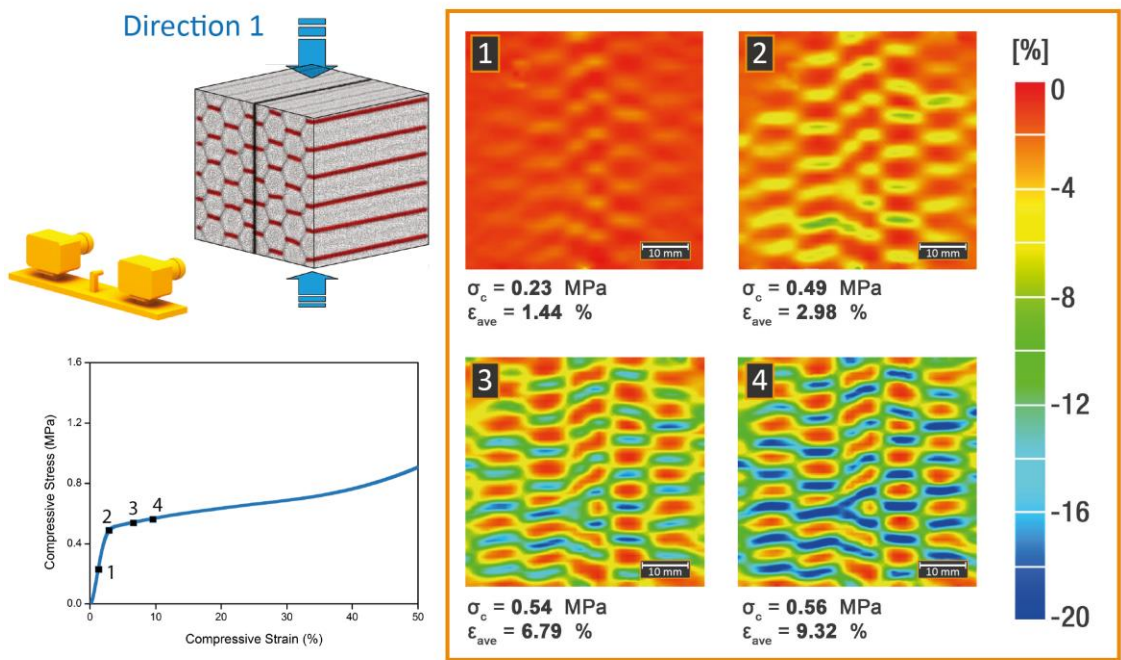


Figure 51 Contour plots of the distribution of compressive strains on the surface of PET foam (T92.100) when loaded in Direction 1.

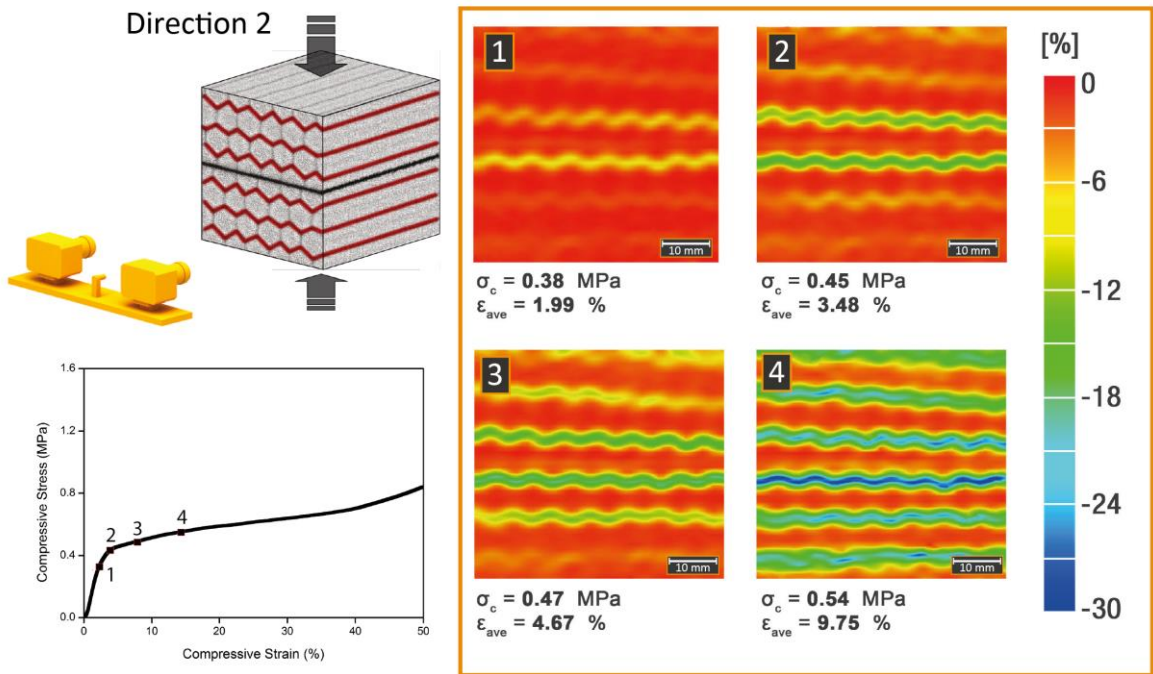


Figure 52 Contour plots of the distribution of compressive strains on the surface of PET foam (T92.100) when loaded in Direction 2.

The border cells located inside plane 2 would have the highest compliance, as their planes are fully transverse to the loading direction. This is in contrast to the cells located in plane 5, which have the highest resistance against deformation, since plane 5 is parallel to the loading direction. In case of regions 1, 3, 4, and 6, the planes of border cells are situated with an angle to the loading direction and therefore are exposed to a combination of compression and shear loading. Nevertheless, the border cells in regions 4 and 6 (loading in Direction 2) naturally have higher compliance, as their planes have a larger angle to the loading direction.

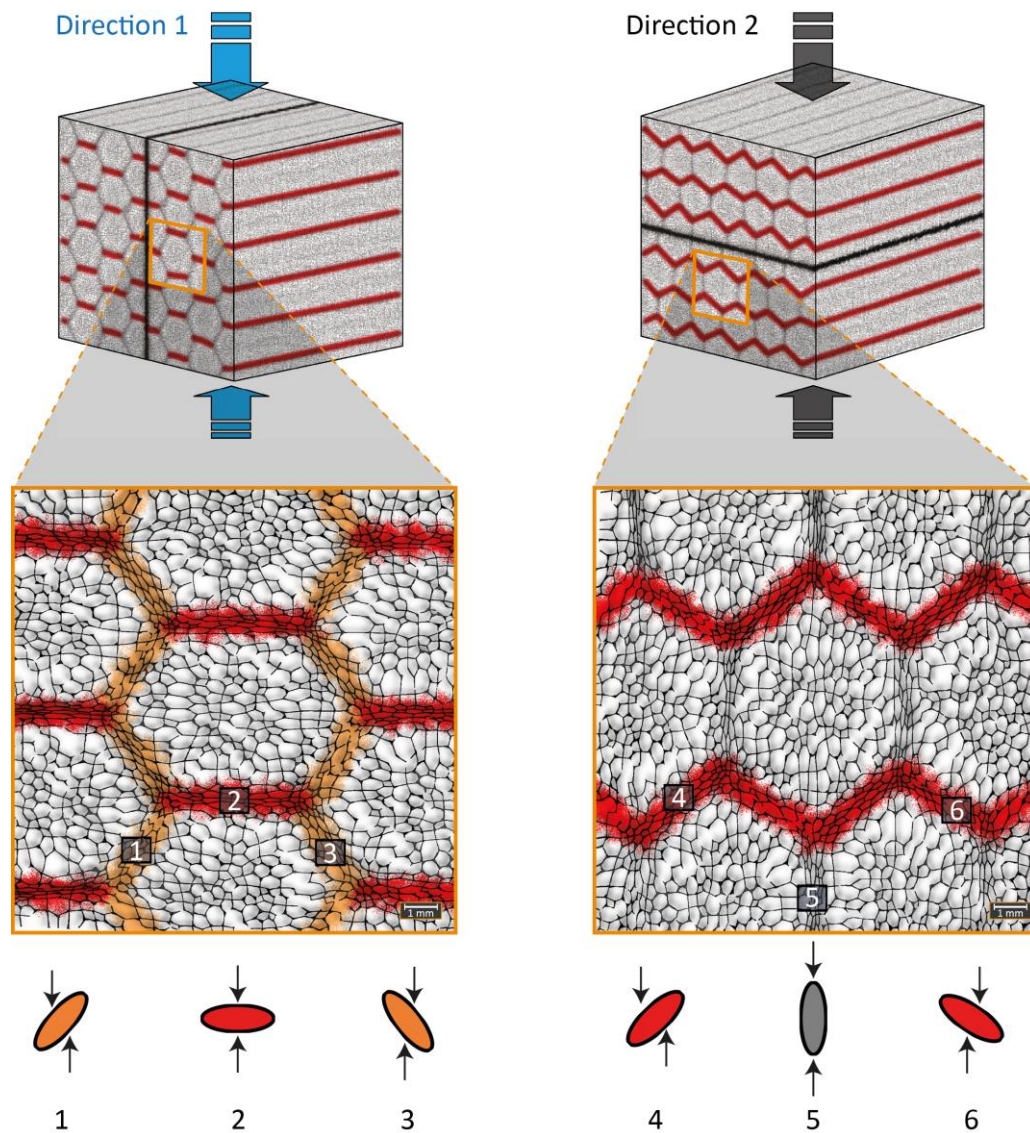


Figure 53 Schematic 2D illustration of how strand border cells are exposed to mechanical stresses during global compression loading.

Therefore, although the global properties are not much different in the two in-plane directions, the strain localization patterns are quite distinct in each case. This special localization of deformation could be one reason for the slight difference between the stress-strain curves of Directions 1 and 2. In Direction 2 (right image in **Figure 53**), the transverse planes of elongated border cells create almost complete crush bands through the width of the sample, which facilitate larger global deformations compared to Direction 1. For example, at comparable compressive stress levels (0.54 MPa in Direction 2; and 0.56 MPa in Direction 1), more than 30 % local straining had occurred in Direction 2, which is considerably higher than the local strain values in Direction 1 (ca. 20 %). Another conclusion is that foam cells inside the strand bulks experience very little deformation (below 5 %) until high global deformations. This is evident in **Figure 51** and **Figure 52** as the regions with red color. This behavior will be discussed in more detail in chapter 5.2.3, where the deformation mechanisms for both border cells and bulk cells are studied.

5.2.2.2 Optically Determined Compressive Stress-Strain Curves

The optical analysis equipment was synchronized with the controller of the testing machine. This allowed for obtaining and recording additional information such as force levels and time steps for each individual captured image during testing. After post-processing of the recorded images and a data export procedure, optically determined compressive stress-strain curves were generated for each loading direction (**Figure 54**). For each loading direction, the grey stress-strain curve denoted as “Average strain” is generated using average strain values from all facets in each captured image during loading. The second stress-strain curve in orange, denoted as “Maximum strain”, is created using the highest strain value recorded for each image. Finally, for each loading direction the global stress-strain curve is also presented for comparison, which is obtained using strain values measured by machine crosshead (transverse) movement. For all three stress-strain representations, the global compressive stress values are used, which are measured by the contact force between the testing plates and the foam specimen surfaces. In loading Direction 3, construction of the optical stress-strain curves was only possible up to a global strain of about 15 %, after which severe crushing of the specimen prevented accurate recognition of the facets. Repetition of the experiment for Direction 3 did not improve the data quality and therefore the data collection is limited to 15 % global strain.

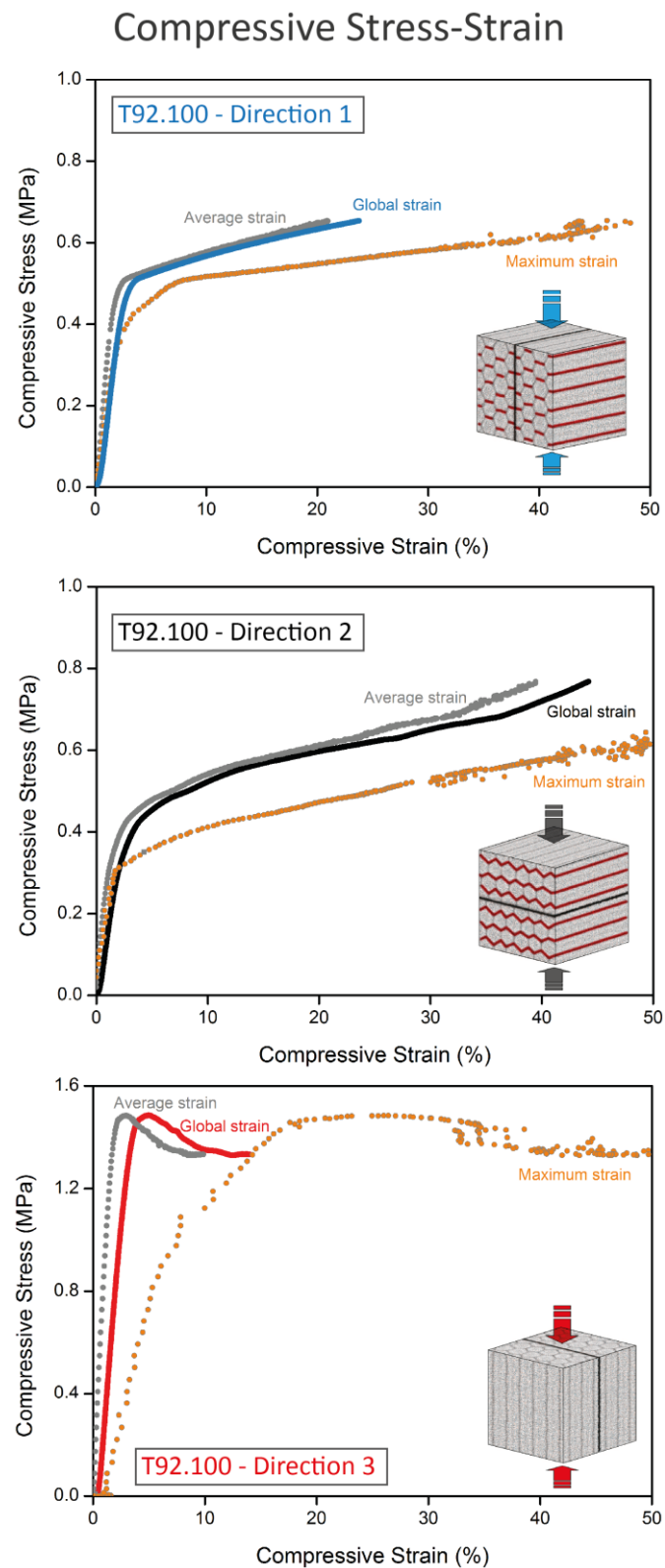
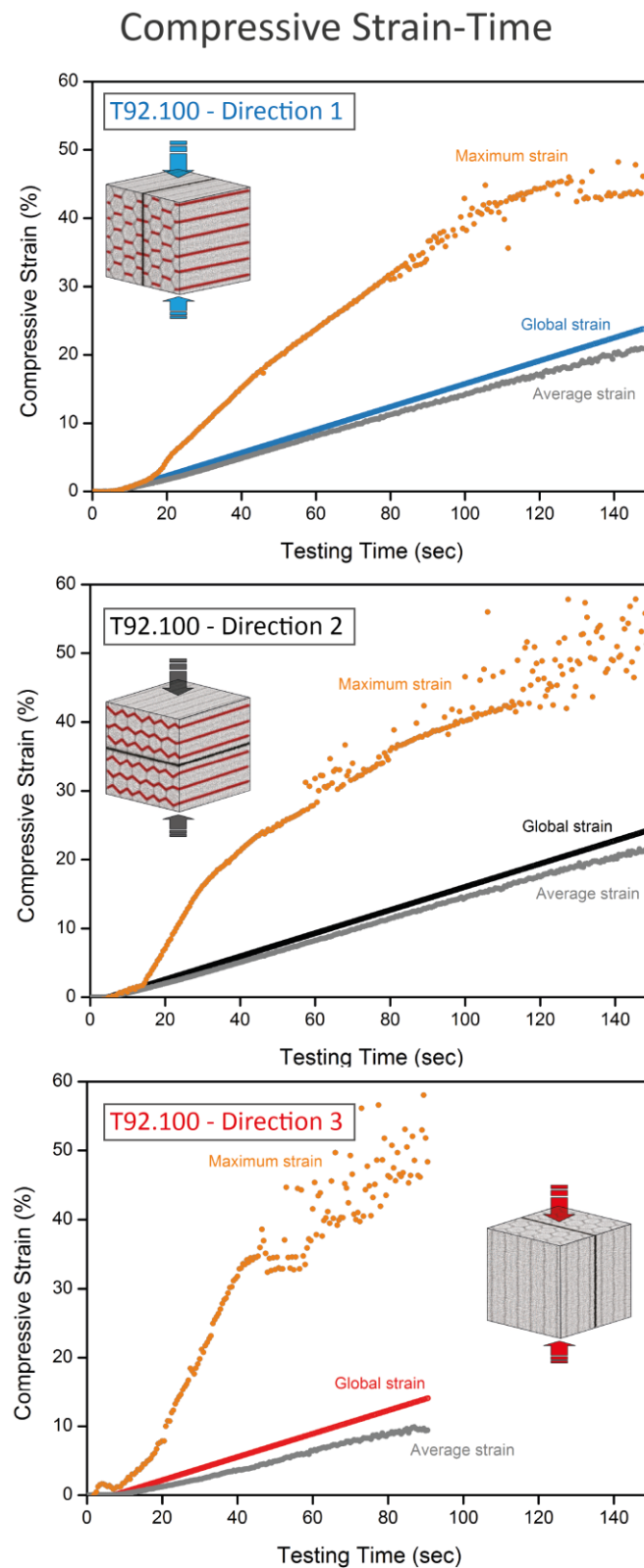


Figure 54 Optically determined stress-strain curves of PET foam T92.100 loaded in different directions.

**Figure 55**

Optically determined strain-time curves of PET foam T92.100 loaded in different directions.

For a better representation of the results, the strain data (global, average, and maximum strains) are also shown as a function of testing time in **Figure 55**. Note that in **Figure 55**, since the tests are displacement controlled (10% compressive strain per minute), the “global” strain values after a time progression of 60 seconds are around 10%.

The results show that in all three loading directions, local plastic strains in the foam sample are much larger than the globally measured strain values. In both in-plane Directions 1 and 2, despite the large localization of cell crushing on the strand borders, values of average compressive strains converge well with the global sample strains measured by the crosshead movement of the loading plates. This is probably due to the rather well distributed crushing zones and eventually more homogenous deformation patterns of the foam samples when loaded in the in-plane directions. In contrast, in out-of-plane loading (bottom graphs in **Figure 54** and **Figure 55**), the maximum deformation is highly localized in smaller regions of the foam. Therefore, the average strain curves for Direction 3 have larger deviations from the global strain curves in both elastic and post-yielding regions. In the elastic zone, the high out-of-plane stiffness of the sample leads to the crushing of the foam cells near the loading plates, while most of the foam volume has experienced very little deformation. This suggests that a correction of the measured elastic modulus would be necessary, at least for the out-of-plane direction. Using the average strain values obtained by optical measurements, realistic values of compression modulus were calculated with minimum influence of edge effects, specimen preparation, and other inaccuracies. **Table 5** compares the optically determined compressive moduli compared to the global values obtained by machine transverse movement.

5.2.2.3 Calculation of Poisson's Ratio

Measuring the Poisson's ratio of foam materials using conventional test methods is usually challenging due to large local deformations, difficulty to attach local strain gauges and other practical reasons. Hence, optical methods have become more popular for such measurements [94, 95]. One advantage associated with optical deformation methods is that, by obtaining the three-dimensional displacement of each facet, simultaneous calculation of different strain modes is possible. Therefore, in addition to the compressive strains, the transverse (contraction) tensile strains were also obtained for each stress level. Results were then used to calculate strain-dependent Poisson's ratio values using Eq. 20, in which ε_{ii} is the compressive strain in direction i and ε_{jj} is the tensile strain in direction j .

$$v_{ij} = -\left(\frac{\varepsilon_{jj}}{\varepsilon_{ii}}\right) \quad (20)$$

Using Eq. 20, the three Poisson's ratio components v_{12} , v_{21} , and v_{31} were calculated and plotted as function of compressive strain (see the orange curves in **Figure 56**). Each graph includes two stress-strain curves in grey color, which represent the uniaxial compression and the resulting transverse tension of the specimen. Similar to previous chapters, the compression stress-strain curves shown in **Figure 56** are made using absolute values of compressive stress and strain. Therefore, values are shown with positive numbers, so that illustrations and comparisons are easier. Nevertheless, for mathematical calculations of Poisson's ratio using Eq. 20, compressive strain is applied as negative values.

As reported in other works too, the Poisson's ratio strongly varies with strain [95] and reduces to smaller values after yielding. Jebur [20] reported variable Poisson's ratios for extruded LDPE foams, which changed with strain. This behavior is corresponding to the fact that only negligible lateral deformation is caused during plastic compressive crushing. Therefore, it is usually reasonable to assume a zero Poisson's ratio in the plateau zone, sometimes referred to as zero plastic Poisson's ratio [96]. Deshpande [104] reported the same phenomenon for PVC foams.

For a material with orthotropic mechanical response, there are in total six components of Poisson's ratio (v_{12} , v_{13} , v_{21} , v_{23} , v_{31} , v_{32}). However, the total number of necessary components is reduced to three due to symmetry conditions. This relation is expressed as:

$$\frac{v_{ij}}{E_i} = \frac{v_{ji}}{E_j} \quad (i, j = 1, 2, 3) \quad (21)$$

For strand PET foams, one can practically neglect the minor differences between the two in-plane directions. Therefore, assuming a transversely isotropic mechanical response, only two components of Poisson's ratio would be sufficient to describe the mechanical properties. For the T92.100 sample studied in this thesis, the two Poisson's ratio components v_{12} and v_{31} were directly obtained by optical measurements. Furthermore, in order to test the applicability of the linear elastic theory according to Eq. 21, the third component v_{21} was optically measured and compared with its calculated values (using the measured values of v_{12} , E_1 and E_2). Results (not shown here) confirmed a good agreement between the measured and calculated curves.

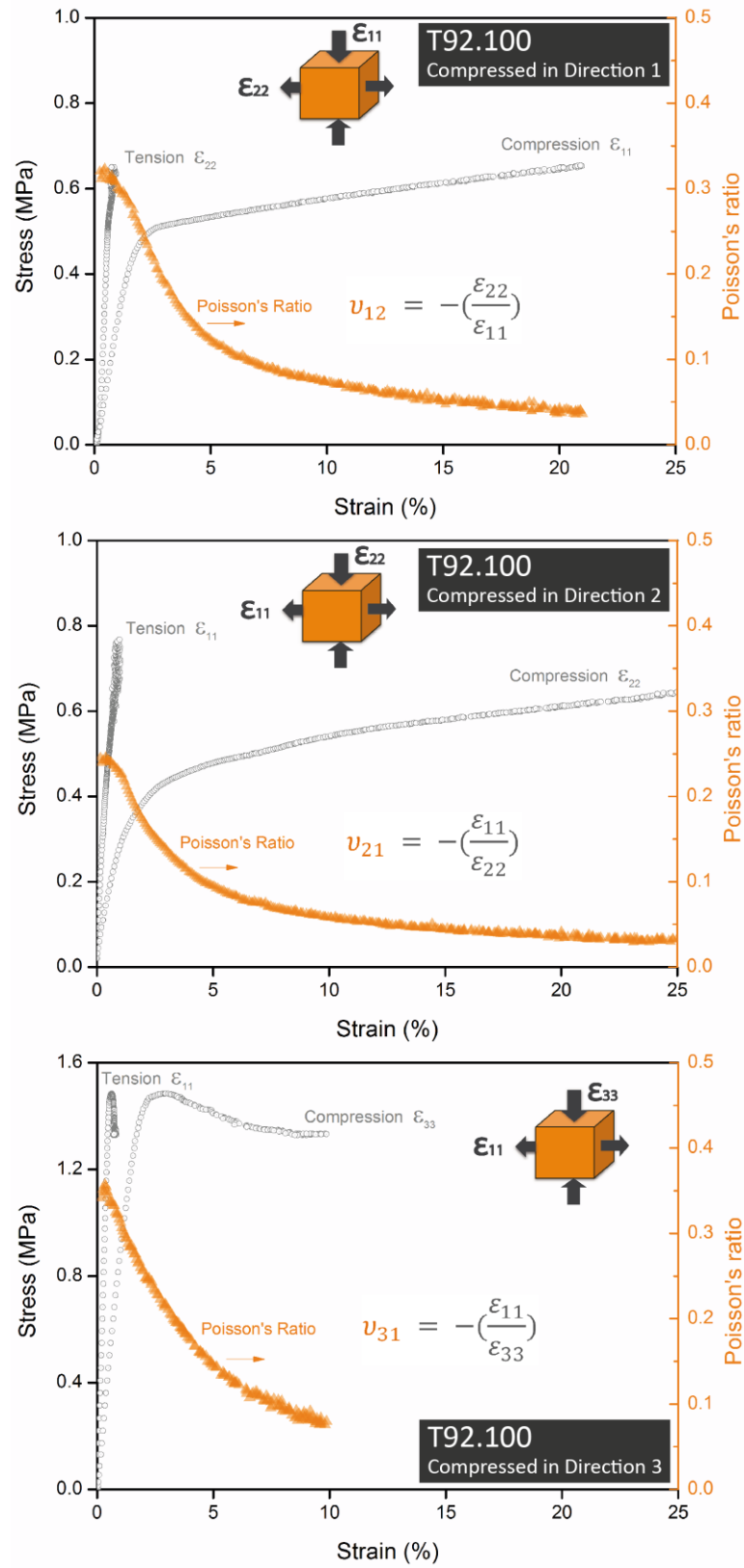


Figure 56 Calculation of strain dependant Poisson's ratio components ν_{12} , ν_{21} , and ν_{31} .

5.2.3 In-Situ (Micro) Compressive Response

In the previous chapters, the global mechanical response as well as the local yielding and failure of the strand PET foam samples were shown and discussed. Nevertheless, in order to understand the underlying mechanisms for the observed macroscopic anisotropy and the distinct local deformation patterns in each loading direction, it is essential to study the microscale deformation behavior of the foam cells. This approach can also provide precious information as input for (multi-scale) numerical simulations. One can first determine, then mathematically define and implement correct material models for FEM simulations, which are capable of accurately linking the mechanical responses at different length scales. By doing this, precise material cards can be created for complex foams, which contain detailed geometrical information for predicting and validating the post-yielding and failure behavior of foams.

Foam cell deformation analysis requires sophisticated equipment, as real-time observation of cell deformation at the microscopic scale is challenging. There are some literature works on studying cell deformation using microscopy methods [14, 176]. Nevertheless, the majority of literature works are performed in offline mode, meaning that a region of sample is observed under a microscope first before and then after multiple loading steps. The obtained information is valuable but limited. Usually for each loading point, the test should be aborted, and the sample removed from the the equipment followed by its repositioning after offline optical captures. All these steps make accurate and reliable measurements difficult and tricky. **Figure 57** shows an early literature work by Easterling [176], in which the cell deformation of a Balsa wood sample loaded in the tangential direction is captured using SEM. The images labelled with “Loading level 1-3” show the deformed wood cells at increasing compressive loads in the radial direction. The images clearly show the deformation mechanism as bending of the cell walls and struts, followed by yielding and plastic bending.

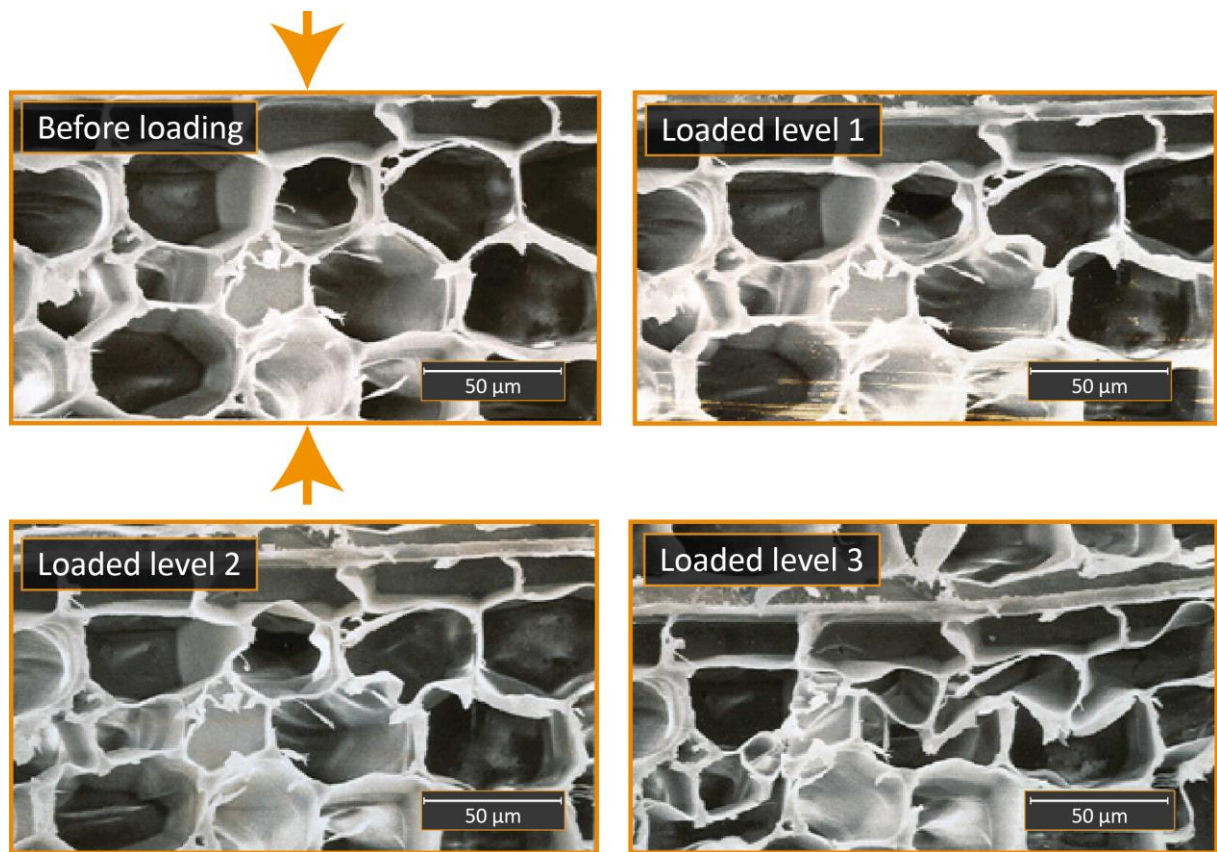


Figure 57 Bending of Balsa wood cells when loaded in the radial direction, reproduced from Easterling [176].

In this thesis, different cell deformation mechanisms of strand PET foam samples are determined using in-situ SEM equipment coupled with a loading module (see chapter 4.4 for experimental details). Cubic foam samples are glued between loading plates and positioned in the loading module, which is mounted on the stage of the SEM equipment (**Figure 58**). Hence, it was possible to track and record the cell deformation throughout the loading and unloading cycles. Although the in-situ SEM technique is more versatile than traditional offline methods, it still involves several technical challenges, which need to be addressed and resolved properly in order to obtain clean and reliable data. For this reason, sensitive and painstaking measurements were repeated multiple times to obtain accurate information. Some technical challenges experienced during in-situ SEM measurements included: *a)* Samples can move and misalign during measurements. This would require stopping the test, repositioning the view field and refocusing the image; *b)* Major deformation zones can develop outside the view field. In these cases, the specimen could be already highly compressed without the chance of observing the (plastic) deformation mechanism within the view field; *c)* Release of the cell gas/air usually happens after yielding. This causes a distortion of the vacuum condition in the chamber. This

condition automatically aborts the SEM capture; *d)* Image quality highly depends on the electron flow (conductive paths). During loading, the contact between the sample and test fixtures was sometimes altered, resulting in a change in image quality. Readjusting of the imaging conditions is then required.

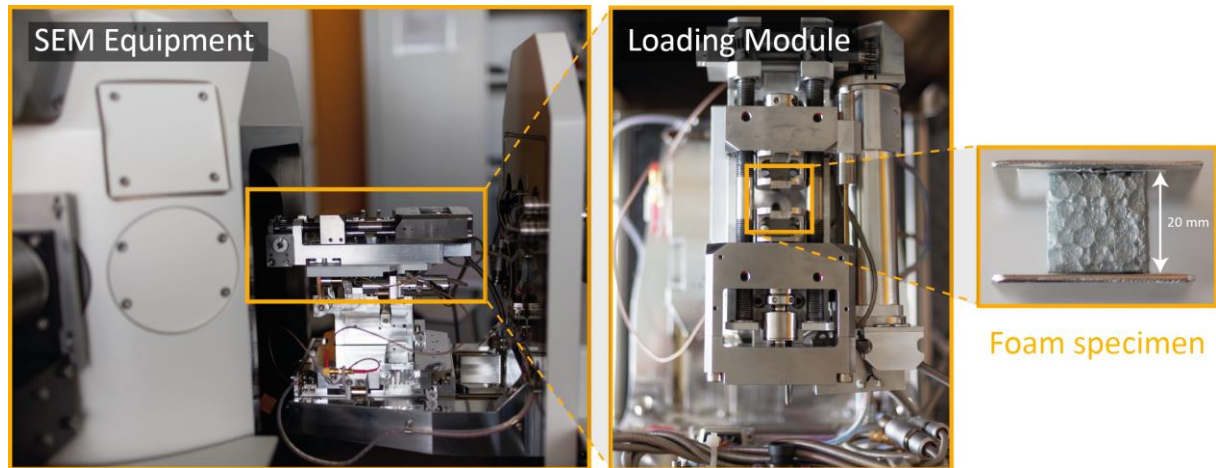


Figure 58 In-Situ compression test equipment consisting of a Scanning Electron Microscope (SEM), a mechanical loading module and sputtered foam samples.

Due to the complexity of the technique and the high number of tests and samples needed, in-situ experiments are extremely time consuming. Therefore, the cell deformation mechanisms in all three loading directions were first identified for the sample T92.100. The learnings about this foam density can be mostly transferred to other densities too. In order to ensure that the terminology used in this chapter is well defined and understood, examples of different cell deformation mechanisms are reminded from chapter 2.3. In general, some of the most well-known deformation responses are cell wall and strut bending, axial compression/tension, buckling, plastic yielding, and brittle fracture. What determines the type of deformation response for a particular foam cell in a specific loading condition depends on many factors, in particular cell shape, aspect ratio and wall/strut slenderness. For simple cell shapes with small orientation, higher cell wall slenderness (thinner and longer walls) can activate buckling mode, while thicker and less slender cell walls tend to yield and plastically bend [13]. In foams with more geometrically complex cell shapes, newer findings are needed to verify the modes of microscopic deformation. For the PET foam studied here, it is most important to understand the difference between cell wall/strut bending and cell wall/strut buckling as two main deformation mechanisms. These two cell deformation mechanisms mainly control the mechanical behavior of strand PET foams when loaded in different directions. **Figure 59** shows these two deformation

mechanisms for the T92.100 sample loaded in the in-plane direction (bending response) and out-of-plane direction (buckling response).

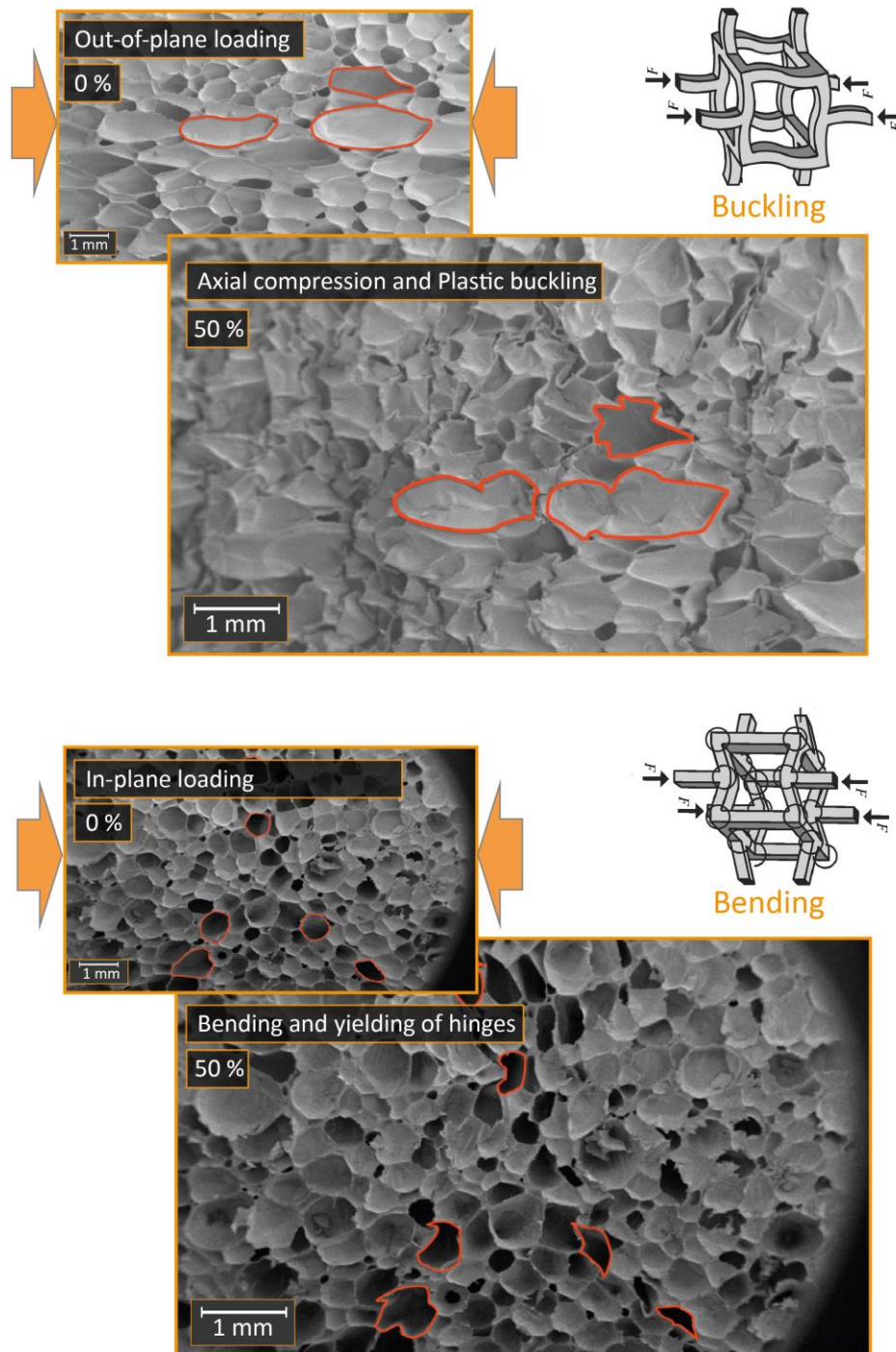


Figure 59 Examples of the two cell deformation mechanisms observed in PET foams. Top: axial compression and buckling; Bottom: yielding and plastic bending of the cells (Both samples are PET T92.100).

The bottom image in **Figure 59** shows the in-plane response of the foam cells, which involves yielding and formation of plastic hinges at the joints. The top image, on the other hand, shows an example of local plastic buckling when the elongated border cells are axially compressed in the out-of-plane direction. As a result, multiple buckling points are seen for the three highlighted cells in red. In the following, it will be shown how these two microscopic responses control the foam properties at different densities. **Figure 60** schematically shows the positioning of the SEM view field in case of the several loading directions and magnifications presented below. The loading arrows with colors blue, black, and red refer to the loading Directions 1, 2, and 3, respectively.

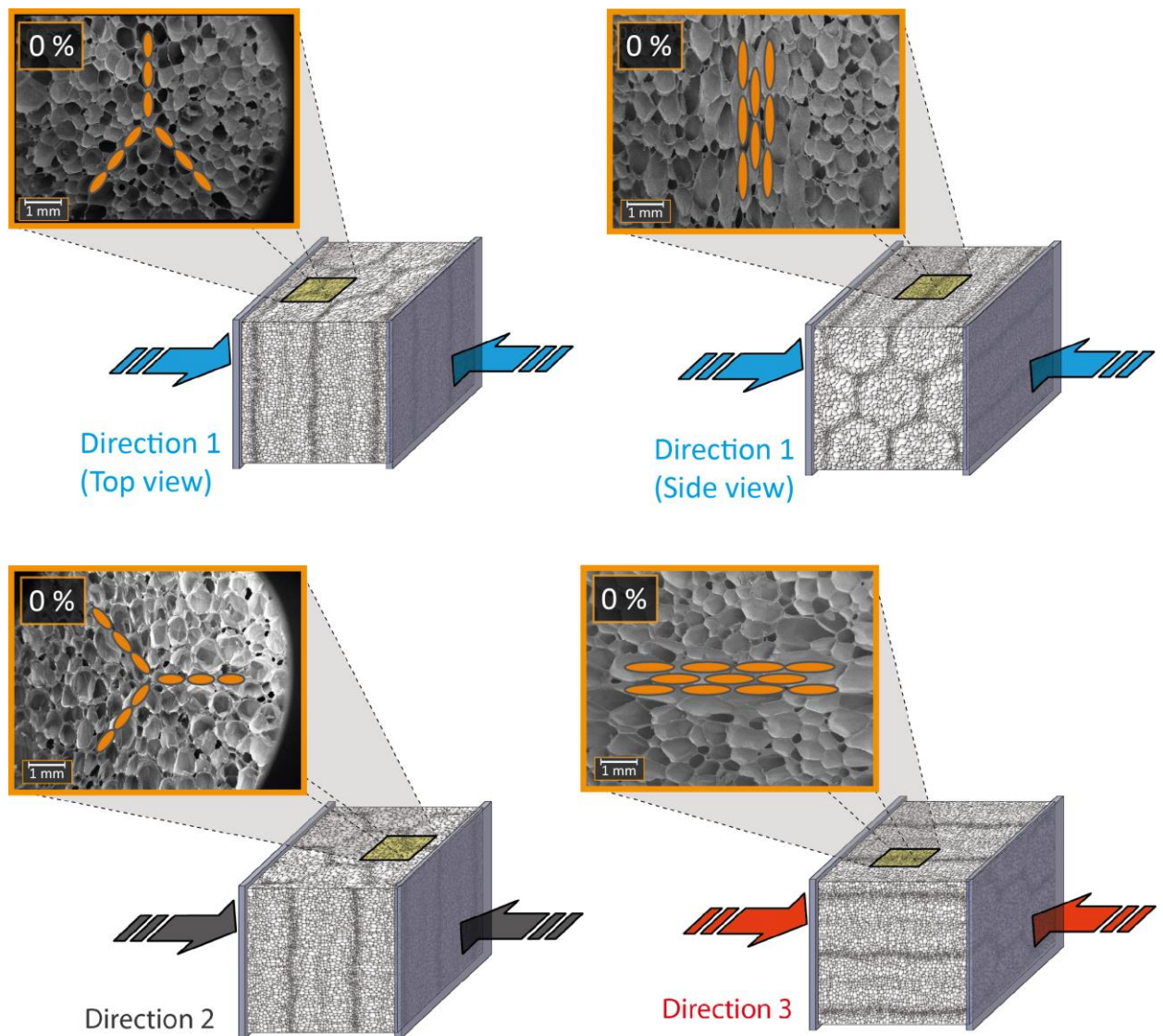


Figure 60 Illustration of the view field for in-situ compression tests in the three loading directions.

5.2.3.1 In-Plane Loading (Directions 1 & 2)

For studying the in-plane cell deformation mechanisms, two different viewing perspectives, namely side view and top view were chosen. **Figure 61** and **Figure 62** show the cell deformation of T92.100 specimen in the in-plane loading Direction 1 from the top view, but at two different magnifications. Similarly, **Figure 63** shows the side view SEM images of T92.100 sample loaded in Direction 1. Each row in **Figures 61-63** includes three images. The left image shows the raw SEM micrograph; the middle image shows the SEM graph with an overlay of individual foam cells emphasized with colored shapes; and the right image includes only the virtual colored cells. Color red shows strand border cells and colors white and black show strand bulk cells. The SEM images clearly suggest that the mode of deformation in the in-plane loading Direction 1 is cell wall/strut bending followed by ductile yielding of the walls and formation of plastic hinges (sometimes even full plastic folds at the joints). The images also show that the deformation takes place in two main stages. In the first stage, the more transversely compliant border cells (red cells) are deformed, as their long and flattened cell walls are weak against bending in the transverse direction. In the second stage, the strand bulk cells (white and black cells) begin to yield and plastically bend. The transition between the two stages, however, does not leave a clear signature in the load-deformation curves. Nevertheless, one can conclude that in the in-plane loading direction the cells located in hexagonal strand border regions deform sooner and easier than the cells located inside the hexagonal strands. This clearly explains the regular full-field deformation patterns captured with DIC measurements in chapter 5.2.2.

Figure 64 shows the cell deformation response of the T92.100 sample when loaded in Direction 2. The behavior in Direction 2 is quite similar to Direction 1, as they are both in-plane loading. Therefore, the main deformation mechanism is yielding and plastic bending of the cell walls/struts. After the elastic bending region, the cell walls start to yield from the hinges and plastically bend until full cell flattening takes place. This pattern happens throughout the foam samples on all hexagonal strands. Therefore, the plastic deformation patterns in the foam cells are regular. Nevertheless, this two-stage deformation is most significant in Direction 1, where the plane containing the strand border cells is positioned perpendicular to the loading direction (see position 2 in **Figure 53**). But in loading Direction 2, some border cell planes are positioned parallel to the loading direction (see position 5 in **Figure 53**). Therefore, there is much higher resistance against bending deformation. This is the reason for the fact that red border cells located in the far right hand side of SEM images in **Figure 64** (loading Direction 2) begin to deform at a later stage.

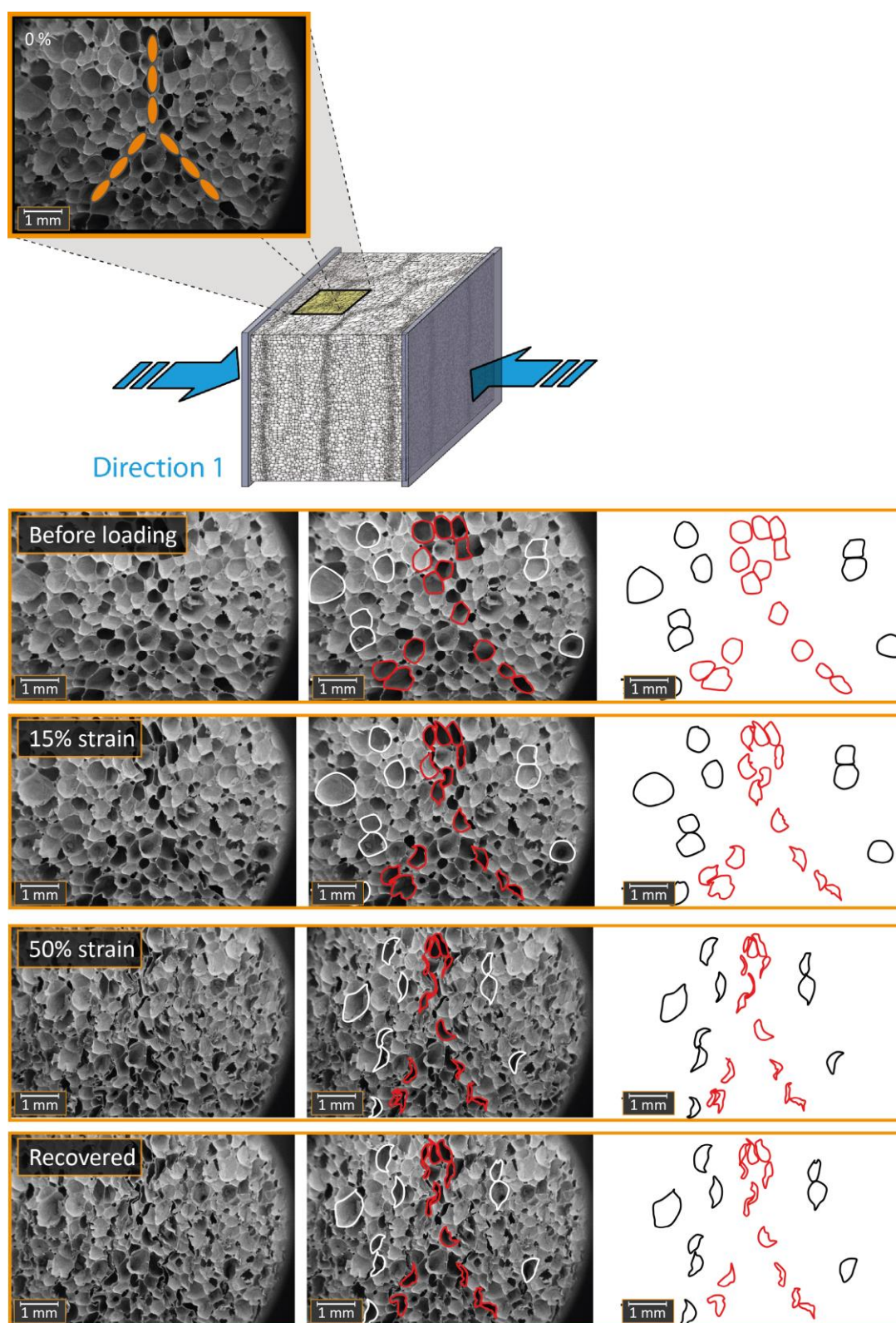


Figure 61 SEM images (top view) of PET foam (T92.100) loaded in Direction 1 at various compressive strain levels.

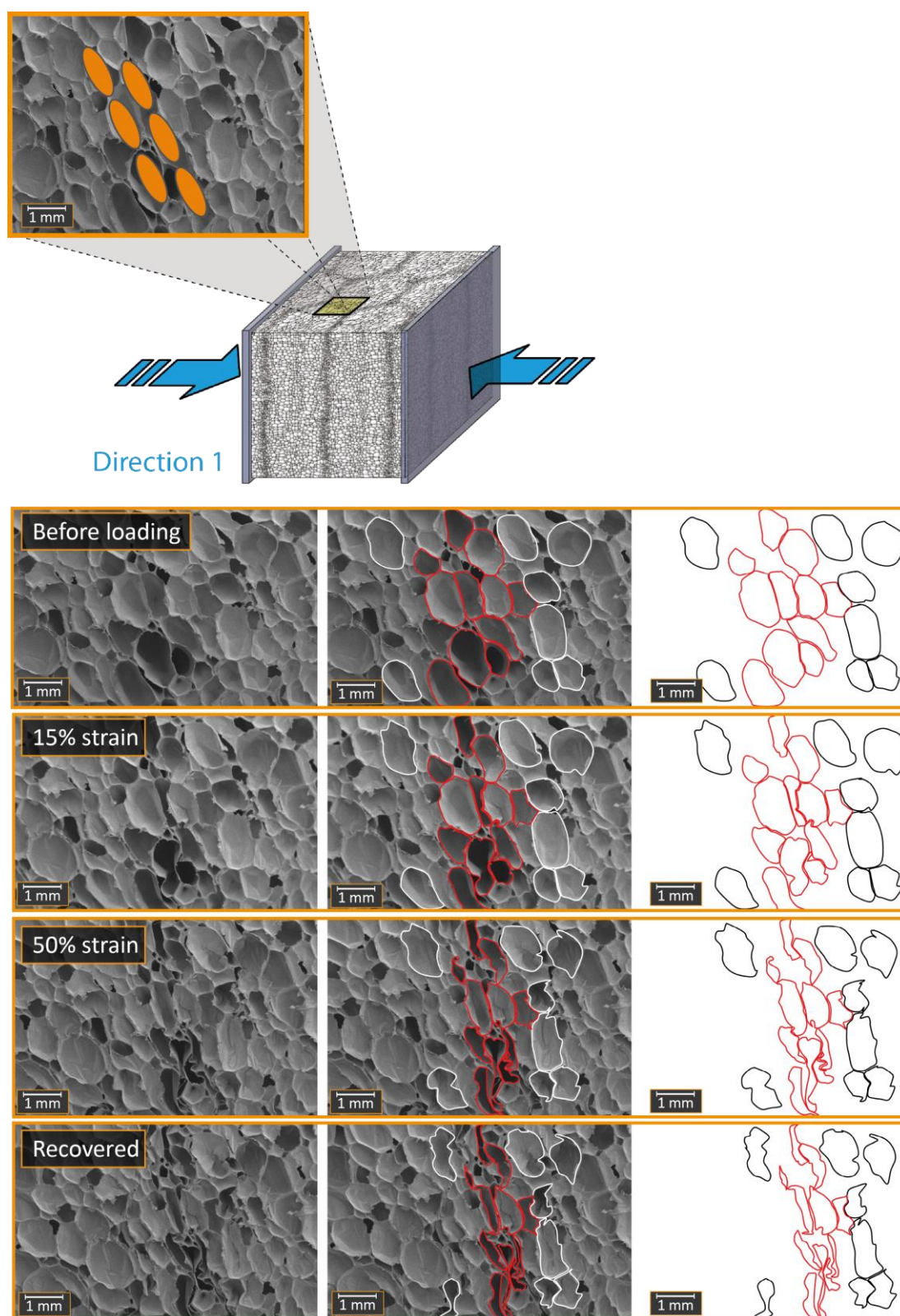


Figure 62 Higher magnification SEM images (top view) of PET foam (T92.100) loaded in Direction 1 at various compressive strain levels.

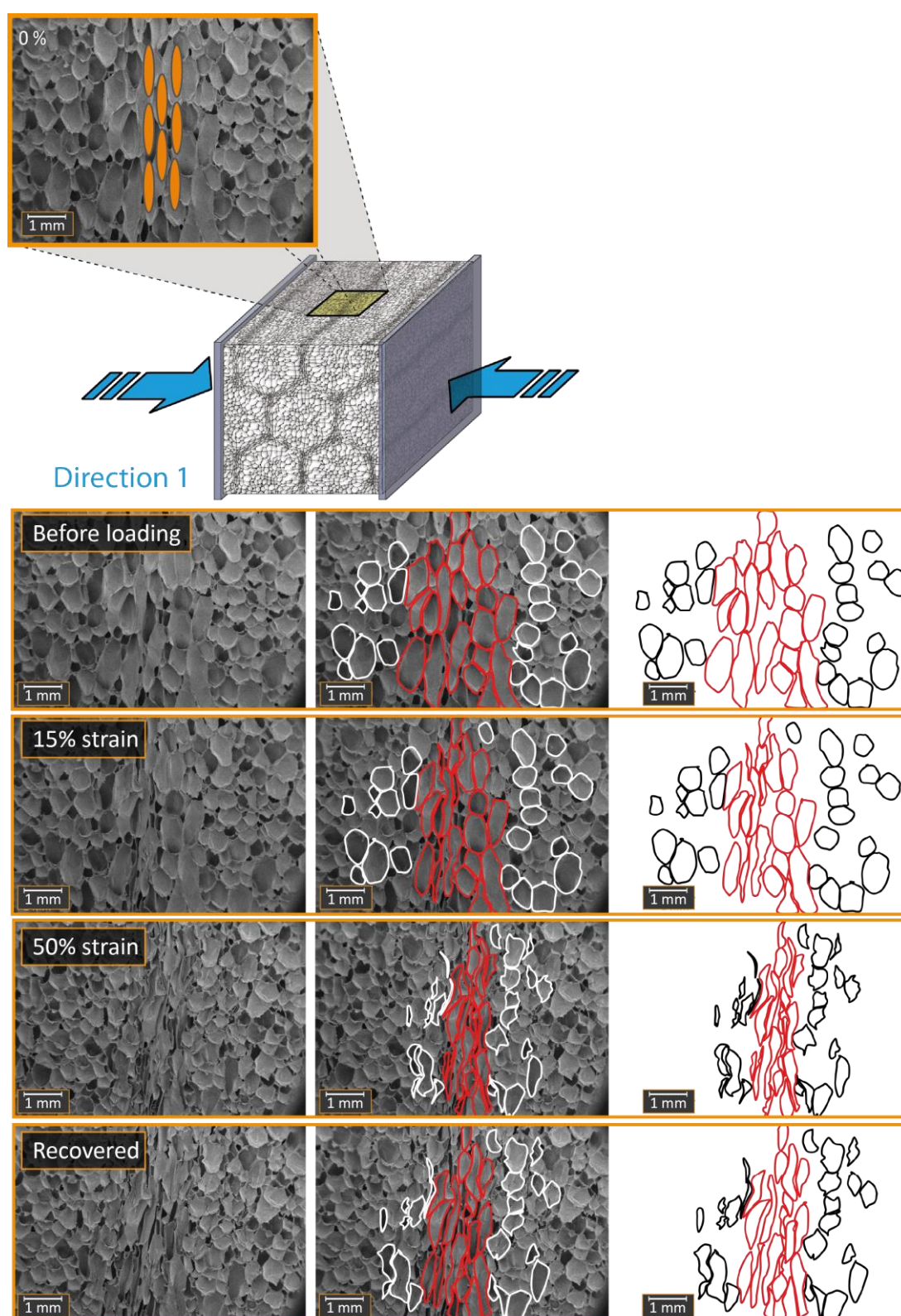


Figure 63 SEM images (side view) of PET foam (T92.100) loaded in Direction 1 at various compressive strain levels.

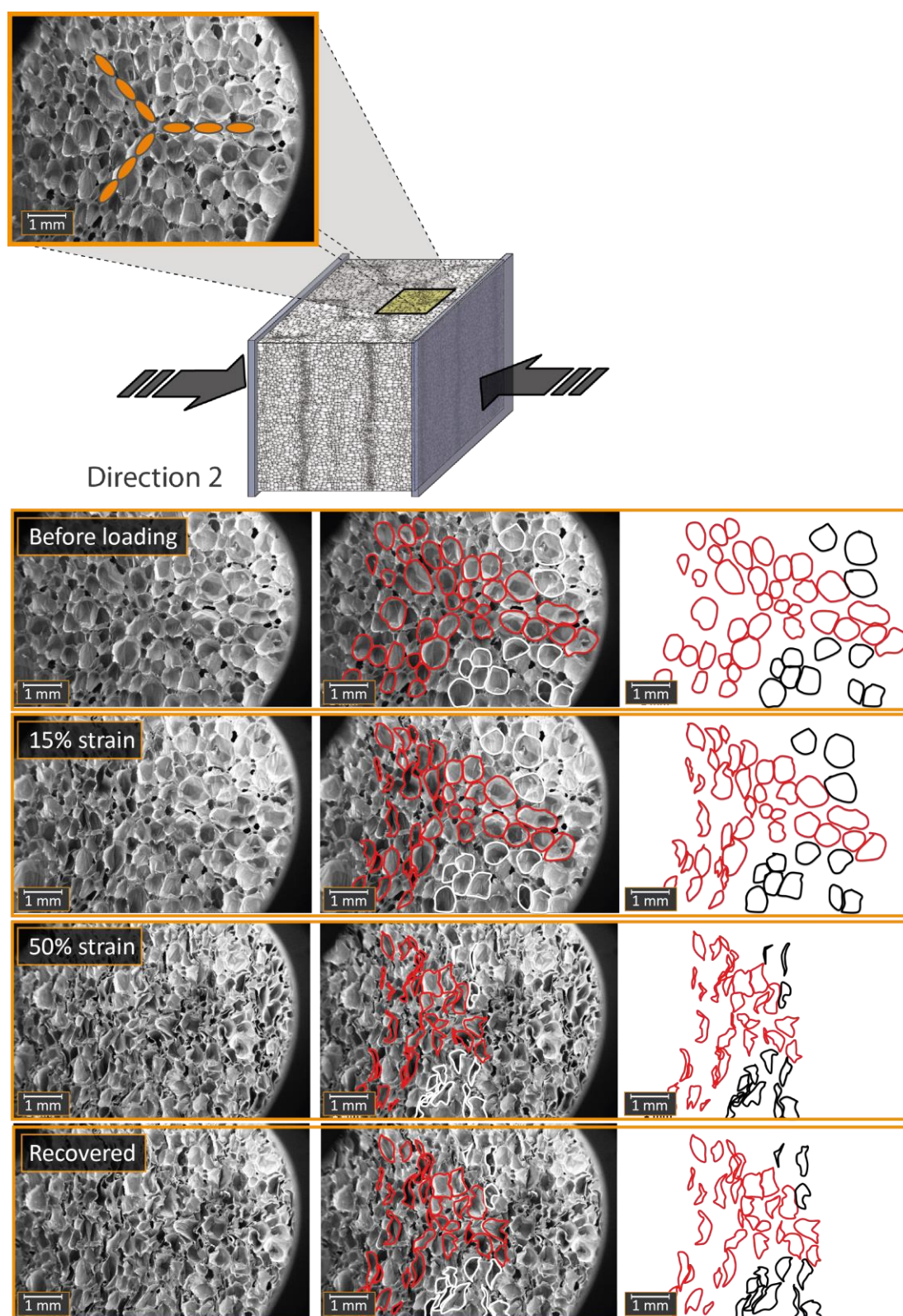


Figure 64 SEM images (top view) of PET foam (T92.100) loaded in Direction 2 at various compressive strain levels.

5.2.3.2 Out-of-Plane Loading (Direction 3)

Performing in-situ SEM tests during out-of-plane loading was more challenging. One reason was the stiffer compressive response, which led to very small elastic deformations followed by local yielding and failure of cells in irregular zones, which were hard to predict. Thus, considering the limited view field of the SEM microscope, it occurred multiple times that yielding took place in a region out of the view field. In these cases, even until high strain levels, the cells in the view field were only elastically deformed and little useful information could be obtained from the SEM captures. Additionally, instances happened in which local yielding and buckling of one array of cells were recorded until a complete crush band was formed, but then the active crushing zone would shift to another location along the sample thickness. In these cases, the tests were aborted to readjust the view field on the next active shear band zones. **Figure 65** shows a panorama picture reconstructed from several individual SEM images in order to show the size of the view field in comparison with only part of the specimen thickness. This limited view field made it necessary to repeat the out-of-plane in-situ tests several times, until suitable zones with local yielding of an array of cells could be clearly captured.

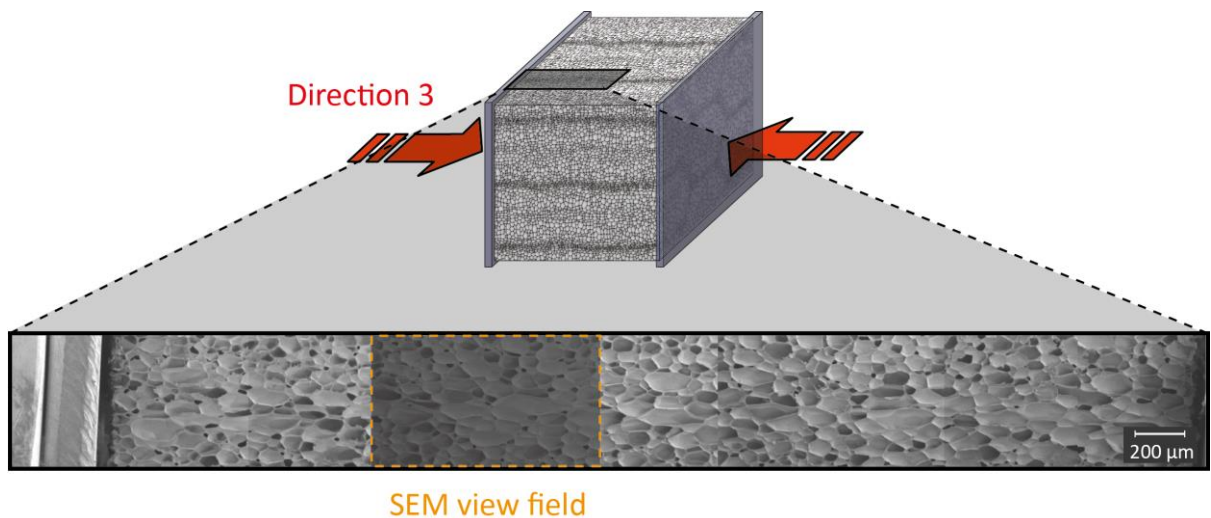


Figure 65 Panorama image of a PET T92.100 sample for in-situ compression tests. Multiple images were taken and stitched to create this image.

Figure 66 shows the SEM snapshots of the PET foam (T92.100) loaded in the out-of-plane Direction 3. The cell deformation mechanism is completely different from in-plane loading directions. Quite comparable to the arrangement of cells in wood [25], the elongated border cells (in red) are tightly packed and interlocked. This comb-like packing of the border cells creates very high resistance against bending of the cell walls. This behavior is comparable to the stretch-dominated response discussed in chapter 2.3.3.

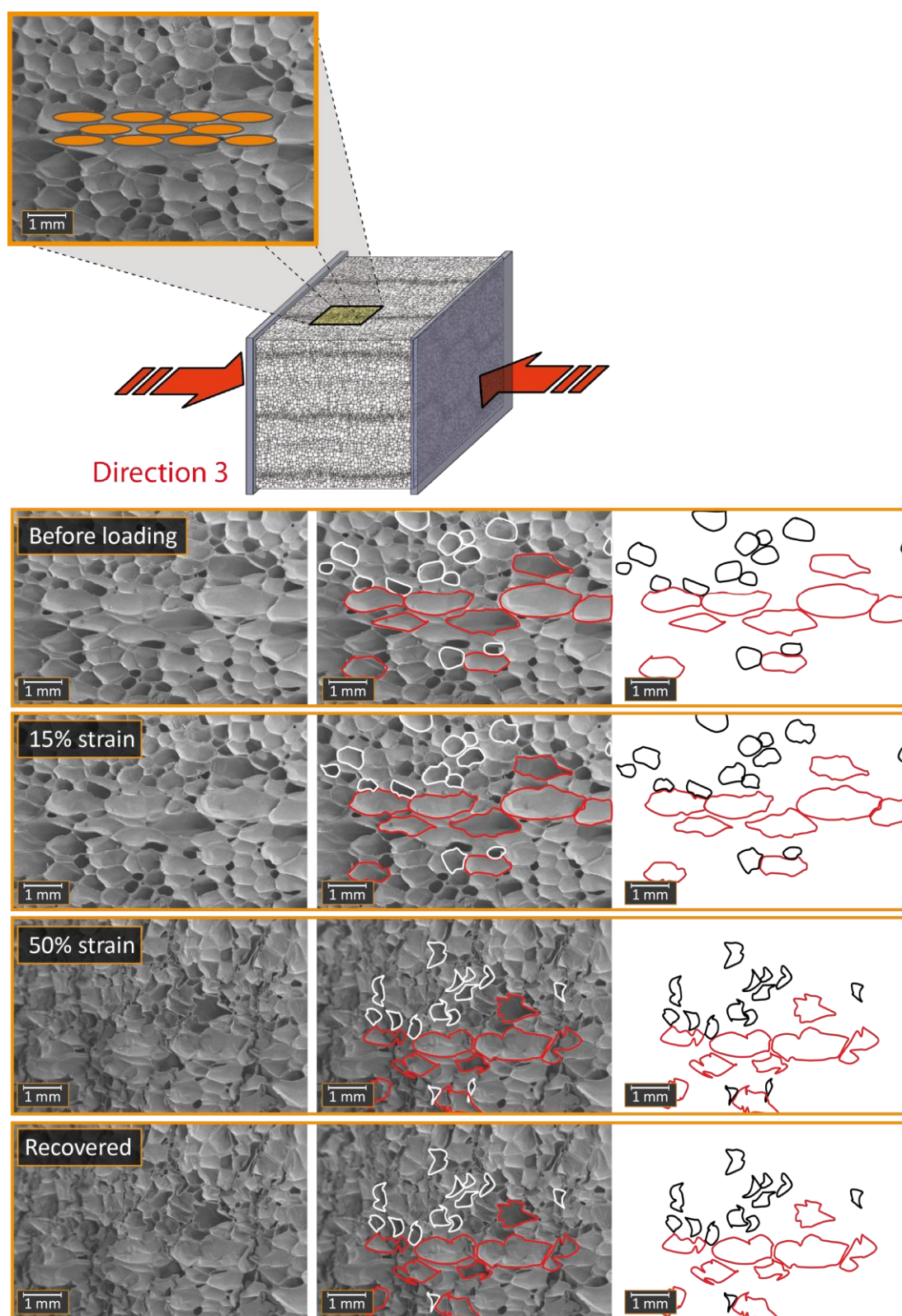


Figure 66 SEM images (side view) of PET foam (T92.100) loaded in Direction 3 at various compressive strain levels.

The special packing of the elongated cells and their higher nodal connectivity induces a behavior like stretch-dominated lattices. Hence, upon compressive loading the elongated cell walls are first axially compressed. After yielding, failure takes place in form of local plastic buckling in the weakest points. In contrast, in the strand bulk region (white and black cells in **Figure 66**), the deformation mechanism is mainly bending and plastic yielding, similar to the in-plane deformation mechanism. These bulk cells have more regular tetrahedral geometries and much less orientation. As a conclusion, out-of-plane loading of T92.100 sample results in local plastic buckling of the elongated border cells, which is then extended to complete crushed bands throughout the width of the sample. Once a band is fully crushed, the stiffness is slightly increased until another array of cells yields in plastic buckling and the formation of another shear band begins. This step-wise failure of the adjacent foam cell arrays is the main reason for the variation of engineering stress level after yielding in the global stress-strain curve of Direction 3 in **Figure 47**.

5.2.4 Effect of Foam Density on Compression Properties

The influence of foam density on the compressive response of PET foams was studied by performing global compression tests on all four foam densities. The engineering stress-strain curves are shown in the top graphs in **Figures 67-69**. In all three loading directions, with increasing foam density the compression modulus is increased, yield stress is shifted to higher values, and the densification strain is reduced. In the out-of-plane direction, at all densities there is clear post-yield softening indicated by a sharp decrease in the stress level. However, the softening trend is unique for the T92.130 sample, for which a linear decrease of stress continues until strain levels around 40 %. Although the reason for the distinct post-yielding behavior of the T92.130 sample is not further studied within this thesis, there could be correlations between this phenomenon and its unique cell size distribution shown in **Figure 46** (chapter 5.1.3). The elongated border cells in the T92.130 sample are much longer, and their size distribution bars are clearly shifted to larger cell sizes. Therefore, one could expect higher magnitudes of local buckling and softening iterations as multiple crushed bands are formed along the specimen thickness. There is also literature work [175] suggesting, that such post-yield softening behavior may indicate a highly ordered cellular structure of the corresponding foam. Interestingly, this post-yield softening trend of the T92.130 sample is different at higher testing temperatures, suggesting that the temperature can also significantly influence the deformation mechanism. Perhaps higher temperatures can reduce the fully plastic moment values and drive more bending deformation than buckling mode.

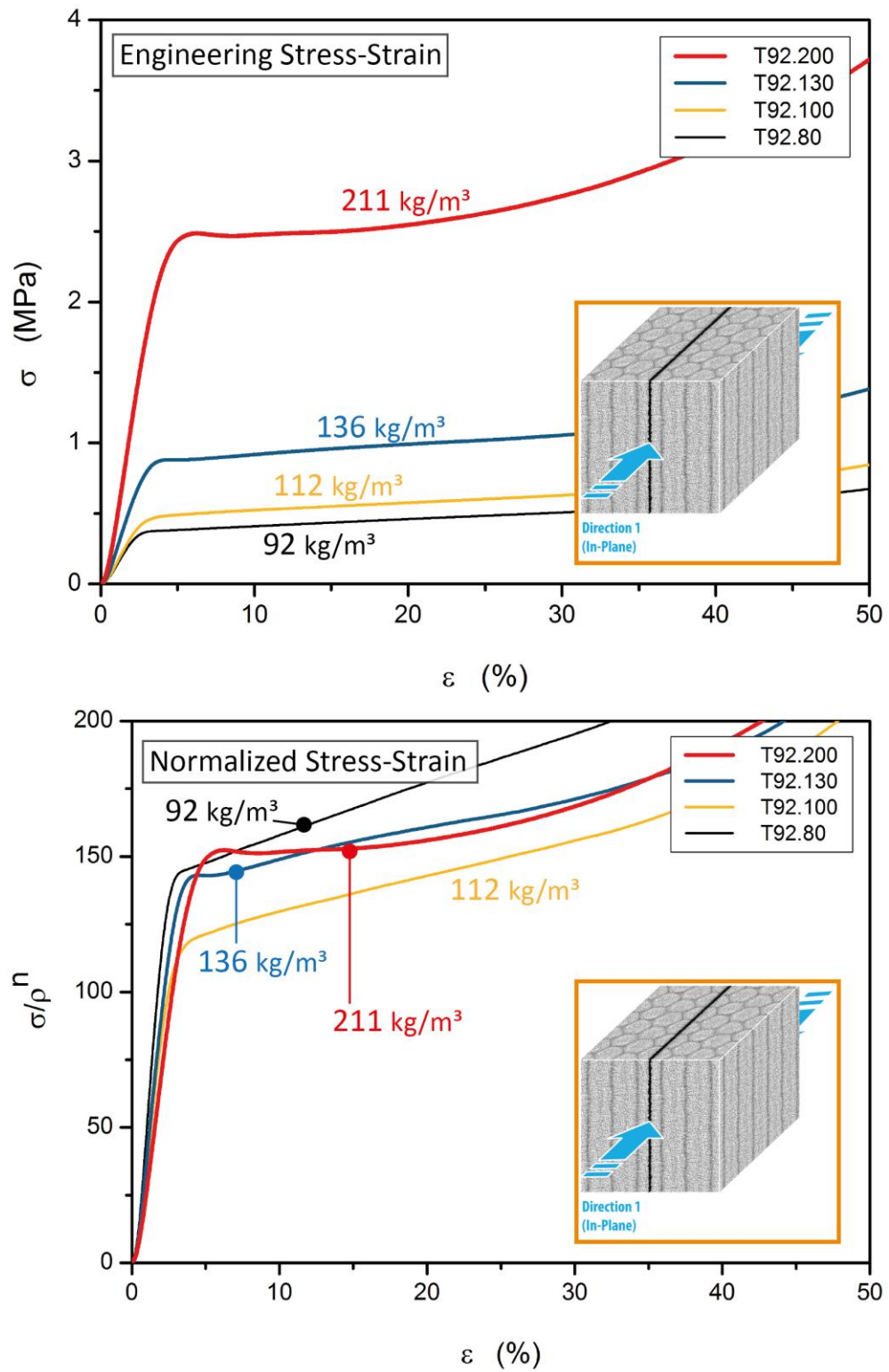


Figure 67 Compressive stress-strain curves of different density PET foams loaded in Direction 1. Top: Engineering stress-strain curve; Bottom: Density normalized stress-strain curve.

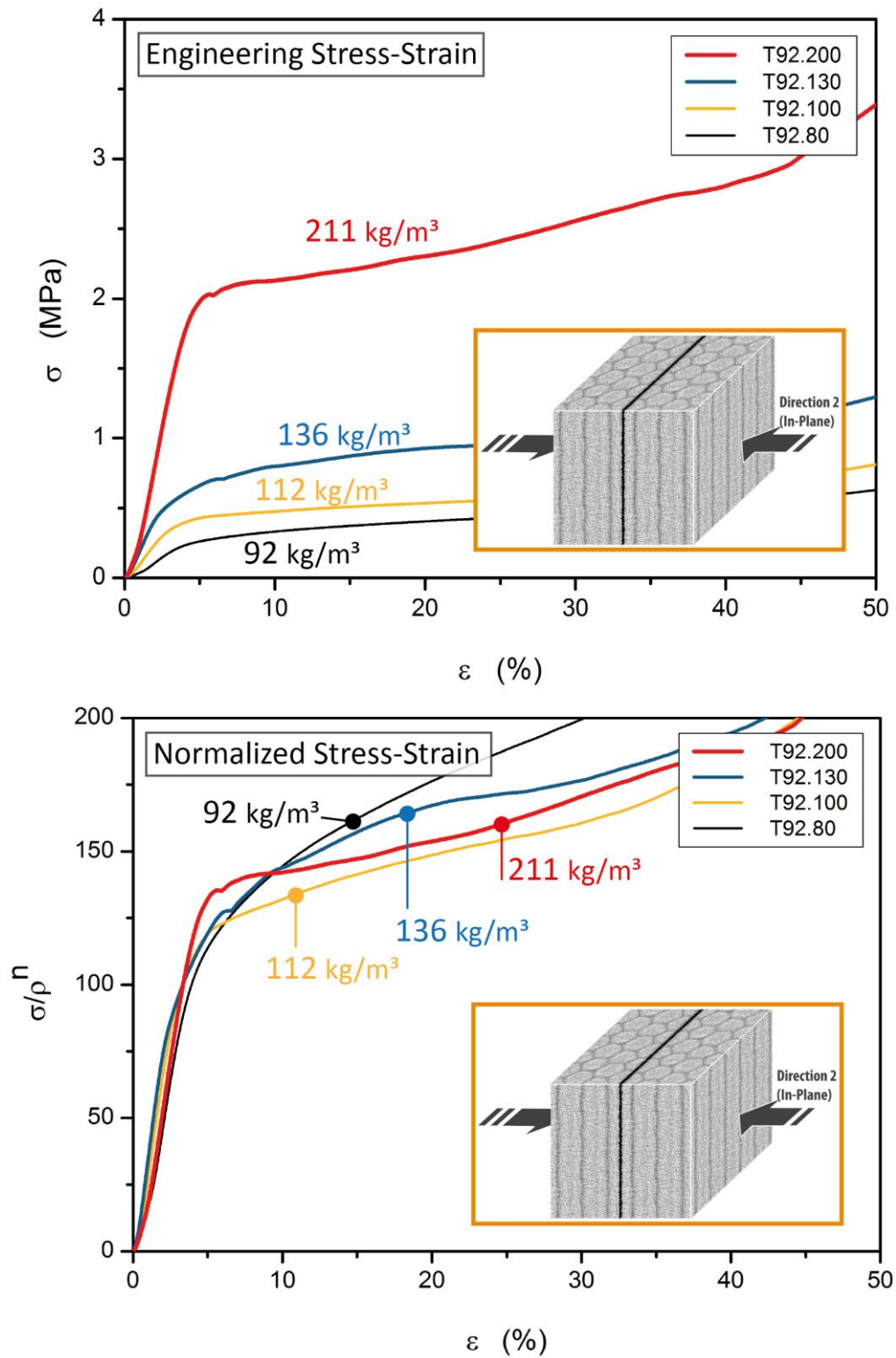


Figure 68 Compressive stress-strain curves of different density PET foams loaded in Direction 2. Top: Engineering stress-strain curve; Bottom: Density normalized stress-strain curve.

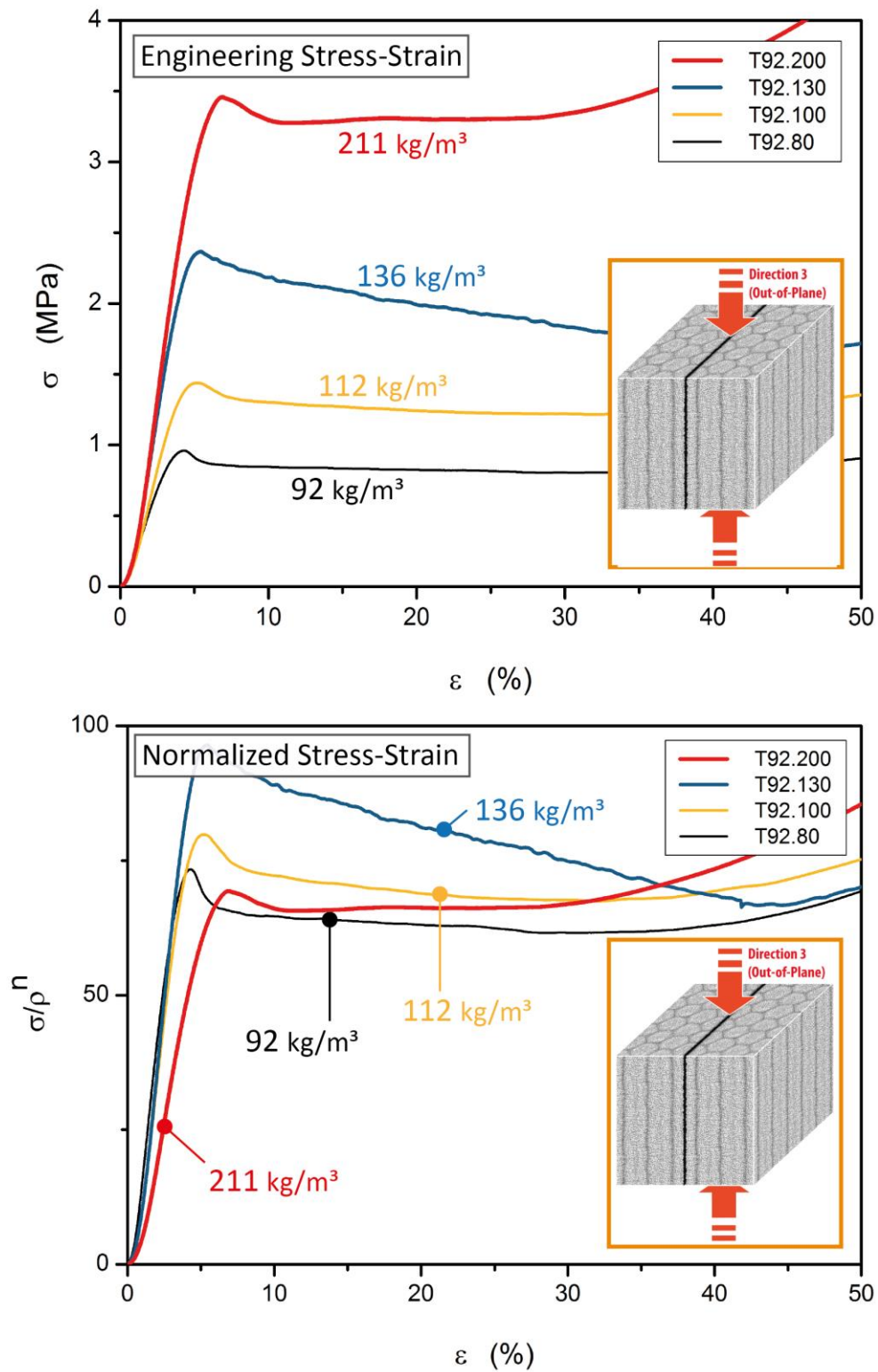


Figure 69 Compressive stress-strain curves of different density PET foams loaded in Direction 3. Top: Engineering stress-strain curve; Bottom: Density normalized stress-strain curve.

Table 6 Summary of the compression properties of strand PET foam at different densities.

		T92.80	T92.100	T92.130	T92.200
	$\rho_f / \rho_s [\%]$	6.81	8.31	10.06	15.62
Direction 1	E_f [MPa]	18.78	21.14	34.91	70.52
	$\sigma_{x10\%}$ [MPa]	0.42	0.53	0.91	2.46
	$\sigma_{0.2\% \text{ offset}}$ [MPa]	0.33	0.41	0.75	2.06
	$E_f / (\rho_f / \rho_s)^n$	10268	7250	7645	5506
	$\sigma_{x10\%} / (\rho_f / \rho_s)^n$	227	181	200	192
	$\sigma_{0.2\% \text{ offset}} / (\rho_f / \rho_s)^n$	179	139	163	160
Direction 2	E_f [MPa]	8.64	14.08	22.58	55.10
	$\sigma_{x10\%}$ [MPa]	0.33	0.47	0.79	2.10
	$\sigma_{0.2\% \text{ offset}}$ [MPa]	0.20	0.33	0.49	1.62
	$E_f / (\rho_f / \rho_s)^n$	5971	5997	6042	5059
	$\sigma_{x10\%} / (\rho_f / \rho_s)^n$	229	200	212	193
	$\sigma_{0.2\% \text{ offset}} / (\rho_f / \rho_s)^n$	141	140	130	148
Direction 3	E_f [MPa]	33.13	44.75	69.49	82.13
	$\sigma_{x10\%}$ [MPa]	0.87	1.32	2.27	3.33
	σ_y [MPa]	0.97	1.46	2.44	3.59
	$E_f / (\rho_f / \rho_s)^n$	1766	1777	2080	1282
	$\sigma_{x10\%} / (\rho_f / \rho_s)^n$	46	52	67	52
	$\sigma_y / (\rho_f / \rho_s)^n$	51	57	73	56

Table 6 contains the test results for compression modulus (E_c), compressive stress at 10% compressive strain ($\sigma_{x10\%}$), and the yield stress (σ_y) of all foam densities loaded in the three directions. For the in-plane test results, measuring accurate values of the yield stress was

difficult. Therefore, for Directions 1 and 2, stress values causing 0.2 % plastic strain ($\sigma_{0.2\% \text{ offset}}$) are reported instead of yield stress. **Table 6** also includes normalized values of the mentioned compression properties, which are calculated based on the density normalization procedure discussed in the next chapter.

5.2.5 Scaling of Compressive Properties with Foam Density

In chapter 2.3, different approaches to scaling foam properties with foam density were briefly reviewed. More recent literature works have used the generic relation expressed in Eq. 1 to describe the density-property relationships in cellular structures. The experimental values of power law exponent, n , can provide insight and information about the underlying mechanisms of deformation. Most foams show ideal bending-dominated deformation mechanism, resulting in exponent values close to two ($n \sim 2$). In contrast, foams with higher degrees of nodal connectivity usually show stretch-dominated deformation behavior and exponent values close to unity ($n \sim 1$). The axial (out-of-plane) deformation of wood is an example of this type of mechanical response. For the strand PET foam studied in this thesis, the compression test results at different densities were used to find the scaling parameters of the properties with foam density. For this purpose, the normalized compression modulus and normalized compression strength were plotted against normalized foam density in **Figure 70**. For the normalization of values, solid PET with density of 1350 kg/m³, Young's modulus of 3.3 GPa, and yield strength of 90 MPa was assumed. Since this information is not directly available by the manufacturer, rather best estimates were used according to available data. Eventually, Eq. 1 was applied to fit the data and calculate the power law exponent, n , for each loading direction.

The fitted lines to the data in **Figure 70** provide a number of useful information. Firstly, slopes of the fitted lines in the two in-plane and out-of-plane loading directions are different, meaning that the anisotropy in the mechanical properties is density dependent. At higher densities, the mechanical properties in all directions become more comparable and the compressive modulus and strength converge towards the same values. A similar behavior has been previously reported for wood. Since the data in **Figure 70** is plotted with logarithmic scale, slopes of the fitted lines represent the power law exponent, n , for each loading direction. The results show that in-plane loading data (Directions 1 and 2) can be fitted to Eq. 1, with n values close to 2. According to the theories previously discussed, this is an indication of a typical bending-dominated mechanical response, which is seen in most closed-cell foams. On the other hand, the fitted line to the out-of-plane loading data (Direction 3) provides n values in the range of 1. This

behavior is expected for lattice-like structures with stronger stretch-dominated and axial response.

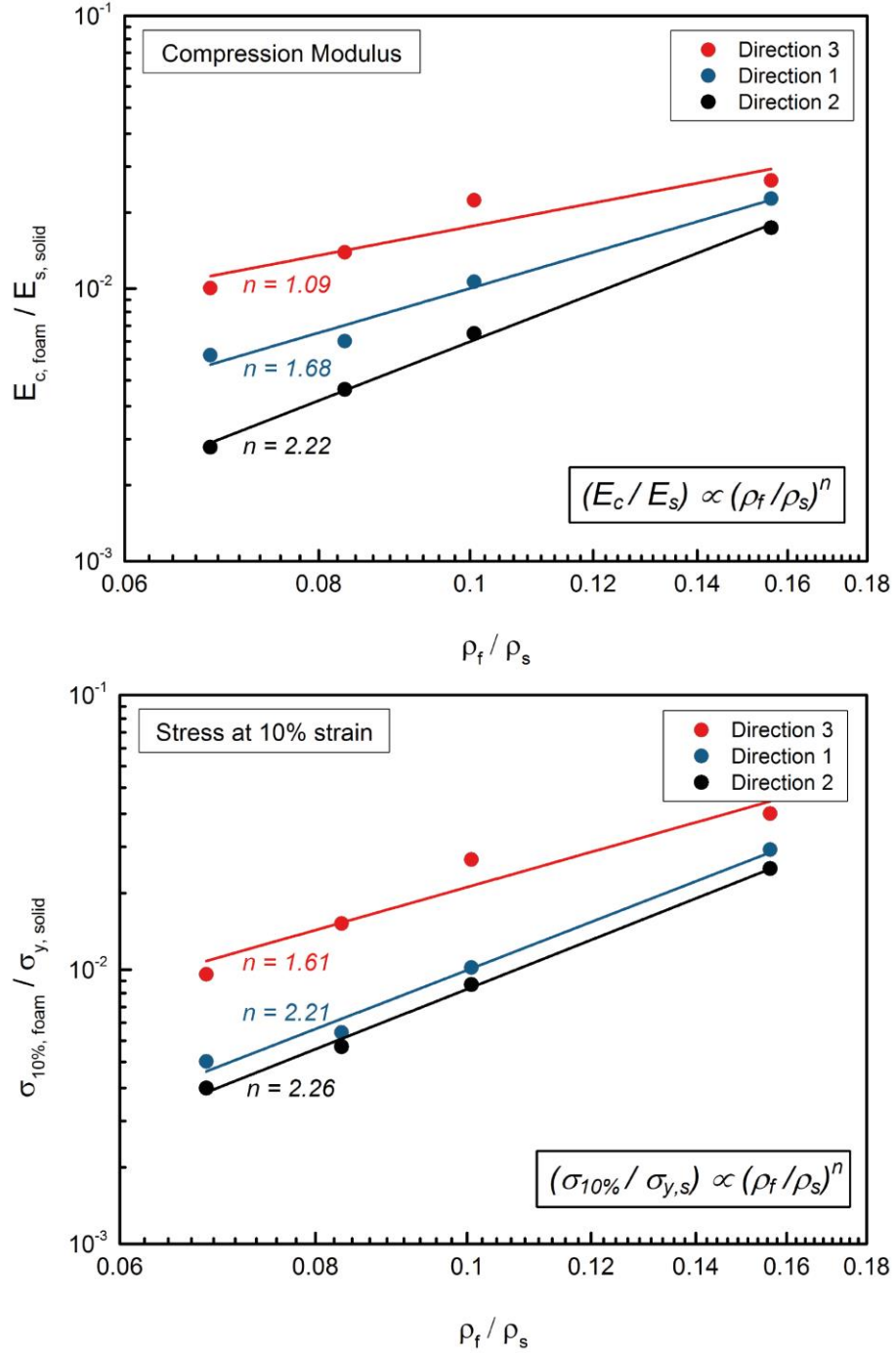


Figure 70

Scaling of experimentally determined compressive properties with relative foam density. (Exponent n is determined by fitting the data to Eq.1).

These observations highlight an important conclusion: Based on the information how the foam properties scale with density, it is possible to determine the fundamental microscale deformation mechanisms controlling the macroscopic mechanical properties. Interestingly, the information obtained from density scaling approach (e.g. values of the power law exponent n) can be directly verified and validated by the cell deformation mechanisms available from the in-situ SEM measurements. For both in-plane loading directions, in-situ SEM confirmed bending-dominated response for both border cells and bulk cells. In alignment with this observation, the fitted data of in-plane properties versus density in **Figure 70** yield n exponent values close to 2. In the out-of-plane direction, the in-situ SEM captures confirmed axial loading and plastic buckling of the elongated interlocked border cells, which are signatures of stretch-dominated microscopic response. The bulk cells, on the other hand, were deformed through bending controlled mechanisms. Nevertheless, the stronger axial response of the border cells show a dominating effect on the overall response and therefore fitting the normalized properties to Eq. 1 yields n values close to 1.

Arezoo [14] showed that if axial compression is the main deformation mechanism (e.g. buckling of the cell walls), the power law exponent will be close to 1, while if cell wall bending is the main deformation mechanism, then the exponent will approach values near 2. This description fits very well to the behavior of the present strand PET foam. As a general conclusion, in-plane loading is controlled by cell wall bending ($n \sim 2$), and out-of-plane loading is dominated by axial compression and plastic buckling ($n \sim 1$).

5.2.6 Change of Failure Mechanism with Density

It is argued in the literature, that the microscale deformations of the foam cells have a direct effect on how accurately the properties scale with the density, or in other words how well the experimentally determined values fit to the empirical relations like Eq. 1. If the cell deformation mechanism remains unchanged at different densities, usually the macroscopic properties can be accurately scaled with density. For example, Zenkert [13] has shown that tensile properties of PMI and PVC foams scale very well with their relative densities, because the tensile properties are controlled by axial stretching of the cell walls, and this mechanism usually remains the same at different densities (and consequently different cell wall and strut slenderness). On the contrary, it is highlighted in the same work that compression and shear properties do not scale well with density. This was attributed to the fact that depending on the foam density and the cell wall slenderness, the cell deformation mechanisms in compression and shear modes involve a

competition between buckling and bending modes. Assuming simple cell shapes, lower density foams have usually thin walls and tend to buckle more easily than higher density foams. This means as the foam density increases, the deformation mechanism is changed and therefore the density-properties relations can no longer be modelled with a single relation representing a specific deformation mode. In the work by Arezoo [14] on PMI foams, it is similarly shown that in compression loading, the deformation mechanism of PMI foam is changed with foam density. For the sample with relatively high density of 110 kg/m^3 , besides bending of the walls, elastic buckling also took place and therefore, the measured properties were lower than values predicted by models. Despite its high density, the slenderness of the cell walls was highest for this specific foam sample. Also, the high slenderness of the cell walls in the mentioned sample caused large differences between the predicted and the measured relative density.

In contrast to conventional foams such as PVC and PMI foams [13], the in-plane compression properties of strand PET foam fit almost perfectly to Eq. 1 (see the blue and black lines in **Figure 70**). This is probably an indication that the deformation mechanism in the in-plane loading direction remains unchanged at all PET foam densities. This is also consistent with the learnings from in-situ SEM data, where regardless of density, in-plane loading of PET foam resulted in regular bending of the cell walls with failure manifested as yielding and plastic bending of the hinges. At first, the more elongated and transversely compliant border cells bend and yield (stage I) and then the more regular-shaped strand bulk cells follow the same deformation mechanism (stage II). This consistency in the in-plane deformation mechanism at all foam densities results in the good fit to the data in **Figure 70**.

Nevertheless, unlike in-plane loading, the out-of-plane compression properties of PET foam do not fit well to the theoretical models. For example, see the value of out-of-plane compression modulus (Direction 3) for the high-density T92.200 sample (the red data point to the most right-hand side of **Figure 70**). The value measured for the out-of-plane compression modulus of the T92.200 sample is significantly lower than the predicted values using Eq. 1. This fact suggests that the out-of-plane deformation mechanism is changed with the foam density shift from 135 kg/m^3 to 210 kg/m^3 . **Figure 71** interestingly shows a clear and distinct transition in the deformation mechanism from low-density foams (T92.80, T92.100, and T92.130) to the highest density sample (T92.200). The data points of the three lower density samples fit almost perfectly to the predicted line, but the value obtained for the T92.200 sample suddenly falls below the theoretical predictions. Hence, the first impression is that the deformation mechanism in the three lower density samples is similar, but probably different for the T92.200 sample. The

data also suggests that the same change in deformation mechanism (from T92.130 to T92.200) is responsible for the reduction of anisotropy in the T92.200 sample. This is hypothesized because the offset between the in-plane and out-of-plane properties (vertical distance of the data points for each density in **Figure 70**) is almost the same in the three lower density foams, but changes for the T92.200 sample. In other words, in T92.200 sample, the out-of-plane deformation mechanism becomes more comparable to the in-plane mechanism. Therefore, it is expected to see a bending-dominated deformation in the out-of-plane response of the T92.200 sample, as opposed to buckling mode for the lower density foams.

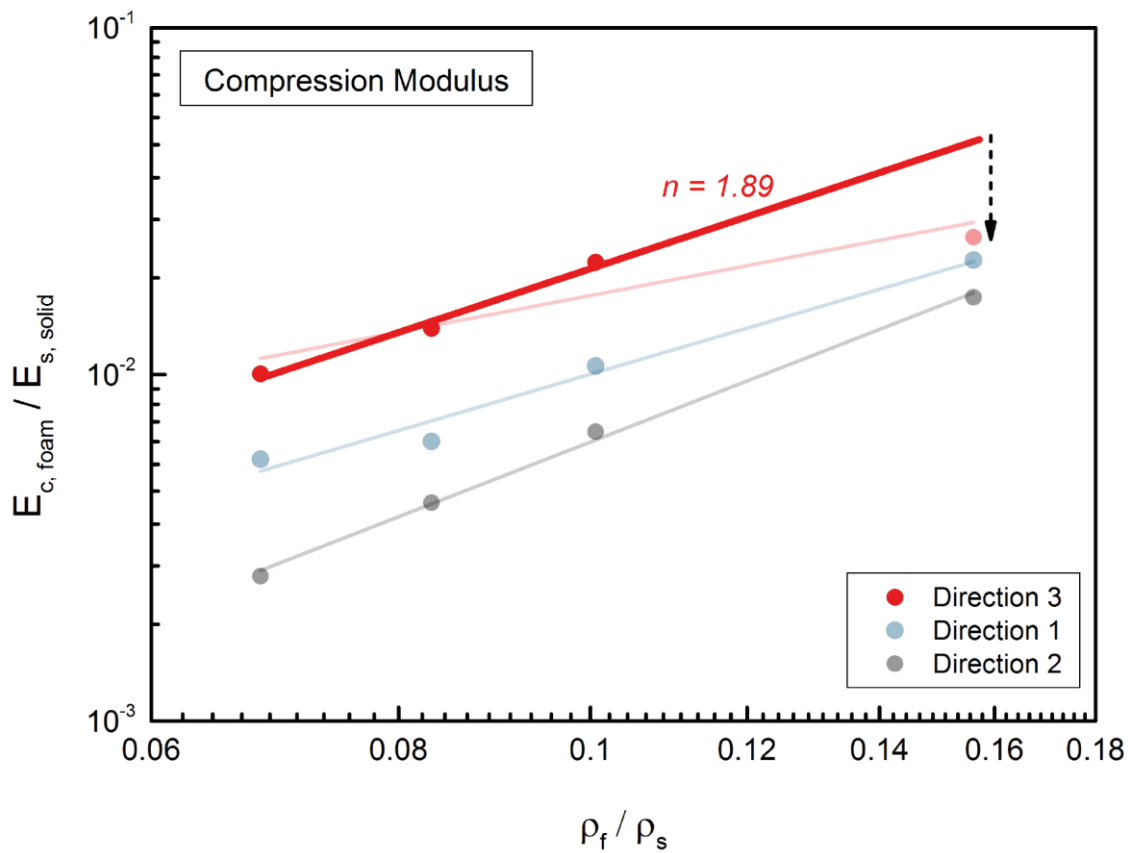


Figure 71 Scaling of experimentally determined compressive properties with relative foam density. (The solid red line is a fit to the three data points from low-density foams).

To show this effect in a different representation, the engineering stress-strain curves of all foam densities were normalized to the relative density of the same sample ($\bar{\rho}^n$), similar to the procedure shown by Zenkert [13]. The normalized stress-strain curves shown in **Figures 67-69** also verify the above-mentioned hypothesis. In general, in both in-plane loading Directions 1 and 2, the normalized stress-strain curves of all densities are more or less fallen into a single trend. This is because the in-plane microscale deformation mechanism of the foam cells remains the

same for all densities (bending-dominated reaction). However, it should be pointed out that, in the normalized curves of loading Direction 1, the curve of the T92.100 sample is somewhat below the other three foam densities. This suggests a slightly different cell deformation mechanism for this density, though no further correlations could be found with its foam morphology. In out-of-plane loading, the normalized stress-strain curves in **Figures 67-69** show a different trend. In the elastic zone, the three lower density samples fall into almost a perfect single line, while the T92.200 clearly stands out. This is consistent with the previously shown results, where the deformation mechanism of T92.200 sample shifted from stretch-dominated (buckling) to bending-dominated.

In the next step, attempt was made to optically verify the above-mentioned hypothesis about the change of microscale deformation mechanisms from T92.130 to T92.200 samples. The suggested change in the deformation mechanism are first correlated to the cell morphologies and ultimately verified by in-Situ SEM analysis in the out-of-plane direction. From a cell morphology perspective, it was shown in chapter 5.1.3 that in the high-density sample T92.200, the length and aspect ratio of the elongated border cells are significantly lower than the other three lower density foams. Comparing those results with the findings here, a clear correlation could be found: Unlike the lower density foams, the out-of-plane deformation mechanism in sample T92.200 is different and becomes more bending-dominated. This is because the cells have less orientation and interlocking characteristics in the T92.200 sample, resulting in their compliance against bending. Because of this change in microscopic response, the increase in compressive properties from T92.130 to T92.200 is much less, than the values predicted based on the three lower foam densities. The reason for the clear transition from buckling mode to bending mode is the fact that the shape of the cells in T92.200 is completely changed. In order to prove this hypothesis, the microscopic compressive deformation modes, obtained from in-situ SEM, were analyzed for different foam densities. **Figure 72** shows snapshots of the undeformed and multiple deformed stages in the out-of-plane loading of T92.100, T92.130 and T92.200 samples. In all three densities, the strand bulk cells (exaggerated with color white) show trends of bending as their main deformation mode. On the other hand, the red strand border cells clearly show axial compression and plastic buckling for the two lower density samples (T92.100 and T92.130), as opposed to bending and plastic yielding in the higher density T92.200 sample. The axial deformation of the more elongated border cells in T92.100 and T92.130 samples is associated with a stronger mechanical response compared to the bending-dominated response seen for T92.200 foam cells.

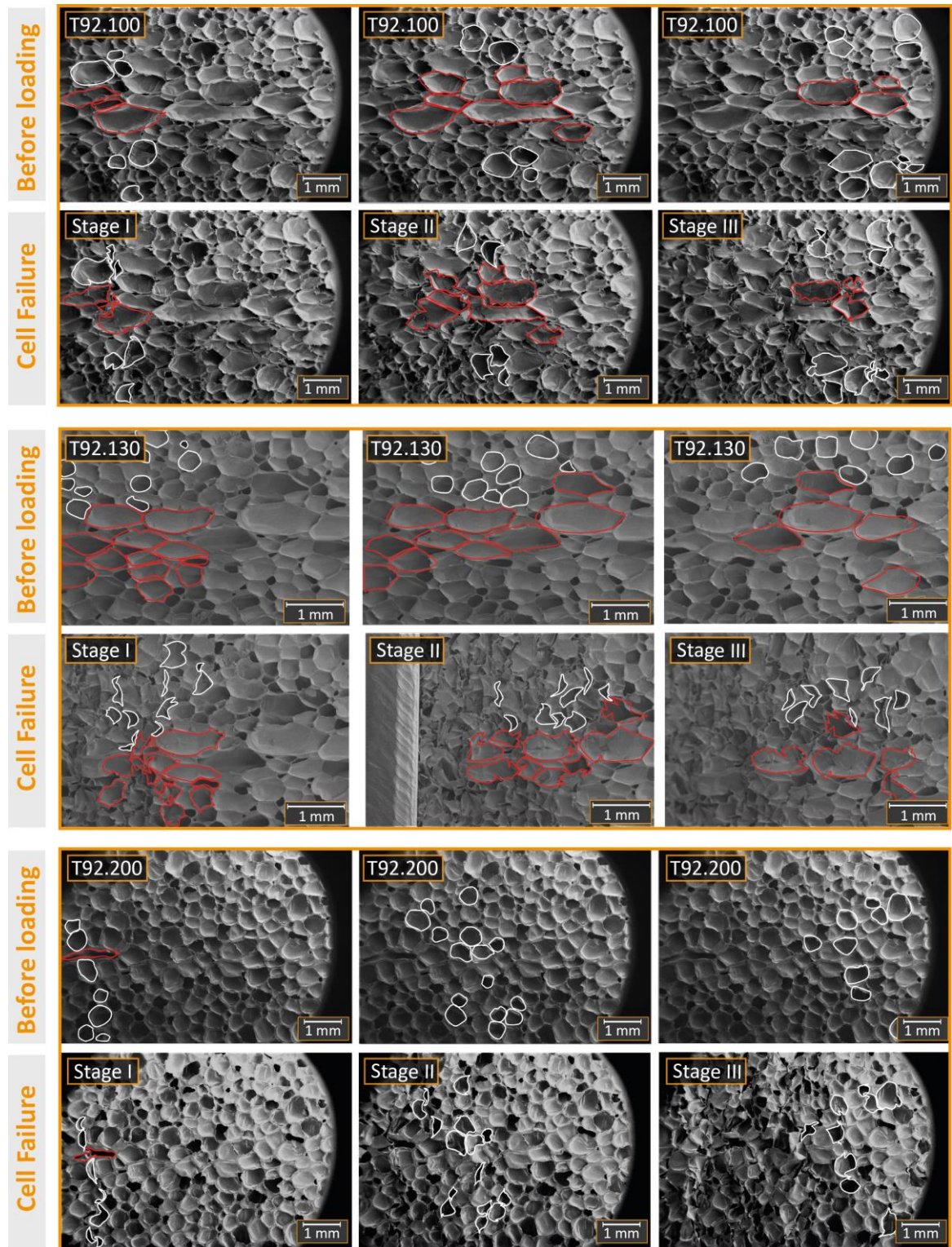
**Figure 72**

Illustration of the change in deformation mechanism of elongated border cells in different density PET foams. The deformation mechanism changes from axial compression/plastic buckling (lower density samples) to bending and plastic yielding (high-density T92.200 sample).

In some literature works [13, 14], the cell deformation mechanism (bending or buckling) is said to be a function of cell wall slenderness. This is because in morphologically complex foams there could be no single law (such as Eq. 2) relating cell geometrical features to relative foam density [14]. In other words, cell size and cell wall slenderness do not necessarily follow a predictable trend moving from one density to another. Therefore, in references [13, 14] taking into account the wall/strut slenderness served as a good criterion for modelling PVC and PMI foams with simpler polyhedral cell geometries. However, in case of the complex cell shapes of strand PET foams studied here, the micromechanisms of deformation are highly affected and mainly determined by the shape and nodal connectivity of the foam cells, especially the elongated strand border cells. For example, in the out-of-plane direction the interlocking elongated cells leave no room for cell wall bending, regardless of the wall slenderness. This particular arrangement of the foam cells results in a much higher stiffness and drives a stretch-dominated axial compression, followed by plastic buckling of the cells.

In this chapter, the compressive properties of strand PET foams were studied and interpreted at different length scales. The topics covered here included macroscopic anisotropy, local foam crush zones, cell deformation mechanisms and property-density scalings. The root cause to mechanical anisotropy was identified and visualized at the cell level and later correlated with the morphological features. It is worth mentioning that the results presented in this chapter on strand PET foams have huge similarities to the properties of wood briefly discussed in chapter 2.6. In low-density wood, too, the ray sections (which have less elongated and rectangular shaped cells) are extended only a few cells in the axial direction [2]. Therefore, most of the wood's bulk is made of the highly elongated cells. In contrast, in hardwoods, the ray cells are sometimes extended hundreds of cells through the axial direction. Hence, the anisotropy is higher at low-density wood.

5.3 Shear Response of PET Foam

The major focus of the present thesis is made on the compressive properties of strand PET foams. However, with regard to the application as sandwich core materials, the shear properties of structural foams are equally important. Therefore, in this chapter the shear response of strand PET foams is studied. Shear properties are obtained using two different experimental approaches. At first, the direct shear test is used to study the global shear response and to understand how shear properties scale with foam density. For direct shear tests, only the in-plane shear response is measured, since it is most relevant for sandwich applications. In the second step, the in-service shear properties of PET foam are investigated by means of sandwich bending tests. Sandwich specimens are analyzed in the scope of a case study representing the application of foam core materials in wind industry. The shell sections of wind turbine blades are usually made of sandwich structures. In addition to PET foam T92.100, two other core materials were used, namely PVC foam and Balsa wood. These core materials are regularly used in the wind industry. The sandwich four-point bending tests were coupled with optical deformation equipment, in order to obtain information about local shear deformations in the core materials.

5.3.1 Global Shear Response

In-plane shear is most important for sandwich core materials, as it represents the mode of shear load in most applications [25]. Therefore, direct (block) shear tests were done following ASTM 273. In general, direct shear tests involve a rather difficult experimental procedure, which requires careful and precise specimen preparation. It happened on multiple occasions, that the failure took place in the interface of the foam and the steel plates, falsifying the measured shear strength values. Also, with some foam densities, the measured values of elongation at break had large scatters. Therefore, for each foam density, measurements were repeated (in some cases up to 20 times) on several specimens in order to obtain meaningful data.

The top graph in **Figure 73** shows global shear stress-strain curves of strand PET foam at all four densities. The curves include measurement data for several test specimens, which show relatively good agreement within each density class. Except for shear strain at break, there is small scatter in the data.

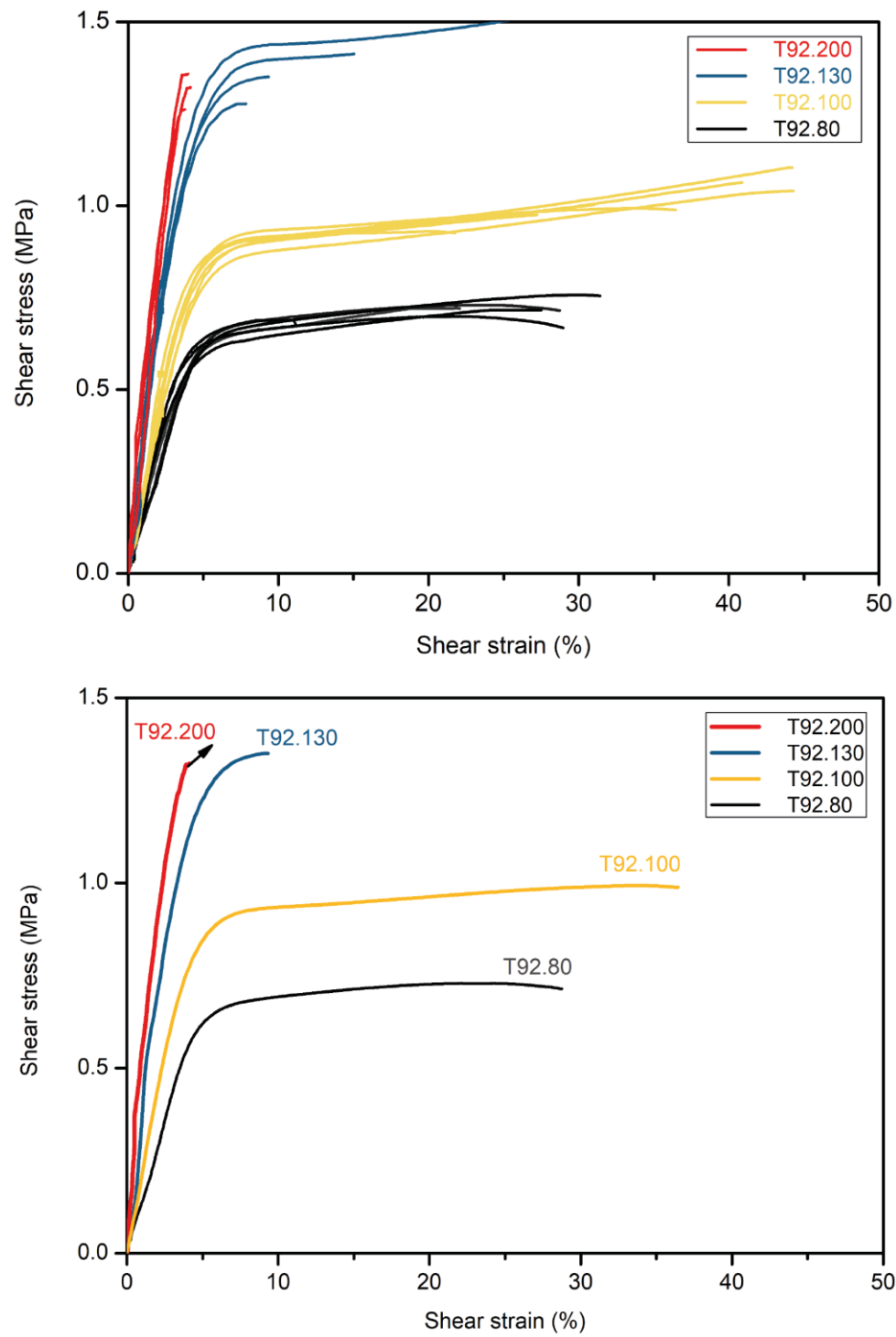


Figure 73 Shear stress-strain curves of strand PET foam T92 at four different nominal densities.

With increasing density, shear modulus and shear strength are increased, though shear strength of the T92.200 sample could not be reported due to experimental challenges. In the T92.200 specimens, the failure mostly began at the interface of the specimen and the steel plates, and it was not possible to obtain a true shear failure through the bulk of the specimen. For this density, more than 25 specimens were tested using three different adhesive compounds. Still, the data reported here could underestimate the true shear strength of this sample. The general reduction of the shear strain at break with increasing foam density is also in agreement with the expectations. However, the scatter in the values of shear strain at break was rather large for all densities and surprisingly, the T92.100 sample shows higher shear strain at break than the T92.80. The reason for this observation was not further investigated. Nevertheless, there could be influences from sample preparation, measurement accuracy, and even correlations to the cell morphology of each foam density.

For a better illustration and comparison, the bottom graph in **Figure 73** shows selected stress-strain curves for each foam density. **Table 7** summarizes the average values of shear properties, namely shear modulus (G), yield stress (τ_y), shear strength (τ_m) and shear strain at break (γ_b). With increasing foam density, all three properties (G , τ_y and τ_m) increase. However, the shear strain at break decreases in higher densities, indicating less ductile behavior.

Table 7 Summary of shear properties of strand PET foam measured by direct foam shear test.

	T92.80	T92.100	T92.130	T92.200
ρ_f / ρ_s [%]	6.81	8.31	10.06	15.62
G [MPa]	15.69 ± 2.06	21.10 ± 0.08	31.45 ± 1.76	40.11 ± 1.16
τ_m [MPa]	0.72 ± 0.02	0.91 ± 0.17	1.41 ± 0.11	-
τ_y [MPa]	0.64 ± 0.02	0.87 ± 0.02	1.31 ± 0.05	-
γ_b [%]	24.98 ± 6.78	35.11 ± 8.11	18.48 ± 10.39	-

5.3.2 Scaling of Shear Properties with Foam Density

Similar to compression properties, the shear properties of PET foam were scaled with the relative foam density using Eq. 1. For normalization, shear modulus of $G_s = 750$ MPa and density

of $\rho_s = 1350 \text{ kg/m}^3$ were considered for the solid PET material. The data for normalized shear modulus versus normalized foam density is shown in **Figure 74**. The linear fit to the data points (the transparent red line) yields a power law exponent value of $n = 1.1$, which is very similar to the value $n = 1.09$ obtained for out-of-plane compression modulus scaling with density.

Furthermore, similar to the observations on the compressive properties, the information shown in **Figure 74** suggests different deformation mechanisms for the lower density samples (T92.80, T92.100 and T92.130) compared to the highest density sample T92.200. As shown with the black arrow, the experimentally measured values of shear modulus for the T92.200 sample is much lower than the prediction based on the three lower density specimens. This indicates that the cell deformation mechanism in shear loading is changed for the T92.200 sample.

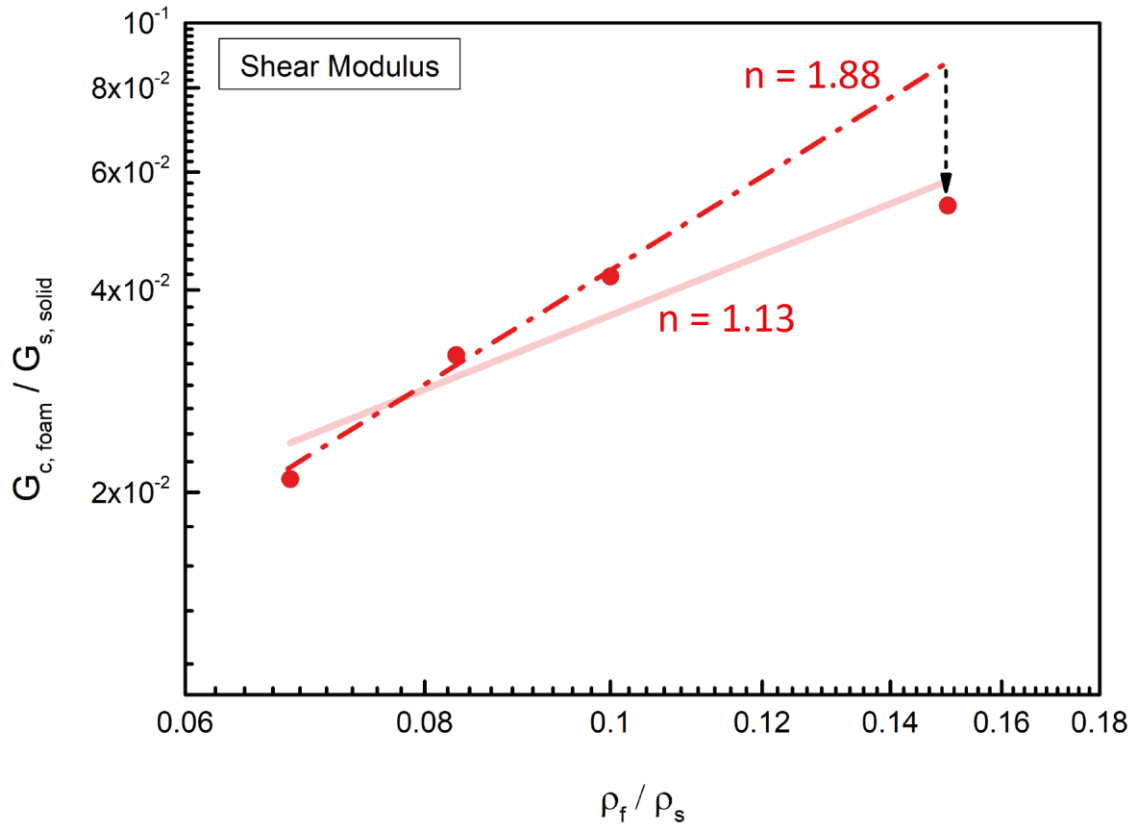


Figure 74 Scaling of relative shear modulus with relative foam density (The dashed red line is a fit to the three data points from low-density foams).

Therefore, it is suggested that the shift in shear deformation mechanism is also correlated to the cell morphology change for the T92.200 sample. However, no further investigations were made to verify this at a microscopic scale.

5.3.3 Local Shear Response

The local shear response of PET foam was studied by means of sandwich bending tests including optical deformation analysis. In an earlier literature work by Xanthos [42], it was shown that sandwich panels with high-density PET foams have bending properties comparable to those of wood panels, plus superior water resistance and good thermal stability. Therefore, as benchmark for strand PET foam, Balsa wood and PVC foams were additionally considered as reference core materials for sandwich specimen preparation. When designed properly, sandwich three-point and four-point bending tests could create a uniform state of shear stress in large sections of the core material. A representative sandwich construction was considered, which is typically used in wind industry. The dimensions chosen for the sandwich beams were also relevant to the target application, which is the shell section of turbine blades (**Figure 75**).

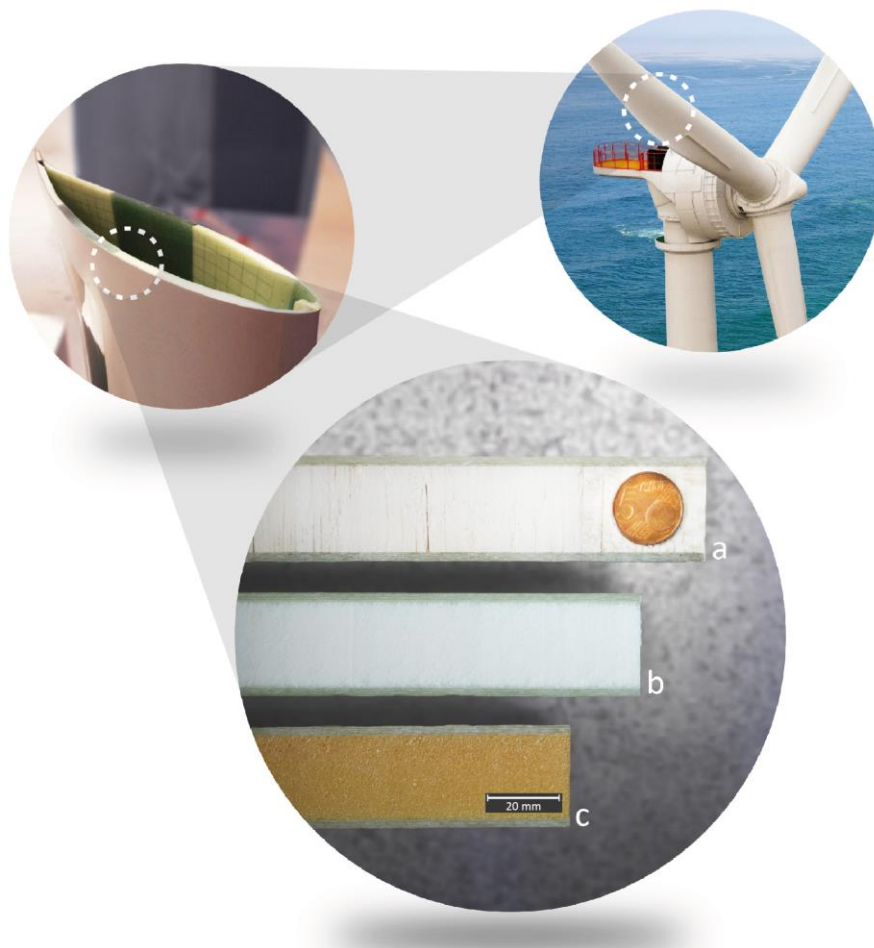


Figure 75 Sandwich structures used in wind industry; a) Balsa core, b) PET foam core, c) PVC foam core.

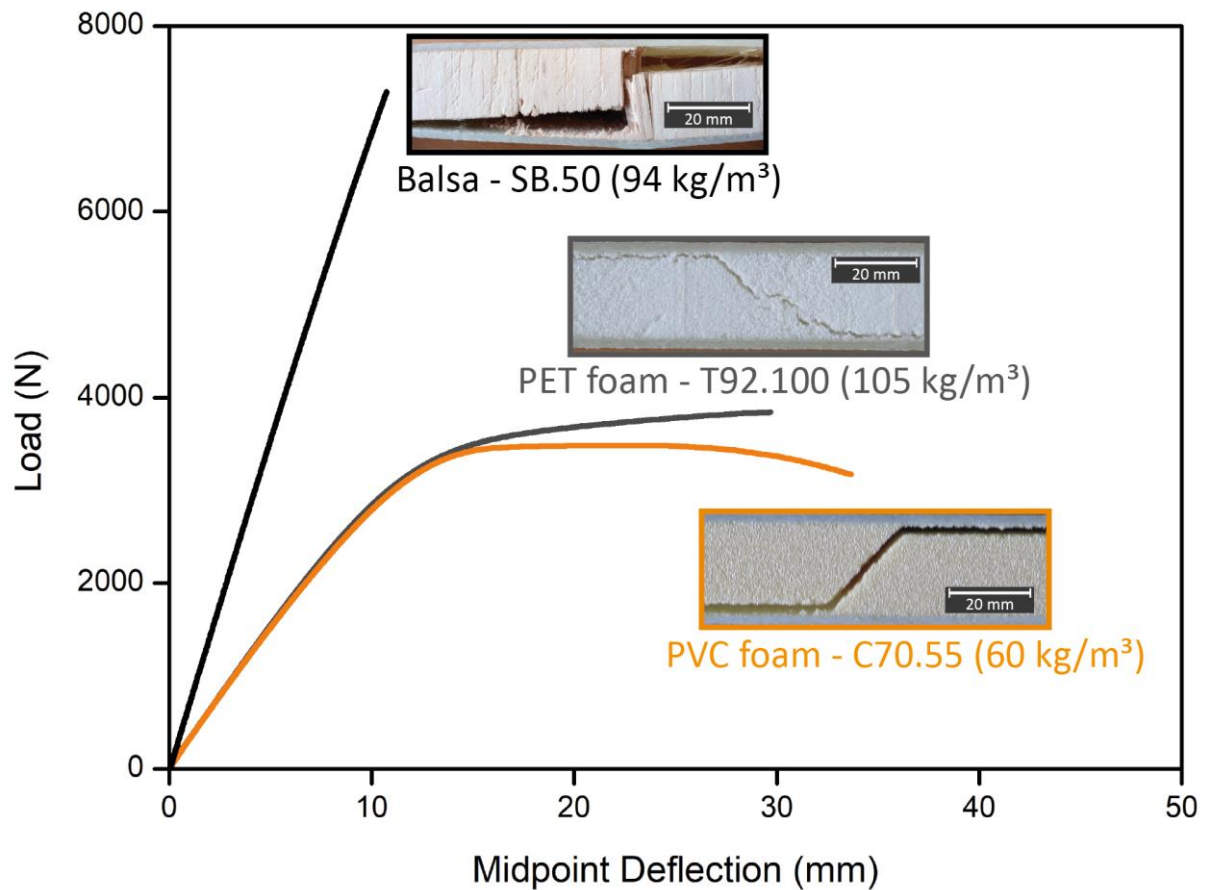
The face sheets were composed of glass fiber reinforced epoxy resin laminates, which provided high stiffness and strength, ensuring that the shear phenomena were mostly controlled by the core materials. Strain values measured by conventional strain gauge technologies may not be comprehensive, as the foam cells could be hindered in motion by the strain gauge. More importantly, a specific local deformation cannot be necessarily representative of the full deformations picture. Therefore, optical deformation analysis was employed to capture the full-field distribution of the shear deformations in the core material. Critical information about the in-service core deformation, such as the initiation of shear failure as well as local core indentation, could be more accurately obtained using such bending tests. These details are completely ignored and irrelevant in block shear tests.

5.3.3.1 Force-Deflection Curves

As explained in chapter 2.5.2, one advantage of sandwich bending tests for studying core shear properties is the possibility to directly measure the core shear strength. If the span lengths are designed to yield core shear failure before other modes, the maximum force at failure can be related to the core shear strength using Eq. 16. In this approach, usually the force-deflection curves are plotted for the sandwich bending tests, and the maximum force values are taken for calculation of the shear strength. **Figure 76** shows force-deflection curves of sandwich specimens measured in four-point bending as well as a summary of the measured properties for different core materials. With the loading and support span lengths of 150 and 500 mm, the shear forces were large enough to yield core shear failure in all specimens. Comparing to Balsa core beams, the foam core specimens have lower sandwich stiffness and core shear strength (comparable to the maximum load values). However, specific shear strength of the three core materials are rather comparable, which is due to the high resin uptake and additional weight of the Balsa core. In addition, the foam cores show more ductility leading to large plastic deformations after core yielding. Therefore, the energy the foam cores absorb until failure is significantly higher than that of Balsa. Both PVC and PET foam core sandwich beams have large and comparable mid-point deflections at failure.

A direct extraction of core shear modulus is not possible in standard sandwich bending tests. Moreover, the contributions of sandwich bending stiffness and shear stiffness to the total beam deflection can not be directly distinguished. Nevertheless, using the analytical method explained in chapter 2.5.2, it was possible to determine the bending stiffness and shear stiffness values of the three sandwich configurations (for comparison, see the values in **Figure 76**). This analytical procedure involves a series of three-point bending tests with varying span lengths and a

following mathematical calculation. Having obtained the analytical values of bending stiffness and shear stiffness, the effective shear moduli of the core materials could be estimated using Eq. 20.



	Sandwich Compliance	Shear Strength	Specific Shear Strength	Bending Stiffness	Shear Stiffness
	[mm/kN]	[MPa]	[Nm/kg]	[Nm ²]	[N]
Balsa	1.44 ± 0.02	1.8 ± 0.12	8410	2302	194013
PET foam	3.22 ± 0.11	0.94 ± 0.05	6145	1474	47566
PVC foam	3.32 ± 0.09	0.84 ± 0.01	8400	1518	50383

Figure 76 Four-point bending load–deflection curves of sandwich beams with Balsa, PET foam, and PVC foam cores and the measured properties [28, 59].

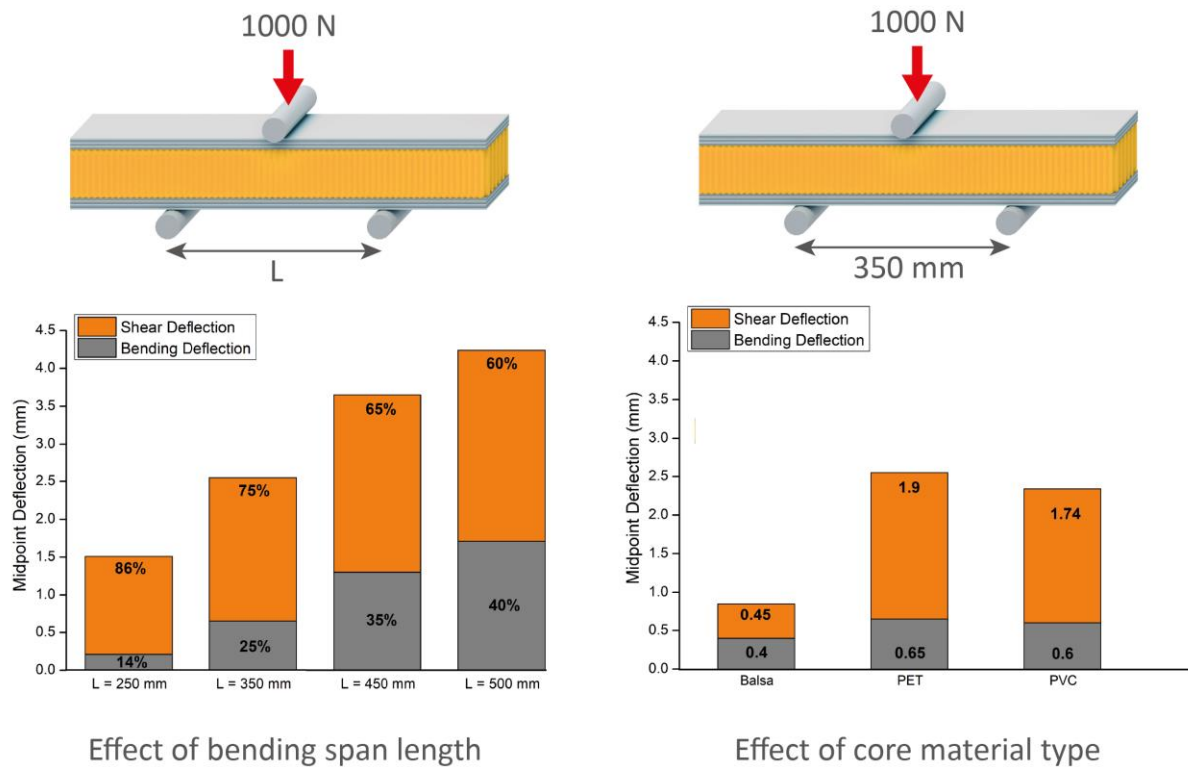


Figure 77 Shear and bending deflection values of sandwich beams with different core materials (right) and different testing span lengths (left).

Another advantage of the discussed analytical method (multiple 3-point bending tests with varying span lengths) is that the contributions of shear deflection and bending deflection can be decoupled using Eq. 18. The left graph in **Figure 77** shows the values of bending and shear deflections for PET foam core sandwich beams loaded at different span lengths (250 to 500 mm) up to 1000 N. Also, the right graph shows the deflection components for sandwich beams with different core materials at a span length of 350 mm and midpoint load of 1000 N. The bar charts in **Figure 77** show the larger effect of span length (L) on the bending deflection compared to shear deflection, which was already predicted by Eq. 18. Moreover, one can notice that the main difference in the deflections of the foam core beams compared to Balsa core beam is due to shear deformations.

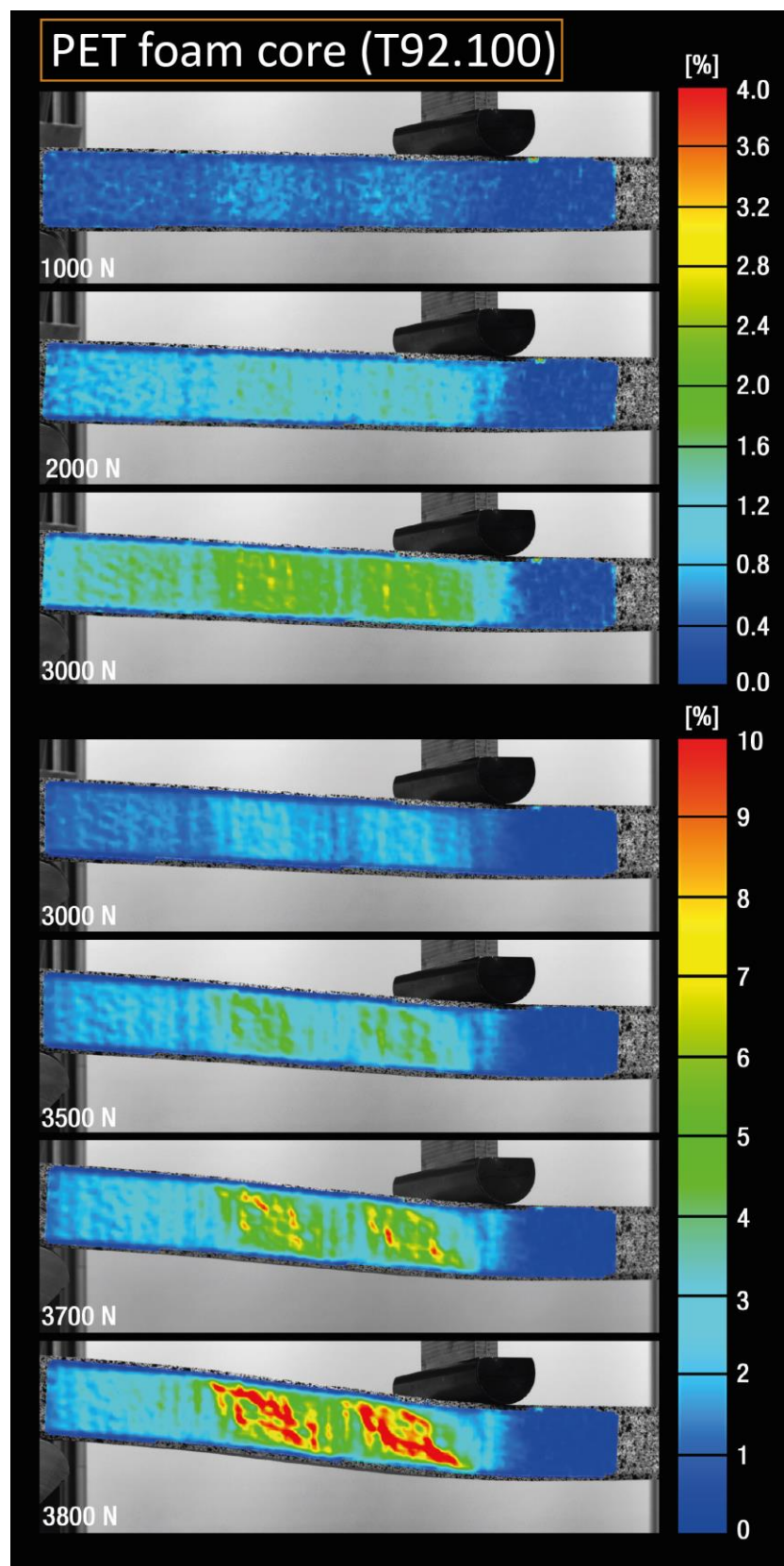
5.3.3.2 Full-Field Shear Deformation Maps

To obtain a broad overview of the shear strain localization and the initiation of core shear failure, optical deformation analysis was performed during four-point bending tests. Due to symmetric loading conditions of the sandwich specimens, optical analysis was done only on the left half of the sandwich beam length, in order to capture more details about the local strain

phenomena. **Figure 36** in chapter 4.5.2 schematically shows the optical analysis equipment and the measurements region chosen on the sandwich beams.

Figures 78 and **Figure 79** show the shear strain distributions on the surface of PET and PVC foam core sandwich beams at different mid-point loading levels. A blue to red color spectrum represents the intensity of the shear strain (in %). Blue colors correspond to little shear strain (for example on the sandwich face sheets), whereas red regions show higher shear strains in one facet. For the purpose of better visualization, the scale of shear strains below load levels of 3000 N is varied between 0 to 4 %, while at higher forces this range is set to 0 to 10 %. In four-point bending, shear stresses can be assumed constant between the loading and the support points (see transverse force diagram, T_x , in **Figure 22** in chapter 2.5.2). As a result, foam cores show a rather uniform shear deformation, especially in the elastic region. This homogeneous shear deformation can be seen in **Figures 78** and **Figure 79** as even color distributions throughout the foam cores.

Since foams undergo large deformations, plastic strains are generally high and more localized after yielding. In case of PET foam core in **Figure 78**, permanent shear strains are initiated from the mid-core region, which theoretically bear the highest shear stresses. On the contrary, in the PVC foam core in **Figure 79**, shear strains seem to be generally higher on one side of the beam (see the snapshot of 3000N), and critical strains are first developed under the loading points and apparently begin growing from the interface regions. This pattern in shear failure initiation has been previously seen and reported by others too [135, 144]. Higher shear strains on one side of the PVC foam core may correspond to density and morphology variations through the foam panel thickness. In particular, the foam density may slightly vary near the foam panel surface. This variation is probably a result of the processing technique of the PVC foam. Foam expansion in the mold can sometimes results in a variation of cell morphology through the thickness of the foam, especially near the mold surface. In the work of Kaya [18] on the same PVC foam grade, a slight difference was observed in the foam density and cell size of samples taken from areas near the top and bottom surfaces of the panel. This is shown in **Figure 81**, which is reproduced from the work of Kaya [18]. Hence, the resin uptake on the two sides of the core were different, resulting in different interface toughness and peel strengths. It seems that here, too, a possibly different foam density and cell structures has caused slightly different shear deformation magnitudes on the top and bottom sides of the PVC foam core.

**Figure 78**

Distribution of shear strains on the surface of the PET foam core sandwich beam, loaded in four-point bending at different mid-point loads.

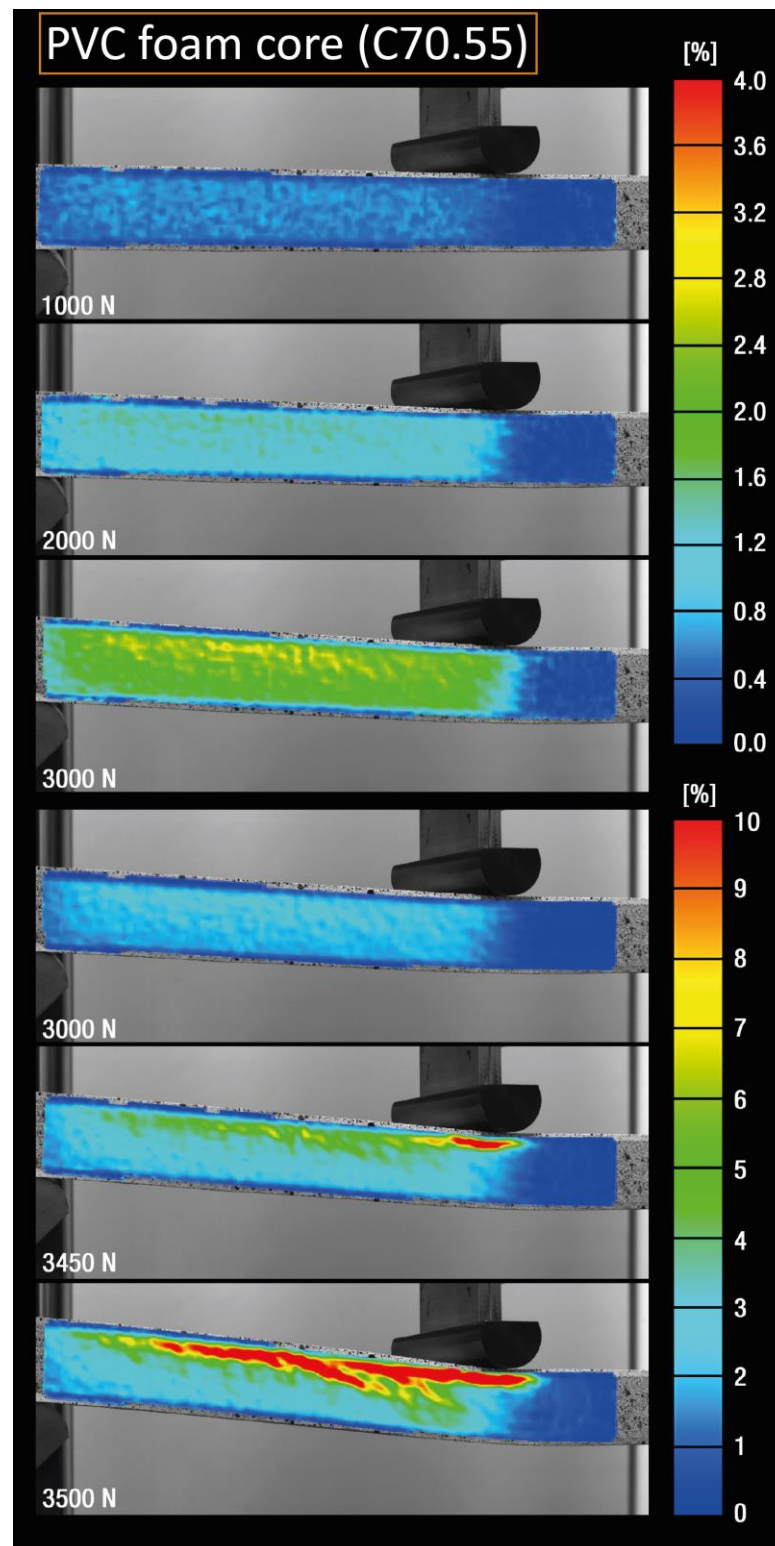


Figure 79 Distribution of shear strains on the surface of the PVC foam core sandwich beam, loaded in four-point bending at different mid-point loads.

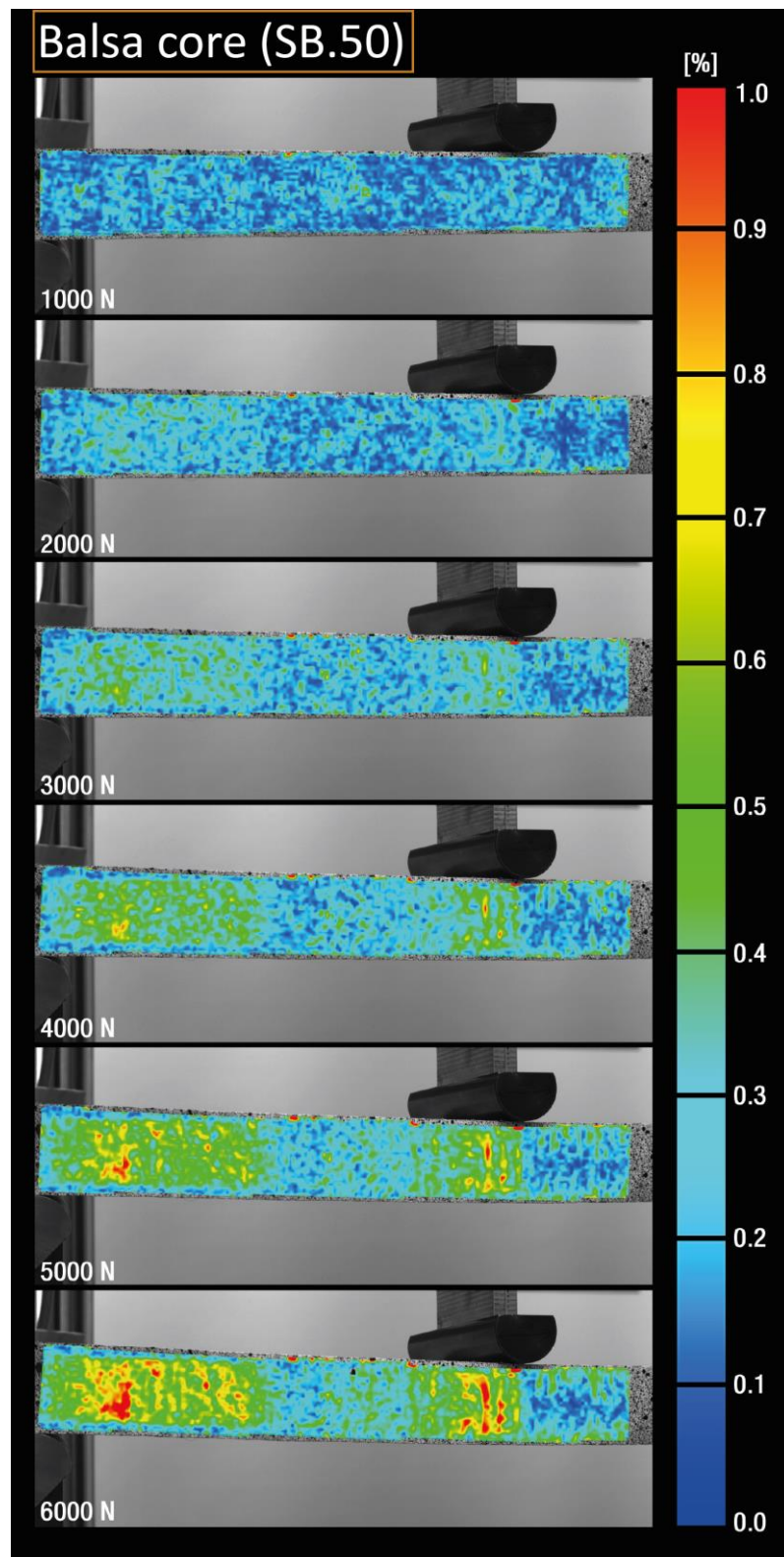


Figure 80 Distribution of shear strains on the surface of the Balsa core sandwich beam, loaded in four-point bending at different mid-point loads.

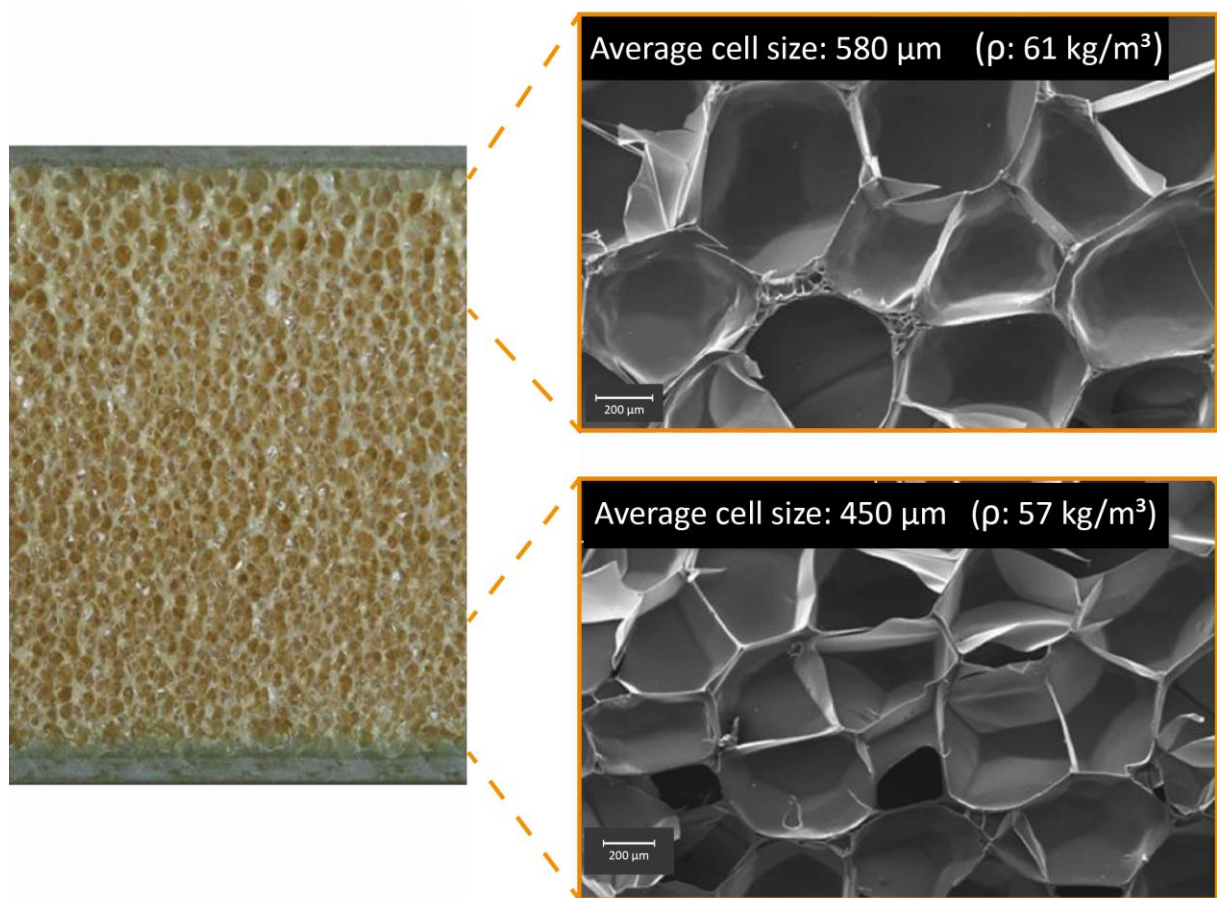


Figure 81 Different cell sizes and foam densities near the two sides of a PVC foam core panel (reproduced from the work of Kaya [18]).

The distinct shear strain patterns in PET and PVC foam cores could be due to different reasons. The high out-of-plane stiffness of the PET core may prevent stress concentrations at the load introduction points and drive the initiation of shear cracks from the mid-core regions. Nevertheless, the microstructures of the surface cells, and consequently different resin uptakes and interface toughness values can also affect the failure behavior of the foam cores [18]. There has long been discussion on the initiation of core shear failure in foam core sandwich structures. Gibson [177], for instance, nicely showed that for a PMI foam core, stiffer face sheets minimize stress concentrations in the core at the loading points and eventually cause the initial cracks to begin at the mid-core region; whereas less stiff face sheets lead to core shear cracks initiating near the loading points (see **Figure 82**). The same concept could be true in case of foam core sandwich systems studied here. The PET foam is an extruded thermoplastic with higher out-of-plane stiffness compared to the PVC foam. Therefore, despite their identical face sheets, stress concentrations under the loading points are apparently more severe in the PVC foam than the

PET foam. This could highly contribute to the different shear failure patterns in the two core materials.

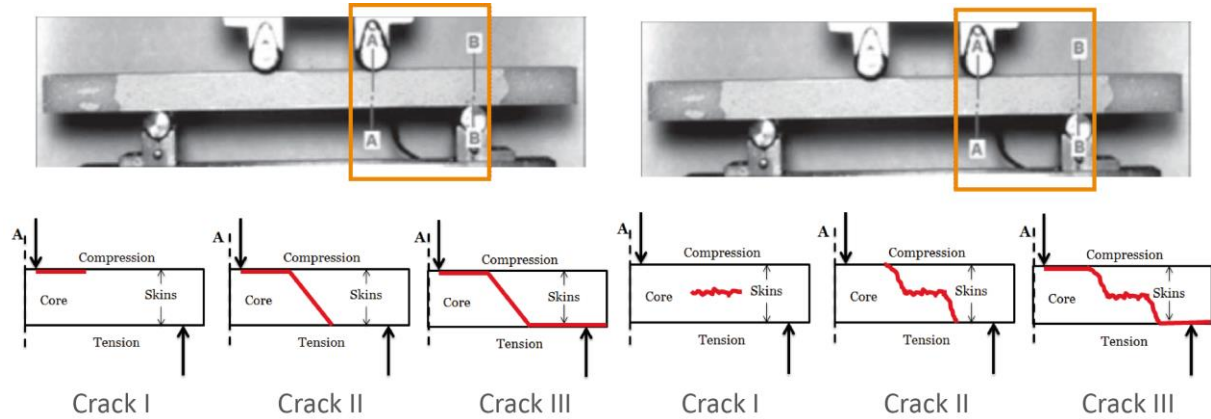


Figure 82 Initiation of core shear cracks in sandwich beams with PMI foam cores. Left: glass fiber reinforced epoxy face sheet, right: carbon fiber reinforced epoxy face sheets (reproduced from reference [177]).

Figure 80, on the other hand, shows the shear strain distribution in a Balsa core sandwich specimen at various loading levels. Since Balsa shows relatively small deformations, the colored shear strain scale is varied between 0 to 1 %. Unlike the foam cores, a large scatter is observed in the local shear strains of Balsa wood. Some parts of the core retain almost no shear deformation throughout the test, even at the vicinity of failure. As the load increases, smaller regions in the core are deformed significantly more. Core failure in Balsa initiated from these regions, which were rather difficult to predict, as reported by other authors too [25, 160, 177].

5.3.3.3 Optically-Determined Shear Stress-Strain Curves

Controllers of both the testing machine and the optical equipment were linked using an analogue signal in order to synchronize the shear strains and the force levels of each recorded image. Force levels were then converted to core shear stresses using Eq. 16. Thus, for each core material, in-situ shear stress-strain curves could be constructed from four-point bending tests. Such in-situ curves could be better alternatives to those obtained by direct foam shear testing, since they are created from more representative loading conditions of the whole sandwich assembly. In addition, measuring core shear properties via sandwich testing is usually free from stress concentrations effects, as opposed to direct shear tests [140].

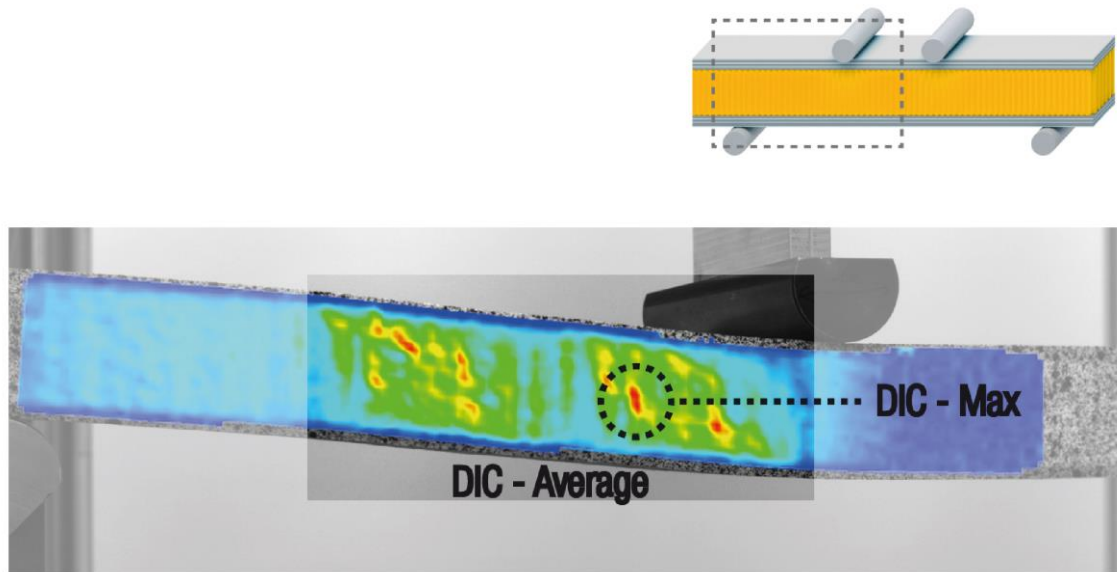


Figure 83 Average shear strain (DIC-Average) is calculated over a large area of the sample surface. Maximum shear strain (DIC-Maximum) is taken from a local facet where the highest strain is reported at the end of the experiment.

Similar to the compressive stress-strain curves showed in chapter 5.2.2, for each core material two sets of optically determined shear stress-strain curves are constructed. Here too, one curve represents average shear strain values of all facets taken from a relatively large section of the core surface, and the other curve is constructed using strain values from a local region with the highest deformation, as schematically shown in **Figure 83**.

Figure 84 shows shear stress-strain curves of the PET foam (top) and PVC foam (bottom). The average and maximum DIC curves of the foam cores lie almost on each other in the elastic region, suggesting that foam cores have rather uniform shear deformations before yielding. In the Balsa core (**Figure 85**), in contrast, the two curves deviate from early stages of the loading, indicating large local variation of elastic strains. The scaling of both axes in Balsa curves is different to those of foam cores in order to show more details. Since yielding is a local phenomenon, local strains become significantly higher and therefore maximum and average strain curves of the foam cores start deviating after yielding. Another interesting observation is the difference in the maximum and average strains at failure for the two foam cores. The PVC foam shows a significantly high local deformation and failure patterns. Therefore, at the vicinity of failure, shear strains on large regions of the core (comparable to strain values in DIC-Average) are significantly lower than the maximum local shear strain under the load introduction points. The PET foam core has a more uniform yielding, which results in comparable values of average and maximum shear strain at failure.

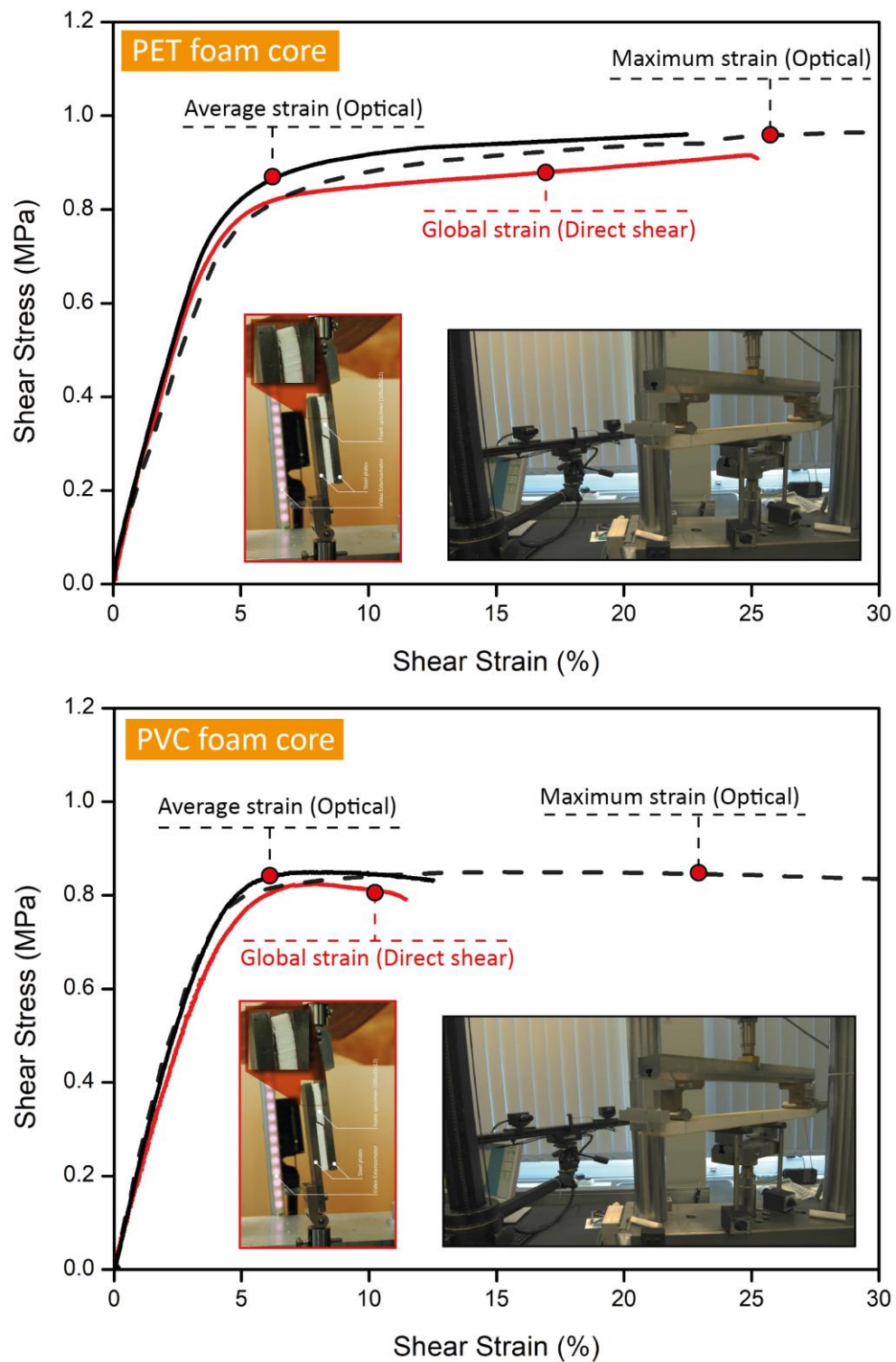


Figure 84 Shear stress-strain curves of PET and PVC foam cores measured by direct foam shear test (red) and four-point bending coupled with optical analysis (black).

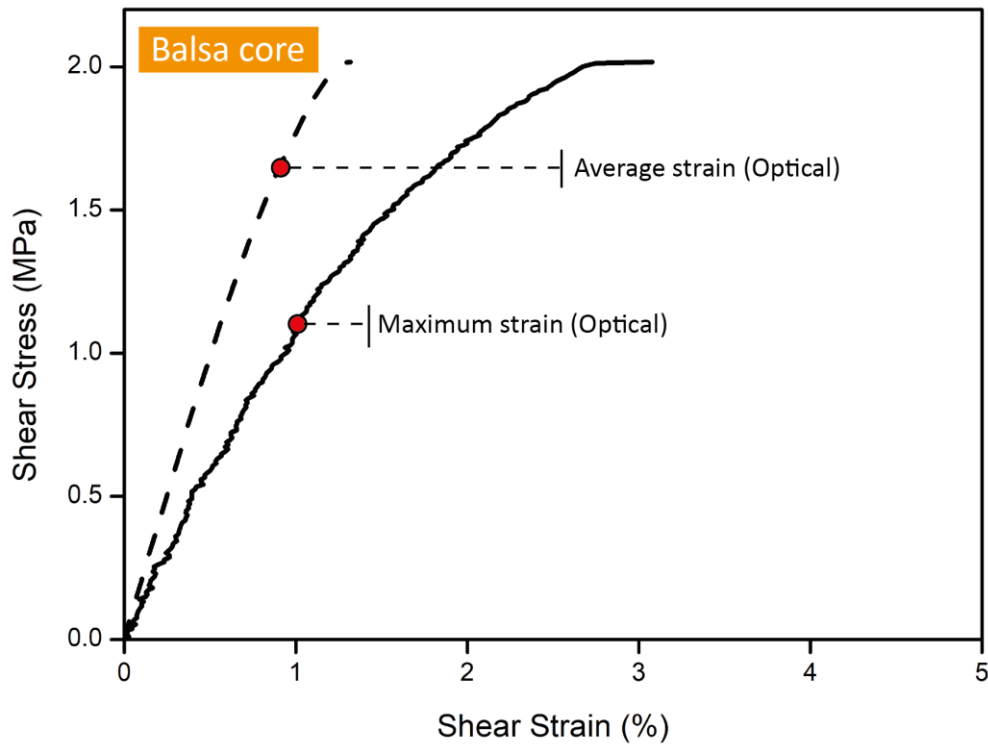


Figure 85 Shear stress-strain curves of Balsa core measured by four-point bending coupled with optical analysis.

Similarly, the optically-determined shear stress-strain curves of the Balsa core are shown in **Figure 85**. The magnitude of shear strain is much smaller than the foam cores, and the deviation between average and maximum strain curves is quite large, even in the linear region. This is a manifestation of the large variation of density and properties in wood. Despite its high shear strength and modulus, the variation in property profiles could influence the reliability of wood in some applications, in particular when involving cyclic loading.

For comparison purposes, in **Figures 84**, the global shear stress-strain curves of the foam cores are also shown in red, which are measured by direct shear testing. The measured values of shear strength and shear modulus agree fairly well in both methods (see the exact values in **Table 8**). Furthermore, the direct shear method is unable to capture a full picture of core deformation. For example, the strain at break of the PVC foam is significantly underestimated with the direct test method. This is because the actual shear strain in some regions of the core could be much higher than the values calculated from relative displacement of the testing plates. Using the stress-strain data of the core materials, their shear moduli were calculated.

Table 8 shows a comparison between shear modulus and shear strength values of all core materials, obtained by different experimental and analytical methods. Since the stiffness values have been estimated using a curve fitting procedure, no standard deviation could be reported. In Eq. 20, the influence of face sheets on shear stiffness is neglected and therefore, the analytically determined shear moduli for foam cores could be over estimated.

Table 8 Shear properties of different core materials measured by diverse experimental and analytical methods.

Core Shear Modulus [MPa]				
	Direct Shear	Optical (Bending)	Analytical (Bending)	Material Datasheet
Balsa core	-	110	103.5	106
PET foam core	21.1 ± 0.08	20	25.4	21
PVC foam core	23.2 ± 0.05	21.5	26.9	22

Core Shear Strength [MPa]			
	Direct Shear	Bending	Material Datasheet
Balsa core	-	1.8 ± 0.12	1.8
PET foam core	0.91 ± 0.17	0.94 ± 0.05	0.9
PVC foam core	0.82 ± 0.11	0.84 ± 0.01	0.85

In this chapter, the shear properties of strand PET foams were studied from different approaches. At first, the global shear properties of different density foams were determined using direct shear test. The density scaling relations in shear were then determined and compared to the compressive response. Similar to compressive loading, the shear properties of the highest density sample (T92.200) was also below the model predictions. This was correlated to the cell morphology of this grade and the strong reduction in cell orientation. Furthermore, the local shear behavior of PET foam was investigated in the scope of sandwich bending tests. Results showed a more uniform and homogeneous shear strain in the PET foam core compared

to both PVC foam core and Balsa core. The uniform local deformation can be attributed to a more homogeneous foam morphology, as a result of a stable foam extrusion process. In contrast, the local deformations in PVC foam core (block expansion) and Balsa core (natural structure) were irregular, probably due to larger variation of local density and property profiles.

Last but not least, the shear properties of all three core materials were reported for different measurement approaches. The results converged rather well and agreed with the theoretical boundary conditions known from literature.

6 Summary

In the present thesis, the multi-scale morphology and the mechanical properties of strand PET foams were investigated. The links between different scale deformation phenomena and the resulting macroscopic mechanical properties were fundamentally established. Strand PET foams are made of packed arrays of hexagonal prisms, which are aligned parallel to the foam panel thickness. The strands have different and distinct foam cell types (shapes) as well as different densities in their surface regions compared to their bulk. The strand border regions (interface zones of hexagonal prisms) have higher density as well as elongated foam cells with thicker cell walls and struts. The relations between density, cell morphology, and the mechanical anisotropy of these strand foams were presented and discussed. For the commercial grade PET foam studied in this thesis (AIREX T92), the patented foam extrusion technique has been optimized concerning materials, process parameters, and particularly the die technology [21]. The hexagonal shape of the breaker plate holes (and consequently the foam strands) ensures the most suitable packing and flawless foam morphology with minimum defects and inter-strand voids. The findings showed that strand PET foams have morphological and mechanical similarities to wood and honeycombs. The out-of-plane compressive response is distinct and fundamentally different to the in-plane response. This is because out-of-plane loading is mostly governed by axial deformation of the cell walls in the elongated interlocked foam cells between the strands. In contrast, in-plane loading is controlled by – the conventionally known - bending of the cell walls and struts. It was later shown that the two distinct cell deformation mechanisms in the out-of-plane and in-plane loading directions (axial deformation versus cell wall bending) have direct correlations to the density-property scaling laws. In other words, in the out-of-plane loading, strand PET foams behave as stretch-dominated cellular structures, whereas in the in-plane loading their response is more bending-dominated. This hypothesis was fully verified by in-situ SEM measurements of the cell level deformation. Furthermore, it was demonstrated that the cell deformation mechanism may change depending on the foam density and the resulting specific cell morphology. The shift observed in the deformation mechanism at higher foam densities was linked to the change in cell shape from elongated to regular polyhedron shapes.

Findings of this thesis showed that the process-induced cell morphology has immense effects on the anisotropy and the mechanical response of strand foams. The cell morphology-properties correlations showed here can be used to optimize the foam properties for different applications. The foaming process allows for new degrees of freedom to the designer [2]. Therefore, stiffness and strength as well as the degree of anisotropy can be controlled over a wide range of foam

densities. But even moving one step ahead, local variations or gradients of foam density, cell morphology and property profiles can be also designed-in [2]. The foaming process parameters can strongly affect the cell morphology (see results in chapter 5.1). With new and improved foam processing methods and engineering equipment, combined with the increasing insight into and control over the physics of foaming (e.g. enabled by numerical simulations), new generations of advanced foams with locally architected density, morphology and mechanical responses will be emerging in the near future.

7 Outlook and Future Work

As a possible future work, findings of this thesis can be used to design local foam density and cell morphology variations to enable and optimize the desired global and local mechanical properties in different loading directions. For strand foams, a relatively small volumetric fraction of elongated border cells can increase the mechanical properties in the cell length direction up to 3 folds. This highlights a great potential for tuning the cell morphology to obtain properties for specific applications. The potential for designing anisotropy into foams and exploiting it in different applications is enormous and at present incompletely realised [2, 25]. Beside foam extrusion, other processing methods such as foam injection molding can be also applied to create cell orientation. Another recent manufacturing method is 3D printing of parts made of polymers, metals and ceramics, which offer huge flexibility for creating complex cellular materials. This has revolutionized the product design in many applications, one recent example being sports shoes. The midsole section can be made of 3D printed lattices with pre-designed structural features. Therefore, locally tuning the mechanical properties, for example through adjustment of the local cell deformation mechanisms, is possible and shoes made to fit individual consumer needs could be soon available. The correlations shown in this thesis can help better understand how the local properties can be tuned in foams and lattices by means of morphology variation. With further development of additive manufacturing technologies, similar fundamental rules can be applied to architecture the lattice morphology in terms of cell shape, orientation, degree of nodal connectivity, and strut slenderness.

Another future work can be developing experimental based multi-scale models, where a precise definition of the fraction of solid in the cell walls and struts is taken into account [16]. The detailed quantitative morphological data presented here can inspire and verify numerical constitutive models, which are capable of correctly predicting the mechanical response of strand foams under different loading cases [14, 25, 131]. There are models proposed in the literature [86], which can take into consideration the morphological anisotropy. These models can be calibrated with the presented data here. Another approach would be creating accurate and realistic Representative Volume Elements (RVE) of the foam structure for multi-scale FEM models. Fed with critical morphological information, these numerical models would be capable of predicting the post-yielding behavior of the foams too, as this is more controlled by lower scale deformation behavior at cell level. The models can be then calibrated (similar to work of Zenkert [178]) using the mechanical data shown and discussed at different length scales in chapters 5.2 and 5.3.

8 References

1. Fleck NA (2004) An overview of the mechanical properties of foams and periodic lattice materials. *Cell Met Polym*
2. Jones DRH, Ashby MF (2005) *Engineering Materials 2: An Introduction to Microstructures, Processing and Design*, 3rd ed. Elsevier
3. Bilkhu SS, Founas M, Nusholtz GS (1993) Material modeling of structural foams in Finite Element Analysis using compressive uniaxial and triaxial data
4. Gioux G, McCormack TM, Gibson LJ (2000) Failure of aluminum foams under multiaxial loads. *Int J Mech Sci* 42:1097–1117
5. Maji AK, Schreyer HL, Donald S, Zuo Q (1995) Mechanical properties of polyurethane-foam impact limiters. *J Eng Mech* 121:528–540
6. Schreyer L, Zuo K, Maji AK (1994) Anisotropic plasticity model for foams and honeycombs
7. Neilsen MK, Krieg RD, Schreyer HL (1995) A constitutive theory for rigid polyurethane foam. *Polym Eng Sci* 35:387–394
8. Ramon O, Mizrahi S, Miltz J (1990) Mechanical properties and behavior of open cell foams used as cushioning materials. *Polym Eng Sci* 30:197–201
9. Sherwood JA, Frost CC (1992) Constitutive modeling and simulation of energy absorbing polyurethane foam under impact loading. *Polym Eng Sci* 32:1138–1146
10. Li QM, Mines R a. W (2008) Strain measures for rigid crushable foam in uniaxial compression. *Strain* 38:132–140
11. Ashby MF, Medalist RFM (1983) The mechanical properties of cellular solids. *Metall Trans A* 14:1755–1769
12. Ashby MF (2006) The properties of foams and lattices. *Philos Trans R Soc A Math Phys Eng Sci* 364:15 LP-30
13. Zenkert D, Burman M (2009) Tension, compression and shear fatigue of a closed cell polymer foam. *Compos Sci Technol* 69:785–792
14. Arezoo S, Tagarielli VL, Petrinic N, Reed JM (2011) The mechanical response of Rohacell foams at different length scales. *J. Mater. Sci.* 46:6863–6870
15. Shulmeister V (1998) Ph.D. Thesis: Modelling of the mechanical properties of low-density foams. Technische Universiteit Delft
16. Mills NJ (2011) Modeling the dynamic crushing of closed-cell polyethylene and polystyrene foams. *J Cell Plast* 47:173–197

17. Poapongsakorn P, Kanchanomai C (2012) Effects of time and stress state on fracture of closed-cell polyvinyl chloride foam. *J Sandw Struct Mater* 14:557–571
18. Kaya B (2013) Master Thesis: Investigation of the skin–core interface in glass fibre reinforced sandwich materials. University of Bayreuth
19. Heinz M (2010) Einfluss der Probengeometrie auf die mechanischen Eigenschaften von Polymerschäumen. University of Bayreuth
20. Jebur QH, Harrison P, Guo ZY, et al (2011) Characterisation and modelling of a melt-extruded LDPE closed cell foam. *Appl Mech Mater* 70:105–110
21. Weber H, De Grave I, Röhl E, Altstädt V (2016) Foamed Plastics. In: Ullmann's Encyclopedia of Industrial Chemistry. pp 1–54
22. (2009) Alcan Composites - Introduction to cores
23. Randall D, Lee S (2002) *The Polyurethanes Book*. Wiley, New York
24. Friedrich K, Breuer U, Altstädt V, Fathi A (2015) *Multifunctionality of Polymer Composites*. Elsevier
25. Gibson LJ, Ashby MF (1997) *Cellular Solids: Structure and Properties*, 2nd ed. Cambridge University Press, Cambridge, UK
26. Gdoutos E. E, Daniel I. M, Wang K-. (2002) Failure of cellular foams under multiaxial loading. *Compos Part A Appl Sci Manuf* 33:163–176
27. Zenkert D (1995) *An introduction to sandwich construction*. EMAS Ltd, Solihull, UK
28. Fathi A, Wolff-Fabris F, Altstädt V, Gätzi R (2013) An Investigation on the Flexural Properties of Balsa and Polymer Foam Core Sandwich Structures: Influence of Core Type and Contour Finishing Options. *J Sandw Struct Mater*. doi: 10.1177/1099636213487004
29. Khemani KC (1997) *Polymeric Foams Science and Technology*. American Chemical Society, Washington
30. Feichtinger K, Ma W, Touzot T (2013) Novel Thermoplastic Foam Structural Core Material with Enhanced Thermoformability, Fatigue Endurance and Elevated Temperature Properties
31. Japon S, Leterrier Y, Manson J-AE (2000) Recycling of poly(ethylene terephthalate) into closed-cell foams. *Polym Eng Sci* 40:1942–1952
32. Koenig J-F, Tusim MH (2004) Developments in StrandFoam Technology. In: *Blowing Agents and Foaming Processes*. Hamburg, Germany, pp 147–156
33. Park CP, Garcia GA (2000) Development of Polypropylene Plank Foam Products. In: *ANTEC 2000 - Proceedings of the 58th Annual Technical Conference & Exhibition*. pp 1876–1880

-
34. Malone BA (1988) Coalesced polyolefin foam having exceptional cushioning properties
 35. Yao PC, Malone BA (1988) Highly loaded coalesced foam
 36. Soares B, Reis L, Silva A (2008) Proceedings. In: 8th International Conference on Sandwich Structures. Porto
 37. Throne JL (2004) Thermoplastic Foam Extrusion: An Introduction. Hnahr Fachbuch
 38. Quintans J, Xanthos M, Dey SK, Yilmazer U (2000) Melt viscoelasticity of polyethylene terephthalate resins for low density extrusion foaming. *Polym Eng Sci* 40:554–566
 39. Köppl T, Raps D, Altstädt V (2014) E-PBT—Bead foaming of poly(butylene terephthalate) by underwater pelletizing. *J Cell Plast*. doi: 10.1177/0021955X14528524
 40. Nofar M, Park CB (2014) Poly (lactic acid) foaming. *Prog Polym Sci* 39:1721–1741
 41. Coccorullo I (2009) Theoretical and experimental study of foaming process with chain extended recycled PET. *eXPRESS Polym. Lett.* 3:84–96
 42. Xanthos M, Dhavalikar R, Tan V, et al (2001) Properties and applications of sandwich panels based on PET foams. *J Reinf Plast Compos* 20:786–793
 43. Guan R, Wang B, Lu D (2003) Preparation of microcellular poly(ethylene terephthalate) and its properties. *J Appl Polym Sci* 88:1956–1962
 44. Xanthos M, Dey SK, Zhang Q, Quintans J (2000) Parameters affecting extrusion foaming of PET by gas injection. *J Cell Plast* 36:102–111
 45. Baldwin DF, Park CB, Suh NP (1996) A microcellular processing study of poly(ethylene terephthalate) in the amorphous and semicrystalline states. Part II: Cell growth and process design. *Polym Eng Sci* 36:1446–1453
 46. Han X, Shen J, Huang H, et al (2007) CO₂ foaming based on polystyrene/poly(methyl methacrylate) blend and nanoclay. *Polym Eng Sci* 47:103–111
 47. Champagne MF, Gendron R, Huneault MA (2003) Branched Polyethylene Terephthalate Foaming Using HFC-134a: On-Line Process Monitoring. *Soc Plast Eng ANTEC*
 48. Park CP, Garcia GA, Watson RG (2002) Expandable Foam From Amorphous Polyester Resin. *Soc Plast Eng ANTEC*
 49. Borer C, Naef UG, Culbert BA, Innerebner F (1990) DE 19800166 A1
 50. Smith HV, Trevitt EW (1992) EP0475142 A2
 51. Hirai T, Ishiwatari S, Shindo M, et al (2003) EP0719626 B1
 52. Ghatta HAK Al, Severini T, Astarita L (1995) US5422381 A
 53. McConnell RL, Khemani KC (1996) US 5482977 A

-
54. Rüger H, Gisler M, Villiger L, Münger C (2009) WO 2009149845 A1
 55. Grinshpun S (2001) Development of hollow strand plastic foam. Soc Plast Eng ANTEC
 56. Ohsol EO (1968) US3413387 A
 57. Meller M, Li J, Dolega J (2013) EP2671911 A1. 1:1–11
 58. Herranen H, Eerme M, Majak J, et al (2012) Design and testing of sandwich structures with different core materials. *Mater Sci* 18:
 59. Fathi A, Keller J-H, Altstaedt V (2015) Full-field shear analyses of sandwich core materials using Digital Image Correlation (DIC). *Compos Part B Eng* 70:156–166
 60. Liang M-T, Wang C-M (2000) Production of engineering plastics foams by supercritical CO₂. *Ind Eng Chem Res* 39:4622–4626
 61. Zingsheim P W. Becker, D. Braun (eds.): *Kunststoff Handbuch*, vol. 2/2. Carl Hanser Verlag, pp 977 –1000
 62. Thomas T, Mahfuz H, Carlsson LA, et al (2002) Dynamic compression of cellular cores: temperature and strain rate effects. *Compos Struct* 58:505–512
 63. Thomas T, Mahfuz H, Kanny K, Jeelani S (2004) High strain rate response of cross-linked and linear PVC cores. *J Reinf Plast Compos* 23:739–749
 64. Saha MC, Mahfuz H, Chakravarty UK, et al (2005) Effect of density, microstructure, and strain rate on compression behavior of polymeric foams. *Mater Sci Eng A* 406:328–336
 65. Shi A, Zhang G, Zhao C (2012) Study of rigid cross-linked PVC foams with heat resistance. *Molecules* 17:14858–14869
 66. Burman M, Zenkert D (1997) Fatigue of foam core sandwich beams—1: undamaged specimens. *Int J Fatigue* 19:551–561
 67. Arezoo S, Tagarielli VL, Siviour CR, Petrinic N (2013) Compressive deformation of Rohacell foams: Effects of strain rate and temperature. *Int J Impact Eng* 51:
 68. Zenkert D, Shipsha a., Burman M (2006) Fatigue of Closed Cell Foams. *J Sandw Struct Mater* 8:517–538
 69. Zenkert D, Burman M (2011) Failure mode shifts during constant amplitude fatigue loading of GFRP/foam core sandwich beams. *Int J Fatigue* 33:217–222
 70. Scherble J, Geyer W, Seibert H, et al (2014) Thermostable microporous polymethacrylimide foams, US8722751 B2
 71. ROHACELL® Triple F - High-performance structural foam cores.
<http://www.rohacell.com/product/rohacell/en/products-services/rohacell-triple-f/pages/default.aspx>. Accessed 2 Dec 2015

-
72. Krebs M, Hubel R (2016) The adjustment of physical properties of viscoelastic foam - The role of different raw materials. *Am Chem Counc*
 73. Gibson LJ, Ashby MF, Schajer GS, Robertson CI (1982) The mechanics of two-dimensional cellular materials. *Proc R Soc Lond A* 382:25
 74. Patel MR, Finnie I (1970) Structural features and mechanical properties of rigid cellular plastics. *J Mater* 5:909
 75. UBE-Industries (1982) JP-Kokai 57 000 144
 76. Ko WL (1965) Deformations of Foamed Elastomers. *J Cell Plast* 1:45
 77. Menges G, Knipschild F (1975) Estimation of mechanical properties for rigid polyurethane foams. *Polym Eng Sci* 15:623
 78. Menges G, Knipschild F (1982) Stiffness and strength - Rigid plastic foams. In: *Mechanics of Cellular Plastics*, N. C. Hily. Applied Science Publ., New York, pp 27–72
 79. Gibson LJ, Ashby MF (1982) The mechanics of three-dimensional cellular materials. *Proc R Soc Lond A* 382:43
 80. Branner K (1995) Capacity and lifetime of foam core sandwich structures. Technical University of Denmark
 81. Maquet V, Martin D, Malgrange B, et al (2000) Peripheral nerve regeneration using bioresorbable macroporous polylactide scaffolds. *J Biomed Mater Res* 52:639–51
 82. Baumann H (1981) DE3108279A1 - Verfahren zur herstellung von modifizierten aminoplast-harzprodukten
 83. Alonso JR Sandwich Panels using recycled thermoplastics
 84. Alfter FW (1978) No Title. *Plastverarbeiter* 29:129–132
 85. Rusch KC (1970) Load-compression behavior of brittle foams. *J Appl Polym Sci* 14:1263–1276
 86. Huber AT, Gibson LJ (1988) Anisotropy of foams. *J Mater Sci* 23:3031–3040
 87. Mills NJJ, Stämpfli R, Marone F, Brühwiler P a. (2009) Finite element micromechanics model of impact compression of closed-cell polymer foams. *Int J Solids Struct* 46:677–697
 88. Dementjev AG, Tarakanov OG Influence of the Cellular Structure of Foams on their Mechanical Properties (in Russian). *Mech Polym* 4:594
 89. Åkermo M, Tomas Åström B (1998) Modelling face-core bonding in sandwich manufacturing: Thermoplastic faces and rigid closed-cell foam core. *Compos Part A Appl Sci Manuf* 29:485–494
 90. Lakes R, Rosakis P, Ruina A (1993) Microbuckling instability in elastomeric cellular solids.

- J Mater Sci 28:4667–4672
91. Jin JF, Chen YL, De Wang N, et al (2002) Structures and physical properties of rigid polyurethane foam prepared with rosin-based polyol. *J Appl Polym Sci* 84:598–604
 92. Zhu HX, Knott JF, Mills NJ (1997) Analysis of the elastic properties of open-cell foams with tetrakaidecahedral cells. *J Mech Phys Solids* 45:319–343
 93. Subramanian N, Sankar B V. (2012) Evaluation of micromechanical methods to determine stiffness and strength properties of foams. *J Sandw Struct Mater* 14:431–447
 94. Pierron F (2010) Mechanical properties of low density polymeric foams obtained from full-field measurements. *EPJ Web Conf* 6:
 95. Pierron F (2010) Identification of Poisson's ratios of standard and auxetic low-density polymeric foams from full-field measurements. *J Strain Anal Eng Des* 45:233–253
 96. Li QM, Mines RAW, Birch RS (2000) The crush behaviour of Rohacell-51WF structural foam. *Int J Solids Struct* 37:6321–6341
 97. Subhash G, Liu Q, Gao X-L (2006) Quasistatic and high strain rate uniaxial compressive response of polymeric structural foams. *Int J Impact Eng* 32:1113–1126
 98. Viana GM, Carlsson LA (2002) Mechanical properties and fracture characterization of cross-linked PVC foams. *J Sandw Struct* {...}. doi: 10.1106/109963602022227
 99. Deng R, Davies P, Bajaj AK (2003) Application of fractional derivatives to modeling the quasi-static response of polyurethane foam. 819–828
 100. Hong S, Jin H, Lu W, Laboratories SN (2008) Full-field characterization of tensile and fracture behavior of a rigid polyurethane foam using Digital Image Correlation
 101. Jin H, Lu W-Y, Hong S, et al (2007) Fracture behavior of polyurethane foams. Vol 10 *Mech Solids Struct Parts A B* 951–954
 102. Pampolini G, Del Piero G (2009) Strain localization in polyurethane foams: Experiments and theoretical model. In: Ganghoffer J-F, Pastrone F (eds) *Mechanics of Microstructured Solids: Cellular Materials, Fibre Reinforced Solids and Soft Tissues*. Springer Berlin Heidelberg, Berlin, Heidelberg, pp 29–38
 103. Iddamalgoda IDIP, Coorey R (2011) Study of non-linear stress-strain curves of locally available low-density polyurethane foams. In: *Proceedings of the Technical Sessions*, Institute of Physics, Sri Lanka. pp 1–8
 104. Deshpande V. S, Fleck N. (2001) Multi-axial yield behaviour of polymer foams. *Acta Mater* 49:1859–1866
 105. Colloca M, Dorogokupets G, Gupta N, Porfiri M (2012) Mechanical properties and failure mechanisms of closed-cell PVC foams. *Int J Crashworthiness* 17:327–336
 106. Tita V, Júnior MFC Anisotropic mechanical behavior of polymeric foams. *SPE - Plast Res*

Online 2–4

107. Caliri Júnior MF, Soares GP, Angélico RA, et al (2012) Study of an anisotropic polymeric cellular material under compression loading. *Mater Res* 15:359–364
108. Luong DD, Pinisetty D, Gupta N (2013) Compressive properties of closed-cell polyvinyl chloride foams at low and high strain rates: Experimental investigation and critical review of state of the art. *Compos Part B Eng* 44:403–416
109. Lo KH, Miyase A, Wang SS (2016) Stiffness predictions for closed-cell PVC foams. *J Compos Mater* 51:3327–3336
110. Tita V, Caliri MF, Angelico RA, Canto RB (2012) Experimental analyses of the poly(vinyl chloride) foams' mechanical anisotropic behavior,. *Polym Eng Sci* 52:
111. Tagarielli VLL, Deshpande VSS, Fleck NA (2008) The high strain rate response of PVC foams and end-grain balsa wood. *Compos Part B Eng* 39:83–91
112. Srinivasagupta D, Joseph B, Majumdar P, et al (2003) Effect of processing conditions and material properties on the debond fracture toughness of foam-core sandwich composites: experimental optimization. *Compos Part A Appl Sci Manuf* 34:1097–1104
113. Chakravarty U, Mahfuz H, Saha M, Jeelani S (2003) Strain rate effects on sandwich core materials: An experimental and analytical investigation. *Acta Mater* 51:1469–1479
114. Kabir ME, Saha MC, Jeelani S (2006) Tensile and fracture behavior of polymer foams. *Mater Sci Eng A* 429:225–235
115. Mills NJ, Zhu HX (1999) The high strain compression of closed-cell polymer foams. *J Mech Phys Solids* 47:669–695
116. Daniel IM, Cho J-M (2011) Characterization of anisotropic polymeric foam under static and dynamic loading. *Exp Mech* 51:1395–1403
117. Viana GM, Carlsson LA (2002) Mechanical properties and fracture characterization of cross-linked PVC foams. *J Sandw Struct Mater* 4:33–113
118. Lim GT, Altstädt V, Ramsteiner F (2009) Understanding the compressive behavior of linear and cross-linked poly(vinyl chloride) foams. *J Cell Plast* 45:419–439
119. Liu Z, Scanlon MG (2003) Scaling Young's modulus of cellular solids. *J Mater Sci Lett* 22:547–548
120. McCullough, Fleck (2000) The stress–life fatigue behaviour of aluminium alloy foams. *Fatigue Fract Eng Mater Struct* 23:199–208
121. Harte A-M, Fleck NA, Ashby MF (1999) Fatigue failure of an open cell and a closed cell aluminium alloy foam. *Acta Mater* 47:2511–2524
122. Shenoi R a., Clark SD, Allen HG (1995) Fatigue behaviour of polymer composite sandwich beams. *J Compos Mater* 29:2423–2445

-
123. Kanny K, Mahfuz H (2005) Flexural fatigue characteristics of sandwich structures at different loading rates. *Compos Struct* 67:403–410
 124. Kanny K, Mahfuz H, Carlsson LA, et al (2002) Dynamic mechanical analyses and flexural fatigue of PVC foams. *Compos Struct* 58:175–183
 125. Carlsson LA, Kardomateas GA (2011) Structural and failure mechanics of sandwich composites. Springer, London New York
 126. Shivakumar KN, Smith SA (2004) In situ fracture toughness testing of core materials in sandwich panels. *J Compos Mater* 38:655–668
 127. Abrate S (2008) Criteria for yielding or failure of cellular materials. *J Sandw Struct Mater* 10:5–51
 128. Zenkert D, Bäcklund J (1989) PVC sandwich core materials: Mode I fracture toughness. *Compos Sci Technol* 34:225–242
 129. Saenz EE, Carlsson LA, Karlsson A (2011) Characterization of fracture toughness (G_c) of PVC and PES foams. *J Mater Sci* 46:3207–3215
 130. Zenkert D, Burman M, Shipsha A (2000) On mode I fatigue crack growth in foam core materials for sandwich structures. *J. Sandw. Struct. Mater.* 2:103–116
 131. Chen CP, ANDERSON WB, Lakes RS, et al (1982) Cellular polymers. *Cell Polym* 13:16–32
 132. Gibson RF (2011) A simplified analysis of deflections in shear-deformable composite sandwich beams. *J Sandw Struct Mater* 13:579–588
 133. Siivola JT, Minakuchi S, Takeda N (2015) Effect of temperature and humidity conditions on polymethacrylimide (PMI) foam core material and indentation response of its sandwich structures. *J Sandw Struct Mater* 17:335–358
 134. Burman M, Zenkert D (1997) Fatigue of foam core sandwich beams—2: effect of initial damage. *Int J Fatigue* 19:563–578
 135. Shipsha, Burman, Zenkert, Ho KT (1999) Interfacial fatigue crack growth in foam core sandwich structures. *Fatigue Fract Eng Mater Struct* 22:123–131
 136. Leijten J, Bersee HEN, Bergsma OK, Beukers A (2009) Experimental study of the low-velocity impact behaviour of primary sandwich structures in aircraft. *Compos Part A Appl Sci Manuf* 40:164–175
 137. (2006) ASTM. C393-06, Standard Test Method for Core Shear Properties of Sandwich Constructions by Beam Flexure
 138. Allen H (1969) Analysis and design of structural sandwich panels. Pergamon Press, London
 139. (2000) ASTM. C273-00, Standard Test Method for Shear Properties of Sandwich Core Materials

-
140. Juntikka R, Hallstrom S (2007) Shear characterization of sandwich core materials using four-point bending. *J Sandw Struct Mater* 9:67–94
 141. Grédiac M, Dufort L, Grediac M, et al (2002) Experimental evidence of parasitic effects in the shear test on sandwich beams. *Exp Mech* 42:186–193
 142. Feichtinger K a. (1989) Test methods and performance of structural core materials -1. Static properties. *J Reinf Plast Compos* 8:334–357
 143. Nordstrand TM, Carlsson LA (1997) Evaluation of transverse shear stiffness of structural core sandwich plates. *Compos Struct* 37:145–153
 144. Kanny K, Jeelani S, Thomas T, et al (2004) Fatigue of crosslinked and linear PVC foams under shear loading. *J Reinf Plast Compos* 23:601–612
 145. Kiepert KT, Miskioglu I, Sikarskie DL (2001) Fatigue issues of polymeric foam sandwich core materials in simple shear. *J Sandw Struct Mater* 3:5–21
 146. Juntikka R, Hallstrom S (2007) Shear characterization of sandwich core materials using four-point bending. *J Sandw Struct Mater* 9:67–94
 147. Zainuddin S, Mahfuz H, Jeelani S (2010) Enhancing fatigue performance of sandwich composites with nanophased core. *J Nanomater* 2010:
 148. Benderly D, Zafran J, Putter S (2003) Shear testing of polymeric foams. *J Test Eval* 31:405–412
 149. O'Connor DJ (1984) An evaluation of test methods for shear modulus of sandwich cores. *Int J Cem Compos Light Concr* 6:3–12
 150. Gdoutos E, Daniel IMM (2008) Failure modes of composite sandwich beams. *Theor Appl Mech* 35:105–118
 151. Herranen H, Eerme M, Majak J, et al (2012) Design and Testing of Sandwich Structures with Different Core Materials. *Mater Sci* 18:
 152. Steeves CA (2012) Optimizing sandwich beams for strength and stiffness. *J Sandw Struct Mater* 14:573–595
 153. Dawood M, Taylor E, Ballew W, Rizkalla S (2010) Static and fatigue bending behavior of pultruded GFRP sandwich panels with through-thickness fiber insertions. *Compos Part B Eng* 41:363–374
 154. Gupta N, Woldesenbet E (2005) Characterization of flexural properties of syntactic foam core sandwich composites and effect of density variation. *J Compos Mater* 39:2197–2212
 155. Lingaiah K, Suryanarayana BG (1991) Strength and stiffness of sandwich beams in bending. *Exp Mech* 31:1–7
 156. Xiong J, Ma L, Pan S, et al (2012) Shear and bending performance of carbon fiber composite sandwich panels with pyramidal truss cores. *Acta Mater* 60:1455–1466

-
157. Ayorinde E, Ibrahim R, Berdichevsky V, et al (2012) Development of damage in some polymeric foam-core sandwich beams under bending loading. *J Sandw Struct Mater* 14:131–156
 158. Thomsen OT, Bozhevolnaya E, Lyckegaard A (2005) Structurally graded core junctions in sandwich elements. *Compos Part A Appl Sci Manuf* 36:1397–1411
 159. Reyes G, Rangaraj S (2011) Fracture properties of high performance carbon foam sandwich structures. *Compos Part A Appl Sci Manuf* 42:1–7
 160. Whisler D, Chen A, Kim H, et al (2012) Methodology for exciting dynamic shear and moment failure in composite sandwich beams. *J Sandw Struct Mater*. doi: 10.1177/1099636212452054
 161. Gibson LJ, Ashby MF, Harley BA (2010) Honeycomb-like materials in nature. In: *Cellular Materials in Nature and Medicine*. Cambridge University Press
 162. Zhang ZY, Richardson MOW (2005) Visualisation of barely visible impact damage in polymer matrix composites using an optical deformation and strain measurement system (ODSMS). *Compos Part A Appl Sci Manuf* 36:1073–1078
 163. Jerabek M, Major Z, Lang RW (2010) Strain determination of polymeric materials using digital image correlation. *Polym Test* 29:407–416
 164. Guastavino R, Göransson P (2007) A 3D displacement measurement methodology for anisotropic porous cellular foam materials. *Polym Test* 26:711–719
 165. Jin H, Lu W-Y, Scheffel S, et al (2007) Full-field characterization of mechanical behavior of polyurethane foams. *Int J Solids Struct* 44:6930–6944
 166. Heinz SR, Wiggins JS (2010) Uniaxial compression analysis of glassy polymer networks using digital image correlation. *Polym Test* 29:925–932
 167. Fan X, Pflug J, Vangrimde B, et al (2002) Four-point bending evaluation of sandwich materials with strain mapping system. In: *Proc. 10th Eur. Conf. Compos. Mater. (ECCM-10)*
 168. Tung SH, Shih MH, Sung WP, Shyu JG Testing method for the mechanical properties of foam heat insulation construction material
 169. McDonald SA, Ravirala N, Withers PJ, Alderson A (2009) In situ three-dimensional X-ray microtomography of an auxetic foam under tension. *Scr Mater* 60:232–235
 170. Roux S, Hild F, Viot P, Bernard D (2008) Three-dimensional image correlation from X-ray computed tomography of solid foam. *Compos Part A Appl Sci Manuf* 39:1253–1265
 171. Périé JN, Leclerc H, Roux S, Hild F (2009) Digital image correlation and biaxial test on composite material for anisotropic damage law identification. *Int J Solids Struct* 46:2388–2396
 172. Zhang D, Zhang X, Cheng G (1999) Compression strain measurement by digital speckle

-
- correlation. *Exp Mech* 39:62–65
173. Chiang F, Uzer G (2008) Mapping full field deformation of auxetic foams using digital speckle photography. *Phys status solidi* 245:2391–2394
 174. Taher ST, Thomsen OT, Dulieu-Barton JM (2011) Mechanical characterization of PVC foam using Digital Image Correlation and nonlinear FE analysis. In: 18th International Conference on Composite Materials (ICCM). Jeju Island, pp 1–5
 175. Hosseinabadi HG, Bagheri R, Altstädt V (2017) A numerical approach to study the post-yield softening in cellular solids: role of microstructural ordering and cell size distribution. *Acta Mech* 228:2005–2016
 176. Easterling KE, Harrysson R, Gibson LJ, Ashby MF (1982) On the mechanics of Balsa and other woods. *Proc R Soc London A Math Phys Sci* 383:31–41
 177. Gibson RF (2010) A mechanics of materials/fracture mechanics analysis of core shear failure in foam core composite sandwich beams. *J Sandw Struct Mater* 13:83–95
 178. Persson K, Shipsha A, Zenkert D (2004) Static indentation and unloading response of sandwich beams. *Compos. Part B Eng.* 35:511–522

Curriculum Vitae

Personal Data	Seyed Amir Fathi born on 13. September 1984 in Teheran	
Marital Status	Married	
Nationality	German	
Education	1998 to 2002	Amirkabir High School <i>Diploma in Mathematics and Physics</i>
	2003 to 2009	Amirkabir University of Technology <i>B.Sc. in Polymer Engineering</i>
	2009 to 2011	Friedrich-Alexander-Universität Erlangen-Nürnberg <i>M.Sc. (hons) in Advanced Materials & Processes (MAP)</i>
Occupation	2012 to 2015	University of Bayreuth <i>Scientific Staff Member</i>
	2016 to present	Adidas AG <i>Senior Manager Technology Innovation</i>

List of Reviewed Publications

A. Fathi, J.-H. Keller, V. Altstädt

Full-field shear analyzes of sandwich core materials using Digital Image Correlation (DIC) *Journal of Sandwich Structures and Materials*

Composites Part B: Engineering (2014)

A. Fathi, V. Altstädt

Book Chapter: Mechanical Properties of Multifunctional Foam Core Materials

Multifunctionality of Polymer Composites (Elsevier 2015)

A. Fathi, F. Wolff-Fabris, V. Altstädt, R. Gätzi

An Investigation on the Flexural Properties of Balsa and Polymer Foam Core Sandwich Structures: Influence of Core Type and Contour Finishing Options

Journal of Sandwich Structures and Materials (2013)

A. Fathi, D. Raps, J. Gensel, V. Altstädt,

Full-field Compression Response of PET Foams: Influence of Multi-Sclae Microstructures

Cellular Materials (In Submission)

A. Abbasi Moud, A. Javadi, H. Nazockdast, A. Fathi, V. Altstaedt

Effect of dispersion and selective localization of carbon nanotubes on rheology and electrical conductivity of polyamide 6 (PA6), Polypropylene (PP), and PA6/PP nanocomposites

Journal of Polymer Science Part B: Polymer Physics (2014)

G. Duan, S. Jiang, V. Jérôme, J. H Wendorff, A. Fathi, J. Uhm, V. Altstädt, M. Herling, J. Breu, R. Freitag, S. Agarwal, A. Greiner

Ultralight, Soft Polymer Sponges by Self-Assembly of Short Electrospun Fibers in Colloidal Dispersions

Advanced Functional Materials (2015)